Université de Genève
Département de Physique Nucléaire et Corpusculaire

Faculté des Sciences
Professeur Giuseppe Iacobucci

Search For Resonances In The Dijet Mass Spectrum With The Atlas Experiment At The Lhc

THÈSE

présenté à la Faculté des Sciences de l'Université de Genève
pour obtenir le grade de Docteur ès science, mention physique
par

Francesco Guescini

de
Fano, Italia

Thèse n° 4954

Genève
2016

UNIVERSITÉ DE GENÈVE

FACULTÉ DES SCIENCES

Doctorat ès sciences
Mention physique

Thèse de *Monsieur Francesco GUESCINI*

intitulée :

"Search for Resonances in the Dijet Mass Spectrum with the ATLAS Experiment at the LHC"

La Faculté des sciences, sur le préavis de Monsieur G. IACOBUCCI, professeur ordinaire et directeur de thèse (Département de physique nucléaire et corpusculaire), Monsieur T. GOLLING, professeur associé (Département de physique nucléaire et corpusculaire), Madame L. DI CIACCIO, professeure (Centre national de recherche scientfique, Université de Savoie, Annecy, France) et Madame C. DOGLIONI, docteure (Département de physique, Université de Lund, Suède), autorise l'impression de la présente thèse, sans exprimer d'opinion sur les propositions qui y sont énoncées.

Genève, le 8 juillet 2016

Thèse - 4954 -

Le Doyen

N.B. - La thèse doit porter la déclaration précédente et remplir les conditions énumérées dans les "Informations relatives aux thèses de doctorat à l'Université de Genève".

alla mia famiglia

For a long period of time there was much speculation and controversy about where the so-called 'missing matter' of the Universe had got to. All over the Galaxy the science departments of all the major universities were acquiring more and more elaborate equipment to probe and search the hearts of distant galaxies, and then the very centre and the very edges of the whole Universe, but when eventually it was tracked down it turned out in fact to be all the stuff which the equipment had been packed in.

Mostly Harmless, Douglas Noel Adams

Abstract

The unprecedented collision energy reached and the considerable integrated luminosity produced by the LHC allow its experiments to investigate the existence of new physics phenomena beyond the Standard Model of particle physics at the TeV scale. This thesis presents the search performed by the ATLAS Collaboration for evidence of new physics manifesting as localised resonances in the dijet invariant mass distribution of events with large transverse momenta. No evidence of resonant phenomena outside of the Standard Model have been observed in the 20.3 fb^{-1} of data collected in 2012 at $\sqrt{s} = 8$ TeV nor in the 3.6 fb^{-1} of data collected in 2015 at $\sqrt{s} = 13$ TeV. Limits have been set at 95% Credibility Level on the cross-section times acceptance of selected benchmark models. Excited quarks with masses below 4.06 TeV and Quantum Black Holes, QBH, with masses below 5.2 TeV have been excluded using the 2012 datasets. These limits have then been further extended to 5.66 TeV (excited quarks) and 8.3 TeV (QBH) using the 2015 datasets. The reach of the dijet analysis at large integrated luminosities and at a collision energy of $\sqrt{s} = 14$ TeV has been investigated. The analysis sensitivity to excited quarks and QBHs for 5σ discoveries is expected to improve by roughly 1 TeV for each additional order of magnitude of integrated luminosity and up to the 3000 fb^{-1} to be delivered by HL-LHC, pushing the analysis reach to 6 TeV and 9-10 TeV for the two above-mentioned models by the end of Run-2.

Résumé

L'énérgie sans précédents atteinte ainsi que la considérable luminosité intégrée produite par le LHC permettent à ses expériences d'étudier l'existence de nouveaux phénomènes physiques au-delà du Modèle Standard de la physique des particules à l'échelle du TeV. Cette thèse présente la recherche d'évidence de nouvelle physique effectuée par la Collaboration ATLAS se manifestant sous forme de résonances dans la distribution de masse invariante des événements à grandes quantités de mouvement transverse. Aucune évidence de phénomènes au-delà du Modèle Standard n'a été observée avec l'analyse de 20,3 fb^{-1} de données collectées en 2012 à $\sqrt{s} = 8$ TeV ni avec les 3,6 fb^{-1} de données collectées en 2015 à $\sqrt{s} = 13$ TeV. Des limites ont été posées à 95% de Niveau de Crédibilité sur la section efficace multipliée par l'acceptance des modèles de référence. Les quarks excités de masses inférieures à 4,06 TeV et les trous noirs quantiques de masses inférieures à 5,2 TeV ont étés exclus par les données de 2012. Ces limites ont été étendues à 5,66 TeV (quarks excités) et 8,3 TeV (trous noirs quantiques) avec les données de 2015. La portée de l'analyse dijet à grandes valeurs de luminosité intégrée et à une énergie de collisions de $\sqrt{s} = 14$ TeV a été examinée. Il est prévue une augmentation de la sensibilité de l'analyse pour les quarks excités et pour les trous noirs quantiques pour des découvertes à 5σ d'environ 1 TeV pour chaque ordre de grandeur supplémentaire de données et jusqu'à 3000 fb^{-1} délivrées par le HL-LHC, amenant la portée de l'analyse à la fin du Run-2 à 6 TeV et 9-10 TeV respectivement pour les deux modèles mentionnées ci-dessus.

Personal Contributions

The results presented in this thesis have been achieved thanks to the coordinated efforts of the members of the ATLAS Collaboration and in particular of the ATLAS dijet analysis team. For this reason the analysis is described in this thesis as one coherent work. However the personal contributions made by the author are outlined below.

- **Chapter 5: Jet Angular Resolution.** The author has personally performed the analysis presented, from the definition of the strategy to the implementation of its framework and the derivation of the results. This work included the validation of the jet origin correction applied in the jet calibration process.
- **Chapter 6: Exotic Dijet Resonance Analysis.** The author has actively participated in the 8 TeV and the 13 TeV analyses presented. The contributions provided cover a wide range of topics, spanning from the analysis framework and software development to the event and jet cleaning and from fit stability and robustness to the analysis sensitivity to small and wide signals.
- **Chapter 7: Quo Vadis Exotic Dijet?** The author has coordinated the analysis described in this chapter and took care of setting the analysis sensitivity strategy and implementing its framework. Particular focus was put on the luminosity and sensitivity scans to determine the discovery luminosity for the benchmark models considered.

Contents

Introduction

What is the most immediate way of finding new physics?

In order to better answer this question, we may look back at some of the most significant discoveries of particle physics made at particle colliders and take some examples. We may take the example of the J/ψ discovery [1, 2] back in 1974, when the observation of a resonance at 3.1 GeV gave the evidence for the existence of a fourth quark: the charm quark. We may also take the example given by the discovery of the τ lepton [3] in 1975, where the observation of a localised excess in the cross section of events with an electron, a muon and at least two additional undetected particles (i.e. the four total neutrinos from the decay of the two τs produced in the collisions) for center of mass energies above 4 GeV lead to the introduction of the τ in the Standard Model of particle physics. Another example would be the Upsilon meson [4] and the observation in 1977 of $b\bar{b}$ resonances, proving the existence of a third quark family. A similar case would be that of the Z and W bosons [5, 6] in 1983, whose discoveries were allowed by the observation of localised excesses in the dilepton mass and transverse mass distributions respectively. More recently, in 1995, the observation of $t\bar{t}$ events made by the CDF [7] and DØ [8] Collaborations marked the discovery of the top quark, completing the picture of three quark families. The most recent example is that of the Higgs boson discovery, performed by the ATLAS [9] and CMS [10] Collaborations in 2012 and achieved by observing a sharp resonance in the $H \to ZZ^* \to 4l$ and $H \to \gamma\gamma$ channels.

Some of these discoveries were real breakthroughs in particle physics, others were experimental confirmations of what some theories were predicting. In all these examples the discovery was given by a localised excess in an invariant mass or energy distribution. It is therefore interesting to pursue this kind of searches where a new resonant particle emerges as a localised excess in the invariant mass distribution of its decay products.

Nowadays, the Large Hadron Collider at CERN is the most powerful particle collider ever built, smashing protons together at an energy in the center of mass frame of 13 TeV. If any new physics phenomena couples to the hadrons being collided, it should also produce hadrons in the final state, manifesting at detector level as jets. For this reason, despite the overwhelming background coming from strong interactions as the LHC collides protons, it is of the highest importance to look in the dijet invariant mass distribution for any striking evidence of physics beyond the Standard Model. Thanks to its model-independent strategy, the dijet analysis is ultimately sensitive to many kinds of new resonances and new processes, such as those produced by Dark Matter mediators, gravitational effects

and the compositeness of the quarks, just to list a few.

This thesis presents the dijet analyses performed by the ATLAS Collaboration on the 2012 8 TeV [11] and 2015 13 TeV [12] datasets and to which the author has personally contributed. The analysis looks for localised excesses in the dijet invariant mass spectrum of inclusive events using a model-independent approach. The background is extracted with a data-driven method and benchmark models are used to set limits on a series of new physics phenomena. The author's contributions cover the development of the analysis framework, the preparation of data and simulation samples, the definition and optimisation of event and jet cleaning criteria, the tests on the stability and robustness of the background extraction procedure, the investigation of the analysis sensitivity and the estimation of the analysis reach in the future.

Chapters 1 and 2 present the Large hadron Collider and the ATLAS experiment respectively. In Chapter 3 an introduction to the Standard Model of particle physics is given. Chapter 4 gives the definition of hadronic jets and how these have been reconstructed and calibrated within the ATLAS Collaboration in 2012 and 2015. The measurement of the jet angular resolution, source of uncertainty for all jet analyses, is presented in Chapter 5. The dijet analysis is thoroughly described in Chapter 6, with a comparison between the 2012 8 TeV and 2015 13 TeV strategies. The study of the dijet analysis reach at very large integrated luminosities is presented in Chapter 7.

Chapter 1

The Large Hadron Collider

The Large hadron Collider, LHC, is a proton-proton collider located at CERN, Geneva, on the boarder between Switzerland and France [13]. It is designed to achieve energies in the center of mass up to $\sqrt{s} = 14$ TeV, which makes it the most powerful accelerator ever built. It was conceived to investigate the accuracy and the limits of the predictions given by the Standard Model of particle physics, SM, up to the TeV scale and in particular to search for the Higgs boson. Its high energy in the center of mass makes it suitable to shed light on the existence of physics beyond the Standard Model.

The LHC is located ∼100 m underground in the same 26.7 km long tunnel that was drilled for the Large Electron Positron collider, LEP. Contrary to particle-antiparticle accelerators, such as Tevatron (proton-antiproton), that may use a single beampipe to circulate the two beams to collide, LHC has two different pipes for the two counter rotating proton beams. In four different interaction regions, IR, around the ring, the two beams cross each other to produce collisions (see Figure 1.1). These locations are occupied by the main LHC experiments: ATLAS (see Chapter 2) at IR1, ALICE (*A Large Ion Collider Experiment* [15]) at IR2, CMS (*Compact Muon Solenoid* [16]) at IR5 and LHCb (LHC *beauty* [17]) at IR8. Of the remaining four interaction regions, two are occupied by collimations systems (IR3 and IR7), one by radio frequency systems (IR4) and one by the beam dump insertion (IR6), which separately extracts the beams out of the machine.

1.1 Acceleration Chain

Protons circulating in LHC are accelerated in five steps (see Figure 1.2). At the beginning of the chain, protons are extracted from gaseous hydrogen molecules and are given an energy of 50 MeV by a small linear accelerator, Linac2. They are then accelerated to an energy of 1.4 GeV by the BOOSTER, the first of the rings composing the proton acceleration chain. Subsequently the Proton Synchrotron, PS, increases the energy of the beam up to 26 GeV, before injecting the protons into the Super Proton Synchrotron, SPS, which boosts the protons to 450 GeV. The protons are now ready to be injected into LHC. The Large Hadron Collider finally accelerates the beams to the final collision energy: 4 TeV in 2012 and 6.5 TeV in 2015.

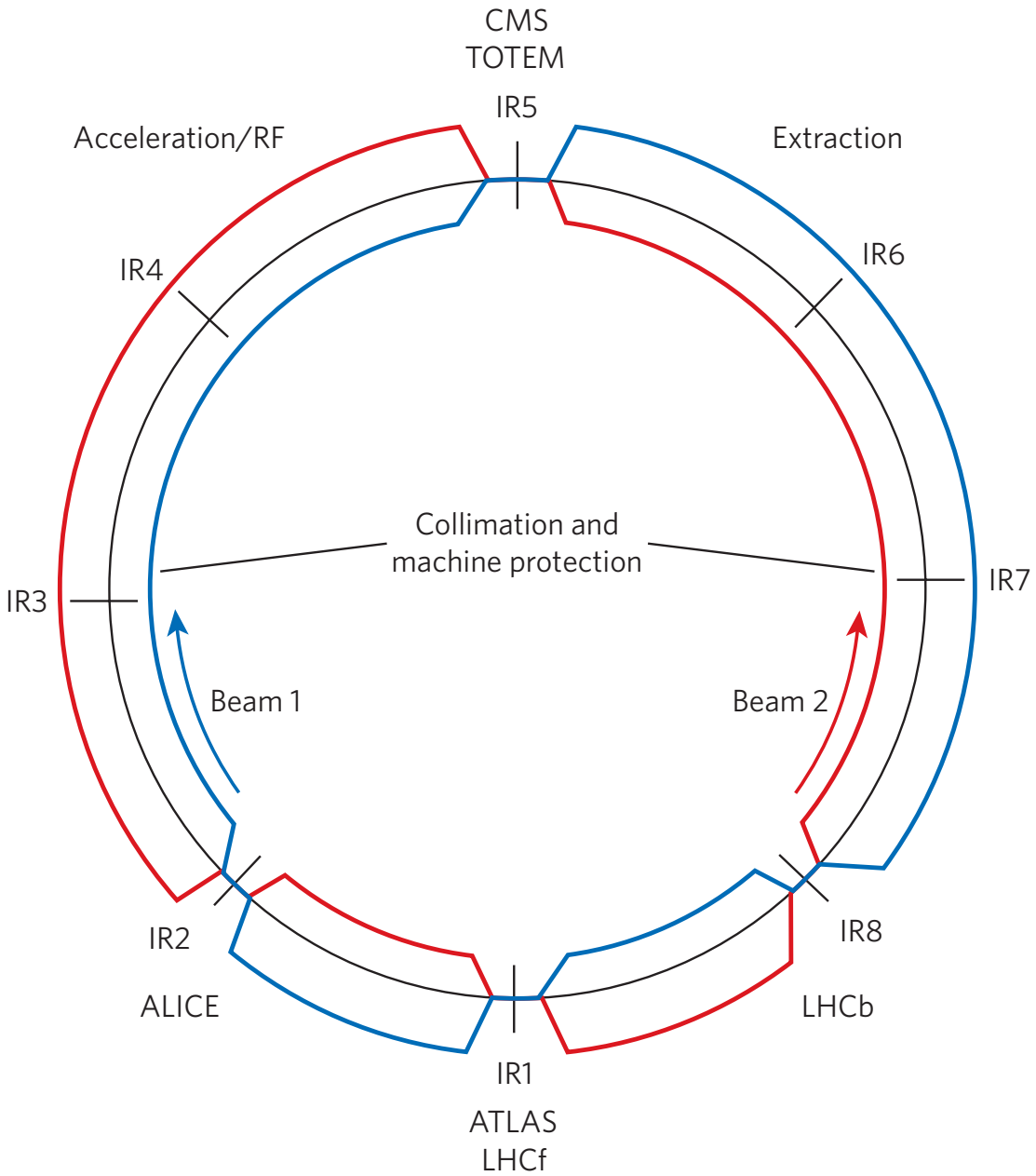

Figure 1.1: schematic representation of the Large Hadron Collider [14]. In evidence are the four Interaction Regions, Ir, where the two proton beams cross and which host the four main Lhc experiments: Atlas (Ir1), Alice (Ir2), Cms (Ir5) and LHCb (Ir8).

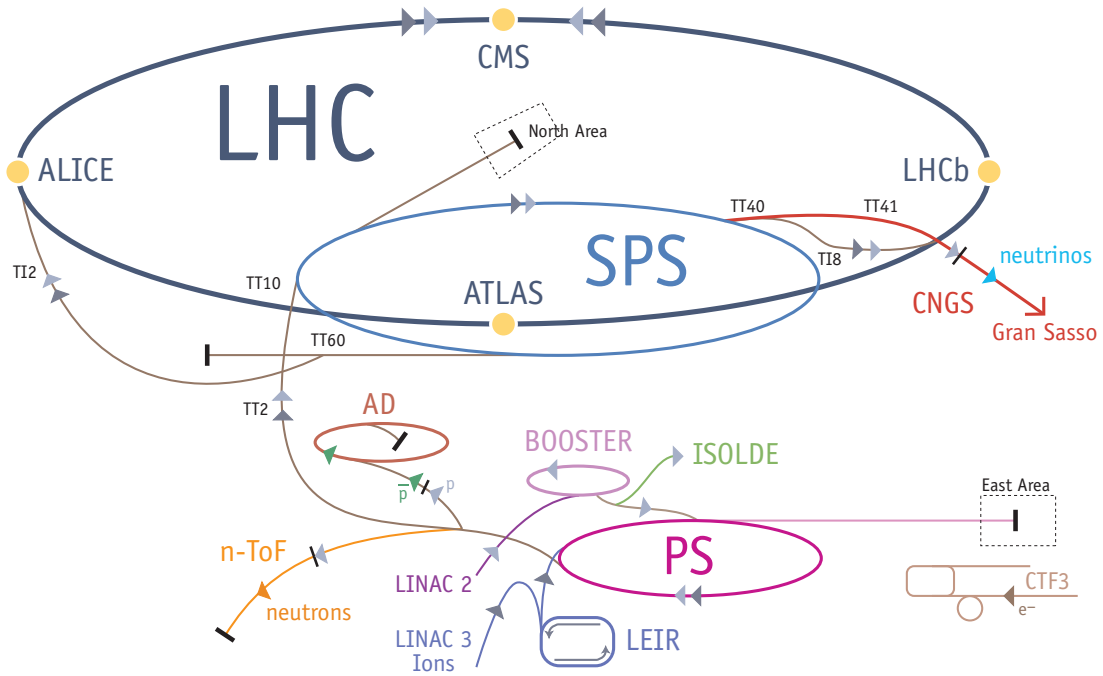

Figure 1.2: schematic representation of the CERN acceleration complex [18].

1.2 Design

LHC is composed of 1232 superconducting dipole magnets providing a field of 8.33 T at an operating temperature of 1.9 K that is reached by using superfluid helium. Each proton beam allows up to 2808 bunches of $\sim 10^{11}$ protons in the configuration where each bunch is separated from the other by 25 ns. The total beam current of 0.584 A corresponds to a stored beam energy of 362 MJ.

LHC has an unprecedented design luminosity of $L = 10^{34}$ cm^{-2}s^{-1}. Such a high luminosity is needed in order to investigate rare events with cross sections of a few pb. In a year of data taking at high luminosity LHC can provide experiments with an integrated luminosity of:

$$\int_{10^7 s} L \, \mathrm{d}t \sim 100 \text{ fb}^{-1} \tag{1.1}$$

When each bucket of the beams is filled, the expected inelastic collision rate is:

$$R = \sigma_{pp}^{\text{tot}} \times L = 80 \text{ mb} \times 10^{34} \text{ cm}^{-2}\text{s}^{-1} \sim 10^9 \text{ Hz} \tag{1.2}$$

where 80 mb is the proton-proton inelastic cross section at $\sqrt{s} = 14$ TeV.

The machine instantaneous luminosity strictly depends on some beam parameters and can be written as:

$$L = \frac{N_\text{b}^2 \, n_\text{b} \, f_\text{rev} \, \gamma_\text{r}}{4\pi \, \epsilon_\text{n} \, \beta^*} \, F \tag{1.3}$$

where the beam distribution is supposed to be gaussian in the transverse plane. N_{b} indicates the number of protons per bunch, n_{b} the number of bunches per beam, f_{rev} the revolution frequency, γ_{r} the relativistic gamma factor, ϵ_{n} is the normalised transverse beam emittance, β^* the beta function at the interaction point and F is the luminosity reduction factor due to the crossing angle between the beams at the interaction point.

Other factors contribute to set a limit on the maximum reachable luminosity. A limit to the maximum particle density per bunch is set by the beam-beam interactions experienced by the particles when traversing the interaction region and by the particles interactions within the same bunch. The safety of the machine plays an important role on the limits of the machine too. The total energy stored in the beam and in the LHC magnets is around 1 GJ. This huge amount of energy needs to be dissipated as safely and quickly as possible in case of a malfunction. The beam dumping system therefore introduces additional limits to the performance of the machine. The synchrotron radiation emitted by the beam, although small compared to LEP, imposes limits on the beam intensity due to the radiation absorbed by the cryogenic system.

Beam loss due to collisions, degradation of the beam intensity and beam emittance constantly contribute to the decay of the luminosity. The decay time is given by:

$$\tau = \frac{N_0^{\mathrm{tot}}}{L_0\ \sigma_{\mathrm{tot}}\ n_{\mathrm{IP}}} \simeq 45\ \mathrm{h} \tag{1.4}$$

where N_0^{tot} is the initial beam intensity, L_0 is the initial luminosity, σ_{tot} the total cross section and n_{IP} the number of interaction points. This results in:

$$N_{\mathrm{tot}}(t) = \frac{N_0^{\mathrm{tot}}}{1 + t/\tau} \tag{1.5}$$

$$L(t) = \frac{L_0}{(1 + t/\tau)^2} \tag{1.6}$$

Additional effects, like Touschek scattering and emittance blow-up, contribute to the limited lifetime of the beam, reducing the previous estimation to approximately $\tau \simeq 15$h.

1.3 Performance

The two proton beams were first successfully circulated in LHC in September 10th, 2008. Nine days later, a faulty electrical connection between two superconducting dipoles caused a large helium leak, resulting in a serious mechanical damage of the LHC. 53 dipoles had to be replaced. The repair and installation of new safety devices took more than one year. In November 2009 the two proton beams were circulated again in LHC and three days later the beams were collided at the injection energy of 450 GeV. In December 2009 LHC achieved the title of world most powerful collider by smashing protons at $\sqrt{s} = 2.36$ TeV, higher than Fermilab's Tevatron $\sqrt{s} = 1.96$ TeV. After the winter technical stop, LHC activities were resumed in February 2010 and in March LHC set a new record by colliding protons at $\sqrt{s} = 7$ TeV. That same year, LHC collided protons until November, delivering

to the experiments an integrated luminosity of 44.8 pb^{-1}. After resuming operations in 2011, in June, LHC finished delivering its first fb^{-1} of data to the experiments. By the end of the same year, LHC had delivered a total of 5.6 fb^{-1}, reaching a peak luminosity of 3.65 10^{33} $cm^{-2}s^{-1}$. In 2012 LHC operations resumed with the collision energy raised to 8 TeV. Throughout the year, 22.8 fb^{-1} of collisions have been delivered with an ever higher instantaneous luminosity of 7.73 10^{33} $cm^{-2}s^{-1}$. During the years 2013 and 2014 the first LHC long shutdown took place, allowing the accelerator to undergo upgrade works in order to increase the collision energy in the center of mass to $\sqrt{s} = 13$ TeV. In 2015 the the LHC has been able to produce 4.2 fb^{-1} of collision data with a peak luminosity of 5.02 10^{33} $cm^{-2}s^{-1}$.

On average, 20.7 and 13.7 interactions per bunch crossing, μ, have happened during the 2012 8 TeV and 2015 13 TeV data taking respectively [19, 20], as measured by the ATLAS detector (see Figure 1.5). Such a high collision rate contributes to the overlap in time of collisions coming from different bunch crossings. This time overlap goes by the name of *pile-up*. Most of these events are dominated by soft QCD interactions, with a consequent generation of low p_T particles. Pile-up events can be divided in *in-time* events, when soft collisions happen between the protons of two bunches crossing an interaction region, or *out-of-time*, when protons interact far from the interaction region. These so-called *minimum bias* events are a huge background to more interesting physics at high p_T.

	2012	2015
$\sqrt{s}$	8	13
$\langle\mu\rangle$	20.7	13.7
$\langle\mu\rangle_{max}$	69.5	28.1
maximum number of colliding bunches	1380	2232
bunch spacing [ns]	50	25, 50
ATLAS recorded integrated luminosity [fb^{-1}]	21.3	3.9
peak luminosity [10^{33} $cm^{-2}s^{-1}$]	7.73	5.02
maximum number of protons per bunch [10^{11}]	1.7	1.21

Table 1.1: LHC performance during 2012 and 2015 data taking [19, 20, 21].

1.3.1 Future

LHC will collide protons at $\sqrt{s} = 13$ TeV until the end of 2018, when the second long shutdown, LS2, will start. Until then, a total of 30-35 fb^{-1} per year are expected, therefore significantly increasing the 13 TeV integrated luminosity collected in 2015 by almost two orders of magnitude [22]. The peak luminosity will reach 10^{34} $cm^{-2}s^{-1}$ and the average number of interactions per bunch crossing will be ∼25–30. Following the LS2 (2018-2019), the LHC will enter the Run-3, doubling the luminosity reached in Run-2 and delivering 300 fb^{-1} over the course of the following three years. At that time the third long shutdown, LS3, will take place (2024-2026), setting the beginning of the High Luminosity

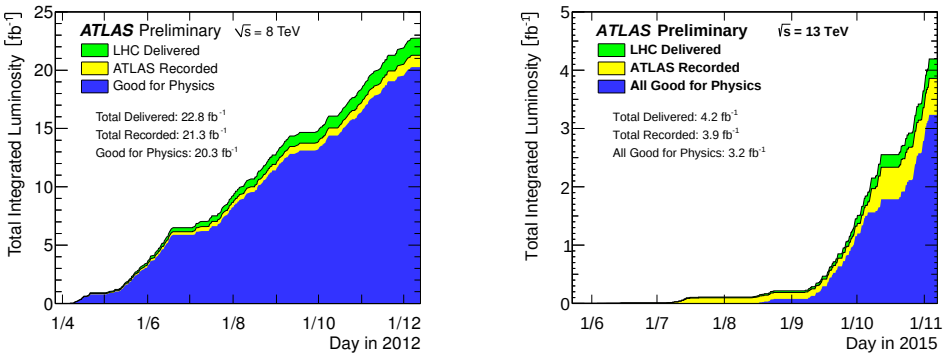

(a) (b)

Figure 1.3: LHC delivered and ATLAS recorded integrated luminosity as a function of time for 2012 (a) and 2015 (b) data taking [19, 20].

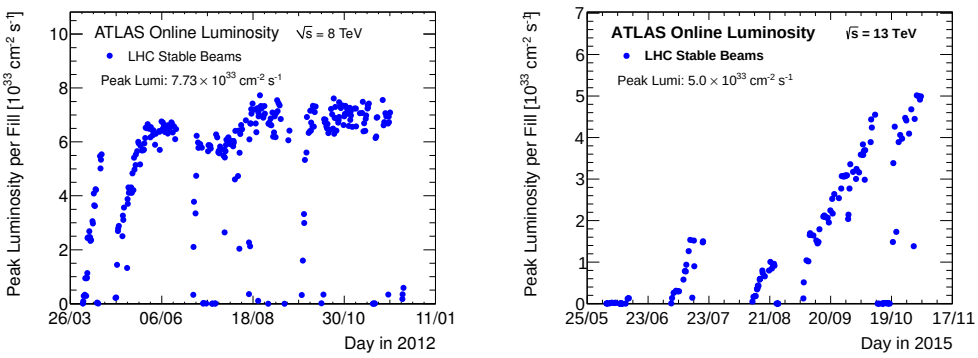

(a) (b)

Figure 1.4: LHC peak luminosity as a function of time for 2012 (a) and 2015 data taking (b) [19, 20].

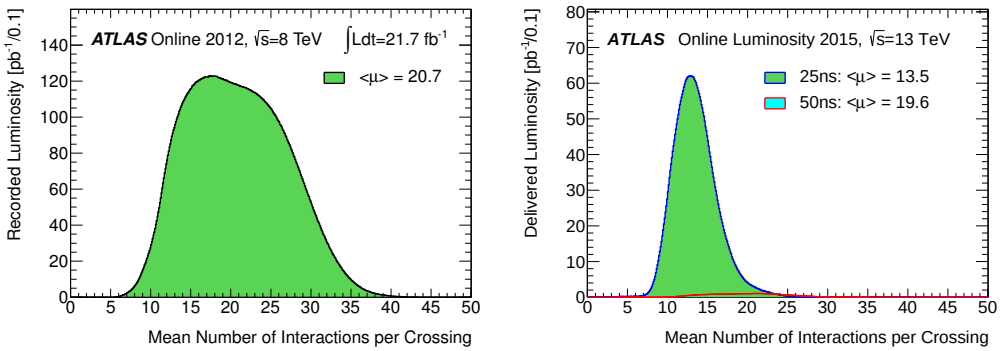

(a) (b)

Figure 1.5: average number of interactions per bunch crossing as measured by ATLAS during 2012 (a) and 2015 (b) data taking [19, 20].

LHC, HL-LHC, era [23, 24].

Chapter 2

The ATLAS Experiment

ATLAS, A Toroidal LHC ApparatuS, is a multi-purpose particle experiment designed for high energy and luminosity proton-proton collisions with an almost complete 4π coverage [25]. ATLAS is 44 m long and 25 m high and weights 7000 tons. It is installed in a cavern underground on the LHC at CERN. It has a cylindrical symmetry, with the barrel region sub-detectors coaxially oriented with respect to the beam and the end-cap sub-detectors perpendicularly oriented to the beam. The structure of the sub-detectors is organised in layers in the barrel region and in disks in the end-caps. ATLAS is composed of three main sub-systems:

- **Inner Detector**, ID: the innermost tracking system, it is immersed in a 2 T strong magnetic field;
- **Calorimeters**: placed outside of the ID solenoid, are responsible for the measurement of the energy of the particles;
- **Muon Spectrometer**, MS: is the outermost tracking device, dedicated to the measurement of muons.

2.1 Coordinate System

The origin of the ATLAS coordinate system is defined as the nominal interaction point, IP. The reference system is right-handed with the beam direction defining the z-axis and the x-y perpendicular plane. The x-axis points to the center of LHC while the y-axis points upwards. The A side of the experiment is the one with positive z (Geneva Airport side) while the C side is the one with z negative values. The (R, ϕ, z) coordinate system is preferred to (x, y, z) due to the symmetry of the experiment.

- R is the distance from the z-axis in the transverse plane:

$$R = \sqrt{x^2 + y^2}$$

- ϕ is the azimuthal angle measured from the x-axis in the transverse plane;

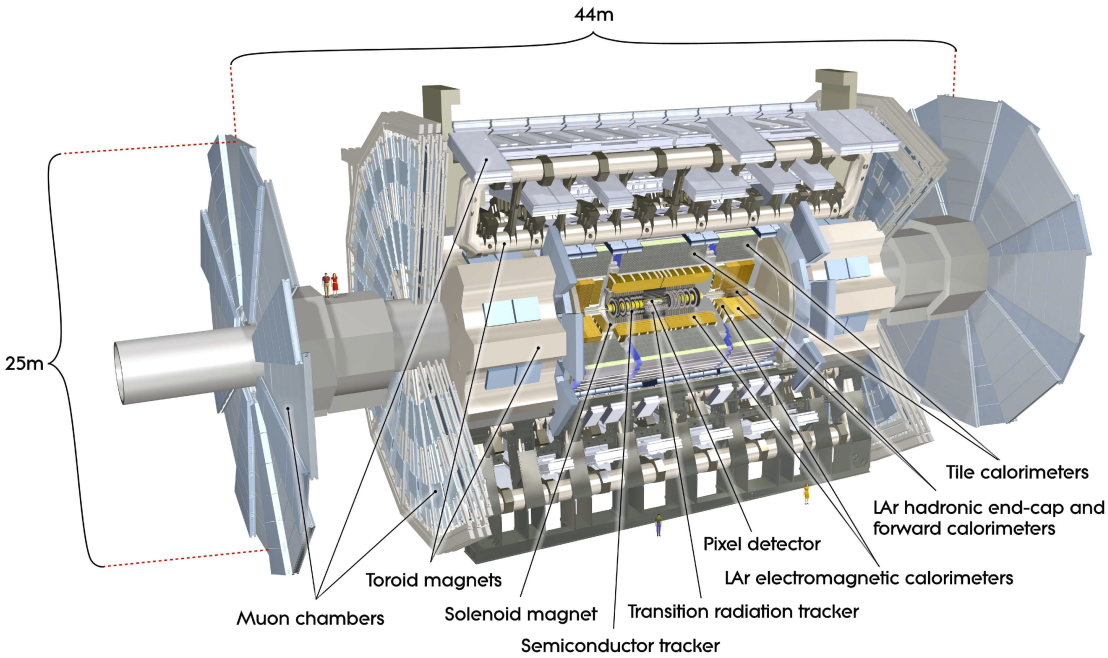

Figure 2.1: cut-away view of the ATLAS experiment [25].

- z is the z-axis coordinate.

The relation between R and z is given by:

$$\theta = \arccos \frac{z}{\sqrt{R^2 + z^2}} \tag{2.1}$$

where θ is the polar angle measured with respect to the beam axis in the longitudinal plane. The pseudorapidity, η, is frequently used in collider experiments instead of the θ polar angle. It is defined as:

$$\eta = -\ln\left(\tan\frac{\theta}{2}\right) \tag{2.2}$$

The pseudorapidity is an ultra-relativistic approximation of the rapidity, y:

$$y = \frac{1}{2}\ln\left(\frac{E + p_z}{E - p_z}\right) \tag{2.3}$$

The convenience of using the pseudorapidity lies in the fact that, given the large momentum, p, of most of the particles produced ($m \ll p$), it is a good approximation of the rapidity, which in turn has Lorentz invariant Δy values. The distance in the pseudorapidity-azimuthal space is defined as:

$$\Delta R = \sqrt{\Delta\eta^2 + \Delta\phi^2} \tag{2.4}$$

Assuming $m = 0$, particle four-vectors are indicated using the parameters: p_{T}, η, ϕ. Two additional parameters are needed in order to describe track trajectories inside the experimental volume. ATLAS uses the d_0 and z_0 parameters at the track perigee, the point of closest approach to the z-axis. d_0 is the distance of the track to the z-axis in the transverse plane, defined positive when the particle trajectory is clockwise. Similarly, z_0 is the z coordinate of the track at perigee.

2.2 Inner Detector

The Inner Detector, ID, is the closest ATLAS sub-detector to the IP. It is designed to provide pattern recognition and momentum resolution for charged particles. Its high granularity and proximity to the IP are fundamental for the reconstruction of particles trajectories and of primary and secondary vertices. It has a η coverage up to $|\eta| < 2.5$ and complete ϕ coverage in order to prevent as much as possible particles to escape undetected from the interaction region. As regards the transverse momentum measurement, the ID can go as low as 0.1 GeV. The ID closeness to the IP requires strong resistance of its components to the hard radiation it is constantly exposed to during machine operation. To reduce the background noise, the detector needs to be continuously cooled down. The ID is 7.024 m long and has a radius of 1.150 m and it is surrounded by a superconducting solenoid providing a magnetic field of 2 T.

The ID consists of four independent sub-detectors:

- **Insertable B-Layer**, IBL, is the innermost layer of the ID and is composed of 280 silicon pixel modules; the IBL has been added to ATLAS in 2014, during the first LHC long shutdown;
- **Pixel Detector**, is a silicon detector with 3 barrel layers and 3 disks per end-cap; provides 3 dimensional space points;
- **SemiConductor Tracker**, SCT, is a silicon detector outside of the Pixel Detector; it has 4 layers and 9 disks per end-cap; it provides 3 dimensional space points from pairs of hits on stereo layers;
- **Transition Radiation Tracker**, TRT, surrounding the SCT, is made of 73 layers of gaseous straws in the barrels and 160 layers in the end-cap regions.

The combination of the four detectors, together with the use of barrel and end-caps, results in accurate tracking and vertex reconstruction as well as flavour tagging.

2.2.1 Insertable B-Layer

The Insertable B-Layer, IBL, is the fourth and innermost layer of the ATLAS Pixel Detector [26, 27]. It has been designed to improve the tracking, vertex reconstruction and flavour tagging capabilities of the ATLAS ID and to compensate for possible inefficiencies of the Pixel B-Layer (see Section 2.2.2). The IBL has been installed after the end of Run-1,

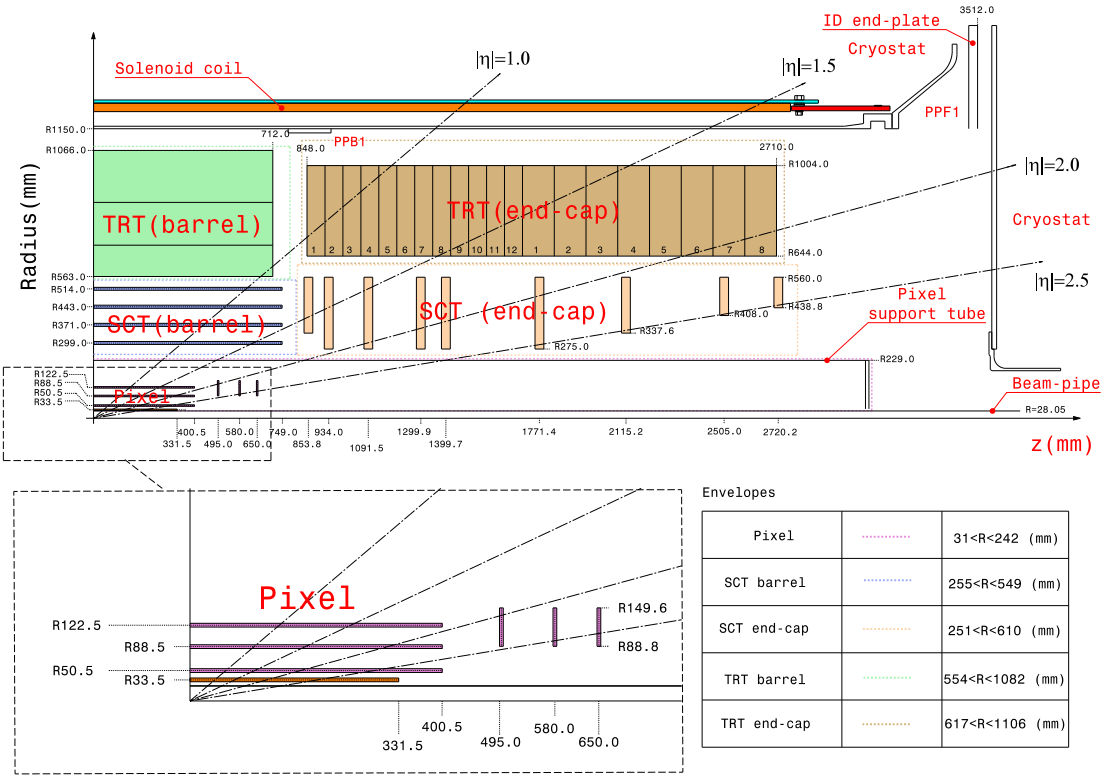

Figure 2.2: schematic representation of the ATLAS Inner Detector in Run-2 [26].

in 2014, during the first LHC long shutdown. It is located in the region between 31 mm and 40 mm from the beam axis and its insertion in the ATLAS ID has been allowed by the use of smaller-radius beam pipe for Run-2. The IBL has a modular structure composed of 14 0.664 m long staves, symmetrically arranged around the beam pipe and covering up to $|\eta| < 3.0$. Each stave is instrumented with 20 silicon sensor pixels: 12 pixel sensors using the same planar technology adopted in the other pixel modules of the ID and 4 pixel sensors using 3D technology on either sides of each stave. The readout of the sensors is performed by the FE-I4, a front-end chip with 26880 channels specifically designed for the IBL modules. Each planar sensor is read by two FE-I4 chips, due to their larger size, while 3D modules are read individually by one FE-I4. A total of 32 front-end chips are used per stave. Due to the its proximity to the ATLAS interaction point, the IBL is designed to withstand fluencies of 5×10^{15} 1 MeV equivalent neutrons per cm^2. The pixel size of the modules is 50×250 µm^2, almost half of that of the rest of the Pixel Detector, to reduce the occupancy. The cooling of the IBL is performed with two-phase CO_2 running in titanium pipes embedded within the staves. The cooling temperature can be as low as $-40°$ C in the pipes and $-15°$ C on the sensors. The significant improvement introduced by the IBL in the ATLAS flavour tagging performance is shown in Figure 4.9.

		radial extension [mm]	length [mm]
ID	envelope	$0 < R < 1150$	$0 < \|z\| < 3512$
beam pipe	Run-1	$29 < R < 36$	
	Run-2	$25 < R < 29$	
IBL	envelope	$31 < R < 40$	$0 < \|z\| < 332$
Pixel	envelope	$45.5 < R < 241$	$0 < \|z\| < 3092$
	3 barrel layers	$50.5 < R < 122.5$	$0 < \|z\| < 400.5$
	2×3 end-cap disks	$88.8 < R < 149.6$	$495 < \|z\| < 650$
SCT	barrel envelope	$255 < R < 594$	$0 < \|z\| < 805$
	end-caps envelope	$251 < R < 610$	$810 < \|z\| < 2797$
	4 barrel layers	$299 < R < 514$	$0 < \|z\| < 749$
	2×9 end-cap disks	$275 < R < 560$	$839 < \|z\| < 2735$
TRT	barrel envelope	$554 < R < 1082$	$0 < \|z\| < 780$
	end-caps envelope	$617 < R < 1106$	$827 < \|z\| < 2744$
	73 straws barrel planes	$563 < R < 1066$	$0 < \|z\| < 712$
	160 straw end-caps planes	$644 < R < 1004$	$848 < \|z\| < 2710$

Table 2.1: ATLAS Inner Detector parameters [26].

2.2.2 Pixel Detector

Together with the IBL, the Pixel Detector is responsible for providing robust tracking and reliable reconstruction of primary and secondary vertices. Its role is fundamental in determining track impact parameters for the identification of B hadrons and their decays. The Pixel Detector is composed of three barrel layers, at distances of 50.5, 88.5 and 122.5 mm from the beam pipe, and three disks per end-cap, at distances of 495, 580 and 650 mm from the IP, allowing a coverage up to $|\eta| < 2.5$. Its high granularity allows for high precision measurements. The silicon sensors are in fact segmented into rectangles in the R-ϕ and longitudinal planes, the *pixels*, providing three-dimensional space points. The size of these pixels ranges from 50×400 µm^2 to 50×600 µm^2. A single module of the Pixel Detector has a sensitive area of 63.4×24.4 µm^2, thickness of 250 µm and is read by 16 front-end electronics chips, each one possessing 2880 channels. The whole Pixel Detector is composed by 1744 modules, giving a total of 80.4 million readout channels. The overall precision of the detector is of 10 µm in the R-ϕ plane and 115 µm in the longitudinal plane, both in the barrels and in the end-caps. Due to the high radiation doses it is exposed to, the Pixel Detector inner barrel layer, the *B-Layer*, was designed to be replaced every few years. This exposure, together with the need of suppressing noise signals, requires the Pixel Detector to be constantly cooled down to a temperature between $-5°$ and $-10°$ C.

2.2.3 SemiConductor Tracker

The SemiConductor Tracker, SCT uses silicon microstrips to track charged particles and it is composed of four barrel layers and nine end-cap disks. Each SCT module is made

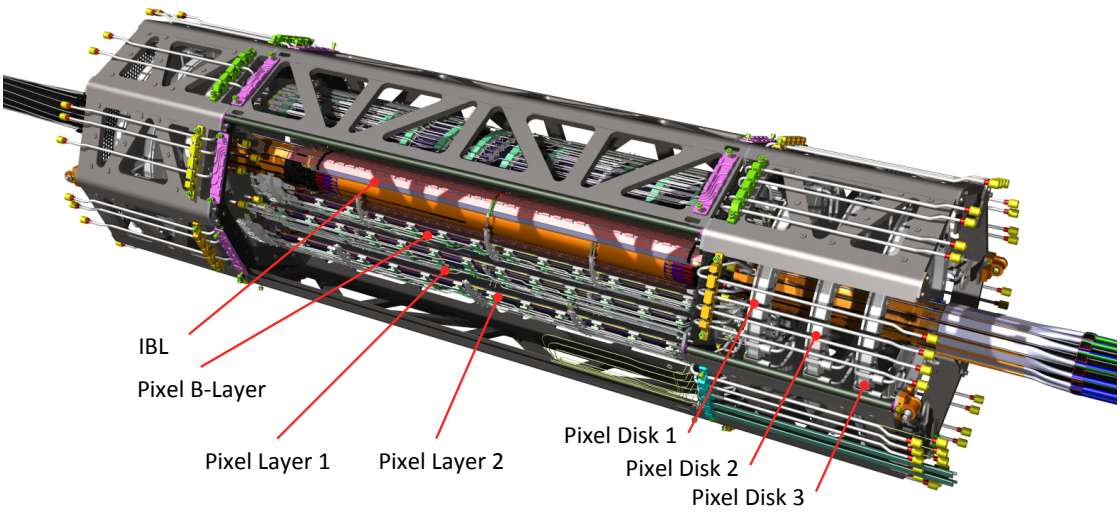

Figure 2.3: representation of the ATLAS Pixel Detector and IBL [26].

of two silicon strips sensors attached back to back with a relative angle of 40 mrad. With this module layout each particle traversing a module has two stereo hits, therefore allowing the three-dimensional reconstruction of the trajectory space points. SCT barrel modules have a rectangular shape and have 64 mm long sensors directed along the z-axis with 80 µm strip pitch, while end-cap modules, wedge shaped, are oriented perpendicularly to the z-axis and are 60 or 120 mm long with an average strip pitch of 80 µm. There are a total of 2112 modules in the barrels and 988 modules in the end-caps, each one with 768 strips, yielding a total of 6.3 million readout channels. The accuracy of the SCT measurements is of 17 µm in the R-ϕ plane and 580 µm in the longitudinal plane. Together with the IBL and the Pixel Detector, the SCT plays a fundamental role in high precision tracking and in the reconstruction of vertices.

2.2.4 Transition Radiation Tracker

The Transition Radiation Tracker, TRT, is a drift tube tracking system located in the outermost volume of the ID. The TRT is composed of 4 mm wide straws filled with 70:27:3 Xe:CO_2:O_2 gas mixture and with a gold-plated tungsten wire inside. Whenever a particle traverses a straw, it causes the ionisation of the gas, whose charges are then collected by applying a strong potential difference between the wall of the straw and the wire. The distance of a particle from the wire, the *drift radius*, can be determined by measuring the time it takes to the wire to collect the ionisation charges. The resolution on the drift radius is 170 µm. The gas mixture is sensitive to the radiation that photons produce in the material between the straws. The number of photons produced is proportional to the relativistic $\gamma = E/m$ factor of the incoming particle. For any given track it is therefore possible to discriminate, to some extent, the nature of the particle, in particular it is

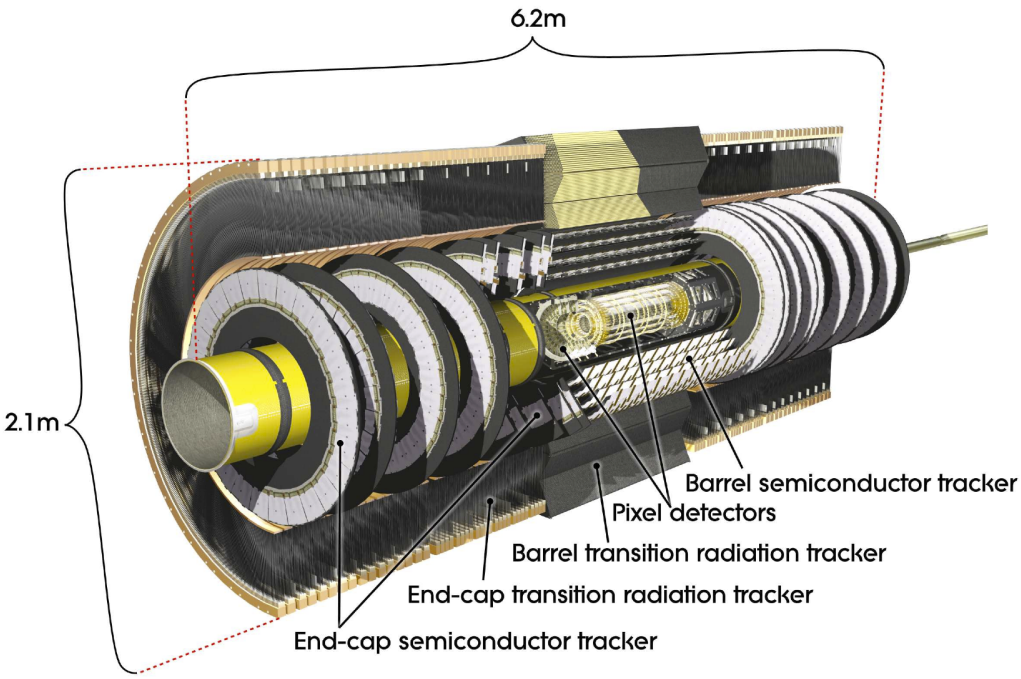

Figure 2.4: cut-away view of the ATLAS Inner Detector in Run-1 [25].

possible to determine whether it is an electron or a much heavier hadron. For energies higher than 1 GeV an electron identification efficiency of 99% can be achieved with a pion rejection factor of 100. In the barrel region the TRT has 73 layers of 144 cm long straws oriented along the beam axis and divided in two at $\eta = 0$, while each TRT end-cap has 18 disks of 37 cm long straws radially arranged. The Transition Radiation Tracker offers a total of 372032 readout channels from 52544 straws in the barrels and 319488 in the end-caps. Since the straws have a much bigger dimension than the silicon strips and pixels, the occupancy level of the TRT is higher, reaching a value close to 50% at LHC design luminosity. The TRT can only provide measurements in the R-ϕ plane with an accuracy of 130 µm. Despite its limited space precision and thanks to its long lever arm, the TRT improves the muon momentum resolution by a factor of two for p_{T} values of 500 MeV.

2.3 Calorimeters

Calorimeters measure the energy deposited in their active volume by charged and neutral particles, interacting electromagnetically or strongly [28]. High energy particles traversing the calorimeters produce a cascade of secondary particles, forming the *shower* (see Sections 3.3 and 3.5). Secondary particles, in turn, contribute to the development of the shower until they have enough energy or until they have completely traversed the calorimeter. The energy loss in the calorimeters can be estimated by the amount of light or ionisation produced by the particles traversing the active media. The purpose of the

calorimeters is to provide the experiment with the measurement of particle direction, jet energy, missing transverse energy, or $E_{\mathrm{T}}^{\mathrm{miss}}$, and particle identification. ATLAS calorimeters are *sampling calorimeters*, which means they are made of a passive material, or absorber, and an active material interleaved in layers. The passive material is a high dense material, typically lead, since it has to facilitate the shower and make it evolve in a limited space. Active material layers are in turn used to measure the energy deposited by the shower. The advantage of this strategy is that showers can be produced, measured and fully contained in a rather limited space. The down side is that part of the shower energy is absorbed by the passive material, therefore the total energy shower has to be estimated from the fraction effectively measured. The depth of the calorimeter is a fundamental parameter in the design. Showers must be in fact completely contained in order to be able to measure their energy. Moreover there is the need to prevent as much as possible punch-through particles from reaching the Muon Spectrometer placed outside of the calorimeters and deposit their energy there.

ATLAS has two calorimeters for the identification of differently interacting particles: the Electromagnetic Calorimeter and the Hadronic Calorimeters, covering together the volume up to $|\eta| < 4.9$.

			layers	coverage		granularity η	granularity ϕ
EM Calo.	presampler	barrel	1	0	$< \eta < 1.52$	0.025	0.1
		end-cap	1	1.5	$< \eta < 1.8$	0.025	0.1
	calorimeter	barrel	5	0	$< \eta < 1.475$	0.025/8 - 0.075	0.025 - 0.1
		end-cap	7	1.375	$< \eta < 3.2$	0.025/8 - 0.1	0.025 - 0.1
Hadronic Tile Calo.		barrel	3	0	$< \eta < 1.0$	0.1 - 0.2	0.1
		end-cap	3	0.8	$< \eta < 1.7$	0.1 - 0.2	0.1
Hadronic End-Cap Calo.		barrel	0				
		end-cap	4	1.5	$< \eta < 3.2$	0.1 - 0.2	0.1 - 0.2
Hadronic Forward Calo.		barrel	0				
		end-cap	3	3.1	$< \eta < 4.9$	1.5	1.3

Table 2.2: ATLAS calorimeters parameters [25].

2.3.1 Electromagnetic Calorimeter

The Electromagnetic Calorimeter is intended to measure electron and photon showers. Showers by muons, produced by bremsstrahlung, are usually negligible up to a muon energy of ∼500 GeV. Electrons and positrons lose energy mainly by ionisation and bremsstrahlung, while high energy photons mostly interact via pair production. High energy electrons and photons are signatures of important processes at LHC and their identification plays a crucial role in ATLAS physics analyses. The design of the EM Calorimeter required strong electron and photon identification against QCD background and high energy and spatial resolutions (both in η and ϕ), with minimal acceptance loss.

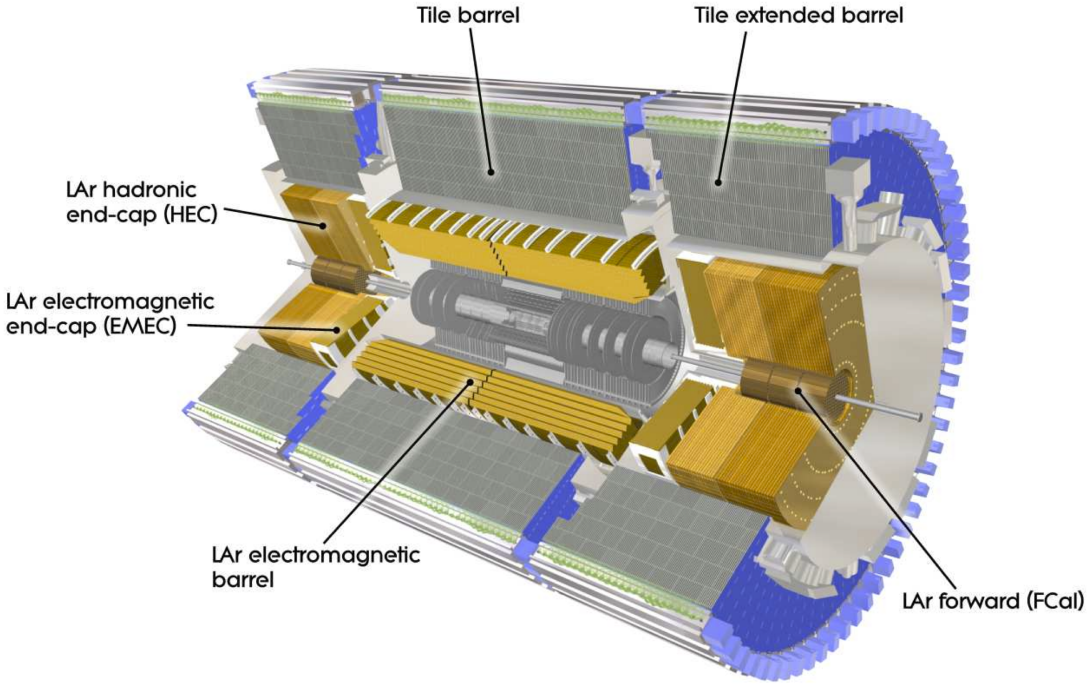

Figure 2.5: cut-away view of ATLAS calorimeters [25].

The EM sampling Calorimeter uses lead as absorber material and liquid Argon, LAr, as active material due to its tolerance to radiations. The internal layers are designed with an accordion shape which provides a complete ϕ coverage without any crack region. The EM Calorimeter is divided in a barrel and two end-caps, each one housed in a separate cryostat. The barrel is 6.8 m long, with an inner radius of 1.15 m and an outer radius of 2.25 m, covering up to $|\eta| < 1.475$. Its thickness varies in η from 22 to 33 radiation lengths, X_0[1]. The end-caps cover the region $1.375 < |\eta| < 3.2$, they go as close to the beam as 0.3 m and have an outer radius of 2 m. Each end-cap is divided in two wheels along the $|\eta| = 2.5$ cone surface. The thickness varies as a function of η from 24 to 38 X_0.

In the $|\eta| < 2.5$ region the EM Calorimeter is divided in three longitudinal layers, with a presampler placed in the front of them at $|\eta| < 1.8$. The purpose of the presampler, which does not have any absorber material, is to provide a correction for any energy loss before the calorimeter. The inner layer, 6 X_0 deep, has the highest granularity, allowing e and γ to be separated from π. The second layer is 16 X_0 deep and collects most of the deposited energy. The last layer has the coarser granularity and is 2-12 X_0 deep. It is used to measure the high energy electromagnetic showers.

The energy resolution of a calorimeter for the measurement of high energy particles

[1] A *radiation length* is the average length a particle interacting electromagnetically travels through a material retaining $\frac{1}{e}$ of its original energy.

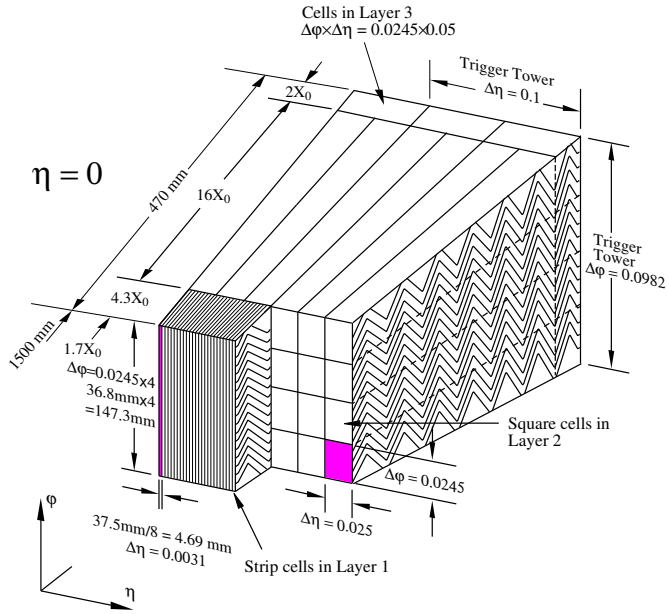

Figure 2.6: ATLAS EM Calorimeter barrel module [25]. The accordion geometry of the layers is visible.

can be generically parametrised as:

$$\frac{\sigma(E)}{E} = \frac{a}{\sqrt{E}} \oplus b \tag{2.5}$$

where a is the stochastic term and b accounts for local non-uniformities in the response. For the ATLAS EM Calorimeter, the parameters are: $a = 10\%$ and $b = 0.7\%$:

$$\frac{\sigma(E)}{E} = \frac{10\%}{\sqrt{E}} \oplus 0.7\% \tag{2.6}$$

2.3.2 Hadronic Calorimeter

The ATLAS Hadronic Calorimeter is placed outside the EM Calorimeter. It is designed to measure jets (see Chapter 4). Since hadronic showers are much deeper than the electromagnetic ones, the Hadronic Calorimeter must be thick enough to fully contain such energetic showers and prevent punch-through hadrons from reaching the Muon Spectrometer. The ATLAS Hadronic Calorimeter is up to 10 interaction lengths, λ, long and divided into three sub-systems: the Hadronic Tile Calorimeter, the Hadronic End-cap Calorimeter and the Forward Calorimeter. Depending on the η region covered, the ATLAS Hadronic

Calorimeter has different energy resolutions:

$$\frac{\sigma(E)}{E} = \frac{50\%}{\sqrt{E}} \oplus 3\% \quad |\eta| < 3.2 \quad \text{barrel and end-cap} \tag{2.7}$$

$$\frac{\sigma(E)}{E} = \frac{100\%}{\sqrt{E}} \oplus 10\% \quad 3.1 < |\eta| < 4.9 \quad \text{forward} \tag{2.8}$$

Hadronic Tile Calorimeter

The Hadronic Tile Calorimeter is a sampling calorimeter that uses steel plates as absorber and plastic scintillators as active material. It is divided into one central barrel and two lateral extended barrels, each one segmented in 64 modules in the transverse plane. The central barrel is 5.8 m long and the extended barrels are 2.6 m long. Both barrels have an inner radius of 2.28 m and an outer one of 4.25 m. The total coverage extends up to $|\eta| < 1.7$, where the central element covers up to $|\eta| < 1.0$ and the lateral ones cover the $0.8 < |\eta| < 1.7$ volume. The depth of the Hadronic Tile Calorimeter ranges from 7.4 λ at $|\eta| = 0$ to 9.7 λ in the lateral barrels.

Hadronic End-Cap Calorimeter

The Hadronic End-cap Calorimeter, HEC, is a sampling calorimeter with copper plates as absorbers and LAr as active material. Its two wheels are symmetrically placed behind the EM Calorimeter wheels, inside the Hadronic Tile Calorimeter extended barrels. The HEC covers the $1.5 < |\eta| < 3.2$ region, therefore overlapping with the Hadronic Tile Calorimeter and the Hadronic Forward Calorimeter. In the transverse plane, the HEC is divided into 32 modules, with an outer radius of 2.03 m and an inner radius of 0.372 m that becomes 0.475 m in the overlap region with the Hadronic Forward Calorimeter.

Hadronic Forward Calorimeter

The hadronic Forward Calorimeter, FCal, is a sampling calorimeter placed inside the HEC and covering the very forward regions of the ATLAS detector: $3.1 < |\eta| < 4.9$. The FCal has three different longitudinal layers, with a total length of 10 λ. The first layer, designed for electromagnetic measurements, uses copper as passive material. The other two layers use tungsten and are meant for hadronic showers measurements. In both cases LAr is used as active material since the forward regions are subject to high radiation doses.

2.4 Muon Spectrometer

The Muon Spectrometer, MS, is ATLAS outermost sub-detector, designed to track high p_{T} muons independently from the ID and to provide muon trigger. Momentum measurements are allowed by the ATLAS superconducting air-core toroid magnetic system (see Section 2.5). The MS was designed to provide 10% p_{T} resolution on 1 TeV p_{T} muons and 50 µm spatial resolution. It covers the pseudorapidity region $|\eta| < 2.7$. The MS is composed of a barrel and two end-caps, each one composed of three layers: inner, middle

and outer. The barrel layers are placed at distances of 5, 7.5 and 10 m from the beam pipe and divided into 16 azimuthal sections and providing full ϕ coverage. The three end-caps wheels have the same ϕ symmetry of the barrels and are positioned at 7.4, 14 and 21.5 m from the Ip. An extra wheel is arranged in the barrel-end-cap transition region at 10.4 m from the Ip.

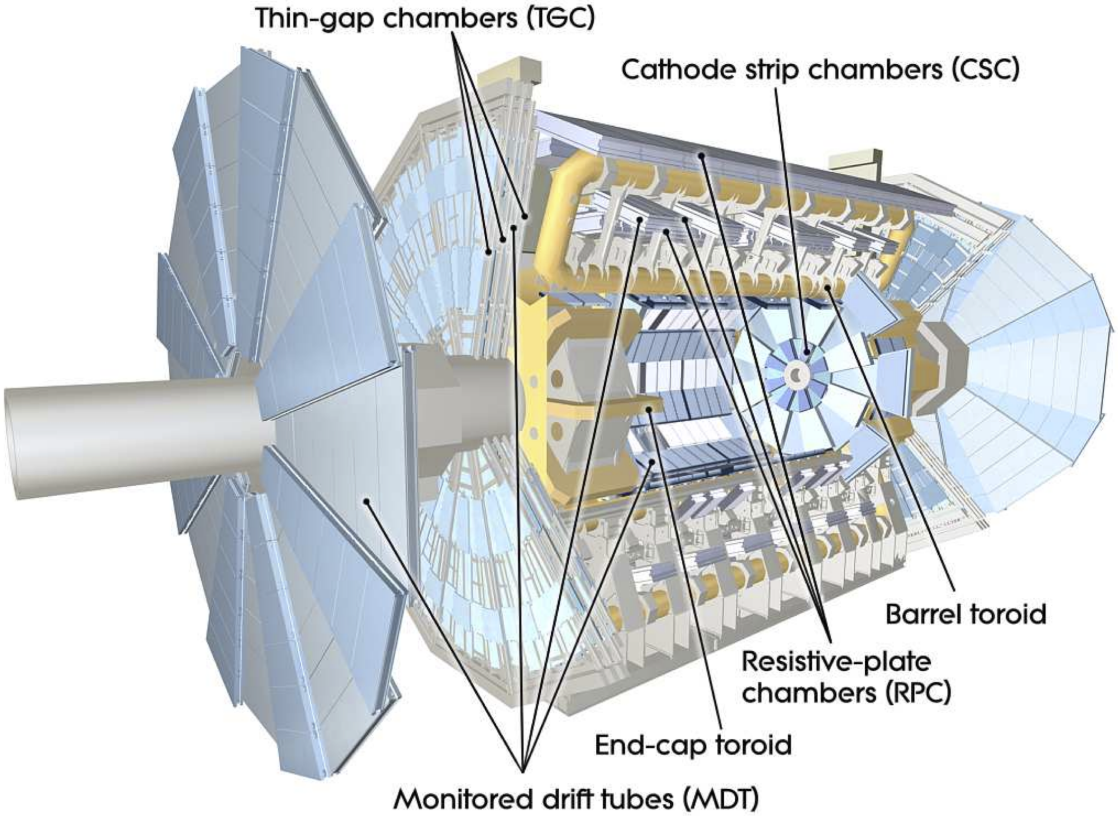

Figure 2.7: cut-away view of the Atlas Muon Spectrometer [25].

The Ms employs Monitored Drift Tube chambers and Cathode Strip Chambers for high precision muon tracking, together with Resistive Plate Chambers and Thin Gap Chambers which are used for muon trigger thanks to their rapid response.

2.4.1 Monitored Drift Tube Chambers

Monitored Drift Tube chambers, Mdt chambers, provide Atlas with high precision muon tracking in the barrel region. Mdt stations are composed of two multi-layers of Mdts divided by a spacer. Each multi-layer has three or four Mdt layers, depending on the region covered. An Mdt is made of a 30 mm diameter aluminium tube filled with 93:7 Ar:CO_2 gas mixture at 3 bar pressure. A gold plated tungsten anode wire is placed inside each tube with a voltage difference of 3040 V with respect to the walls. When a track

	coverage	chambers	channels
MDT	$0 < \eta < 2.7$	1150	354 000
CSC	$2.0 < \eta < 2.7$	32	31 000
RPC	$0 < \eta < 1.05$	606	373 000
TGC	$1.05 < \eta < 2.7$	3588	318 000

Table 2.3: ATLAS Muon Spectrometer parameters [25].

traverses a tube, its position is inferred from the arrival time of the charge clusters collected by the wire. A single MDT has a resolution of 80 µm but in a fully assembled chamber this value drops to 35 µm. Track position is measured only in the chamber transverse plane, i.e. ATLAS longitudinal plane, where tracks are bent by the toroidal magnetic field.

2.4.2 Cathode Strip Chambers

Cathode Strip Chambers, CSC, offer high precision muon measurements in the end-cap regions. Unlike MDT chambers, CSCs can manage the high particle rates typical of the forward regions without suffering for the high occupancy. CSCs are multi-wire proportional chambers with anode wires oriented radially and cathode strip oriented perpendicularly to the wires. From the measurement of the charge collected by the segmented cathode strips it is possible to resolve the position of the hit. CSCs have a precision of 40 µm in the bending plane and 5 mm in the non-bending plane. The small volume of the chambers allows small drift times and a time resolution of 7 ns.

2.4.3 Resistive Plate Chambers

Resistive Plate Chambers, RPC, provide muon trigger in the barrel region. An RPC is a gaseous detector with parallel electrode plates. Two parallel resistive plates, made of phenolic-melaminic plastic laminate, at a distance of 2 mm are immersed in a 4.9 kV/mm electric field provided by graphite electrodes at a voltage of 9.8 kV. The gap is filled with $C_2H_2F_4 : \mathrm{Iso} - C_4H_{10} : SF_6$ 94.7:5:0.3 gas mixture. Traversing muons generate avalanches along their tracks that are read by capacitive coupling to metallic strips on the outer sides of the resistive plates. RPCs have a spatial resolution of 10 mm in both longitudinal and transverse planes. The ϕ coordinate from the RPCs is used together with precise η coordinate from the MDTs to track the muons. The ∼1.5 ns time resolution of the RPCs justifies their adoption for muon triggering.

2.4.4 Thin Gap Chambers

Thin Gap Chambers, TGCs, are multi-wire proportional chambers providing muon tracking and triggering in the end-caps. TGCs are operated at a voltage of 2.9 kV and use a gas mixture of $CO_2 : \mathrm{n} - C5H_{12}$ 55:45. The radial coordinate is measured by gold-coated anode wires and the azimuthal coordinate is measured by pick-up strips. Four TGC wheels are mounted per end-cap.

2.5 Magnet System

ATLAS magnet system is composed of four superconducting magnets working at a temperature of 4.6 K: the Central Solenoid, the Barrel Toroid and the two End-Cap Toroids. The Barrel Toroid and the End-Cap Toroids together form ATLAS air-core superconducting magnetic system. The choice of an air-core magnet, instead of a stronger iron-core, was driven by the request of minimising multiple scattering in the Muon Spectrometer.

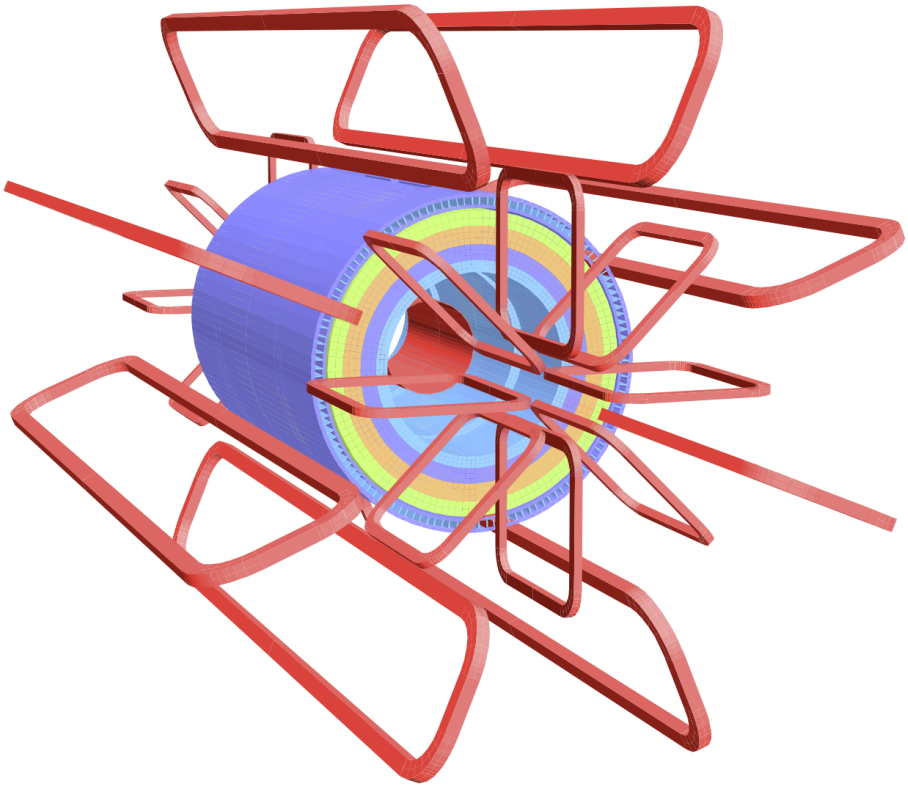

Figure 2.8: geometry of the magnet system end calorimeter steel [25].

2.5.1 Central Solenoid

The Central Solenoid provides a 2 T strong axial magnetic field for the Inner Detector. Its flux is returned by the hadronic calorimeter. The Central Solenoid has an inner radius of 2.46 m, an outer one of 2.56 m and it is 5.8 m long.

2.5.2 Barrel Toroid

The Barrel Toroid provides a 0.5 T toroidal magnetic field to the Muon Spectrometer barrel volume. It is composed of eight coils surrounding the calorimeters. The Barrel

Toroid has an inner diameter of 9.4 m and an outer diameter of 20.1 m and it is 25.3 m long.

2.5.3 End-Cap Toroids

The End-Cap Toroids provide a 1.0 T magnetic field in the end-cap volumes. The End-Cap Toroid is formed by eight small superconducting coils positioned on each side of the Central Solenoid and inside the Barrel Toroid volume..

2.6 Trigger and Data AcQuisition

The average size of an ATLAS event is about 1.5 MB. Multiplying by the LHC average bunch crossing rate of 40 MHz, a data stream of 60 TB/s is obtained. To reduce the data stream to a sustainable output bandwidth of 1500 MB/s, corresponding to an event rate of 1 kHz, ATLAS uses a Trigger and Data AcQuisition system, TDAQ. The purpose of the TDAQ is to reduce the amount of data to store by selecting only interesting events, removing those not containing hard scattering processes such as Minimum Bias soft collisions. The operation of the trigger system is regulated by *trigger menus*, specifying thresholds, trigger items and selection criteria to be adopted at each stage of the trigger chain. Data streams are tagged accordingly to the adopted trigger menu. ATLAS TDAQ is organised in two distinct levels: a Level 1 trigger (L1) and a High Level Trigger, HLT [29]. These two trigger levels work in chain, refining the selection operated by the previous trigger.

2.6.1 Level 1 Trigger

Level 1 trigger, L1, is hardware-based and uses information from the coarser sections of the calorimeters and Muon Spectrometer trigger chambers to reduce the event rate down to 100 kHz (75 kHz in Run-1). L1 trigger uses informations from the coarser sections of the calorimeters and Muon Spectrometer trigger chambers. It searches for high p_{T} muons, electrons, photons, jets, τ leptons decaying into hadrons and $E_{\mathrm{T}}^{\mathrm{miss}}$. L1 trigger defines Regions of Interest, ROIs, in the η-ϕ plane in correspondence of identified trigger features. L1 has a latency of 2.5 µs.

2.6.2 High Level Trigger

The High Level Trigger, HLT, is a software-based trigger using fully reconstructed events to perform the last step of the online event selection. The HLT reduces the event rate coming from L1 down to 1 kHz (400 Hz in Run-1), with a latency of 0.2 s. In Run-1, the HLT was divided in two consecutive step: the Level 2 trigger and the Event Filter. These two steps have been merged in Run-2 to reduce code duplication and have a more flexible HLT. Events succeeding the HLT are then written to mass storage.

2.6.3 Data Streams

The data collected by ATLAS is organised in four streams:

- **calibration stream**: it is used to collect data employed in the calibration of the ATLAS sub-detectors;
- **debug stream**: it collects the events that could not be successfully processed online by the trigger in the allocated time and have thus been momentarily saved to disk in order to be processed at a later stage;
- **express stream**: it collects a small fraction of the events and it is used to derive calibrations for the rest of the events being collected at that time;
- **physics stream**: it collects the data to be used in the physics analyses.
- **delayed stream**: a special physics stream used in Run-1 to store additional events to be processed at a later stage (e.g. events collected in 2012 have been processed in 2013, during the first LHC long shutdown).

Each one of the stream families is then further organised in categories aimed for specific usage. In Run-1, a series of physics streams was put in place for each one of the main branches of physics analysis, such as B-physics, electrons and photons, jets, hadronic τ and $E_{\mathrm{T}}^{\mathrm{miss}}$, muons. In Run-2, most of these streams have been merged into a main physics stream common to most of the analyses.

2.7 Athena

The complexity of the ATLAS experiment imposes the use of a modular software framework to manage the reconstruction, the analysis and also the event simulation. The advantage of a modular framework lies in its intrinsic flexibility and ease of development and maintenance. Athena is the ATLAS software framework. The purpose of Athena is to provide users with a common software skeleton into which developers can plug their code. Extendability and flexibility allow common functions to be implemented into the framework for re-use, encouraging a common approach and granting a robust coding and debugging. Athena is designed to handle both simulation and reconstruction of events. Common interfaces and data objects are implemented into ATLAS software framework to ensure communication between different algorithmic modules.

The definition within Athena of an Event Data Model, EDM, for data classes ensures commonality across experiment sub-systems, allowing the use of common software between different processes and the interchangeability of software modules. For example, simulated data and data from ATLAS are converted from a byte stream to Raw Data Objects, RDOs. The module responsible for producing Prepared Raw Data, PRD, from RDOs takes as input any RDO, enabling the use of the same algorithms for data and simulation. As a consequence, the reconstruction module producing Event Summary Data, ESD, and Analysis Object Data, AOD, takes as input any PRD, prescinding from its source. ESDs are the output of the reconstruction process and contain all of the event information, making the files too cumbersome to be adopted in most of the analyses. On the other hand, AODs contain only physics objects, such as particle four vectors, and are therefore much more manageable.

Chapter 3

The Standard Model Of Particle Physics

The Standard Model, SM, is the framework enclosing our current knowledge on particle physics. The SM describes in a rather simple and elegant way fundamental particles and their behaviour under the action of the electromagnetic, weak and strong interactions[1][2] [30, 31, 32]. It provides a perturbative and renormalisable theoretical framework suitable for the calculation of cross sections and the prediction of experimentally observable phenomena. The SM was originally developed in the 1960s by Glashow, Weinberg and Salam and finalised in the following years when confirmations from a variety of different experiments decided the success of the theory. Within the SM, particles are identified as being either *fermions* or *bosons*. Fermions, by definition, have half-integer spin values and are regarded as the ultimate constituents of matter. They can be divided into families of quarks and leptons: the quarks interacting via electromagnetic, strong and weak forces while the leptons interacting only electromagnetically and weakly. Both quarks and leptons have six members that can be arranged in three families of two quarks or two leptons each. As a distinction between the two classes of fermions, quarks are said to have a *flavour* while leptons have a *leptonic number* defined by their families. The masses of the fermions extend up to a few hundreds GeV. On the other hand, bosons have integer spin values and are identified as the carriers of the fundamental interactions. The photon is the carrier of the electromagnetic interaction and is massless. The $W^{\pm}$ bosons together with Z are the carriers of the weak force. Gluons mediate the strong interaction between color charged particles, i.e. quarks. The Higgs boson is a scalar boson which doesn't carry any force but is the responsible for the mass of all the particles within the SM and has been discovered at the LHC in 2012.

From a mathematical point of view, the SM is a gauge field theory based on the

[1] Gravitational interaction is more feeble compared to the other interactions and is not included in the SM since there is no coherent description of such force to be used together with the other three.

[2] This chapter is an introduction to some of the most relevant aspects of the Standard Model and theories beyond it. The reader who is interested in having more details is invited to read [30, 31, 32], where the material for this chapter has been collected. This chapter is based on [33].

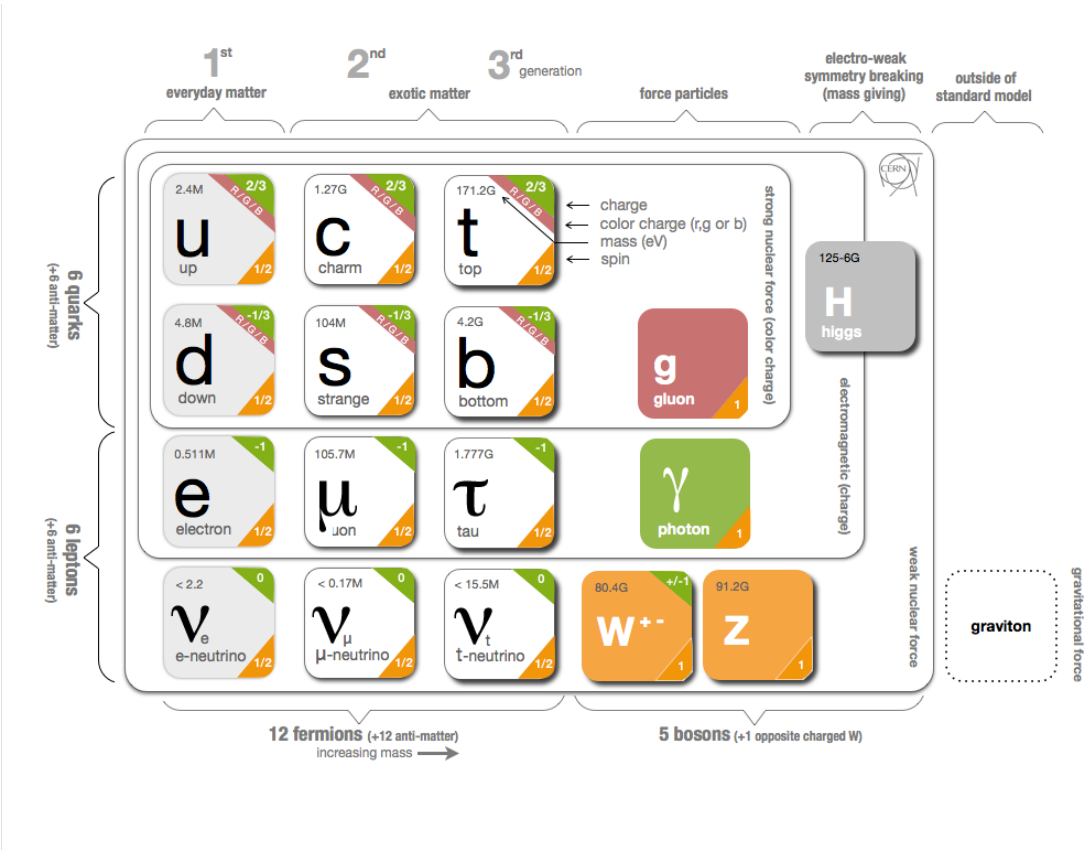

Figure 3.1: summary of the Standard Model particles.

symmetries of the $SU(3)_C \times SU(2)_L \times U(1)_Y$ group, where the interactions are generated from the requirement of local gauge invariance. The subgroup $SU(2)_L \times U(1)_Y$ is the core of the SM, describing Quantum ElectroDynamics (QED) and weak interactions as a whole. On the other side, the $SU(3)_C$ block is an extension of the QED formalism, given by the $U(1)_{EM}$ group, for Quantum ChromoDynamics (QCD) interactions.

Despite its strong experimental confirmations, the SM is nevertheless far from being a complete theory. Physics subjects like general relativity, dark matter, dark energy and neutrino oscillations do not fit inside the SM frame and constitute a motivation for a theory beyond the SM.

3.1 Electro-Weak Interaction

The Electro-Weak, EW, interaction unification is the heart of the SM and was formalised in the 1960s by Glashow, Weinberg and Salam. Before its unification with the Electro-Magnetic, EM, interaction, the weak interaction was described by Fermi's theory, assuming a point-like interaction coupling between the four fermions. This theory reveals its limits when applied at high energies, where divergences arise. This behaviour can be

avoided by the introduction of weak vector bosons. The first attempt to frame the weak interaction into a gauge theory was with the $S\text{U}(2)_L$ group. The idea was based on the observation that weak Charged Current, CC, interactions associate pair of particles like $e \leftrightarrow \nu_e$ and $\mu \leftrightarrow \nu_\mu$ in interactions like β decay, $p \to n\overline{e}\nu_e$, and neutrino scattering, $\nu_\mu N \to \mu X$. The L subscript came from the observation that only left-handed particles are coupled to CCs. In terms of particle fields, weak CCs are formalised as:

$$j_\mu^+ = \overline{\nu}\gamma_\mu \tfrac{1}{2}(1-\gamma^5)e = \overline{\nu}_L\gamma_\mu e_L \tag{3.1}$$

$$j_\mu^- = \overline{e}\gamma_\mu \tfrac{1}{2}(1-\gamma^5)\nu = \overline{e}_L\gamma_\mu \nu_L \tag{3.2}$$

where $\frac{1}{2}(1-\gamma^5)$ is the chiral left projector which introduces the coupling to only left-handed particles and thus parity violation in weak interactions. A left-handed doublet can be arranged from e and ν, together with a right-handed e singlet:

$$\chi_L = \begin{pmatrix} \nu \\ e \end{pmatrix}_L \qquad \chi_R = e_R \tag{3.3}$$

usually called *weak isospin doublet* and *singlet*. A right-handed neutrino singlet is not introduced since there is no observation of such particle, although there exist evidence of non-vanishing neutrino mass[3]. Making use of Pauli 2×2 matrices, σ_i, which are a fundamental representation of $S\text{U}(2)$, we may rewrite CCs as:

$$j_\mu^\pm = \overline{\chi}_L\gamma_\mu\sigma_\pm\chi_L \tag{3.4}$$

$$\sigma_\pm = \tfrac{1}{2}(\sigma_1 \pm \sigma_2) \tag{3.5}$$

The effect of the $\sigma_\pm$ operators is that of changing one state of the $S\text{U}(2)_L$ doublet to the other. σ_+ transforms the electron into a neutrino while σ_- transforms the neutrino into an electron. σ_+ and σ_- are identified as generators of the weak isospin. The third component of the chosen $S\text{U}(2)_L$ representation, namely σ_3, can be used to define a new current, orthogonal to the previous two:

$$\begin{aligned} j_\mu^3 &= \overline{\chi}_L\gamma_\mu\tfrac{1}{2}\sigma_3\chi_L = \\ &= \overline{\nu}_L\gamma_\mu\tfrac{1}{2}\sigma_3\nu_L - \overline{e}_L\gamma_\mu\tfrac{1}{2}\sigma_3 e_L \end{aligned} \tag{3.6}$$

$\frac{1}{2}\sigma_3$ defines the third generator of the weak isospin. This charge-preserving current cannot be identified with the weak Neutral Current, NC, since this is experimentally observed to have both left and right-handed terms while j_μ^3 couples only to left-handed particles. The identification of a triplet of currents is remarkable since it forms the basis for a gauge theory of weak interactions.

The idea of unification came to Glashow in 1961 [34]. He proposed to combine $S\text{U}(2)_L$ weak isospin group with $U(1)_{E\text{M}}$ electromagnetic group into a unified $S\text{U}(2)_L \times U(1)$ group. Since $U(1)_{E\text{M}}$ doesn't have any defined transformation property under $S\text{U}(2)_L$, a new $U(1)$

[3]The inclusion of neutrino mass into the SM picture is still an open issue. According to certain models the introduction of neutrino mass is foreseen in a theory beyond the SM. For a comprehensive description of the introduction of neutrino mass within the SM through the Majorana mass mechanism see [32].

symmetry group with singlet properties under $S\text{U}(2)_L$ has to be defined. This is achieved by defining the *weak hypercharge*, Y, as the generator of the new $U(1)_Y$ symmetry:

$$Y = 2(-T_3 + Q) \tag{3.7}$$

$$T_3 = \tfrac{1}{2}\sigma_3 \tag{3.8}$$

where T_3 is the third component of the weak isospin. The associated current is:

$$j_\mu^Y = \overline{\psi}\gamma_\mu Y \psi \tag{3.9}$$

The electromagnetic current, in turn, can be written as:

$$j_\mu^{E\text{M}} = j_\mu^3 + \tfrac{1}{2} j_\mu^Y \tag{3.10}$$

	T	T_3	Q	Y
ν_L	1/2	+1/2	0	-1
e_L	1/2	-1/2	-1	-1
e_R	0	0	-1	-2

Table 3.1: $S\text{U}(2)_L \times U(1)_Y$ quantum numbers for the electron family.

Numbers in Table 3.1 show the commutation properties between $S\text{U}(2)_L$ and $U(1)_Y$. $S\text{U}(2)_L$ doublets have the same $U(1)_Y$ value, while this is not true for $U(1)_{E\text{M}}$. j_μ^Y is invariant under $S\text{U}(2)_L$ transformations:

$$j_\mu^Y = -\overline{e}_R\gamma_\mu 2 e_R - \overline{e}_L\gamma_\mu 1 e_L - \overline{\nu}_L\gamma_\mu 1 \nu_L \tag{3.11}$$

The $S\text{U}(2)_L \times U(1)_Y$ symmetry provides two weak CCs and two NCs. Of the two NCs, one violates the parity while the other couples to both left and right-handed particles. It is important to underline that all these ideas where formalised well before the discovery of NCs in 1973 at CERN and Fermilab.

3.2 Glashow-Weinberg-Salam Model

Weinberg [35] and Salam [36] contributed to the development of the Standard Model by extending the BEHHGK mechanism[4] to the non-abelian $S\text{U}(2)_L \times U(1)_Y$ group, giving mass to all the gauge bosons while retaining the photon massless.

The locally gauge invariant electro-weak Lagrangian is:

$$\begin{aligned}\mathcal{L} = \overline{\psi}_L\gamma^\mu[i\partial_\mu - g\mathbf{T}\cdot\mathbf{W}_\mu - \tfrac{1}{2}g'YB_\mu]\psi_L + \\ + \overline{\psi}_R\gamma^\mu[i\partial_\mu - \tfrac{1}{2}g'YB_\mu]\psi_R + \\ - \tfrac{1}{4}\mathbf{W}_{\mu\nu}\cdot\mathbf{W}^{\mu\nu} + \\ - \tfrac{1}{4}B_{\mu\nu}\cdot B^{\mu\nu}\end{aligned} \tag{3.12}$$

[4]The BEHHGK mechanism takes its name from the initials of the people who independently developed it in 1964: Englert and Brout [37], Higgs [38] and Guralnik, Hagen and Kibble [39]. Sometimes it takes the name of *Higgs mechanism*.

where, in order to preserve the $SU(2)_L \times U(1)_Y$ invariance, fermion and boson mass terms cannot be inserted. The BEHHGK mechanism is introduced by adding a $SU(2)_L \times U(1)_Y$ invariant Lagrangian for the Higgs scalar filed, ϕ, to the electro-weak Lagrangian:

$$\mathcal{L}_\phi = (D_\mu \phi)^\dagger (D^\mu \phi) - \mu^2 \phi^\dagger \phi - \lambda \phi^\dagger \phi \tag{3.13}$$

where D_μ is the covariant derivative for the $SU(2)_L \times U(1)_Y$ symmetry:

$$D_\mu = i\partial_\mu - g\mathbf{T} \cdot \mathbf{W}_\mu - \tfrac{i}{2} g' Y B_\mu \tag{3.14}$$

and $\mu^2 < 0$ and $\lambda > 0$. The ϕ_i fields can be arranged as a weak isospin doublet with hypercharge $Y = -1$:

$$\phi = \begin{pmatrix} \phi^+ \\ \phi^0 \end{pmatrix} = \tfrac{1}{\sqrt{2}} \begin{pmatrix} \phi_1 + i\phi_2 \\ \phi_3 + i\phi_4 \end{pmatrix} \tag{3.15}$$

in order to be $SU(2)_L$ invariant. As a consequence of choosing $Y = -1$ for the doublet, it follows from $Q = T_3 + \frac{1}{2}Y$ that ϕ^+ is positively charged while ϕ^0 is neutral. The symmetry may be broken and ϕ may be expanded around the vacuum state as:

$$\phi(x) = \tfrac{1}{\sqrt{2}} \begin{pmatrix} 0 \\ v + H(x) \end{pmatrix} \tag{3.16}$$

Upon substitution of the last expression for $\phi(x)$ into the Lagrangian and retaining all the terms up to second order:

$$\begin{aligned} \mathcal{L}_\phi = & [\tfrac{1}{2}(\partial_\mu H)^2 - \lambda v^2 H^2] + \\ & + \tfrac{1}{8} g^2 v^2 (W^1_\mu W^{1\mu} + W^2_\mu W^{2\mu}) + \\ & + \tfrac{1}{8}(g W^3_\mu - g' B_\mu)(g W^{3\mu} - g' B^\mu) + \\ & + \text{kinetic terms for } \mathbf{W} \text{ and } B + \\ & + \text{higher order terms} \end{aligned} \tag{3.17}$$

The first term of the Lagrangian describes the massive scalar field H, $m_H = \sqrt{2\lambda v^2} = \sqrt{-2\mu^2}$. The second term collects the mass terms for the W^1 and W^2 gauge fields. According to the definition given in Section 3.1 the two fields may be combined to give the $W^\pm$ bosons. The mass of these bosons is found to be $m_W = \frac{1}{2} g v$. As regards the third term, we observe that, due to the structure of the third $SU(2)_L$ generator, the gauge boson fields W^3_μ and B_μ are mixed into one mass term. From the linear combination of W^3_μ and B_μ two new vector gauge bosons may be defined. In addition, since only one combination of W^3_μ and B_μ has a mass term, the other one, orthogonal to the first, will be necessarily massless. Therefore the vector gauge fields Z_μ and A_μ may be introduced:

$$Z_\mu = -B_\mu \sin\theta_W + W^3_\mu \cos\theta_W \tag{3.18}$$

$$A_\mu = B_\mu \cos\theta_W + W^3_\mu \sin\theta_W \tag{3.19}$$

defining the Z boson and the photon respectively. θ_W is identified as the *Weinberg angle* and it is a parameter of the SM whose value is not predicted and needs to be measured

experimentally. On comparison of Equations 3.17 and 3.18, it is straightforward to see that:

$$\sin\theta_W = g' \tag{3.20}$$
$$\cos\theta_W = g \tag{3.21}$$

Equations 3.18 and 3.19 may be inverted:

$$W^3_\mu = A_\mu \sin\theta_W + Z_\mu \cos\theta_W \tag{3.22}$$
$$B_\mu = A_\mu \cos\theta_W - Z_\mu \sin\theta_W \tag{3.23}$$

Therefore, going back to the electro-weak locally gauge invariant Lagrangian, see Equation 3.12, the Neutral Current interaction term may be extracted. Upon substitution:

$$\begin{aligned} g j^3_\mu W^{3\mu} + \tfrac{1}{2} g' j^Y_\mu B^\mu = (g \sin\theta_W j^3_\mu + \tfrac{1}{2} g' \cos\theta_W j^Y_\mu) A^\mu + \\ + (g \cos\theta_W j^3_\mu - \tfrac{1}{2} g' \sin\theta_W j^Y_\mu) Z^\mu \end{aligned} \tag{3.24}$$

The first term on the right is the electromagnetic interaction, $e j^{E\text{M}}_\mu A^\mu$, therefore, recalling Equation 3.10:

$$g \sin\theta_W = g' \cos\theta_W = e \tag{3.25}$$

The Weinberg angle is defined by the weak isospin and weak hypercharge interaction coupling constants:

$$\tan\theta_W = \frac{g'}{g} \tag{3.26}$$

The particular choice we operated for the ϕ isospin doublet and its ground state granted the null mass of the photon. The vacuum state, ϕ_0, was chosen to break the $S\text{U}(2)_L \times U(1)_Y$ symmetry but not the $U(1)_{E\text{M}}$ symmetry generated by $Q = T_3 + \frac{1}{2}Y$ so that ϕ_0 is a singlet under any $U(1)_{E\text{M}}$ rotation:

$$\phi_0 \to [1 + i\Lambda(x)Q]\phi_0 = \phi_0 \tag{3.27}$$
$$Q\phi_0 = \left(T_3 + \tfrac{1}{2}Y\right)\phi_0 = 0 \tag{3.28}$$

and the electro-magnetic gauge boson is therefore massless. The bosons mass spectrum can be summarised as:

$$\begin{aligned} m_{W^\pm} &= \tfrac{1}{2} g v \\ m_Z = \tfrac{1}{2} v \sqrt{g^2 + g'^2} &= \tfrac{1}{2} v = \frac{m_{W^\pm}}{\cos\theta_W} \\ m_\gamma &= 0 \\ m_H = \sqrt{2\lambda v^2} &= \sqrt{-2\mu^2} \end{aligned} \tag{3.29}$$

The parameters introduced by the Glashow-Weinberg-Salam model are just four: the coupling constants g and g' and the Higgs potential parameters λ and v, where $v^2 =$

$-\mu^2/\lambda$. Rather than this theoretical values, for convenience, other four values, associated with experimental observables, are commonly used as parameters of the Standard Model: the fine-structure constant α, the Fermi constant G_F, the Z boon mass m_Z and the Higgs boson mass m_H:

$$\begin{aligned} \alpha &= \tfrac{1}{4\pi} g^2 g'^2 \\ G_F &= \frac{1}{v^2\sqrt{2}} \\ m_Z &= \tfrac{1}{2} v \\ m_H &= \sqrt{2\lambda v^2} \end{aligned} \tag{3.30}$$

3.3 Quantum ChromoDynamics

Quantum ChromoDynamics, QCD, is the theory describing the strong interactions between particles carrying colour charge: quarks and gluons [40]. QCD is based on the $SU(3)_C$ symmetry group, whose eight generators make it a non-Abelian theory and lead also to the self-interaction of its gauge fields, the gluons, carrying colour charge themselves.

The QCD lagrangian may be written as:

$$\mathcal{L} = i \sum_q \overline{\psi}_q^j \gamma^\mu (D_\mu)_{jk} \psi_q^k - \sum_q m_q \overline{\psi}_q^j \psi_q^j - \tfrac{1}{4} G^a_{\mu\nu} G_a^{\mu\nu} \tag{3.31}$$

where the covariant derivative is defined as:

$$(D_\mu)_{jk} = \delta_{jk}\partial_\mu - i g_s (T_a)_{jk} G^a_\mu \tag{3.32}$$

with the index $a = (1, 2, ..., 8)$ running over the eight $SU(3)_C$ generators, the indices j and k representing the three colour charges (red, green and blue) and the index q the quark flavours. In Equation 3.31, ψ_q^k is a quark with colour k, G^a_μ represents the gluon fields and T_a are the $SU(3)_C$ generators. The $-\frac{1}{4} G^a_{\mu\nu} G_a^{\mu\nu}$ term is the kinetic term for the gluon fields. Similarly to the photon in QED, no gluon mass term appears in Equation 3.31. On the other hand, though, gluon self-coupling terms are featured within the gluon kinetic term entering the equation.

The strong running coupling constant, g_s, depends on the transferred momentum in the interaction, Q^2:

$$g_s(Q^2) = \frac{g_s(\mu_R^2)}{1 + [\frac{g_s(\mu_R^2)}{12\pi}](33 - 2n_f) \ln \frac{Q^2}{\mu_R^2}} \tag{3.33}$$

where n_f is the number of quark flavours and μ_R is the *renormalisation scale* introduced to take care of UV divergences in the renormalisation process of the strong coupling constant. g_s becomes less and less strong as Q^2 increases but, on the other hand, it tends to infinity for sufficiently small values of Q^2. A scale value, Λ_{QCD}, can be defined by setting the denominator of Equation 3.33 equal to zero, so that the equation reads:

$$g_s(Q^2) = \frac{12\pi}{(33 - 2n_f) \ln \frac{Q^2}{\Lambda^2_{\text{QCD}}}} \tag{3.34}$$

Λ_{QCD}, experimentally measured to be ∼200 GeV, defines the boundary between two fundamental features of QCD that set it apart from any other force: *asymptotic freedom* and *confinement*. For $Q^2 \gg \Lambda_{\text{QCD}}$, i.e. at short distances, quarks and gluons behave as being asymptotically free and their interaction can be treated perturbatively. Instead, for $Q^2 \simeq \Lambda_{\text{QCD}}$ the coupling becomes large and QCD cannot be treated perturbatively anymore. As a consequence, at large distances, the strong potential leads to the impossibility of observing coloured objects alone, hence their confinement in colorless bound states. It is remarkable to notice that the lightest $q\overline{q}$ bound state, the neutral pion, has a mass of 135 GeV that is very close to the QCD confinement scale Λ_{QCD}.

The complex phenomenology of QCD in the final states of particle collisions is handled through jets (see Chapter 4).

3.4 Proton-Proton Collisions

The characterisation of *pp* collisions is a rather complex task. Protons are composite particles and consequently their internal structure may give rise to multiple hadronic interactions within the same collision. Additionally, the partons involved can produce Initial as well as Final State Radiation, ISR and FSR respectively, before finally hadronising into observable particles. Hadronic collisions therefore are extremely complex since they involve both perturbative and non-perturbative QCD in the calculation of the processes. They can be divided into a *hard scattering process* plus an *underlying event*. The most interesting processes in particle physics involve high momentum transfer, producing high p_{T} particles, and are therefore identified as being hard scattering processes. On the other hand, lots of soft collisions between partons take place alongside any hard scattering process. These constitute the underlying events, which account for the largest fraction of the total *pp* cross section. Underlying events are a mixture of Single Diffractive (SD), Double Diffractive (DD) and Non-Diffractive (ND) events. In the case of diffractive events, a color neutral object is exchanged between the interacting protons, giving a spray of particles with a flat distribution in $|\eta|$. In Non-Diffractive events the interaction between two quarks of the colliding protons happens trough the exchange of a coloured object. An abundance of particles with higher p_{T} is produced in this case in the $\eta \simeq 0$ region. These events represent the major source of background to more interesting, low cross section processes.

In the QCD asymptotic freedom regime, the hadron can be considered as an ensemble of partons, each one carrying a fraction x of the hadron momentum with a probability given by the *Parton Distribution Function*, PDF:

$$f(x)\mathrm{d}x \equiv P(x' \in [x, x + \mathrm{d}x]) \quad f = q, \overline{q}, g \tag{3.35}$$

As a consequence, the *factorisation theorem* allows us to write the generic hadron-hadron

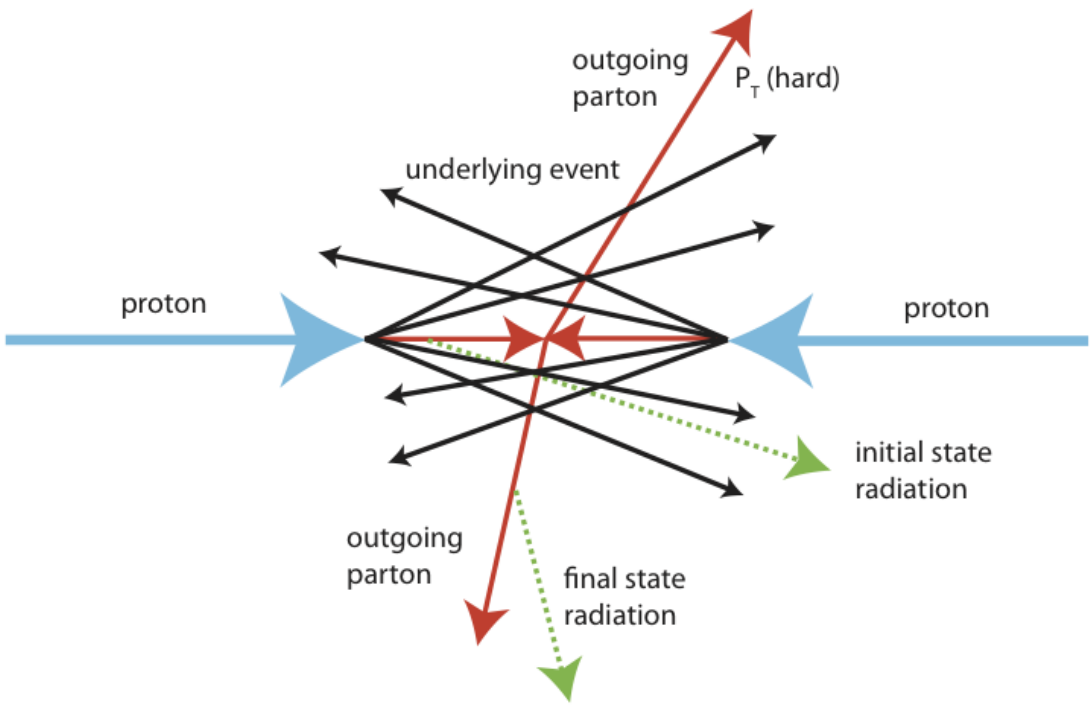

Figure 3.2: representation of a pp collision with hard scattering and underlying events. The incoming protons are pictured in light blue, the partons involved in the hard scattering are red, the partons participating to the underlying event are black while initial and final state radiation is green.

cross section as an incoherent sum of the independent parton subprocesses:

$$\sigma(h_1 h_2 \to cd)(Q^2) = \\ = \sum_{a,b=q,\bar{q},g} \int_0^1 \mathrm{d}x_1 \mathrm{d}x_2 \; f_{a,h_1}(x_1, \mu_F^2) \; f_{b,h_2}(x_2, \mu_F^2) \; \hat{\sigma}^{(ab\to cd)}(Q^2, \mu_F^2) \tag{3.36}$$

The hadronic cross section is given by the convolution of the parton cross section, $\hat{\sigma}$, together with the PDFs, $f_{a,h_1}(x_1, \mu_F^2)$ and $f_{b,h_2}(x_2, \mu_F^2)$. h_1 and h_2 represent the incoming hadrons and Q^2 is the momentum transferred in the hard scattering. The sum is extended to all the quarks and gluons in the hadrons that may contribute to the process. The integral is over the fraction of momentum carried by the two interacting partons, x_1 and x_2, identified as a and b from h_1 and h_2 respectively. μ_F is the *factorisation scale*, an arbitrary energy scale introduced to discern between short and long distance physics. A parton emitted with momentum larger than μ_F is regarded as contributing to short distance physics and is therefore included in the short distance parton cross section, $\hat{\sigma}$. Partons with lower momenta belong to the hadron structure and are absorbed in the PDFs. The scale μ_F is usually chosen to be of the order of Q^2. It is worth stressing here that although PDFs and $\hat{\sigma}$ depend on the factorisation scale, the total cross section does not.

Since α_s is small at high energies, the short distance cross section can be calculated as a perturbation serie, where each term corresponds to a higher order contribution to the total cross section. At Leading Order, LO, the cross section is given by the parton scattering cross section at tree level. The factorisation theorem rests upon the assumptions of the PDFs being universal and of the interactions being fast enough not to alter the distributions within the hadrons.

3.5 MC Event Simulation

Monte Carlo, MC, generators are tools employed to simulate the physics of particle collisions. They play a fundamental role in the evaluation of the expected experimental performances and in the validation of the reconstruction software. They combine rigorous calculations from perturbative QCDand Quantum ElectroDynamics, QED, together with phenomenological descriptions of the interactions. A generic hard scattering process can be resolved into four stages, organised in space and time: the hard scattering interaction, ISR and FSR, the hadronisation and decay, the underlying event. The hard scattering process, describing the interaction of the incoming partons, is the heart of any collision. The transferred momentum, Q^2, between the partons defines the scale of the interaction. For large Q^2 values, perturbative QCD calculations can be performed. The incoming partons are coloured objects and may therefore radiate bosons in the interaction, producing ISR and FSR. The radiated objects, in turn, may continue the radiation cascade. This process takes the name of *parton showering*. The momenta involved in the process are generally low and a phenomenological approach is applied to model this stage. When a certain cut-off threshold in the transferred momentum is reached, the parton showering is terminated and the color connected partons are recombined into color singlets hadrons. This stage goes by the name of *hadronisation* and does not depend on the hard process. Afterwards, the produced unstable hadrons, together with heavy objects like top quarks, vector gauge bosons and Higgs bosons, decay accordingly to their Branching Ratios, BR, until they reach a stable configuration. Finally the interaction of the partons not participating to the hard process is simulated. Underlying events are dominated by low Q^2 QCD interactions, thus requiring the adoption of model dependent descriptions.

Once the event is fully simulated at the physics level, MC-generated particles are propagated through the detector, simulating the interactions with the active and passive materials of the experiment. An algorithm based on the GEANT4 software [41] and customised with the ATLAS geometry, G4ATLAS, takes care of propagating the particles. Finally, the response of the ATLAS experiment to the passage of the particles is translated into signals and the simulated hits are then translated into RDOs, as explained in Section 2.7. This last stage takes the name of *digitisation* and is the prelude to the full event reconstruction, similarly to what is done for data.

3.5.1 PYTHIA

PYTHIA [42] is a multipurpose MC event generator for hadronic interactions at colliders which combines perturbative QCD at Leading Order, LO, with phenomenological models.

The PYTHIA generator contains also libraries for the simulation of ISR, FSR, hadronisation processes, decays, underlying events, SM and SUSY phenomena. The transition between perturbative and non-perturbative QCD is governed by a parameter, $p_{\mathrm{T}}^{\mathrm{min}}$, corresponding to the minimum momentum transfer in the hard scattering. This parameter determines the number of multiple parton-parton interactions within the same proton-proton collision and regulates the divergences of the cross section at low momenta. After the parton interaction is calculated, the partons are fragmented into hadrons. PYTHIA adopts a *string hadronisation model* based on the linearity of the colour potential at large distances. PYTHIA can be interfaced with other MC generators to take care of the parton showering process.

3.5.2 POWHEG

POWHEG [43] is a MC generator interfacing NLO QCD calculations with parton showering. POWHEG gets its name (POsitive Weight Hardest Emission Generator) from assigning its events weights greater than zero, thanks to a completely different approach to the treatment of the parton emissions with respect to other common MC generators. The generator can be adopted for a number of different processes such as Z pair production, heavy quark production, single top, lepton collisions, Drell-Yan vector boson production, W production and Higgs production. POWHEG can be interfaced to HERWIG and PYTHIA for the shower generation.

3.5.3 HERWIG

HERWIG [44] is a MC generator at LO for lepton and hadron collisions. HERWIG simulates hard scattering processes together with ISR and FSR and adopts a *cluster based model* in the parton showering process. As PYTHIA, HERWIG can be configured to provide parton showering within other MC generators.

3.5.4 BLACKMAX

BLACKMAX [45] is MC generator dedicated to the simulation of processes involving the production of Quantum Black Holes, QBH, and their thermal decay to two-body final states. Unlike other QBH generators, BLACKMAX allows the black holes to rotate, recoil and possess a charge (EM and colour) while also taking into account the brane tension and brane splitting in models with extra dimensions. No interference between QCD and QBH is taken into account as it is considered negligible in any case. BLACKMAX can be interfaced to work with PYTHIA and HERWIG.

3.5.5 QBH

QBH [46] is another Quantum Black Hole MC generator. Unlike BLACKMAX, QBH conserves local gauge symmetries in its black hole decays and is able to handle multi-jet final states (despite these might be suppressed in some models). Additionally, the generator

can only handle 0-spin QBHs. The QBH generator can be interfaced with PYTHIA to take care of ISR, FSR, multiple interactions, showering, fragmentation and decay processes.

3.5.6 Other MC Generators

Other MC generators adopted in the analyses and studies presented in this thesis include: SHERPA [47], CalcHEP [48] and MadGraph [49].

Chapter 4

Hadronic Jets

Jets of hadrons are physics objects that describe the complex phenomenology of parton hadronisation and showering originating from strong interactions (see Section 3.3). The purpose of jets is to bridge the gap between the hard scatter partons produced in strong interactions, such as in the *pp* collisions produced in the LHC, (including possible new physics phenomena) on one hand and the final state readings of a detector, such as the ATLAS ID or calorimeters, on the other hand. As such, the definition of *jet* can vary and can be tuned to the needs of the analysis, although its definition needs to be theoretically sound.

As explained in Section 3.3, partons are not directly observable due to QCD confinement (and extremely short decay time in the case of top quarks). What is actually observed in a detector are the particles produced in the hadronic showering, as a spray of a large number of collimated particles. Thanks to energy and momentum conservation, it is possible to determine the kinematic properties of the originating parton starting from the detector readings, such as the tracks from the parton shower reconstructed in the ID and the energy deposits in the electromagnetic and hadronic calorimeters produced by the hadronic shower.

Due to the relevance of this topic to the exotic dijet analysis, jets are described in detail in this chapter. Section 4.1 presents the definition and properties of jet algorithms, with a particular focus on the anti-k_t family. Section 4.2 highlights the various type of inputs and jets that are used within the ATLAS experiment. Section 4.3 goes through each of the steps needed to calibrate the jets reconstructed, from the raw calorimeter inputs to the true energy and kinematics of the hard scatter parton, accounting for all possible losses and detector misreadings. Section 4.4 highlights the methods adopted to tag the flavour of a jet.

4.1 Algorithms

Jet algorithms are used to group together inputs from the detectors and combine their four-momenta into a collection of jets, providing a picture of the hard scatter collision.

4.1.1 Requirements

In order to have a common set of rules that would standardise objects and allow for the comparison of experimental jet-physics results with theory calculations, in 1990 the Snowmass accords [50] made a first attempt at defining the criteria that jet algorithms have to meet:

- simple to implement in an experimental analysis;
- simple to implement in the theoretical calculation;
- defined at any order of perturbation theory;
- yield finite cross section at any order of perturbation theory;
- yield a cross section that is relatively insensitive to hadronisation.

While the first two points are dictated by a practical computation point of view, the remaining three stem from the necessity for a valid jet algorithm to give the correct jet multiplicity in presence of soft radiation (infra-red safety) or splitting of the input constituents (collinear emission safety), often referred together as IRC safety [51].

Infra-Red Safety

Infra-Red, IR, safety requires a jet algorithm not to be affected in its results if soft, infra-red, radiation is emitted by the initial state constituents. It is not desirable for a jet algorithm to deliver different results whether soft terms are added or not. This is a typical problem of cone algorithms (see Section 4.1.3), where seeds are used to group the inputs based only on their angular distance. In this scenario, the presence of additional soft radiation between two harder terms can cause their merging into a single jet. See Figure 4.1.

Collinear Emission Safety

Collinear emission safety ensures that if a parton were to split into two collinear partons, the jet algorithm results would not change. The splitting into two softer terms can alter the jet seeds and result in a different reconstructed-jet collection. This is graphically represented in Figure 4.2.

4.1.2 Definition

In 2007, the Les Houches accords [52] defined a common set of rules that jet algorithm definitions need to meet to avoid ambiguities when discussing jet physics results. According to these, jet algorithm definitions must provide:

- the **jet algorithm**, describing the process by which the inputs are mapped into a jet collection;

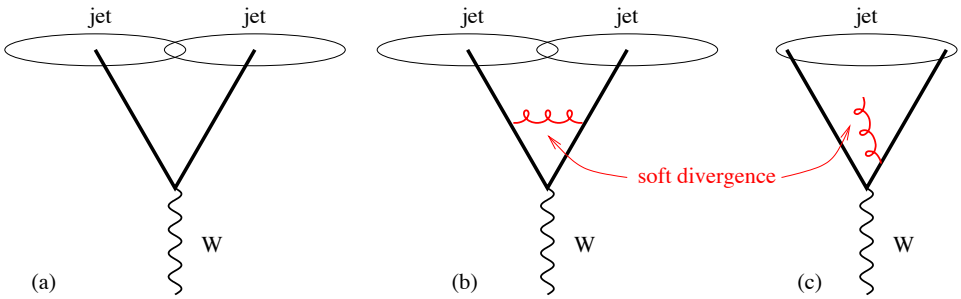

Figure 4.1: example of IR emission and its effect on jet algorithms [51]. While in (a) two jets are reconstructed, in (c) the addition of soft radiation, negligible in terms of energy and geometrically in between the two harder partons, causes the algorithm to group them in the same jet. This is a problem of most jet cone algorithms, where only the angular distance between the inputs is taken into account. (b) and (c) are two examples of soft-term corrections that cancel out in calculations but that can give very different experimental results if not treated coherently.

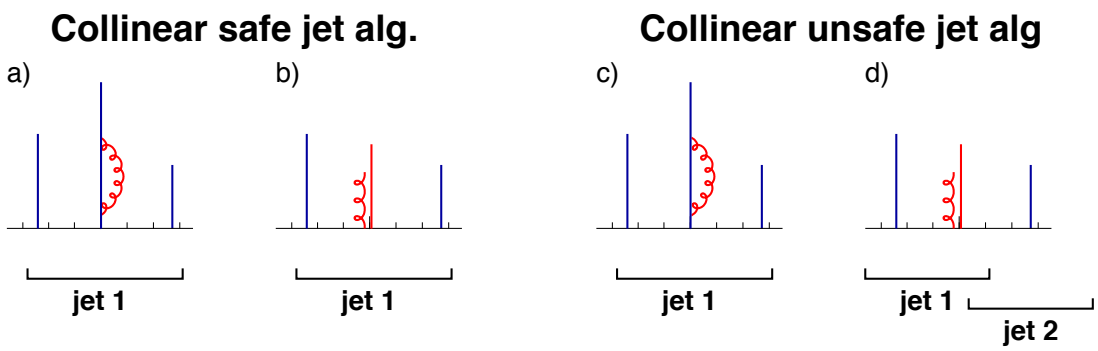

Figure 4.2: example of collinear splitting and its effect on jet algorithms [51]. The total energy is the same in all the four configurations but while in a) and b) the same jet is reconstructed, whether one contribution has a correction or it is split into two softer terms, in c) and d) a collinear un-safe algorithm reconstructs two different sets of jets.

- the **jet algorithm parameters**;
- the **recombination scheme**, defining the method to combine the four-momenta of the constituents grouped in a same jet.

4.1.3 Cone Algorithms

Jet cone algorithms were the first to be implemented, back in the '70s, because of their simplicity and their rapid jet reconstruction [51]. Typical cone algorithms start from constituents, the seeds, ordered by their energy, and draw around them circles of radius R in the η-ϕ plane. All constituents falling within such radius are added to the seed. Once all the seeds have been iterated, a split/merge step is performed in order to resolve ambiguities between close jets. Cone algorithms are generally not IRC-safe, however an exception is given by the SISCone algorithm [53].

4.1.4 Sequential Recombination Algorithms

Sequential recombination algorithms are the most common algorithms nowadays. The strategy at the core of these algorithms is to progressively combine constituents if their distance, defined according to a specific metric, is below a certain value, until no further combination is possible [54].

The k_t algorithms[1] belong to this family. They are based on the distance metric:

$$d_{ij} = \min(p_{\mathrm{T}i}^{2p}, p_{\mathrm{T}j}^{2p}) \frac{\Delta_{ij}^2}{R^2} \tag{4.1}$$

$$d_{iB} = p_{\mathrm{T}i}^{2p} \tag{4.2}$$

where

$$\Delta_{ij}^2 = (\phi_i - \phi_j)^2 + (\eta_i - \eta_j)^2 \tag{4.3}$$

and $p_{\mathrm{T}i}^{2p}$ is the transverse momentum elevated to $2p$, d_{ij} is the distance between two components, i and j, d_{iB} is the distance between component i and the beam, B, and R is the jet radius parameter. The algorithm iteratively looks for the smaller distance among all possible combinations of components, including the beam. If the smallest distance is d_{ij}, i and j are combined into a new component; if the smallest distance is d_{iB}, component i is a jet and it is removed from the list of components. It is clear that these algorithms are not affected by IRC safety issues, since the clustering process does not make use of seeds. The behaviour of the k_t family algorithms can be significantly changed by the choice of the parameter p, which defines the order by which harder and softer components are combined and so the clustering sequence of the event. Despite originally being computational intensive algorithms, sequential recombination algorithms have become progressively faster, thanks also to the release of the FastJet package [55, 56].

[1] k_t is the transverse momentum of the component.

The k_t Algorithm

Setting $p = 1$ in equation 4.2 defines the k_t algorithm[2]. This algorithm iteratively combines first the softer components, reconstructing back the showering process of the originating parton. By un-doing the last clustering step, it is possible to obtain the hardest components of the jets. This makes the algorithm extremely useful when studying the substructure of jets and is hence widely adopted with large radii for boosted-system studies. On the other hand, though, the shape of k_t jets is quite irregular, posing some complications with their calibration (see Section 4.3.3).

The Cambridge/Aachen Algorithm

The Cambridge/Aachen, C/A, algorithm is obtained when setting $p = 0$ in equation 4.2. The clustering sequence of this algorithm is defined only by angular ordering of the input components. Also in this case, the jet shape is quite irregular.

The anti-k_t Algorithm

The anti-k_t algorithm is obtained by setting $p = -1$, hence using the inverse of the squared p_T of the components to define the distance metric[3]. By doing so, soft components are immediately combined with hard components. The jet reconstruction process follows therefore the showering process of the original parton and no substructure information can be deduced by undoing its last clustering step, as it was the case for k_t jets. The advantage of the anti-k_t jet algorithm lies in the regular circular shape of the jets obtained (see Figure 4.3), which allows an easy area computation and hence easy pile-up subtraction and jet calibration.

4.2 Jets in ATLAS

Jets in ATLAS are reconstructed using the FastJet software package [55, 56] and jet algorithms are chosen according to the intended use of the jets. The most common jet algorithm in ATLAS is the anti-k_t (see Figure 4.4), due to its regular jet shape and relatively easy calibration. The Cambridge/Aachen algorithm is used for boosted-system studies, where the substructure of the jets plays a crucial role. The radius parameter in jet algorithms ranges from standard values of 0.4 and 0.6 (depending on the need to recover more soft radiation at larger radii) to 1.0 and 1.2 for large-R jets aimed for studies investigating the jet substructure of collimated boosted objects. Small radii jets, i.e. radii of 0.2 and 0.3, are adopted to investigate the internal composition of jets with large radii. As for jet algorithms and radii, jet inputs can also vary depending on the purpose of the study (see Figure 4.5).

[2] Any value $p \geq 1$ provides similar results.
[3] Any value $p \leq -1$ provides similar results.

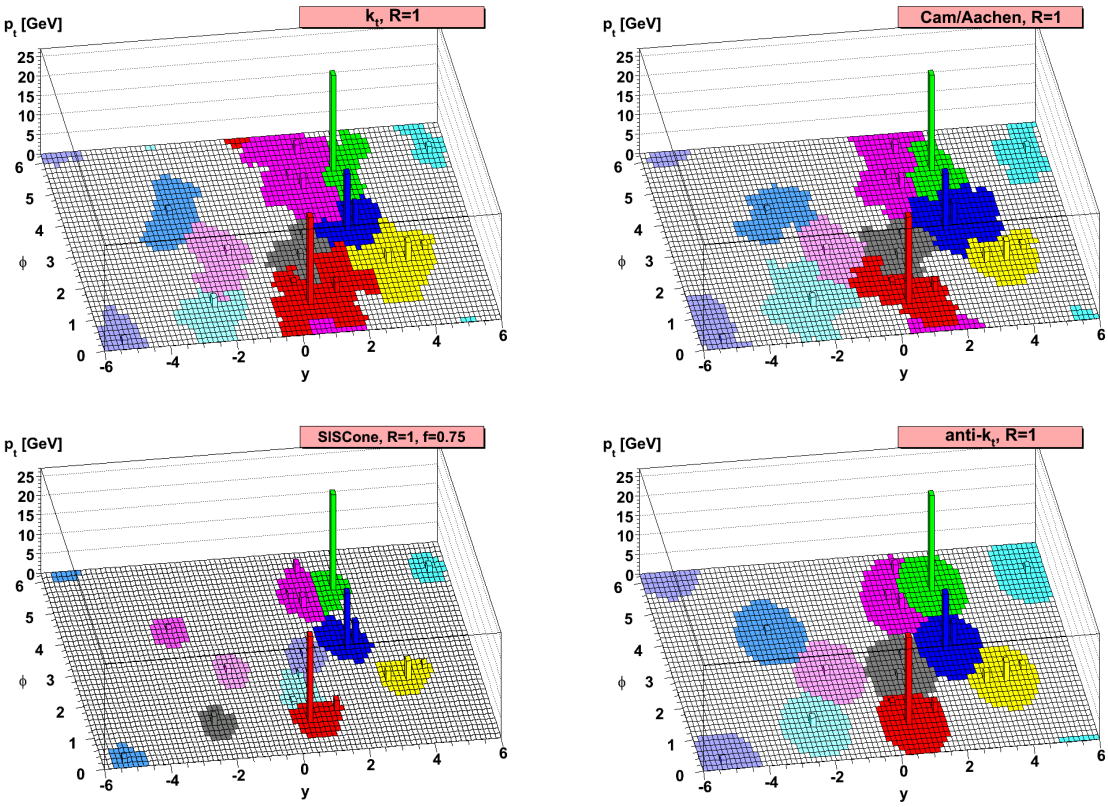

Figure 4.3: example of jet algorithms reconstructing the same event [54]. From top left, clockwise: k_t algorithm, Cambridge/Aachen algorithm, anti-k_t algorithm and SISCone algorithm. It is possible to observe the jet shapes produced by the different algorithms. In particular the irregular shapes of k_t and C/A jets are evident, while the anti-k_t and SISCone jets present a more circular shape. It is worth noticing how the anti-k_t algorithm handles the overlapping region of close jets: the hardest jet gets all the softer components within the jet radius, cutting the circular shape of the sub-leading jet.

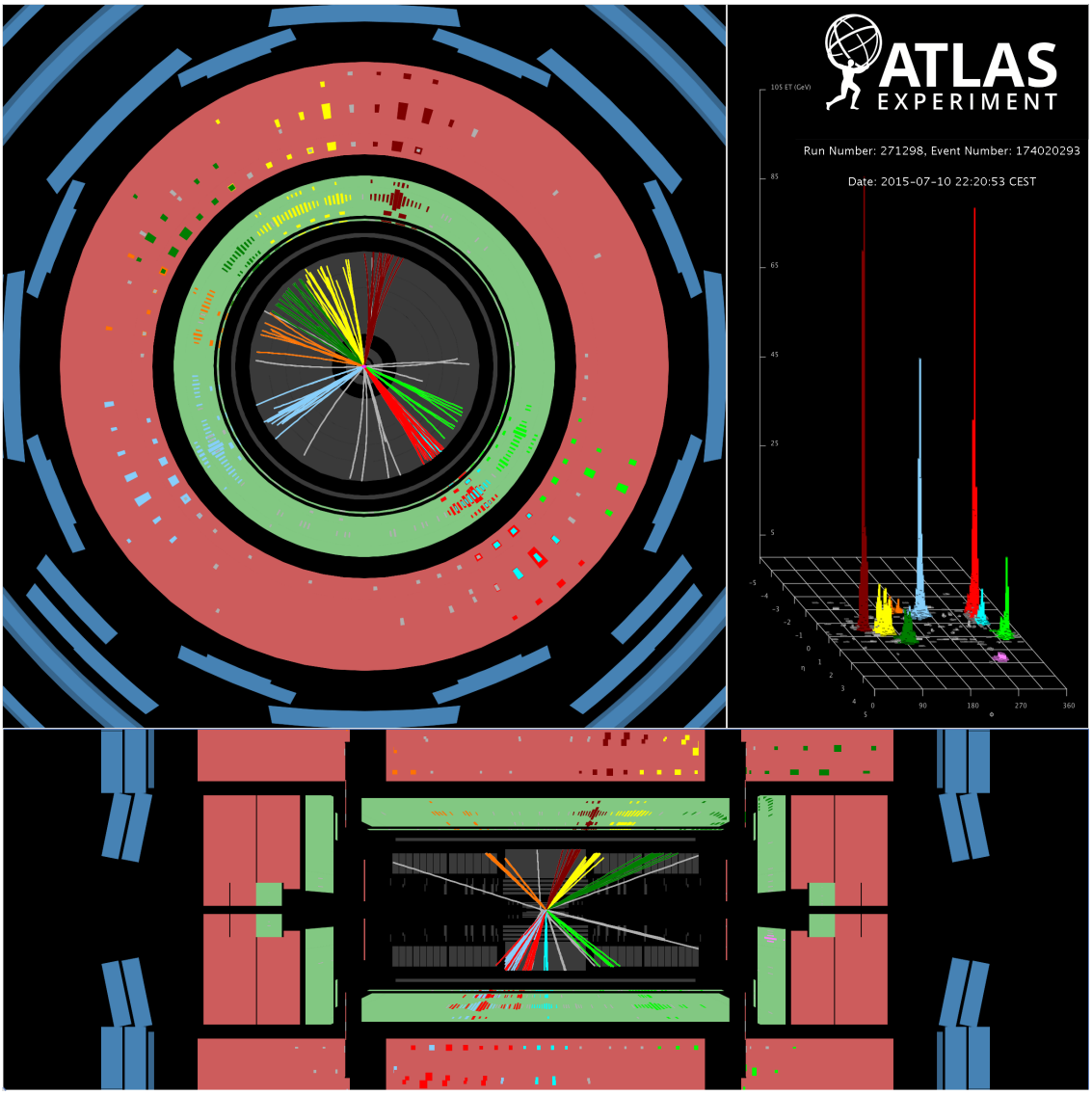

Figure 4.4: ATLAS display of an event from Run-2 with nine reconstructed jets with $p_{\mathrm{T}} > 50$ GeV [57]. The top right panel shows the η-ϕ map of the calorimeter cells (the z-axis representing the transverse energy measurement) and how these are grouped by the anti-k_{t} algorithm.

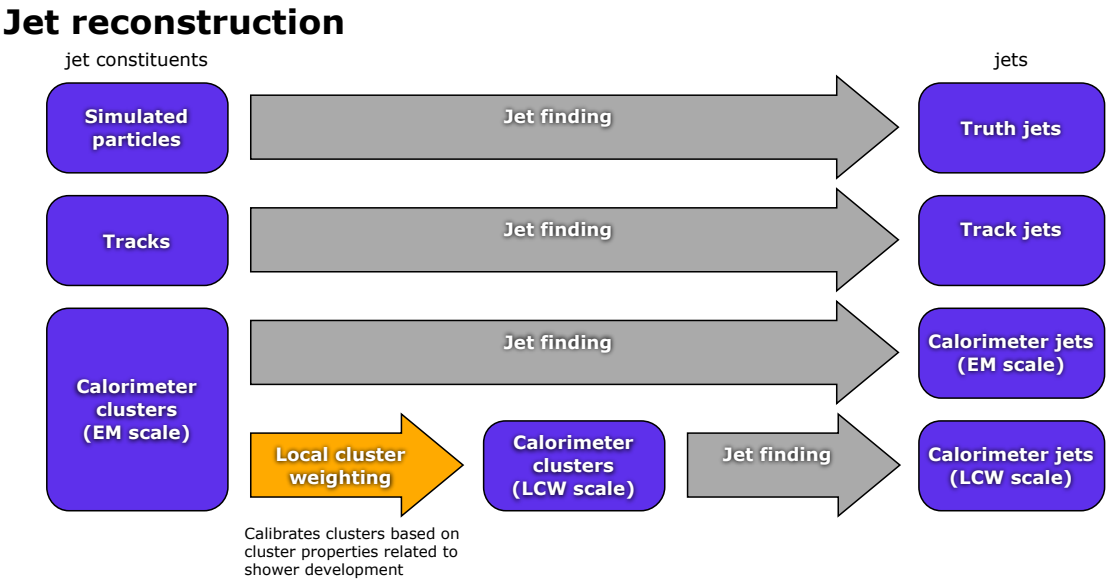

Figure 4.5: jet reconstruction process for different inputs and calibration schemes [58]. See Section 4.3 for information on Electromagnetic, EM, scale jets and Local Cluster Weighting, LCW, scale jets.

4.2.1 Truth-Jets

Simulated particles from MC generators with lifetime τ longer than 30 ps are used to build *truth-jets* [59]. Due to their negligible contribution to calorimeter energy deposits, neutrinos and muons are generally not included in the truth-jet inputs collection. Truth-jets are used in calibration and angular resolution studies (see Section 4.3 and Chapter 5) and to test the jet algorithm performance.

4.2.2 Track-Jets

Tracks from the ID are used to construct *track-jets*, a useful alternative to the jets built from calorimeter energy deposits. Despite the fact that they are missing the contributions from neutral particles (around a third of the jet components), track-jets have the advantage of providing a completely independent measurement of jets with respect to the calorimeter energy deposits and are more robust against pile-up. For these reasons, track-jets are used for calorimeter-independent measurements and calibrations (see Chapter 5).

Tracks fulfilling the following quality criteria[4] on impact parameters, kinematic properties and number of hits are used to reconstruct track-jets:

- z_0: the track impact parameter in the longitudinal plane has to be less than 200 mm;
- $z_0 \cdot \sin\theta$: the track impact parameter along the z-axis has to be less than 100 mm;

[4]Track quality criteria may differ from analysis to analysis and evolve over time. These quality criteria have been used in Run-1 and are of relevance for the Jet Angular Resolution studies reported in Chapter 5.

- d_0: the track impact parameter in the transverse plane has to be within 5 mm of the interaction vertex;
- $\frac{\Delta d_0}{d_0}$: the significance of the d_0 impact parameter has to be less than 100;
- $p_{\mathrm{T}} > 0.5$ GeV;
- $|\eta| < 2.5$: tracks have to be within the volume of the ID;
- $\frac{\chi^2_{\mathrm{fit}}}{n.d.f.}$: the χ^2 of the track fit over the number of degrees of freedom has to be lower than 5;
- $n_{\mathrm{hit}}^{\mathrm{B-Layer}}$: no requirements on the number of hits in the first pixel layer (B-Layer);
- $n_{\mathrm{hit}}^{\mathrm{Pixel}}$: at least one hit in the Pixel Detector;
- $n_{\mathrm{hit}}^{\mathrm{SCT}}$: at least six hits in the SCT;
- $n_{\mathrm{hit}}^{\mathrm{Si}}$: at least 6 hits in the silicon detectors (Pixel and SCT);
- $n_{\mathrm{hit}}^{\mathrm{TRT}}$: no requirements on the number of hits in the TRT.

4.2.3 Calorimeter-Jets

The most widely used jets are reconstructed from groups of noise-subtracted energy deposits in the ATLAS calorimeters and are called *calorimeter-jets*, sometimes also called *calo-jets* or simply *jets* when there is no ambiguity[5].

Calorimeter Energy Deposits

Calorimeter energy deposits provide a measurement of the energy deposited by electrically-charged and neutral particles. They are provided with a good geometrical resolution, thanks to the high granularity of the ATLAS calorimeter. Energy deposits are organised into *topoclusters* before they are provided as inputs to the jet reconstruction algorithms.

Topoclusters

Topological clusters, or *topoclusters*, are three-dimensional clusters of calorimeter cells [60]. Topoclusters are the inputs for the reconstruction of calorimeter jets and are designed to suppress pile-up and electronic noise contributions, respectively $\sigma_{\mathrm{noise}}^{\mathrm{pile-up}}$ and $\sigma_{\mathrm{noise}}^{\mathrm{electronic}}$, to the cell energy measurements. Due to the large number of collisions per bunch crossing produced by the LHC, the dominant contribution to the noise in the calorimeter cells is given by pile-up. It is possible therefore to define for each calorimeter cell an energy significance value as $\zeta = E_{\mathrm{cell}}/\sigma_{\mathrm{noise}}$. The topoclustering algorithm uses cells whose energy-to-noise ratio is above 4 as seeds to iteratively cluster neighbour cells that have themselves an energy-to-noise ratio above 2. Once this step is terminated, the neighbour cells with $\zeta > 0$

[5] Here and in the rest of this thesis, the term *jet* refers to *calorimeter jet* unless otherwise stated.

are finally added to the proto-cluster[6]. As a last step, before the topoclusters are fed to the jet algorithm, local maxima are identified and used as seeds to split the proto-clusters into the final topoclusters. The topocluster four-vector is finally computed by using the topocluster energy, obtained by summing the energy contribution from all the cells, the topocluster centroid, defined as the energy-weighted average of the cells, and by setting its mass to zero and its origin to the interaction point. Since the energy of the topoclusters is at the electromagnetic scale and no correction is yet applied to compensate the difference in response to hadronic showering, these are also called EM topoclusters.

4.3 Calibration

Once jets have been reconstructed, they undergo a calibration process in order to restore the original hard scatter parton energy and correct for any detector-related effect [58, 59, 61]. These corrections account for:

- **hadronic shower response**: the calorimeter response to hadronic showers is lower than that to electromagnetic ones ($e/h > 1$) due to a considerable fraction (up to 40%) of energy being dissipated in undetectable form, such as energy used to break nuclear bindings and release nucleons [28]; this difference in response can be fixed at hardware level by using compensating calorimeters but since this is not the case of ATLAS, a calibration needs to be applied;
- **dead material**: energy deposited in non-instrumented volumes of the calorimeter;
- **leakage**: energy deposited outside of the calorimeter; this is the case of *punch-through* jets, i.e. showers traversing the calorimeter and leaving signals in the ATLAS Muon Spectrometer;
- **out of calorimeter jet**: energy deposits belonging to the original parton shower but not included in the jet by the algorithm;
- **energy deposits below noise threshold**: energy deposits belonging to the original parton shower but falling below the noise threshold;
- **pile-up**: energy deposits from other in-time and out-of-time pp interactions (see Section 1.3).

The jet calibration is performed as a series of ordered consecutive steps, each one taking care of a specific correction. It is applied in bins of jet p_{T} and jet pseudo-rapidity. Despite often referring to the jet calibration scheme as *Jet Energy Scale*, JES, this does not affect only the scaling of the jet energy but all of the jet four-vector components. When applied to jets reconstructed from EM topoclusters, the calibration is also called EM+JES. Jet calibration factors are derived from MC samples and are completed with

[6]Starting from Run-2 an additional rule has been added to the topoclustering algorithm to prevent topoclusters to grow from the calorimeter presampler using neighbours in the same layer, therefore reducing the impact of pile-up even further.

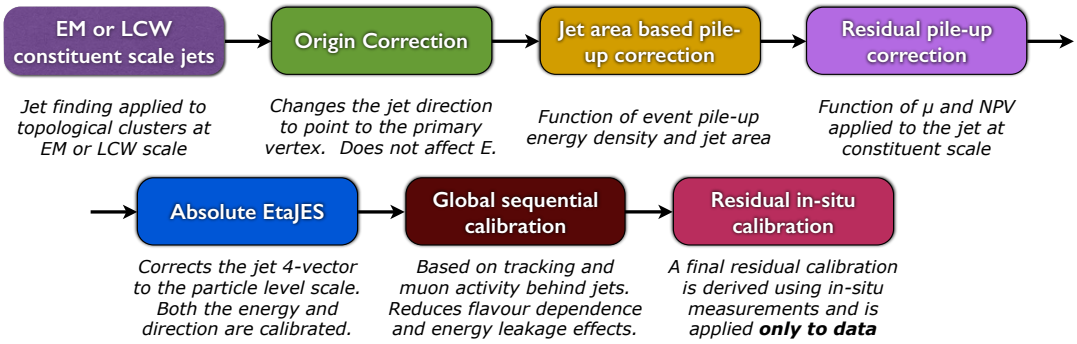

Figure 4.6: JES calibration chain [59]. μ is the average number of interactions per bunch crossing and NPV is the number of primary vertices reconstructed per bunch crossing. The Absolute EtaJESstep restores the jet energy measured at detector level to that of the original jet shower, i.e. the particle level scale.

data-driven methods for residual corrections. In the calibrations process, jets are first made to be pointing to the hard scatter vertex, then the effects of pile-up are removed and the energy is calibrated using factors derived from MC simulation. At this stage, additional corrections are applied to reduce differences in response of jets originating from gluons and quarks and jets not contained in the calorimeter. As a last step, a correction to account for residual differences in calibration between data and MC is applied to data. The full chain of corrections composing the JES calibration scheme is represented in Figure 4.6 and details about each step are given in the following sections.

4.3.1 Local Calibration of Topoclusters

In the jet reconstruction process there is the option to calibrate the energy of the topoclusters to the hadronic scale before these are fed to the algorithms for jet reconstruction (see Figure 4.5). This calibration method goes by the name of *Local Cluster Weighting*, LCW, and is an alternative to the EM topoclusters. Jet reconstructed from LCW topoclusters need to undergo the same calibration process as their EM jets counterpart, with the only difference that the step restoring the jet energy to the hadronic scale (see the Absolute EtaJES step in Figure 4.6 and Section 4.3.4) is less significant. The calibration of jets reconstructed from LCW topoclusters is also called LCW+JES.

4.3.2 Origin Correction

The default pseudorapidity and azimuthal angle values are obtained by making the jet point to the center of the ATLAS detector, i.e. the nominal interaction point. However,

due to the length of the beamspot[7], an improvement in jet η resolution is achieved by making the jet point to the event primary vertex, i.e. the vertex with the highest scalar sum of track p_{T}^2. Given the much smaller transverse size of the collision volume, the jet ϕ angle gets only a negligible correction. For further details, see Chapter 5.

4.3.3 Pile-Up Correction

In order to reduce the contribution to the jet energy from in-time and out-of-time pile-up, an area-based subtraction method has been put in place [62]. This method uses the area of a jet, A, and the average calorimeter energy density in the η-ϕ plane, ρ, to remove the effect of pile-up. The area of the jet is computed by means of *ghost particles* [63], fictitious particles of infinitesimal energy (so that their contribution to the jet energy is negligible). Ghost particles are uniformly distributed in the η-ϕ plane before starting the jet clustering process and then they are used to measure the area of the jet based on the number of these particles that were clustered together with the jet. The event energy density, on the other hand, is computed by averaging the p_{T}/A values of the anti-k_{t} jets reconstructed in the central volume of the detector ($|\eta| < 2.0$). Dedicated studies have shown that the value of ρ is indeed proportional to the number of primary vertices in an event, n_{PV} [59]. Even after the jet area correction is applied, a dependency of the jet p_{T} on pile-up is still observed. This is removed by applying a correction that is function of n_{PV} and of the average number of interactions per bunch crossing, $\langle\mu\rangle$. The total pile-up correction can thus be written as:

$$p_{\mathrm{T}}^{\mathrm{corrected}} = p_{\mathrm{T}}^{\mathrm{EM}} - \rho \times A - \alpha \times (n_{\mathrm{PV}} - 1) - \beta \times \langle\mu\rangle \tag{4.4}$$

where α and β are MC-derived constants binned in η and extrapolated from the dependence of the jet p_{T} on n_{PV} and $\langle\mu\rangle$ respectively.

4.3.4 Jet Energy Scale Calibration

The jet energy scale calibration restores the reconstructed jet energy to the true jet energy while also correcting the jet four-vector direction in η. It is derived purely from a MC dijet sample with isolated jets that have undergone origin and pile-up corrections. A residual bias in the jet p_{T} is still observed as a function of η after the energy calibration. This is partly due to the gaps and dead material in the calorimeter and it is resolved by applying an additional correction to the jet pseudorapidity. The jet energy response, defined as $E^{\mathrm{jet}}/E^{\mathrm{truth}}$ and corresponding to the inverse of the jet energy calibration, and the residual jet η bias are shown in Figure 4.7.

4.3.5 Global Sequential Corrections

After the restoration of the jet energy scale, some dependencies of the jet response on the longitudinal and transverse shape of the jet and on the flavour of the originating parton are observed. These effects are mitigated by the Global Sequential Calibration,

[7] In 2012 the length of the beamspot ranged between 40 and 55 mm.

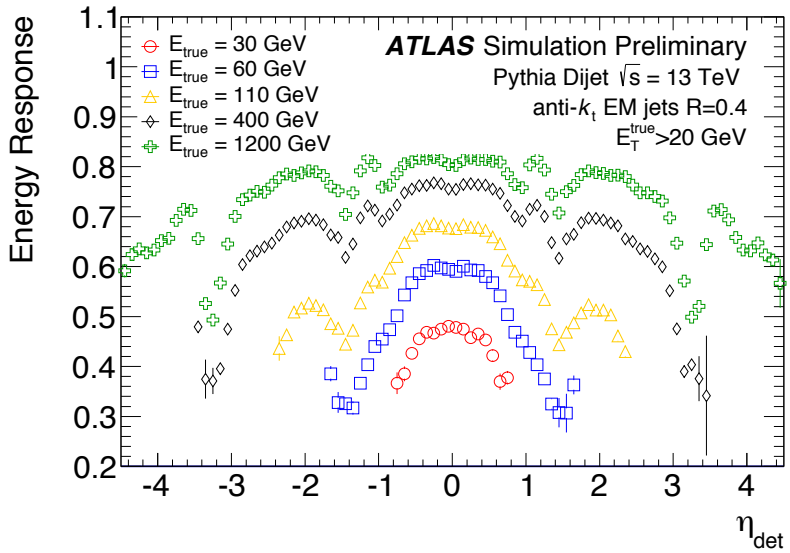

(a)

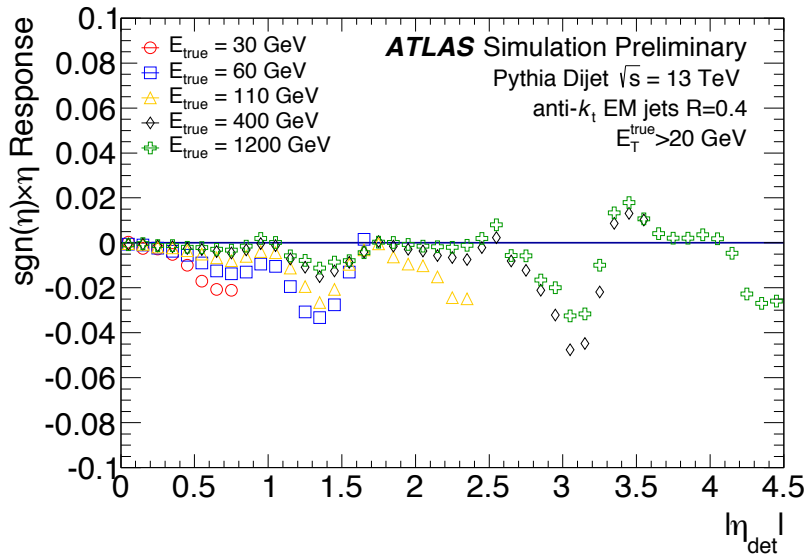

(b)

Figure 4.7: jet energy response (a) and jet η bias (b) measured after origin and pile-up corrections and before the jet energy scale correction have been applied [61].

GSC, which consists of a series of MC-based corrections that make use of the information on the topology of the jet in the calorimeter and on the tracking from the Inner Detector and the Muon Spectrometer. Overall, the GSC improves the jet energy resolution without altering the average jet energy scale set in the previous JES calibration step. The GSC is a five-stages correction that uses:

- the fraction of jet energy deposited in the first layer of the Hadronic Tile Calorimeter;
- the fraction of jet energy deposited in the third layer of the Electromagnetic Calorimeter;
- the number of tracks ghost-associated to the jet[8];
- the jet width as measured from the p_{T}-weighted average of the spread of its tracks;
- the number of track segments reconstructed from the Muon Spectrometer alone and ghost-associated to the jet.

In the case of LCW jets, only the last three steps are applied since the calorimeter-based corrections have already been taken care of in the cluster calibration process.

4.3.6 In-situ Correction

The very last step of the JES calibration process is the correction for any residual difference observed between data and MC and that is caused by limitations of the simulation. The *in-situ* correction can be expressed as:

$$\frac{\mathcal{R}_{\mathrm{MC}}}{\mathcal{R}_{\mathrm{data}}} = \frac{\langle p_{\mathrm{T}}^{\mathrm{jet}}/p_{\mathrm{T}}^{\mathrm{ref}}\rangle_{\mathrm{MC}}}{\langle p_{\mathrm{T}}^{\mathrm{jet}}/p_{\mathrm{T}}^{\mathrm{ref}}\rangle_{\mathrm{data}}} \tag{4.5}$$

where $p_{\mathrm{T}}^{\mathrm{ref}}$ is the p_{T} of a well calibrated reference physics object used to balance the jet p_{T}, $p_{\mathrm{T}}^{\mathrm{jet}}$. The jet p_{T} ratios from data and MC are then compared in order to derive the correction. Since the jet calibration procedure described throughout this section is able to accurately restore the energy of jets reconstructed in MC samples to their truth scale energy, the in-situ correction accounts for the residual differences observed between MC and data, as the latter may respond differently to the MC-based calibration. For this reason, the in-situ correction is applied to data only. The in-situ correction uses central, well calibrated jets, Z bosons, photons and systems of low p_{T} jets as reference objects to derive the final calibration factors. Despite the in-situ corrections derived from 2012 data being applicable, in first approximation, to 2015 data too (thanks to the negligible changes in the detector), the fact that all the other MC-based corrections described in the previous sections have been derived from new MC samples with updated physics and detector modeling required a new calculation of the in-situ factors for the 2015 data [61].

[8]Ghost association matches a track to a jet if a fictitious track with identical η and ϕ but negligible p_{T} would be included in the jet by the clustering algorithm. See also Section 4.3.3.

4.3.7 Run-1 and Run-2 Differences

Since the jet calibration process has evolved over time in ATLAS and since this thesis is focusing on both the 8 TeV and 13 TeV dijet analyses, a general overview of the JES scheme is presented and the differences between Run-1 and Run-2 are highlighted [61].

Detector The installation of the IBL in 2014 added 0.04 X_0 of material in the central volume of ATLAS, which can be regarded as negligible. However the IBL services amount to around 5 X_0 in the forward region ($|\eta| > 4.5$) and lead to a modulation in the calorimeter response in ϕ. Anyway these changes are not significant for the calibration of early Run-2 high-p_{T} jets.

Beam Conditions The most important modifications to the beam in Run-2, i.e. energy and bunch spacing, have only minor effects on the jet calibration. The increase of the beam energy from 4 TeV to 6.5 TeV caused a change in the quark/gluon fraction of the jets. However this flavour effect has no significant consequences for the systematic uncertainties. The halving of the bunch spacing, from 50 ns to 25 ns, doubled the amount of out-of-time pile-up but since the detector is designed to operate at 25 ns, no relevant effects are observed. Finally the instantaneous luminosity reached in 2015 is comparable to that of 2012, hence no additional differences are observed.

LAr Calorimeter Energy Reconstruction While in 2012 the timing and energy of the LAr calorimeter were reconstructed using 5 sampling points, these have been reduced to 4 in 2015.

Topocluster Reconstruction In Run-2 topoclusters have been forbid from growing using neighbours in the calorimeter presampler layers, hence reducing the effects of pile-up.

Muon Track Segments The association of track segments in the Muon Spectrometer to the calorimeter jet has migrated in Run-2 from ΔR matching to ghost matching. Timing threshold for muon tracks have also been tightened.

Track Reconstruction The installation of the IBL has improved the track reconstruction and hence the jet calibration, since tracks are used to measure the jet fragmentation (see Section 4.3.5). The impact on the systematic uncertainties however is negligible.

Detector Simulation The simulation of hadronic inelastic scattering has been reduced to the use of two models in Run-2 instead of three as in Run-1. A dependence of the calorimeter cells response on the particle azimuthal position with respect to the cell center was observed in Run-1 but never accounted for until Run-2, leading to a change in the energy measurement in the Hadronic Tile Calorimeter cells.

4.3.8 Uncertainties

The uncertainties on the jet energy measurement are one of the dominant sources of uncertainty for many analyses and searches. Among these is the dijet high mass study of this thesis, in which the jet uncertainties reduce the sensitivity to the benchmark signals used to set limits. These uncertainties (systematic and statistic) vary as functions of jet η and p_{T} and come from different sources, such as: in-situ methods, single-hadron calorimeter response, η-intercalibration, pile-up corrections and jet flavour. At large p_{T}, the dominant contributions to the JES uncertainty come from the in situ measurement and above 1.8 TeV the uncertainties are estimated from the calorimeter response to single hadrons. Figure 4.8 shows a comparison of 2012 and 2015 jet energy scale uncertainties as well as their breakdown. In both cases, jet uncertainties of 6% are expected for very low-p_{T} jets, while jets of medium p_{T} have uncertainties as low as 1%. Uncertainties of high-p_{T} jets, on the other hand, rise up to 3%.

A total of 65 different sources of systematic uncertainties, or *nuisance parameters*, on JES have been identified for 2012 jet studies and 74 for 2015. These large numbers become unmanageable rather quickly, due to the considerable computational time that is required to propagate the effects of each single uncertainty component. For this reason a reduced set of nuisance parameters is derived by means of an eigenvector decomposition. This method identifies the independent contributions to the uncertainty components matrix and builds a set of the orthogonal components with the largest eigenvalues with an additional term given by the quadrature sum of the weaker elements. Thanks to this method, reduced sets of 15 and 3 uncertainty components have been derived for the 2012 and 2015 analyses respectively. These sets have been observed to significantly reduce the time required to evaluate the jet calibration systematics effects on the analyses while retaining most of the uncertainty uncorrelated information.

4.4 Flavour Tagging

The identification of the jet flavour is a crucial component of many analyses whose results depend on the flavour of the hard scatter partons[9] [65, 66, 67]. Long-lived hadrons, such as B-hadrons, have relatively long life times, of the order of a few picoseconds. The relativistic boost at the LHC makes a large fraction of these decay a few millimiters away from the primary vertex, hence producing displaced secondary vertices that can be reconstructed and exploited to tag the jet flavour. The identification of jets originating from b quarks, commonly referred to as *b-tagging*, is based on the tracking information from the ID. The track selection can vary between tagging algorithms but the common strategy is to select tracks with small impact parameter and with p_{T} greater than a few hundred MeV. The selected tracks are then associated to the jets using ΔR matching. The most relevant improvements introduced in Run-2 affecting the performance of b-tagging are the installation of the IBL and the introduction of a neural-network-based algorithm

[9] Among these is also the dijet analysis looking for high mass resonances in the invariant mass spectrum of b-tagged dijets [64].

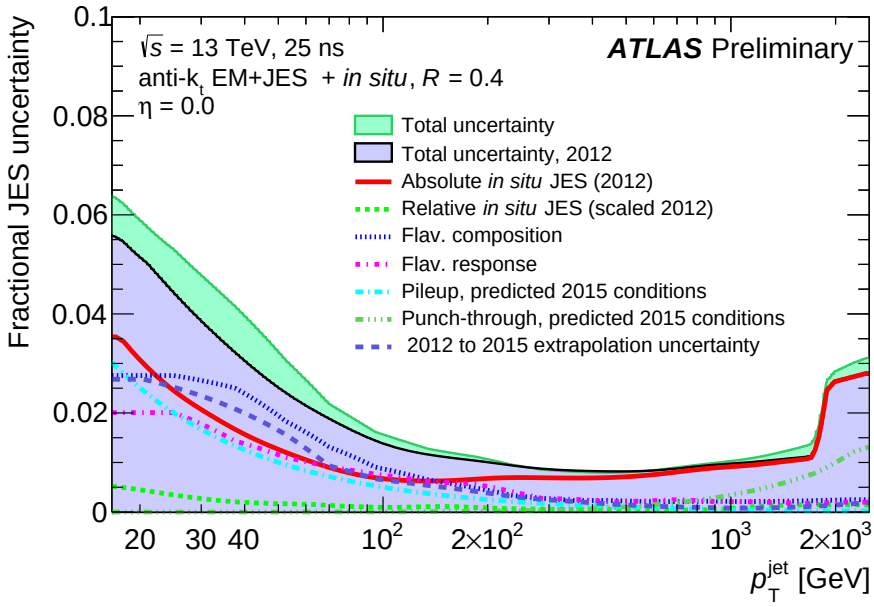

(a)

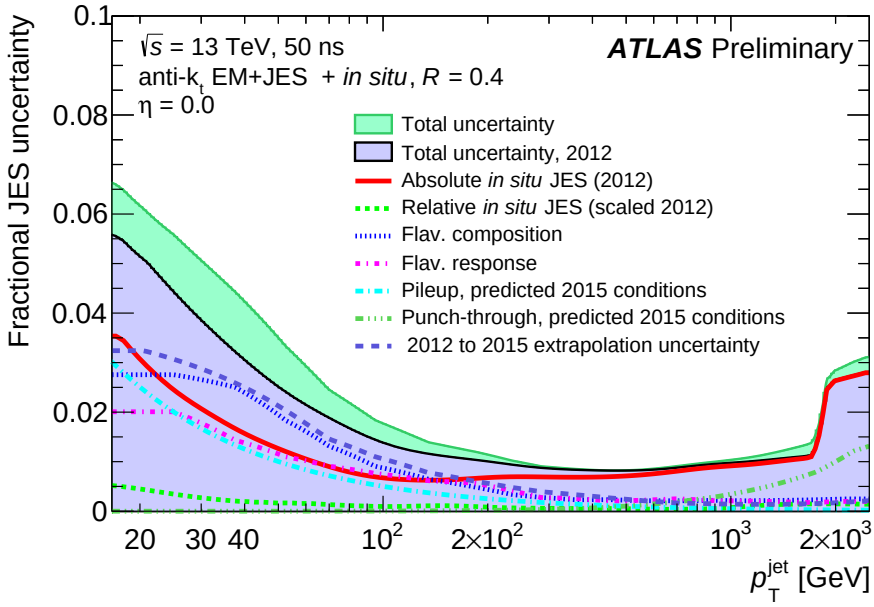

(b)

Figure 4.8: jet energy scale uncertainties for 2012 and 2015 (estimated) as a function of jet p_{T} for 25 ns (a) and 50 ns (b) bunch spacing [61]. The purple-shaded areas show the total JES uncertainty as it was measured in 2012 data. The components of the total uncertainty are represented by the dotted and dashed lines. The purple dashed line shows the uncertainty on the extrapolation of the 2012 JES to the 2015 conditions and the green shaded areas show the estimated JES uncertainty in 2015.

to handle shared hits. These have significantly improved the impact parameter resolution and the tracking in dense environments, such as in the jet core [68]. The b-tagging algorithms in ATLAS make use of the tracking information to produce output weights to discriminate between different jet flavours. Algorithms are calibrated using data samples and cut values on their output discriminants are provided so that they correspond to specific tagging efficiencies, or *working points*. Four classes of algorithms can be identified based on the input information they employ to tag jets:

- track impact parameter;
- inclusive secondary vertex;
- full decay chain and multi-vertex reconstruction;
- combination of the discriminants from other algorithms.

4.4.1 IP2D and IP3D

The IP2D and IP3D algorithms employ the significance of the impact parameters of tracks associated to jets. The sign of such significance is defined as positive if the track's point of closest distance to the primary vertex is located in front of the primary vertex when seen from the jet position. The Probability Distribution Function, PDF, of the track signed impact parameters are used to make b-jet and light-jet ratios which are then combined to build Log-Likelihood Ratio, LLR, discriminants. Similarly, LLRs can be built to discern b-jets from c-jets and c-jets from light-jets. IP2D uses the significance of the track transverse impact parameter while IP3D uses both the track transverse and longitudinal impact parameters significance. Given the typically large values of the longitudinal impact parameter significance of tracks from pile-up jets, IP3D is less robust than IP2D against pile-up.

4.4.2 SV1

The SV1 algorithm performs the reconstruction of the B-hadron secondary vertex. The tagging procedure starts from the reconstruction of secondary vertices from of all possible combination of selected track pairs. Vertices are then selected based on their quality and likelihood of originating from B-hadrons and the remaining tracks are then iteratively added. Quantities such as the vertex energy, mass, significance of its 3D displacement and ΔR between vertex and jet are used as flavour discriminants.

4.4.3 JetFitter

The JetFitter algorithm attempts to reconstruct the full decay chain, from primary vertex to B-hadron vertex to C-hadron vertex. A Kalman filter is employed to find a line that accommodates the three vertices, so that these can be reconstructed even with only one track available, therefore significantly improving the vertex reconstruction efficiency. The mass and the energy fraction reconstructed from the tracks associated to each vertex are used to build a likelihood which is in turn employed to discriminate the jet flavour.

4.4.4 MV1

MV1 is a jet flavour tagging algorithm used in Run-1 that combines the output discriminants from IP3D, SV1 and JetFitterCombNN (a neural network combination of IP3D and JetFitter outputs) into a neural network to extract a discriminant that takes advantage of the different approches of the three algorithms to provide the best jet flavour discriminant. A variant of MV1 with improved c-jet rejection, MV1c, was developed by performing the algorithm training using also c-jets as background.

4.4.5 MV2

MV2 is a Run-2 updated version of the MV1 algorithm and it is based on a boosted decision tree directly exploiting the output discriminants from the IP2D, IP3D, SV1 and JetFitter algorithms together with the jet p_{T} and η. The MV2 algorithm is provided in two variants: MV2c20 and MV2c00 which are trained on two different background sets of jets. MV2c00 is trained on a pure sample of light-jets, while MV2c20 is trained on a mixture of 80% light-jets and 20% c-jets, which significantly improves its c-jet rejection at the expenses of slightly reducing the light-jet rejection. Figure 4.9 shows a comparison of the light-jet and c-jet rejection power of the MV1c and MV2c20 algorithms as a function of the algorithm b-tagging efficiency [67]. The introduction of the IBL in Run-2 significantly improves the b-tagging performance for jets with p_{T} below $\sim$ 200 GeV, since at higher p_{T} a large fraction of b-hadrons decay outside the IBL volume.

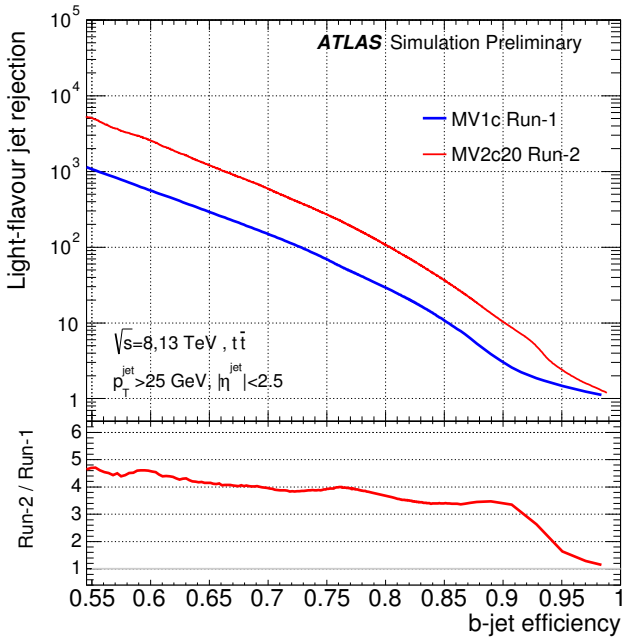

(a)

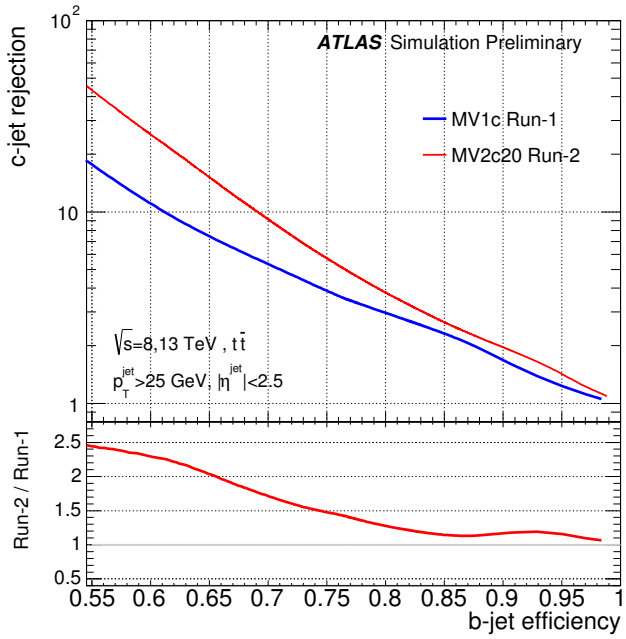

(b)

Figure 4.9: Light-jet (a) and c-jet (b) rejection of the MV1c and MV2c20 algorithms as a function of the b-jet efficiency of the algorithm [67]. The curves show the rejections obtained at $\sqrt{s} = 13$ TeV in events in which the IBL was present.

Chapter 5

Jet Angular Resolution

The independent jet measurements given by the ATLAS ID and calorimeters can be exploited to obtain a data-driven measurement of the Jet Angular Resolution, JAR [69][1]. The two variants of jet, i.e. *track-jets* and *calo-jets* introduced in Sections 4.2.2 and 4.2.3 respectively, have complementary features. On one hand calo-jets have good energy resolution, since they are reconstructed from energy deposits of charged as well as neutral particles, on the other track-jets are more pile-up robust, since they are reconstructed using only tracks associated to the PV. These two independent jet measurements can therefore be employed to provide a data-driven estimation of the JAR. The Root Mean Square, RMS, of the η and ϕ distances between calo-jets and track-jets with respect to jets reconstructed using truth particles in Monte Carlo samples, *truth-jets*, has been measured first to estimate the absolute JAR of the two jet collections (see Section 5.4). Based on these results, the RMS of the η and ϕ distances between ΔR-matched calo-jets and track-jets is then computed for data and MC samples (see Section 5.5). These values are taken as a data-driven estimation of the JAR and are of particular relevance for analyses such as the dijet angular search and all those that are sensitive to the geometrical topology of the events. MC smearing factors, necessary to align the MC angular resolution to that measured in data, are derived in Section 5.6. Section 5.7 illustrates the significant JAR improvement introduced by the jet origin correction.

5.1 Data and Monte Carlo Samples

The studies described in this Section have been performed using 8 TeV data from period B, which were collected between May 1st and June 18th 2012 and corresponds to an integrated luminosity of 5.47 fb^{-1}. The default Monte Carlo dataset for data comparison is a dijet sample generated using PYTHIA8 [42] with AU2 tune [70] and CT10 PDFs [71]. Systematics uncertainties on MC measurements have been evaluated using a set of MC

[1]This Section is based on the results of my ATLAS authorship qualification task and documented in [69]. All the studies and measurements reported there, with the only exception of the JAR uncertainties extrapolation described in the appendix, have been performed by the author of this thesis.

simulations produced with different generators, underlying event tunes and detector modeling. These are:

- Pythia8 [42] sample generated using Au2 tune [70] and Ct10 Pdfs [71] with additional dead material in the Id to estimate the effects of detector mismodeling; specifically this sample has been produced with 5% additional dead material in the whole Id, 20% more Pixel and Sct services and 15% more radiation lengths, X_0, at the end of Sct and Trt end-caps and at the Id end-plate;
- Herwig [44] sample generated using Ee3 tune [72] and Cteq6l1 Pdfs [73];
- Sherpa [47] sample generated using default Sherpa tune and Ct10 Pdfs [71];
- Powheg [43] sample generated using Au2 tune [70] and Ct10 Pdfs [71] and showered by Pythia [42].

5.2 Event and Jet Selection

The event selection is based on the recommendations for 2013 b-tagged analyses and uses the jet calibrations and uncertainties for 8 TeV data released in 2014. These can be summarised as follows.

- Events must pass the Good Run List, Grl, i.e. events must be from a run when the Atlas detector was fully operational and ready for data taking.
- Events must pass any of the single jet triggers with E_{T} threshold between 15 GeV and 360 GeV (lowest un-prescaled). No trigger selection is applied to Mc.
- The primary vertex in data is required to have at least two tracks.
- Events must not have any Em Calorimeter nor Hadronic Tile Calorimeter errors (see Section 6.6.1). Incomplete events are removed.
- Events must not have jets in the Hadronic Tile Calorimeter hotspots. The presence of masked modules, either temporarily or permanently, during the data taking, required the introduction of a correction to compensate the lack of energy reading in the Hadronic Tile Calorimeter (namely Bch_corr_cell, see Section 6.6.1). This correction was however observed to be the cause of hotspots in the η-ϕ map of the leading jets. It was thus decided to remove these events whenever one of the leading jets would be in the neighbourhood of a masked cell. The effect was simulated a posteriori in Mc to reproduce the same amount of *holes* in the Hadronic Tile Calorimeter and the same resolution effects. See below for more details.
- No *ugly* or *bad* jets, nor jets from background (see Section 6.6.1).
- At least two jets within the Atlas tracking volume: $|\eta| < 2.5$.
- No Mc events where the simulated pile-up jets have p_{T} higher than the hard scatter partons.

5.3 MC to Data Reweighting

In order to have MC to be as close as possible to data and recover any difference between the actual conditions of data taking in 2012 and the simulated conditions, the MC samples have been reweighed to have the same pile-up features and the same p_{T} distribution as data. As a first step the MC samples have been reweighted event by event to restore pile-up conditions similar to those of data. This was done through the PileupReweightingTool [74] and using the average number of interactions per bunch crossing, μ. MC calo-jets have then been reweighted to have the same p_{T} distribution as data. Figure 5.1a shows calo-jet p_{T} spectra for data and MC samples after event selection and reweighting. Figure 5.1b shows calo-jet η distributions for data and MC, which are observed to be compatible within a few percent even though these distributions are not directly reweighed to each other. The $\Delta\eta = |\eta_{\mathrm{calo-jet}} - \eta_{\mathrm{track-jet}}|$ and $\Delta\phi = |\phi_{\mathrm{calo-jet}} - \phi_{\mathrm{track-jet}}|$ distributions of ΔR matched calo-jet and track-jet reported in Figure 5.2 show a fairly good agreement between data and MC, with only minor differences in the tails.

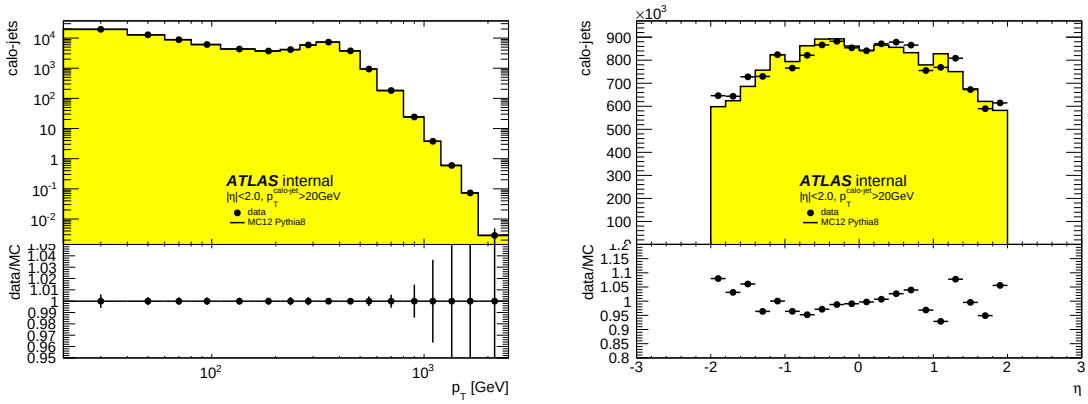

(a) p_{T}. (b) η.

Figure 5.1: p_{T} (a) and η (b) spectra for data and MC calo-jets that are ΔR matched to track-jets after pile-up and p_{T} reweight. Differences in the η spectra are observed to be within 10%.

5.4 MC-Based Jet Angular Resolution

The JAR has to be intended here as the RMS of the distance between a truth-jet and a calo-jet or a track-jet, so the smaller the distance the better the resolution. The absolute η and ϕ JARs are measured for calo-jets and track-jets in bins of truth-jet η and p_{T}. For each event that passes the selection, a loop is done over the collection of truth-jets looking for matching calo-jets and track-jets. The matching is done by selecting the closest jet (calo-jet and track-jet) in $\Delta R = \sqrt{\Delta\eta^2 + \Delta\phi^2}$, with an upper limit set at $\Delta R = 0.4$ to avoid the tails coming from events where the jet corresponding to the truth-jet was not

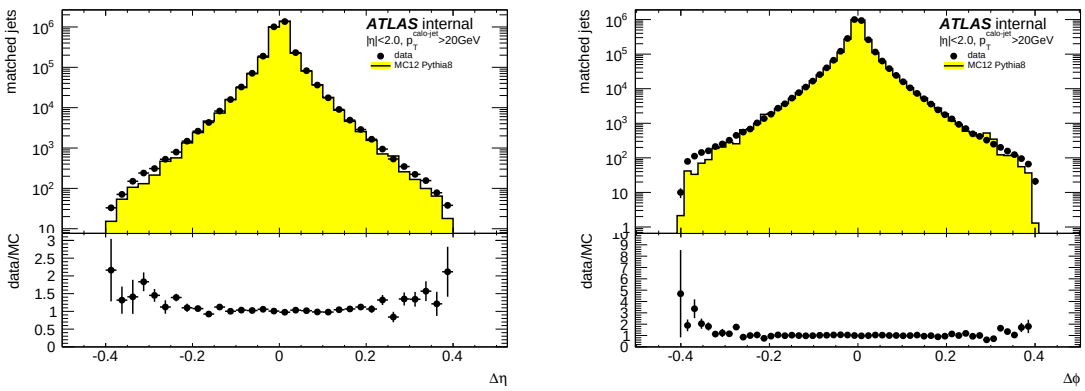

(a) $\Delta\eta$. (b) $\Delta\phi$.

Figure 5.2: calo-jet to track-jet $\Delta\eta$ (a) and $\Delta\phi$ (b) distributions for data and MC. The agreement between the distributions is found to be quite good, with only minor discrepancies in the tails.

reconstructed. In case either a track-jet or a calo-jet match is not found, the truth-jet is rejected. Since the Inner Detector coverage in pseudorapidity is limited to $|\eta| < 2.5$, truth-jets are required to be within $|\eta| < 2.0$ so that any situation where a jet is on the edge of the Inner Detector is avoided. Transverse momentum thresholds are set for truth-jets at 30 GeV, for calo-jets at 20 GeV and for track-jets at 10 GeV in order to prevent any low p_{T} reconstruction turn-on effect and account for the poorer energy resolution capabilities of the track-jets. For these studies calo-jet p_{T} reweighting is not applied as we are looking simultaneously at calo-jets, track-jets and truth-jets.

Calo-jet and track-jet angular resolutions are reported in Figure 5.3 as a function of truth-jet p_{T} and in Figure 5.4 as a function of truth-jet η. As Figure 5.3 indicates, η and ϕ resolutions are observed to be comparable for calo-jet and track-jets separately. The better resolution of calo-jets with respect to track-jets is explained by the fact that electrically neutral particles are not taken into account when reconstructing track-jets but their energy deposits contribute to the performance of the calorimeter and thus to the calo-jet resolution. The improved JAR at high transverse momenta is explained by the better performance of the detectors in the barrel region, where high p_{T} jets are concentrated, as well as because high p_{T} jets are more collimated. Looking at Figure 5.4 we observe again how the track-jet angular resolution is almost flat in pseudorapidity and azimuthal angle thanks to the uniformity of the ID performance. Calo-jets, on the other hand, have a better η resolution than ϕ resolution thanks to the implementation of the origin correction. Moreover, calo-jets profit from the highly collimated topology of jets in the forward regions and have thus a better resolution at high pseudorapidity.

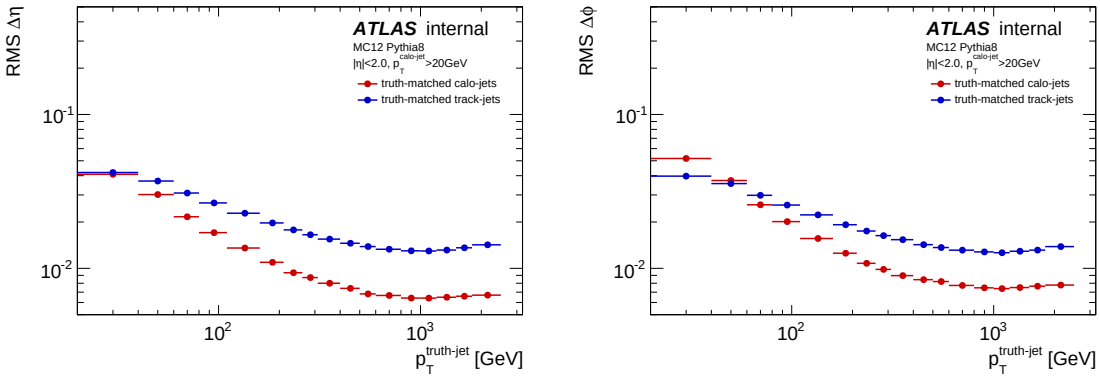

(a) Rms $\Delta\eta$. (b) Rms $\Delta\phi$.

Figure 5.3: Rms of calo-jet and track-jet $\Delta\eta$ (a) and $\Delta\phi$ (b) as a function of truth-jet p_{T}.

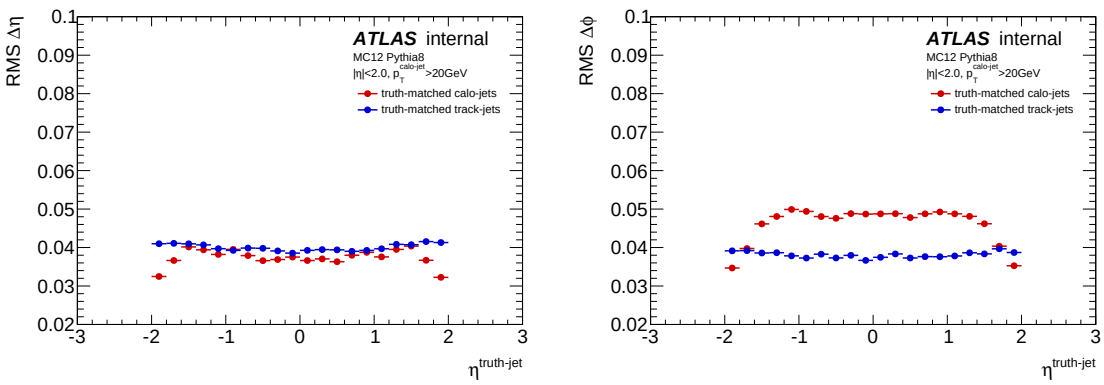

(a) Rms $\Delta\eta$. (b) Rms $\Delta\phi$.

Figure 5.4: Rms of calo-jet and track-jet $\Delta\eta$ (a) and $\Delta\phi$ (b) as a function of truth-jet η.

5.5 Data-Driven Jet Angular Resolution

Given the good agreement between data and Mc and the comparable resolution of calo-jets and track-jets, it is possible to get an estimate of the Jar in a data driven way, i.e. by looking at the Rms of the distance between matching calo-jets and track-jets. In this case as well, the matching is done in ΔR with an upper cut at 0.4, in order to remove events where one of the jets is not reconstructed. Once again, calo-jets are required to be within $|\eta| < 2.0$ in order to have a complete overlap with the Id volume. Transverse momentum thresholds are set at 20 GeV for calo-jets and 10 GeV for track-jets to avoid turn-on effects in the reconstruction process. Calo-jets are reweighed to match the p_{T} distribution of data.

Systematics uncertainties on the modeling and simulation of track-jets are taken into

account. Three sources of uncertainty in particular are considered: the passive material in the simulation (such as services, cables and support structures), the hard-scattering and fragmentation modeling of the MC generator and the tracking efficiency. The contribution coming from the dead material simulated in the geometry of the detector is estimated from a dedicated MC sample where additional material is put in the simulation of the ID (see Section 5.1). The uncertainty coming from the hard-scatter and fragmentation model is evaluated repeating the angular measurements using a set of MC samples produced with different MC generators (see Section 5.1). The tracking efficiency uncertainty is taken into account by repeating the track-jet reconstruction process (on the default MC sample) while randomly removing tracks from the collection according to the known tracking efficiency of the ID [75]. The uncertainties are then estimated as the difference between the nominal results and those obtained with the alternative samples and are then added in quadrature as independent factors of uncertainty.

Figure 5.5 shows the data-driven angular resolution as a function of calo-jet p_{T} in data and MC. The yellow band represents the MC angular resolution together with the associated systematic uncertainties. Similarly, η and ϕ resolutions as functions of calo-jet pseudorapidity are shown in Figure 5.6. Data and MC results are compatible within systematic uncertainties. For completeness, Figures 5.7 and 5.8 show the breakdown of the MC uncertainties: default MC sample (PYTHIA8, red), default MC sample with track-jets re-reconstructed after removing some of the tracks according to the known ID tracking efficiency (PYTHIA8 tracking, blue), MC sample with additional dead material in the ID volume (PYTHIA8 material, light blue), HERWIG MC sample (HERWIG, teal), SHERPA MC sample (SHERPA, green), POWHEG MC sample (POWHEG, light green).

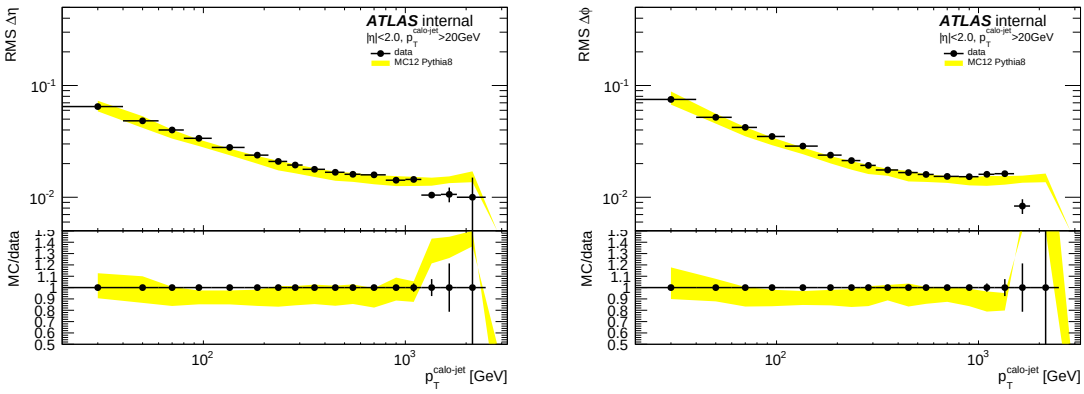

(a) RMS $\Delta\eta$. (b) RMS $\Delta\phi$.

Figure 5.5: data and MC η (a) and ϕ (b) resolutions as functions of calo-jet p_{T}. The yellow band represents MC resolution with systematic uncertainties included. Data and MC resolutions are consistent within uncertainties. The lack of high p_{T} jets in data results in lower $\Delta\eta$ and $\Delta\phi$ RMS values.

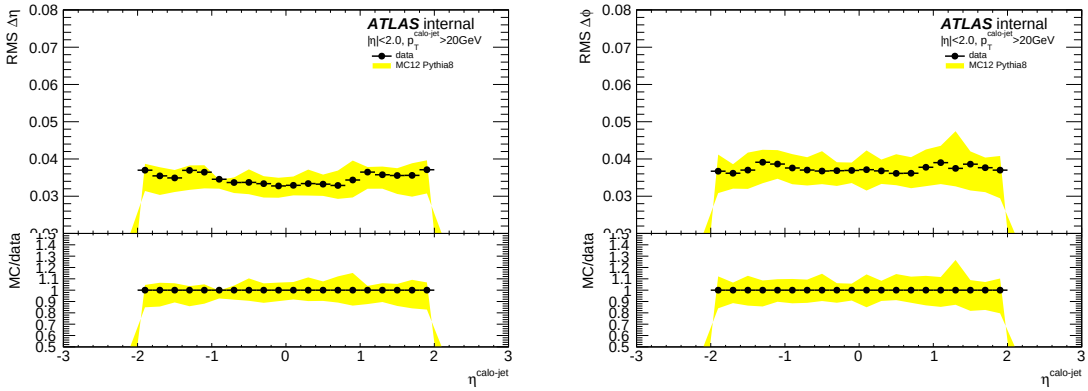

(a) RMS $\Delta\eta$.

(b) RMS $\Delta\phi$.

Figure 5.6: data and MC η (a) and ϕ (b) resolutions as functions of calo-jet η. The yellow band represents MC resolution with systematic uncertainties included. Data and MC resolutions are consistent within uncertainties.

5.6 MC Smearing Factors

MC smearing factors can be derived from p_{T}-η resolution maps to restore a more data-like JAR. For this specific purpose, the angular resolution is defined as the σ of the gaussian function that fits the $\Delta\eta$ or $\Delta\phi$ distribution. η resolutions are reported in Figure 5.9 and ϕ resolution are reported in Figure 5.10. Due to the lack of statistics, the bins corresponding to energies greater than 1.5 TeV have been set to zero. As previously observed, data and MC angular resolutions are observed to be similar, with small dependence on the pseudorapidity and improving at high p_{T} values.

For each p_{T}, η bin the smearing factor has been defined as:

$$\text{smearing factor} = \sigma^2_{\text{data}} - \sigma^2_{\text{MC}} \tag{5.1}$$

Results are shown in Figure 5.11. As already noticed in Figures 5.2, 5.5 and 5.6, the comparable η and ϕ resolutions of data and MC lead to very small smearing factors.

5.7 Jet Origin Correction

As it has been observed in Figure 5.3, the calo-jet η resolution is better than the track-jet's. However, before the inclusion of the origin correction into the jet calibration, the situation was different, as it is shown in Figures 5.12 and 5.13. The η resolution is clearly improved by requiring the calo-jets to point to the reconstructed primary vertex (using the ID vertex reconstruction info) instead of the center of the detector. It can be observed that such correction restores the η calo-jet resolution vs. p_{T} close to the values of the ϕ resolution and significantly improves the resolution vs. η. As expected, no significant effect is observed on the calo-jet ϕ resolution, since the origin correction works mainly

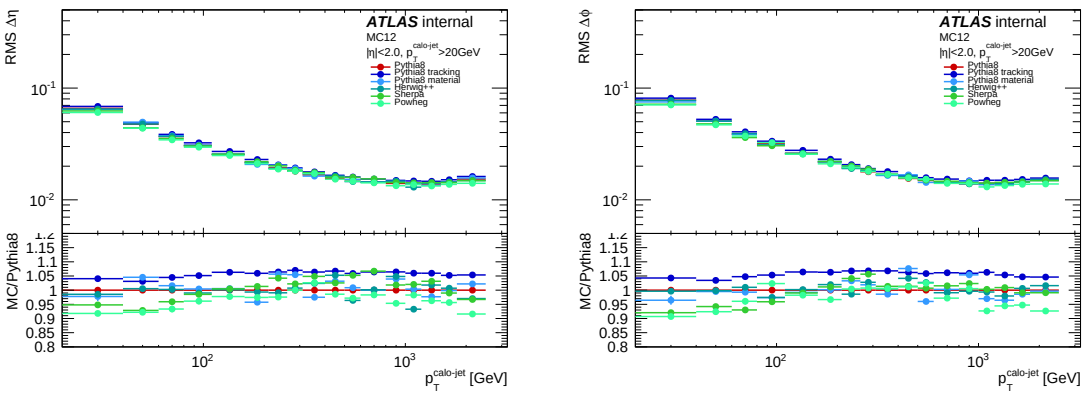

(a) (b)

Figure 5.7: η (a) and ϕ (b) angular resolutions as functions of calo-jet p_{T} calculated for several MC generators.

on the z-axis. Despite the first JES calibrations released for the 2012 dataset were not including the jet origin correction, the encouraging results and the validation provided by the JAR studies led to its reintroduction.

5.8 Conclusions

The Jet Angular Resolution has been measured using a data-driven technique which exploits the redundant jet reconstruction of the ATLAS detector. The angular resolution of calo-jets and track-jets with respect to truth-jets has been measured in MC. Results show that despite the better angular resolution of tracks with respect to the capabilities of the calorimeter cells, calo-jets often have a better resolution than track-jets. This is explained by the fact that calo-jets, unlike track-jets, are reconstructed from the contributions of charged and neutral particles. Moreover the use of the origin correction compensates the poor calo-jet η resolution due to the size of the beam spot (see Figures 5.3 and 5.4). The calo-jet angular resolution has been measured using track-jets as reference. The results shown in Figures 5.5 and 5.6 exhibit a good agreement of data and MC within systematic uncertainties. Nevertheless it is possible to observe that both the η and ϕ resolutions as functions of calo-jet p_{T} are slightly worse for data than for MC, suggesting the possible need for smearing factors. The differences observed between data and MC at high p_{T} are due to the lack of jets in data. The breakdown of the MC systematics components, shown as a yellow band in the previous plots, are reported in Figures 5.7 and 5.8. Figures 5.9 and 5.10 show the width of the calo-jet and track-jet $\Delta\eta$ and $\Delta\phi$ in bins of calo-jet p_{T} and η. Very little dependence is observed in η, as in Figure 5.6. The bins corresponding to jet energies above 1.5 TeV have been removed due to the limited statistics and the consequent fluctuations. Smearing factors for MC have been derived from Figures 5.9 and 5.10 and are shown in Figure 5.11. As described previously, MC smearing factors are

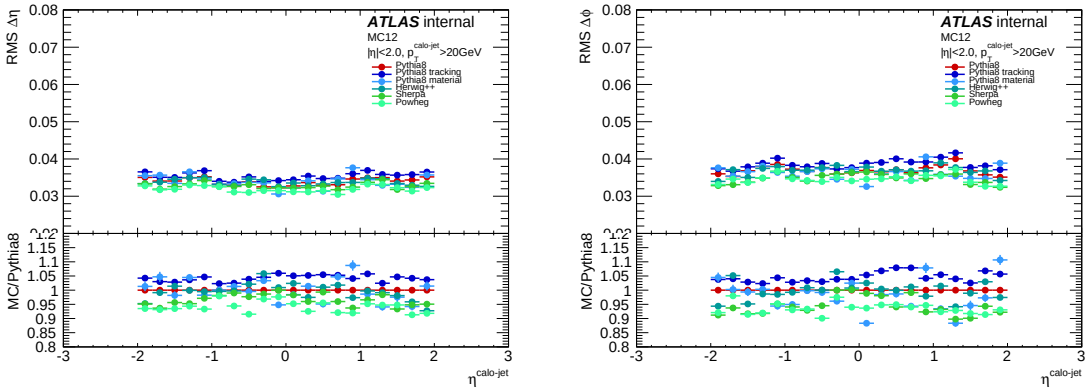

(a) (b)

Figure 5.8: η (a) and ϕ (b) angular resolutions as functions of calo-jet η calculated for several MC generators.

needed in order to match the JAR measured in data. However, the values of the factors are very small ($O(10^{-4} - 10^{-5})$) and affect mostly the low p_{T} bins. Finally the calo-jet origin correction has been observed to be a valid tool to significantly improve the η angular resolution by including vertex information from the more accurate Inner Detector into the jet reconstruction.

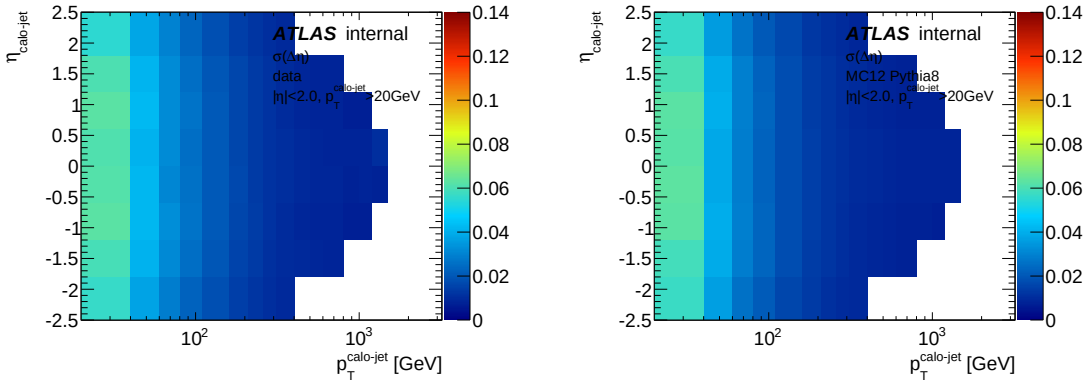

(a) (b)

Figure 5.9: σ of calo-jet and track-jet $\Delta\eta$ for data (a) and MC (b) as a function of calo-jet p_{T} and η. Bins corresponding to energies greater then 1.5 TeV have been set to zero due to lack of statistics.

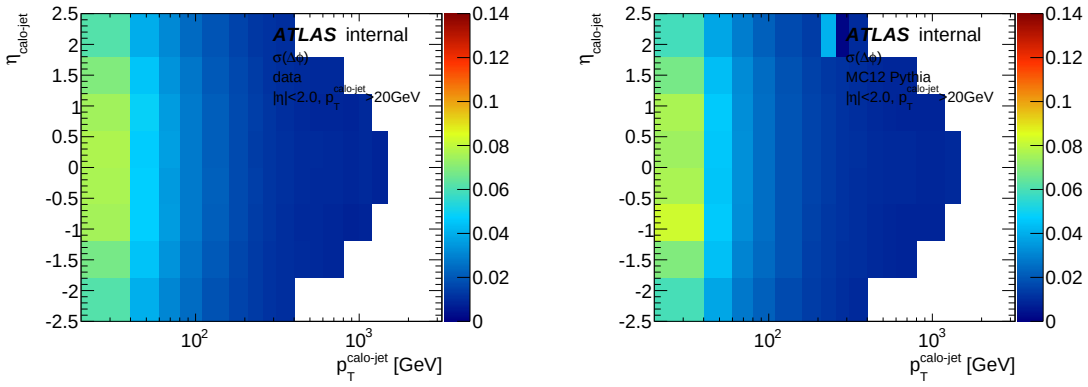

(a) (b)

Figure 5.10: σ of calo-jet and track-jet $\Delta\phi$ for data (a) and MC (b) as a function of calo-jet p_{T} and η. Bins corresponding to energies greater then 1.5 TeV have been set to zero due tot lack of statistics.

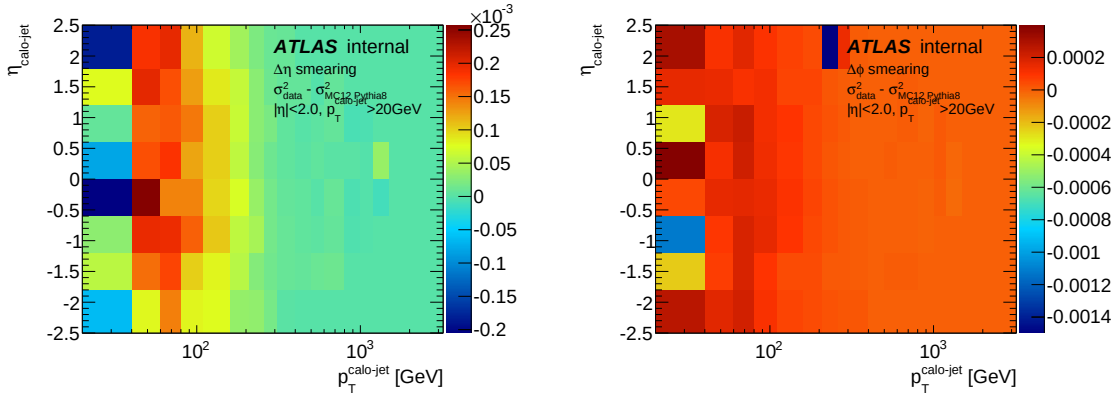

(a) (b)

Figure 5.11: MC smearing factors for η (a) and ϕ (b) resolutions in bins of calo-jet p_{T} and η. Values are very small or negative, confirming that the MC smearing can be ignored.

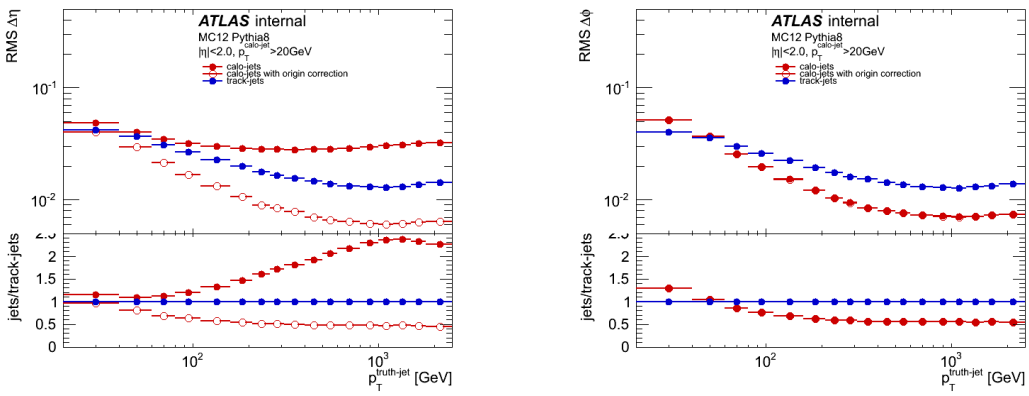

(a) RMS $\Delta\eta$. (b) RMS $\Delta\phi$.

Figure 5.12: RMS of $\Delta\eta$ (a) and $\Delta\phi$ (b) as functions of truth-jet p_{T}. Values for calo-jets, calo-jets with origin correction and track-jets are shown.

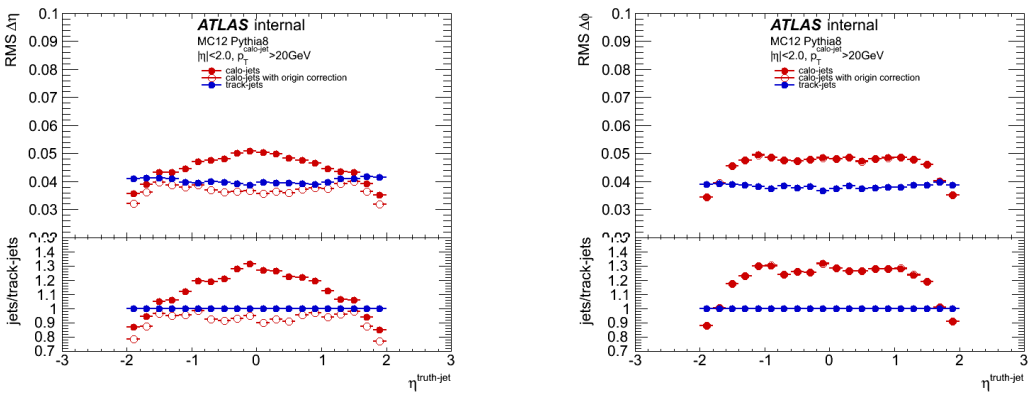

(a) Rms $\Delta\eta$.

(b) Rms $\Delta\phi$.

Figure 5.13: Rms of $\Delta\eta$ (a) and $\Delta\phi$ (b) as functions of truth-jet p_{T}. Values for calo-jets, calo-jets with origin correction and track-jets are shown.

Chapter 6

Exotic Dijet Resonance Analysis

Collisions produced by the LHC may lead to the production of particles outside the frame of the Standard Model of particle physics. If these particles are generated from parton-parton interactions, they may as well produce parton-parton final states. Given the large cross section of *pp* interactions at the LHC, it is therefore of paramount importance to look for *exotic* physics phenomena lying outside the known theories and manifesting as two-jet, or *dijet*, final states. Moreover, the search for exotic dijet resonances is model-independent, as it looks for localised excess in a inclusive event selection, without making any model-driven assumption.

6.1 Dijets From QCD And Beyond the Standard Model Processes

The SM predicts a steeply and smoothly falling dijet invariant mass, m_{jj}, distribution. On the other hand, dijets in Beyond the Standard Model, BSM, theories give localised m_{jj} distributions, peaked around the mass value of the BSM particle decaying in two jets. Together with the typically large production cross sections and branching ratios into dijet final states of these models, the peaked-signal expectation allows efficient searches of new physics phenomena starting from little amounts of data.

In the Standard Model, *pp* collisions produce dijet final states mainly via QCD parton scattering, with only minor contributions from other SM processes. The $2 \rightarrow 2$ parton cross section has poles in the t-channel which favour the production of dijets at small angles with respect to the beam axis, or, in other terms, at large rapidity, in the forward regions of the detector. At large energy scales of interaction however, jets are produced at large angles, in the central region of the detector. This is also the case of most BSM models, which are predicted to be produced mostly with high transverse momentum and small rapidities.

Useful insights into the dijet analysis can be gained from simple considerations on the two-parton scattering process [76].

6.1.1 Two-Parton Scattering

The two-parton scattering process, where the incoming partons, 1 and 2, interact to produce the outgoing partons, 3 and 4:

$$1 + 2 \to 3 + 4 \tag{6.1}$$

can be described in terms of the Mandelstam variables:

$$\hat{s} = (p_1 + p_2)^2 \tag{6.2}$$

$$\hat{t} = (p_1 - p_3)^2 = -\frac{1}{2}\hat{s}(1 - \cos\theta^*) \tag{6.3}$$

$$\hat{u} = (p_2 + p_3)^2 = -\frac{1}{2}\hat{s}(1 + \cos\theta^*) \tag{6.4}$$

$$\hat{s} + \hat{t} + \hat{u} = 0 \tag{6.5}$$

where p_i are the four-momenta of the massless partons, θ^* is the scattering angle of the partons in the collision frame, which is related to the partons rapidity in the collision frame, y^*, through:

$$\cos\theta^* = \tanh y^*. \tag{6.6}$$

In the laboratory frame the partons rapidities are given by:

$$y_i = \frac{1}{2}\ln\frac{E_i + p_z^i}{E_i - p_z^i} \tag{6.7}$$

and are connected to y^* through:

$$y^* = \frac{1}{2}(y_3 - y_4). \tag{6.8}$$

The momentum difference of the two colliding partons gives the collision frame a boost with respect to the laboratory frame corresponding to a rapidity, y_{B}:

$$y_{\mathrm{B}} = \frac{1}{2}(y_3 + y_4) = \frac{1}{2}\ln\frac{x_1}{x_2} \tag{6.9}$$

where x_i are the proton momentum fractions carried by the colliding partons.

At Leading Order, LO, the QCD matrix elements participating to the pp interaction show a similar behaviour, i.e. have a t-channel pole for small scattering angles, with the only exception of $q_1\overline{q}_1 \to q_2\overline{q}_2$, which is in turn flat as it is an s-channel process. In the approximation of QCD background dominated by t-channel processes, the angular distribution can be approximated as[1]:

$$\frac{d\sigma}{d\cos\theta^*} \sim \frac{1}{\hat{t}^2} \sim \frac{1}{(1 - \cos\theta^*)^2} \tag{6.10}$$

[1]Note that in reality only $|\cos\theta^*|$ is measured as the outgoing partons cannot be discerned.

The BSM physics benchmark models taken into account for the analysis produce narrow resonances through s-channel interactions and the angular dependence can be expressed in terms of $\cos\theta^*$ polynomials. In the case of excited quarks (see Section 6.3.3) this is:

$$\frac{d\sigma}{d|\cos\theta^*|} = \text{constant}. \tag{6.11}$$

Using this info alone, it is already possible to evaluate the $\cos\theta^*$ cut that maximizes the signal sensitivity. By integrating the signal and the background cross sections between $-\cos\theta^*{}_{\text{Max}}$ and $\cos\theta^*{}_{\text{Max}}$ and then maximising $S/\sqrt{B}$, where S and B are the number of signal and background events, we obtain the value:

$$|\cos\theta^*{}_{\text{Max}}| = 1/\sqrt{3} \simeq 0.58 \tag{6.12}$$

or:

$$|y^*_{\text{Max}}| \simeq 0.66 \tag{6.13}$$

which goes in the same direction as the fiducial volume cut for jet reconstruction that is applied anyway to guarantee optimal jet performance.

6.2 Strategy

The strategy of the exotic dijet analysis can be broken down in three steps: the construction of the dijet invariant mass spectrum, the search for localised excesses and the limit setting on benchmark models in case no excesses are observed. The strategy to decide whether the analysis is ready to look in the signal region, the so-called *blinding strategy*, is also an essential part of the analysis.

6.2.1 Dijet Invariant Mass Spectrum

The exotic dijet resonance analysis looks for localised excesses in the dijet invariant mass spectrum. The event selection is enriched in potential new physics phenomena by selecting mainly hard scatter central dijet events. This is achieved by setting a cut on the jet rapidity in the collision frame, y^*, as described in Section 6.1.1. The m_{jj} distribution from data is not unfolded to correct for any detector effect but is instead used as is.

6.2.2 Search Phase

New physics resonances, or *bumps*, standing out of the smooth QCD distribution can be identified and isolated by removing the background contribution. This is achieved in a data-driven fashion via a fit employing a smooth function that does not accommodate local excesses. This strategy does not use any MC simulation, that would introduce modelling dependencies into the analysis and theoretical uncertainties. The search for localised bumps is performed by means of the BUMPHUNTER algorithm [77], which scans through all the possible combinations of consecutive bins composing the dijet mass distribution and ranging from a width of two bins up to half of the spectrum, looking for the most discrepant

interval of bins in the observed data entries compared to the fitted background. A series of statistical tests are performed in the process of determining the data-to-background compatibility.

6.2.3 Limit Setting

If no significant discrepancies between the observed data and the extrapolated background are observed in the search phase, limits are set on the cross section times acceptance of benchmark models with dijet signatures and on model-independent gaussian-like resonances and Breit-Wigner-like resonances with PDF effects included. The Bayesian method is used and systematic uncertainties on the signal entering the analysis are taken into account at this stage.

6.2.4 Blinding

In order to avoid any possible analysis bias that may arise from the premature observation of the signal region in data (i.e. the dijet mass spectrum and other related kinematic distributions), a blinding strategy is defined beforehand. Two opposite approaches have been employed in the 8 TeV and the 13 TeV analyses.

8 TeV Since the full 8 TeV dataset (20.3 fb^{-1}) dijet analysis [11] was preceded by an intermediate publication [78] using the first 13 fb^{-1} of that same dataset, it was possible to perform tests on a reduced set of the data without introducing any bias in the analysis nor allow the inference of any significant result. One fourth of the full dataset, corresponding to 5.1 fb^{-1}, was un-blinded to perform all the tests and checks required by the analysis before freezing the procedure and proceeding with the full dataset un-blinding.

13 TeV One of the lessons learnt from the full 8 TeV dataset analysis is that the quality of the fit using a given function can substantially change when the dataset statistics is increased even by a factor of four. For this reason a dedicated strategy has been put in place to measure quantitatively what function gives the best fit of the dijet invariant mass spectrum for the background extrapolation. This effectively removed the need for any blinding, as the analysis strategy could be frozen before the 13 TeV data taking started.

6.3 Data And MC Samples

6.3.1 Datasets

The 2012 8 TeV and 2015 13 TeV dijet analyses have been performed using two independent datasets.

8 TeV

The 2012 dijet analysis used 20.3 fb^{-1} of pp collisions at $\sqrt{s} = 8$ TeV. The data format adopted was centrally produced NTUP_SLIMSMQCD ntuples from the JetTauEt-

miss physics stream (i.e. the data stream on which jet, hadronic τ and $E_{\mathrm{T}}^{\mathrm{miss}}$ triggers are applied) and the HadDelayed physics stream (i.e. the physics delayed stream). Additionally, events from the debug streams have been included in the form of NTUP_COMMON ntuples. These events, 24 in total passing the dijet analysis selection, have been treated in the same way as the events from the JetTauEtmiss stream.

13 TeV

The 2015 dijet analysis used 3.6 fb^{-1} of pp collisions at $\sqrt{s} = 13$ TeV. The data format used is EXOT2 DXAOD produced centrally from the physics main stream and the debug stream.

6.3.2 MC QCD Background

Despite the dijet analysis using a data-driven background estimation (see Section 6.2.2), MC QCD background samples have been employed for data comparisons and performance studies. These samples have been produced at leading order in Run-1 and Run-2 analyses using PYTHIA 8.160 [42] MC generator. While for the 8 TeV analysis the MC generator was set to the AU2 tune [70] and using CT10 [71] PDFs, for the 13 TeV analysis the more recent A14 tune [79] and NNPDF2.3 LO PDFs [80] were adopted. Additionally, Run-2 studies have been performed with MC samples reconstructed with the 25 ns and 50 ns bunch spacing configurations to emulated the LHC bunch schemes in 2015. Differences in the two setups have been found to be negligible thanks to the pile-up robustness of the dijet analysis. NLO QCD and electro-weak Sudakov [81] factors have been used to reweight the LO distributions from PYTHIA to more accurate descriptions of the physics phenomena. The NLO factors have been derived in bins of dijet invariant mass from the comparison of dedicated simulations using NLOJET++ [82, 83, 84] (NLO) and PYTHIA(LO) generators:

$$\mathrm{NLO\ factor}(m_{\mathrm{jj}}) = \frac{\mathrm{NLO}^{\mathrm{NLOJET++}}(\mathrm{m_{jj}})}{\mathrm{LO}^{\mathrm{PYTHIA}}(\mathrm{m_{jj}})} \tag{6.14}$$

EW factors instead have been provided by the authors of [81]. Figure 6.1 shows the entity of the corrections introduced by the NLO and EW factors. See Figure 6.7 for a comparison of m_{jj} distributions between data and PYTHIA with NLO and EW corrections applied.

QCD background samples have been also produced using the NLO MC generator POWHEG [43]. However, these samples have been found to fail in the correct simulation of the kinematics of subleading jets. For this reason, POWHEG samples have been excluded from the dijet analysis.

6.3.3 Signal Benchmark Models

A series of signal benchmark models have been generated to set limits in the search for new physics. Benchmark models have been chosen to span the whole phase space of qg, qq and gg dijet signatures. An overview of the signal benchmark models used in the 8 TeV dijet analysis [85] and their cross section as a function of the mass is given in Figure 6.2.

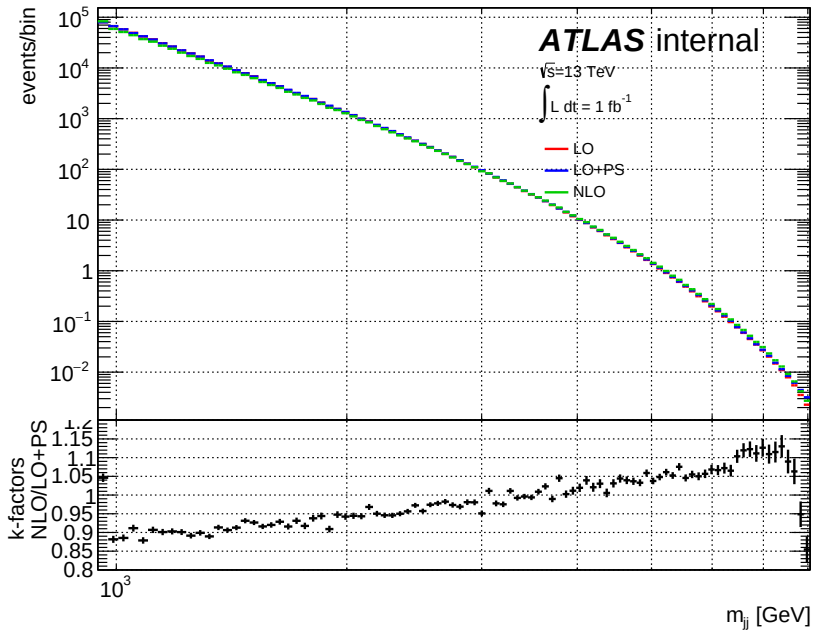

(a)

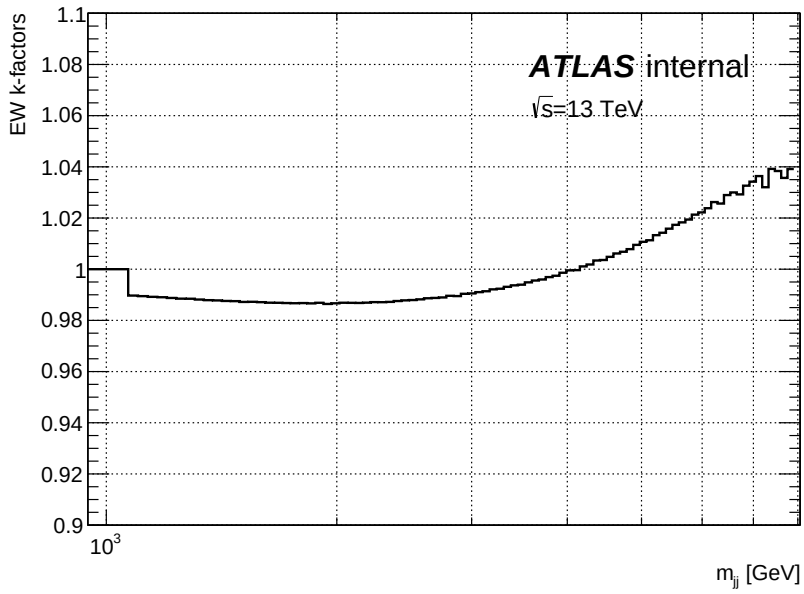

(b)

Figure 6.1: NLO (a) and EW (b) factors in bins of m_{jj} [12]. Both corrections enhance the high mass tail of the distribution.

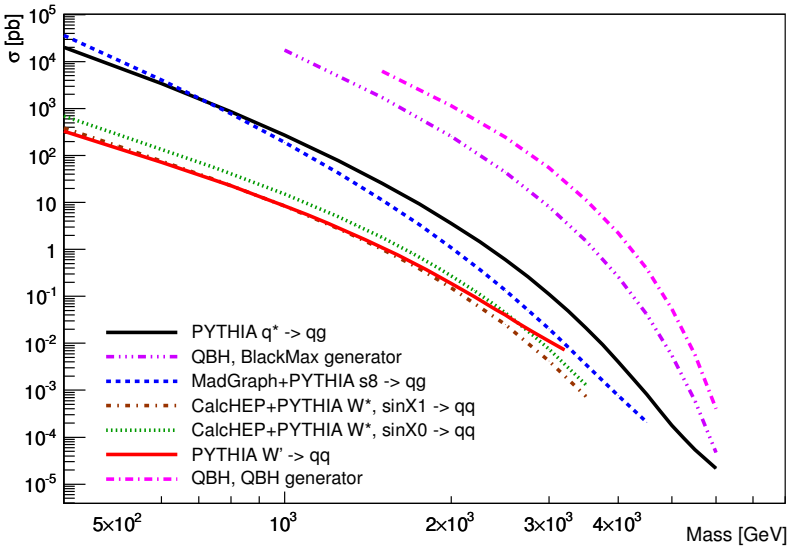

Figure 6.2: cross sections of the benchmark models used in the 8 TeV dijet analysis as a function of their mass [85].

Excited Quarks

Various theories state that quarks are composite objects and, as a consequence, they can have excited states (q^*) [86, 87]. Quarks can be excited through their interaction with gauge bosons and can return to their lowest state by emitting a gauge boson, leading to a dijet signature in the case of a gluon emission: $q^* \to qg$. For this reason, excited quarks are a common benchmark in dijet analyses looking for physics Beyond the Standard Model. Excited quarks have been simulated assuming spin $\frac{1}{2}$, SM quark couplings, compositeness scale set to their mass and renormalisation and factorisation scales set to the mean p_{T} of the two partons. Only excited u and d quarks have been simulated for the 8 TeV analysis, while b quarks have been added for the 13 TeV analysis. All possible decays of these quarks have been simulated in final states. MC q^* samples have been produced for 8 TeV and 13 TeV analyses using PYTHIA and the same tuning and PDF sets as the relative QCD background samples.

Quantum Black Holes

If the universe contains enough extra dimensions, gravitational effects should become evident at a scale, M_{D}, that is much smaller than the Plank scale[2]. In such conditions, the LHC might be able to produce Quantum Black Holes (QBH).

[2]Plank's scale corresponds to $1.22 \cdot 10^{19}$ GeV.

ADD Model According to the Arkhani-Hamed–Dimopoulos–Dvali (ADD) model [88], the QBH scale could be below the TeV scale if more than five extra dimensions exist[3]. Production of black holes would therefore be a threshold effect, manifesting whenever the energy of the interaction crosses the M_{D} threshold. In the most simple scenario, QBHs would evaporate isotropically through Hawking radiation, nevertheless gravitational effects favour a decay into two-body final state, effectively putting the dijet analysis in the position to be sensitive to gravitational effects. Two generators with completely different approach to the simulation of QBHs have been adopted: BLACKMAX and QBH (see Sections 3.5.4 and 3.5.5). Interference between QBH and QCD have not been simulated as the gravitational effects should exceed QCD rapidly enough once the M_{D} threshold is crossed. Results are compatible between the two generators, both at 8 TeV and 13 TeV (see Section 6.14.2).

RS Model The Randal–Sundrum (RS) model [89] is an alternative QBH model relying on a single extra dimension and decaying to $q\overline{q}$ and gg final states. Signal samples implementing the RS model have been produced using the QBH generator and employed to set limits in the 2015 dijet analysis. Due to the intrinsic features of the RS model, the QBH limits set with this model are much lower than those set using the ADD samples (see Section 6.14.2).

W'

Heavy charged vector bosons, such as W' [90], have been chosen as an alternative model for limit setting. The W' samples adopted have been simulated using PYTHIA8 and assuming V-A SM couplings. Decays have been forced to $q\overline{q}$ pairs of any flavour. No interference between W' and SM bosons has been simulated.

Excited W

Excitations of the W boson (W^*) [91, 92, 93] decaying to $q\overline{q}$ have been included in the selection of benchmark models for the 8 TeV dijet analysis. Unlike the other models considered, the W^* rapidity distribution does not have a maximum in the central region of the detector. It is instead shifted toward $\eta \simeq 1$. Despite this feature, the analysis acceptance of this signal is comparable to that of others models. Samples have been generated using the CalcHEP generator [48] interfaced with PYTHIA for the hadronisation and showering.

Color-Octet Scalar

The color-octet scalar model (S8) [94] was introduced in the 8 TeV dijet analysis to consider also signals with gg final states. These family of resonances have been predicted by extra dimension and technicolor models. The samples employed in the analysis have

[3]The samples used in the analysis have been simulated with 6 extra dimensions.

been generated at LO with MadGraph [49] interfaced with PYTHIA for the hadronisation and showering.

Z'

A Z' vector boson with A-V coupling to quarks only has been included among the signal samples used in the 13 TeV dijet analysis. This particular Z' is a leptophobic model mediating interactions between SM particles and Dark Sector Particles, DSPs [95, 96]. However, in the scenario of the dijet analysis, Z' bosons would be produced in $q\bar{q}$ interactions and decay to the same channel, without actually mediating with DSPs. The event matrix elements have been produced with MadGraph5 [97] and then showered using PYTHIA8. Different values of the Z' coupling to quarks have been simulated and the results are presented in Section 6.14 as a scan over the values considered.

6.4 Trigger

Collisions produced by the LHC are selected for this study by means of a trigger strategy that requires the presence of at least one jet in the event. Single-jet triggers demand at least one jet with a transverse momentum above a given threshold to be reconstructed in the event. Since jet multiplicity is almost always equal or above two, no dijet trigger is implemented in the ATLAS trigger menu as this would not reduce the trigger rate and the allocated trigger bandwidth. Two different trigger strategies have been adopted for the 8 TeV and 13 TeV analyses, both based upon single-jet triggers.

6.4.1 8 TeV

The trigger strategy adopted in the 8 TeV analysis has been developed to extend as much as possible the m_{jj} distribution range toward lower values, making use of the stream of events that was promptly collected and reconstructed by the experiment as well as the stream whose reconstruction was delayed until the end of the data taking (the delayed stream, see Section 2.6.3). This sophisticated strategy allowed a much stronger statistical power of the dijet mass spectrum.

Trigger Map

The trigger strategy for the 8 TeV analysis is given by the combination of eleven jet triggers chained with a logical OR and applied to the normal data stream, plus an additional jet trigger applied to the delayed stream, as listed in Table 6.1.

Ten of the triggers applied to the normal data stream are single jet Event Filter triggers (e.g. EF_j*_a4tchad), meaning that these triggers require the presence of at least one anti-k_{t} jet with radius $R = 0.4$ at the Event Filter level with a transverse energy deposit, E_{T}, at the hadronic scale above a given threshold. The value of this threshold is what makes the triggers different from each other and it ranges from 15 GeV for the lowest trigger to 280 GeV for the highest trigger. Given the high rate of energy

trigger	full efficiency threshold [GeV]	integrated luminosity [fb^{-1}]	data stream
EF_j145_a4tchad_ht700_L2FS	460	20.34	normal
EF_j280_a4tchad	411	1.17	normal
EF_j220_a4tchad	341	0.26	normal
EF_j180_a4tchad	273	$7.90{\cdot}10^{-2}$	normal
EF_j145_a4tchad	241	$3.64{\cdot}10^{-2}$	normal
EF_j110_a4tchad	185	$9.84{\cdot}10^{-3}$	normal
EF_j80_a4tchad	135	$2.32{\cdot}10^{-3}$	normal
EF_j55_a4tchad	99	$4.43{\cdot}10^{-4}$	normal
EF_j35_a4tchad	59	$4.54{\cdot}10^{-4}$	normal
EF_j25_a4tchad	47	$7.87{\cdot}10^{-5}$	normal
EF_j15_a4tchad	27	$1.48{\cdot}10^{-5}$	normal
EF_j220_a10tchem_delayed	333	17.33	delayed

Table 6.1: triggers used in the 8 TeV analysis with their full efficiency threshold and effective integrated luminosity.

releases produced by *pp* collisions in the calorimeter and the limited computing and storage resources available, triggers are *prescaled* by factors ranging from one to infinity, depending on the trigger energy threshold and the instantaneous luminosity of the collisions. Triggers with low energy values can have prescale factors, p, of the order of 10^6, meaning that only one out of p times that the trigger fires an events is randomly written to disk. As a consequence, triggers with different prescales collect different integrated luminosities. The random nature of the prescale method has the effect that two triggers with thresholds below the trigger jet E_{T} may give different firing results. The eleventh trigger applied to the normal data stream, namely EF_j145_a4tchad_ht700_L2FS, requires a jet with E_{T} greater than 145 GeV and the scalar sum of all the event jets' E_{T} (for jets with E_{T} larger than 45 GeV), H_{T}, to be greater than 700 GeV. Thanks to the relatively low rate of events passing this requirements, this trigger is *un-prescaled*, meaning that its prescale factor is set to 1. The trigger applied on the delayed stream, namely EF_j1220_a10tcem_delayed, requires the presence in the event of an anti-k_{t} trigger jet with radius $R = 1.0$ at the Event Filter level with E_{T} greater than 220 GeV at the EM scale. This trigger is also un-prescaled. Since triggers use jet p_{T} and other observables, such as H_{T}, that are reconstructed online while the analysis uses jets reconstructed offline and fully calibrated, the offline leading jet p_{T} distribution does not have a sharp threshold at low values but instead a smooth turn-on given by the smearing of the jet p_{T} resolution. The efficiency of a trigger can be estimated by means of the *bootstrap method* (a *tag and probe* method to all intents and purposes), i.e. by selecting events using a jet trigger with a lower E_{T} threshold and that is fully efficient in the turn-on region of interest and then emulating the trigger decision of the trigger under investigation on these events. By dividing the jet p_{T} distribution of the emulated trigger (*probe*) by that of the trigger with lower threshold (*tag*), the trigger

efficiency curve is obtained. For each trigger, the 99.5% efficiency threshold is taken as the point above which the trigger reaches the full efficiency plateau. Values for this plateau are reported in Table 6.1.

A trigger map is built from all the eleven triggers applied to the normal stream, which assigns to each trigger the p_{T} region extending from its full efficiency threshold up to the full efficiency threshold of the next trigger. This map maximises the statistics available in each region, since the prescale values are inversely proportional to the trigger E_{T} threshold.

The luminosity collected by each trigger is computed for all the Luminosity Blocks, LBs, the trigger was active using the ATLAS LumiCalc tool [98]. Values are reported in Table 6.1.

Triggers Combination

The trigger strategy employed requires each event to be associated with a weight that accounts for the prescale factors, so that the weighted sum of the events restores the smooth distribution that would have been obtained if no prescale factors were introduced. This event weighting scheme follows the *inclusion method* described in [99].

The inclusion method starts from the consideration that a given event could be independently triggered from many fully efficient triggers in the scheme, with different threshold and prescale factors.

The probability, P, for an event to be selected is computed from the probability of being rejected by all triggers in the chain:

$$P = 1 - P_{\mathrm{rejection}} = 1 - \prod_{i=1}^{n_{\mathrm{triggers}}} P^{i}_{\mathrm{rejection}} = 1 - \prod_{i=1}^{n_{\mathrm{triggers}}} \left(1 - \frac{1}{p_i}\right) \tag{6.15}$$

where p_i are the trigger prescale values. Note that this probability is independent from which trigger has effectively triggered the event.

In order to avoid any spikes in the event probability distribution, average prescale values, $\langle p_i \rangle$, should be used in Equation 6.15, so that the average probability is used instead. The average prescales are defined from the integrated luminosity collected by the trigger, L_i:

$$L_i = \sum_{j}^{n_{\mathrm{runs}}} L_{ij} \tag{6.16}$$

and its effective luminosity, L^{i}_{eff}:

$$L^{i}_{\mathrm{eff}} = \sum_{j}^{n_{\mathrm{runs}}} L^{ij}_{\mathrm{eff}} = \sum_{j}^{n_{runs}} \frac{L_{ij}}{p_{ij}} \tag{6.17}$$

so that:

$$\langle p_i \rangle = \frac{L_i}{L^{i}_{\mathrm{eff}}} \tag{6.18}$$

The event weight, w, is therefore given by the inverse of such probability:

$$w = \frac{1}{P} = \frac{1}{1 - \prod_{i=1}^{n_{\text{triggers}}} (1 - \frac{1}{\langle p_i \rangle})} \tag{6.19}$$

The statistical advantage of combining multiple triggers can be shown in terms of the *effective entries* composing the m_{jj} distribution, i.e. the number of entries that would have the same poissonian relative error if all the events had unitary weight. The number of effective entries can be computed as:

$$n_{\text{effective entries}} = \frac{n^2_{\text{weighted entries}}}{\sigma^2_{\text{weighted entries}}} = \frac{\left(\sum_i^{n_{\text{entries}}} w_i\right)^2}{\sum_i^{n_{\text{entries}}} w_i^2} \tag{6.20}$$

An effective weight, $w_{\text{effective}}$, is defined so that:

$$n_{\text{weighted entries}} = n_{\text{effective entries}} \cdot w_{\text{effective}} \tag{6.21}$$

A comparison of the effective entries when using one trigger or the combination of two or of all the eleven triggers used is shown in Figure 6.3. Despite all strategies having the same statistical power above ∼1 TeV, since this is the region covered by the highest trigger alone, at low masses the benefit of including more than one trigger is evident and provides a gain of up to 50%.

Delayed Stream

The delayed stream from Run-1 (see Section 2.6.3) has just one single jet trigger that is used in the analysis: EF_j1220_a10tcem_delayed, an un-prescaled trigger that is fully efficient above 333 GeV and has recorded 17.33 fb^{-1} of data. It is important to notice that the inclusion of the delayed stream in the analysis allows the fully efficient and un-prescaled trigger selection threshold to be pushed down to 333 GeV from the 460 GeV of the EF_j145_a4tchad_ht700_L2FS trigger. At the same time, since the normal and the delayed stream both cover the leading jet p_{T} region above 333 GeV, particular care must be taken in order not to double count events when the two streams are added together. This can be avoided by splitting the entire dataset available in three datasets:

- **normal**: events from the normal stream when the delayed stream was not active;
- **overlap**: events from the normal stream when the delayed stream was active and with leading jet $p_{\text{T}} < 333$ GeV;
- **delayed**: events fromt the delayed stream;

With this subdivision, the delayed dataset has always an integrated luminosity of 17.33 fb^{-1}, while the normal and overlap datasets have a total luminosity, together, of 2.9 fb^{-1}. The m_{jj} distribution of each one of these three datasets is shown in Figure 6.4.

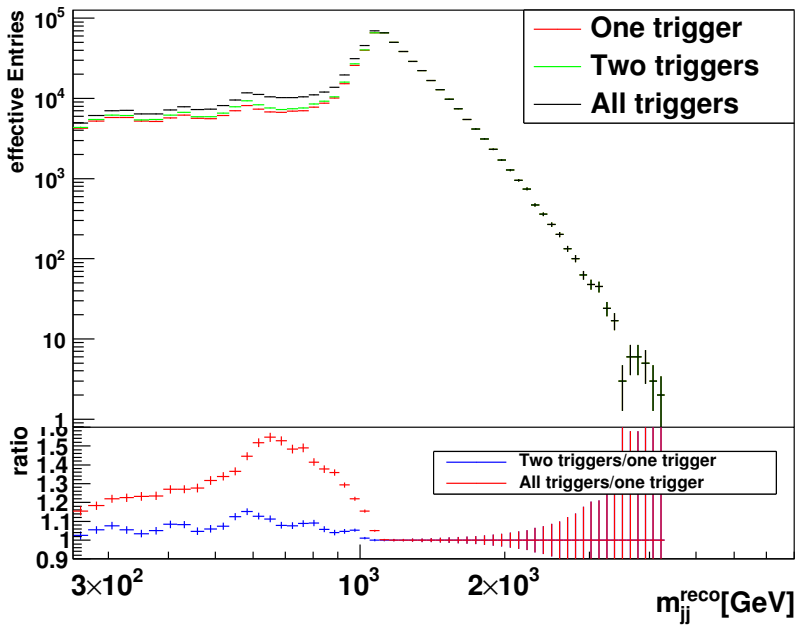

Figure 6.3: comparison of the effective entries composing the m_{jj} distribution when using the EF_j145_a4tchad_ht700_L2FS trigger alone ("one trigger"), in combination with another trigger ("two triggers") or in combination with all the other ten triggers used for the normal stream ("all triggers") [85].

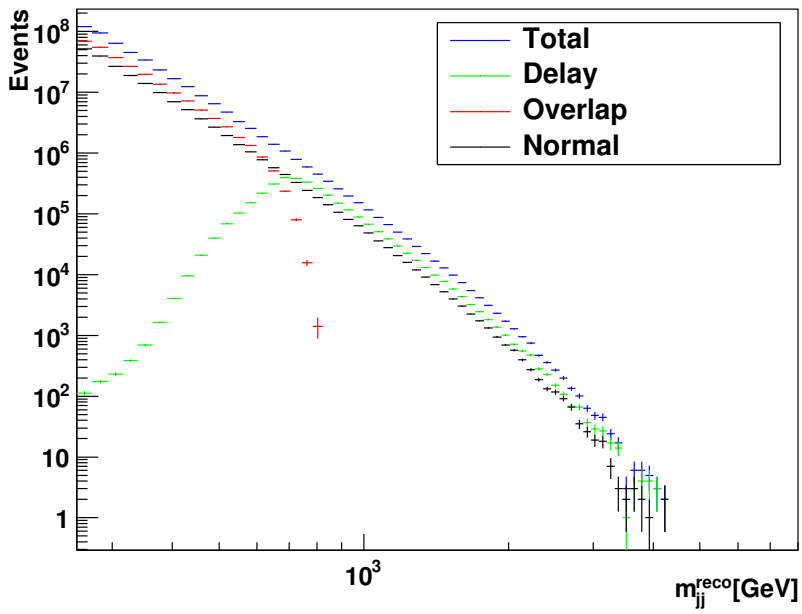

Figure 6.4: m_{jj} distributions using events from the normal, overlap and delayed datasets, together with their total combination [85].

Stream Combination

The most straightforward way to combine the normal, overlap and delayed datasets is to sum their events and their respective weights. However, this would result in a drastic reduction of the effective entries, since the weighted events from the normal stream would overwhelm the statistical power of the events with unitary weight from the delayed stream, as it can be understood from Equation 6.20. This is not an optimal solution, as better results could be obtained by simply using the delayed stream alone.

The most sensible way to combine the streams while also improving the statistical power of the final results is to consider the normal dataset and the delayed plus overlap datasets as two independent measurements of the same distribution but with different statistical power and then take the weighted average of the two. For a given measure x, this becomes:

$$\langle x \rangle = \frac{\sum_i^{n_{\mathrm{entries}}} x_i \sigma_i^{-2}}{\sum_i^{n_{\mathrm{entries}}} \sigma_i^{-2}} \tag{6.22}$$

with error given by:

$$\sigma_x^2 = \frac{1}{\sum_i^{n_{\mathrm{entries}}} \sigma_i^{-2}} \tag{6.23}$$

This is the procedure adopted for the dijet analysis. In this case, the m_{jj} distributions from the two combined datasets (normal and delayed plus overlap) are first normalised by their luminosity, then the average of the content of each bin composing the distribution is

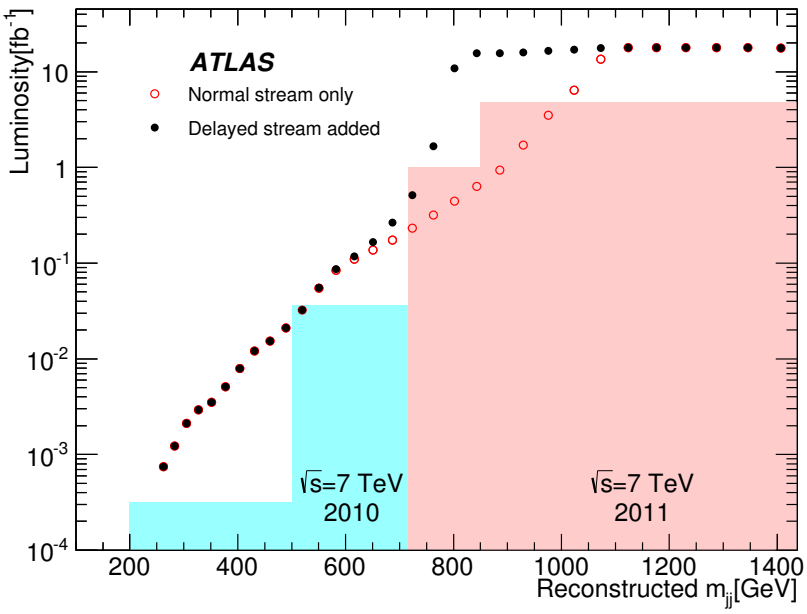

Figure 6.5: effective luminosity available in each of the bins of the m_{jj} spectrum [85]. Red empty circles show the luminosity of the normal stream, while the black dots show the total luminosity of the normal and delayed stream combinations. Turquoise and pink shaded areas show the luminosity and the extension of the spectra of previous 7 TeV dijet analysis public results: 315 nb^{-1} and $m_{\mathrm{jj}} > 200$ GeV [100], 36 pb^{-1} and $m_{\mathrm{jj}} > 500$ GeV [101], 1 fb^{-1} and $m_{\mathrm{jj}} > 717$ GeV [102], 4.8 fb^{-1} and $m_{\mathrm{jj}} > 850$ GeV [103]

computed, together with its error. Finally, the total distribution is scaled to the sum of the luminosity of the two input datasets, i.e. 20.3 fb^{-1}.

The effective luminosity for each bin of the mass spectrum is shown in Figure 6.5. The open red circles show the luminosity given by the normal stream alone, while the black points show the luminosity available after the inclusion of the delayed stream. The turquoise and pink shaded boxes show the luminosity available in previous 7 TeV publications and the extension of their m_{jj} spectra. The 8 TeV spectrum built from the combination of different streams outperforms spectra of the previous dijet publications in almost every bin.

Time-Dependent Corrections

As described in Section 6.6.1, the Hadronic Tile Calorimeter module masking is time-dependent. The presence of time-dependent corrections complicates the streams combination, since the two do not cover the same period of time. Corrections are therefore applied to the normal and delayed streams independently. These corrections are computed, for each bin, as the inverse of the ratio between the number of events passing all selection

cut except for the Hadronic Tile Calorimeter masking over the number of events passing all the cuts. This correction is an approximation, since it should be applied at the stage when the trigger event weights are computed, not after the distributions are made. In any case, the ratio of the corrected distributions from the normal and the delayed streams is compatible with a flat line, meaning that any time-dependent discrepancy in the two streams has been removed.

6.4.2 13 TeV

For the 13 TeV dijet analysis, the lowest un-prescaled single jet trigger has been used to select events. At the instantaneous luminosity values reached during the 13 TeV data taking, this corresponded for the whole 2015 to HLT_j360, a trigger which sets a 360 GeV threshold on the jet p_{T} reconstructed by the High Level Trigger and calibrated to the hadronic scale. This trigger is seeded at Level-1 by L1_J100, which requires at least one jet reconstructed with p_{T} greater than 100 GeV at the EM scale. Table 6.2 shows the evolution scheme for the lowest un-prescaled single jet triggers for 13 TeV data taking.

trigger	L1 seed	max luminosity [$\mathrm{cm}^{-2}\mathrm{s}^{-1}$]
HLT_j360	L1_J100	$6.5{\cdot}10^{33}$
HLT_j380	L1_J100	$1.0{\cdot}10^{34}$
HLT_j400	L1_J100	$2.0{\cdot}10^{34}$

Table 6.2: lowest un-prescaled single-jet trigger evolution scheme for 13 TeV data taking [12]. The instantaneous luminosity values reached in 2015 allowed to keep HLT_j360 as the lowest un-prescaled single-jet trigger throughout the whole year.

The use of one single-jet trigger, unlike the 8 TeV analysis, is justified by the fact that the 2015 analysis is focusing on the exploration of the larger mass regions opened up by the increased center of mass energy of the *pp* collisions produced by the LHC. It is thus desirable to avoid the work that was needed for the 8 TeV analysis to extend the analysis reach to lower mass values and use a simpler, but still effective, trigger strategy.

Trigger Efficiency

The trigger turn-on curves are shown as a function of leading jet p_{T} and m_{jj} in Figure 6.6. These curves have been obtained with 1 fb^{-1} of data (selected using the next single-jet trigger with lower p_{T} threshold) and PYTHIA MC samples using the analysis selection cuts.

The trigger is considered as fully efficient above the 99.5% threshold. These plateau levels are used to define conservative jet p_{T} and event m_{jj} cut values (see Table 6.3).

Debug Stream

Over the course of data taking, it was observed that the amount of events coming from the debug stream increased with the dijet invariant mass of the event. This led to the

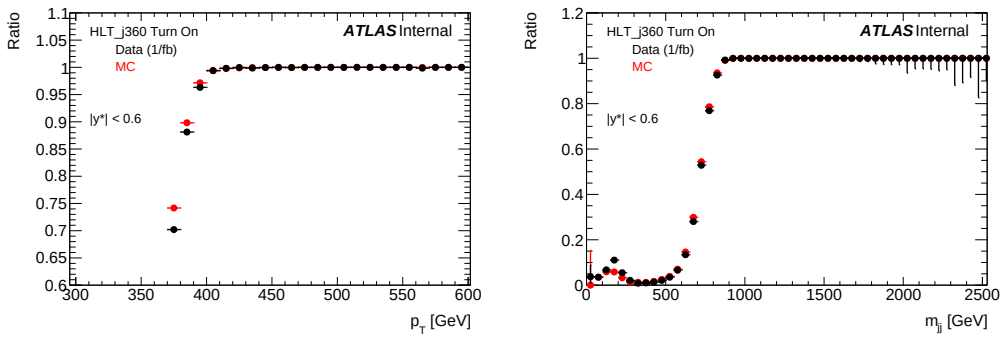

(a) (b)

Figure 6.6: trigger efficiency curves for HLT_j360 as a function of leading jet p_{T} (a) and m_{jj}(b) [12].

	99.5% efficiency threshold [GeV]	cut [GeV]
leading jet p_{T}	409	440
m_{jj}	900	1100

Table 6.3: trigger 99.5% efficiency points and cut values for leading jet p_{T} and m_{jj}.

observation that the frequency of time-outs in the muon reconstruction was significantly affected by the amount of punch-through jets. It was therefore deemed necessary to include into the analysis these events in order to avoid a bias in the m_{jj} spectrum at high mass values. A fix for the problem has been developed but was not applied during the 2015 data taking.

Saturated Towers

During the initial 50 ns data taking occurred in June and July 2015 a problem with one of the trigger Bunch Crossing Identification, BCID, algorithms and involving high-p_{T} jets was observed. Jets reconstructed online are assigned a BCID by means of two dedicated algorithms that analyse the shape of the energy pulse reading in the calorimeter over several consecutive bunch crossings [104]. In order for the L1 trigger to withstand the LHC's 40 MHz collision rate, the L1 trigger uses the calorimeter info organised into so-called *trigger towers*, which have a granularity reduced to $\Delta\eta \times \Delta\phi = 0.1 \times 0.1$ for $|\eta| < 2.5$. The energy readings are then passed on to the Finite Input Response, FIR, filter and the Peak Finder for final processing of the ADC values and the assignment of the jet to the BCID with the highest reading. Above the 255 GeV energy threshold, all jet triggers are considered as interesting and are required to fire. For this reason the trigger chain does not need to have a linear response above this threshold and is therefore allowed to saturate. In the occurrence of highly energetic jets, and hence of several consecutive saturated ADC samples, the Peak Finder may fail in the assignment

of the correct BCID. Therefore a second dedicated BCID algorithm that uses the trigger pulse rising edge is employed. Whenever a saturated ADC sample is detected, the algorithm checks the preceding two samples against two threshold values and, if these are exceeded, the jet is assigned to the first saturated sample BCID, otherwise it is assigned to the following one. Since the two BCID algorithms run in parallel, in case of disagreement, the earlier BCID is assigned to the jet. However, due to a misconfiguration of the saturated trigger tower BCID algorithm, the L1 trigger was systematically fired one bunch crossing too early, thus causing the loss of the correct collision due to the trigger dead time and biasing the triggering of high-p_{T} jet events. The first hint of this problem came from the observation of a systematic discrepancy in the tail of the m_{jj} distribution between data and Pythia MC samples (since the analysis is run un-blinded), as shown in Figure 6.7a. Since PYTHIA is a LO generator, NLO and EW, correction factors have been applied to check the possibility that the observed discrepancy may have been caused by a limitation of the generator (see Section 6.3.2 for more details about NLO+EW corrections). The issue was identified and solved by the start of the 25 ns data taking (see Figure 6.7b) but, because of this problem, periods A-C, corresponding to an integrated luminosity of 72 pb^{-1}, are not included in the analysis dataset.

In order to be readily responsive to any further trigger BCID problem that may arise, additional checks have been put in place. These involve the comparison of the L1 trigger ROI energies and HLT jet energies against offline jets. In addition, a dedicated L1 data stream has been created to store events with saturated calorimeter towers, allowing a more comprehensive analysis of these critical events.

Mis-Timed Events

Following the implementation of the checks aimed at highlighting possible trigger BCID issues, during the 25 ns data taking it was observed that some of the events recorded in the dedicated L1 stream had towers whose timing was off by 25 ns. Investigations have revealed this problem to be caused by an unexpected effect of the trigger FIR filter in the default BCID algorithm following a Run-2 upgrade.

The affected events have been recovered from raw data and re-reconstructed time-shifting the calorimeter information by 25 ns. Since the tracking information could not be time-shifted, the effect of this missing information was investigated and found to be negligible and in the worst scenario still within the m_{jj} statistical uncertainty. Since these events represent a considerable 10% of the events with E_{T} values in the Hadronic Tile Calorimeter above 1200 GeV and since their EM and hadronic shower energies are shifted up by 40% and 100% on average during the reconstruction, effectively pushing the events in the tail of the m_{jj} distribution, they have been included in the analysis dataset, with the only exception of two events.

6.5 Jet Selection

Performance and cleaning selection criteria have been applied to the jets employed in the analysis to ensure good quality of the reconstructed events and an un-biased m_{jj} distri-

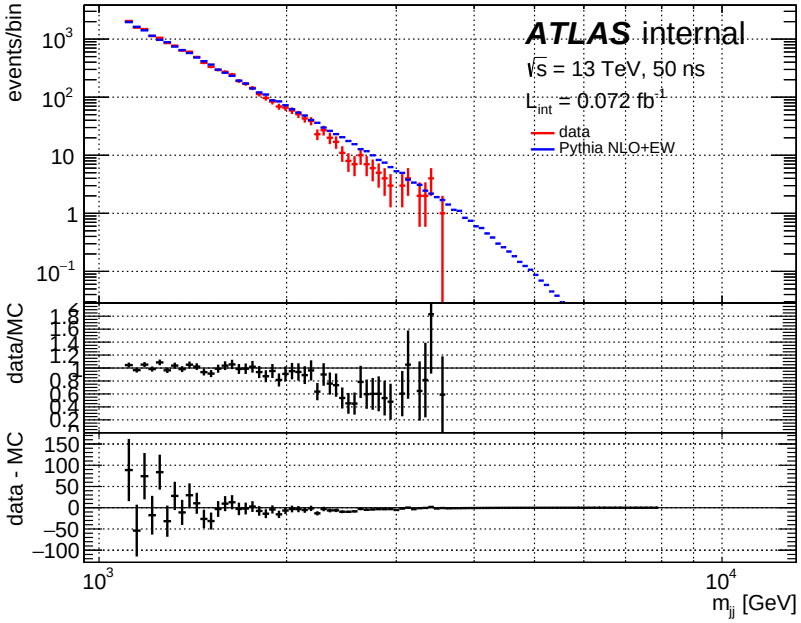

(a)

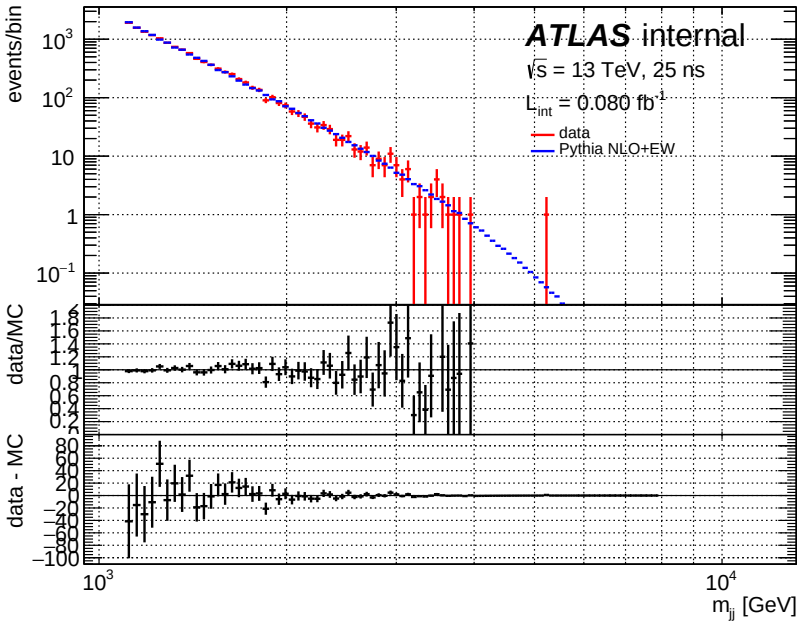

(b)

Figure 6.7: dijet invariant mass distributions from early 50 ns (a) and 25 ns (b) Run-2 data taking compared to Pythia MC. The event deficit in data at large m_{jj} values due to the trigger saturated towers issue is visible in the 50 ns distribution. MC distributions are scaled to the respective data integrals and NLO and EW corrections have been applied (see Section 6.3.2).

bution. These criteria include the choice of the radius employed in the jet reconstruction and the choice of the lower cut on the dijet invariant mass.

6.5.1 8 TeV

Jets used in the analysis are reconstructed using the anti-k_t algorithm and calibrated according to EM+JES scheme (see Chapter 4).

Jet Radius

A dedicated study was performed to assess the performance of the analysis using either jets with radius $R = 0.4$ or $R = 0.6$. This investigation was based on the excited quark signal significance, defined as:

$$\text{significance} = \frac{S}{\sqrt{S+B}} \tag{6.24}$$

where S and B are the number of signal and background events in the region around the signal peak. Results have highlighted a slightly higher significance for $R = 0.6$ jets, while the RMS is comparable for the two radius options. This is explained by the fact that a larger radius jet is able to collect a larger fraction of the radiation produced in the jet shower, thus providing a more precise signal mass. For these reason, and in line with previous dijet publications, the radius $R = 0.6$ is adopted.

The CMS Collaboration has adopted so-called *wide jets* in its search for resonances in the dijet invariant mass spectrum at 8 TeV [105] and 13 TeV [106]. CMS's wide jets are constructed by adding to the closest of the two leading jets (anti-k_t $R = 0.5$ at 8 TeV and $R = 0.4$ at 13 TeV) any other jet falling within $R < 1.1$. This choice was motivated by a reduction in the analysis susceptibility to gluon radiation in the final state and an improvement in the sensitivity.

Lowest m_{jj}

The lowest dijet invariant mass value that can be used in the analysis is defined by the lowest jet p_T allowed and the detector volume, hence the angle between the jets. However the effect of additional *pp* interactions in the same event, *pile-up* events, needs to be taken into account as it directly affects the energy of the reconstructed jets and their multiplicity. A cut on jet p_T at 50 GeV is shown to remove any effect originating from pile-up at the cost of having to increase the smallest dijet mass value available for the analysis. As pile-up is directly connected to the number of reconstructed primary vertices in an event, the m_{jj} distribution was plotted against it, using jets with p_T above 50 GeV (see Figure 6.8a). The linear fit of the average m_{jj} as a function of primary vertices is compatible with a constant, therefore showing that any pile-up dependency is removed by using only jets above 50 GeV. Similar results have also been observed for the jet p_T (see Figure 6.8b) and jet multiplicity. MC studies, performed using samples that include pile-up simulation, have shown that the fraction of reconstructed leading jets that are matched to a truth jets is above 96% for p_T values above 50 GeV (see Figure 6.9). Considering also that the jet

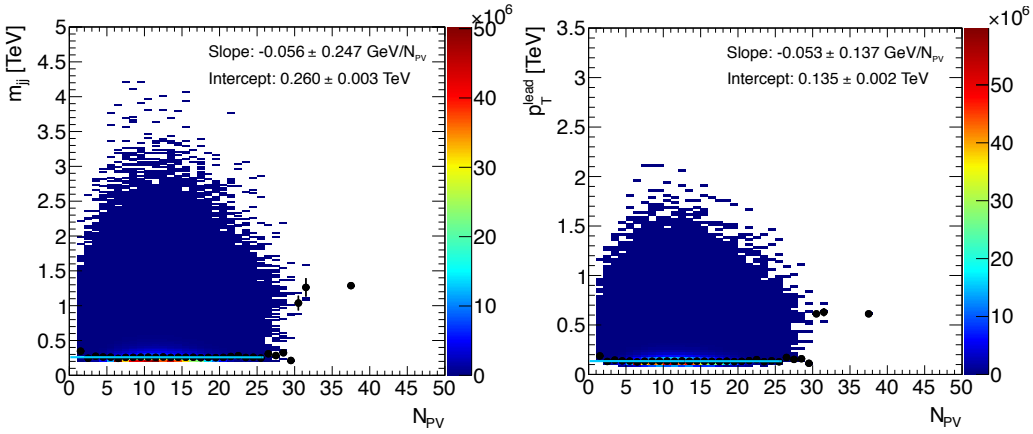

(a) (b)

Figure 6.8: average dijet invariant mass (a) and leading jet p_{T} (b) as a function of reconstructed number of primary vertices for events with leading jets with $p_{\mathrm{T}} > 50$ GeV.

reconstruction efficiency plays a role in these numbers, an upper limit to the effect of the pile-up contribution can be deduced. The lowest m_{jj} value that can be used in the analysis is obtained by taking the ratio of the dijet mass distribution of MC events with a jet p_{T} cut applied at 50 GeV over the distribution of MC events without any jet p_{T} cut. This curve reaches the full efficiency plateau at 250 GeV, meaning that all the events above this threshold are selected and there is no shaping effect in the distribution that is caused by the jet p_{T} cut. 250 GeV is therefore the minimum m_{jj} for the analysis.

6.5.2 13 TeV

As for the 8 TeV analysis, jets are reconstructed using the anti-k_{t} algorithm and calibrated following the EM+JES+GSC scheme (see chapter 4).

Jet Radius

The jet radius adopted is $R = 0.4$, since this is the first jet collection supported by the jet performance group for the early 13 TeV data analyses. However, as it was observed for the 8 TeV analysis, very little changes between $R = 0.4$ and $R = 0.6$ in terms of sensitivity and results can still be reliably compared.

Lowest m_{jj}

The 50 GeV jet p_{T} lower cut adopted in the 8 TeV analysis is kept in order to remove contributions from pile-up. However, since the trigger strategy exploits only one trigger, the lowest m_{jj} cut value is obtained as the trigger threshold of full efficiency. As reported in Table 6.3, the threshold value obtained from data is 900 GeV, however the m_{jj} cut was

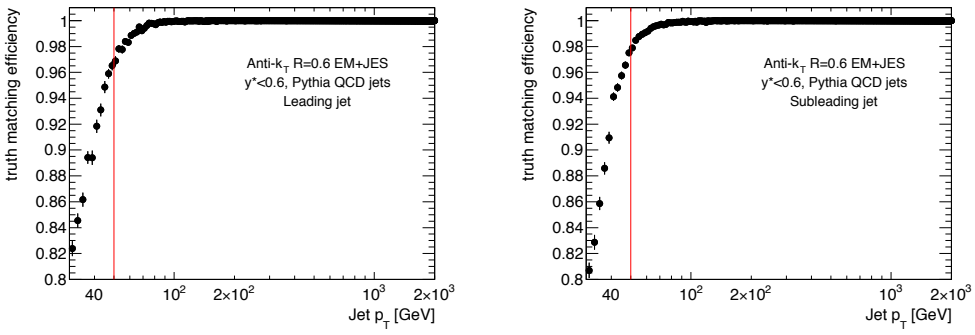

(a) (b)

Figure 6.9: truth matching efficiency of leading (a) and subleading (b) jets as a function of jet p_{T}. Above 50 GeV the rate at which jets from pile-up events are reconstructed as one of the leading jets is below 4%. Note that the jet reconstruction efficiency plays a non-negligible role in these curves.

conservatively set at 1100 GeV using MC samples before data taking started and before the final jet calibration was available.

6.6 Event Selection

Event selection cuts are applied to retain only the events collected when the detector was fully functional and reject all those with data corruption. Additional selection cuts are added to ensure the quality of the events and enrich the sample with hard scatter collisions. As described in the following sections, the 13 TeV analysis employs most of the selection cuts of the 8 TeV analysis.

6.6.1 8 TeV

The analysis steps for the 8 TeV dijet search have been applied according to the following sequence (additional details about the cuts applied are given below in this section).

1. **Total events**. The number of events available from the normal and delayed streams before any selection.

2. **Blinding** (if applied). One out of every four events is selected based on its EventNumber.

3. **Jet recalibration**. Jets are recalibrated according to the most recent jet calibration constants before moving on with the event selection.

4. **Trigger**. The event must fullfil the trigger strategy requirements, as detailed in Section 6.4.1.

5. **GRL**. Events must be from a run and luminosity block listed on the Good Run List. See below for more details.

6. **Vertex**. The reconstructed primary vertex must have more than one track: $n_{\mathrm{trk}}^{\mathrm{vtx}} > 1$.

7. **Calorimeter errors**. Reject events that present calorimeter data integrity problems (identified by the dedicated flags: larError = 2 or tileError = 2). Reject events with missing information (flag: CoreFlags). Reject events if a module of the calorimeter has tripped (as indicated by the TileTripReader tool [107]). See below for more details.

8. **Masked modules**. Reject the event if any of the two leading jets or any other jet with p_{T} greater than 30% of the subleading jet falls within a masked Hadronic Tile Calorimeter module. See below for more details.

9. **Jet $\boldsymbol{\eta}$**. Require the leading jets to be within $|\eta| < 2.8$.

10. **Tile hotspot**. Reject the event if any of the leading jets is associated with a Hadronic Tile Calorimeter hotspot from period B that was not masked at the reconstruction stage (as indicated by the TTileTripReader tool [107]).

11. **Ugly jets**. Reject the event if any of the two leading jets or any other jet with p_{T} greater than 30% of the subleading jet corresponds to the Ugly jet definition. See below for more details.

12. **Bad jets**. Reject the event if any of the leading jets corresponds to the BadLooser jet definition. See below for more details.

13. **Jet $\boldsymbol{p_{\mathrm{T}}}$**. Require the leading jets to have $p_{\mathrm{T}} > 50$ GeV to remove jets from pile-up collisions. See Section 6.5.1.

14. **$\boldsymbol{y^*}$**. Require the leading jets to have $|y^*| < 0.6$ to enrich the event selection with central hard scatter events. See Section 6.1.1.

15. **$\boldsymbol{m_{\mathrm{jj}}}$**. Require the event to have $m_{\mathrm{jj}} > 250$ GeV to remove the bias from the jet p_{T} cut. See Section 6.5.1.

The event cut flow is reported in Table 6.4 for the normal and delayed plus overlap datasets. Note that for MC samples are applied only the kinematic selection cuts and the emulation of the Hadronic Tile Calorimeter masked cells.

Good Runs List

Good Runs Lists are released by the ATLAS Data Quality team and contain all the run numbers and associated luminosity blocks where the detector was functional and whose data can thus be used [108]. The record of these runs changes according to the ATLAS

selection criteria	$n_{\text{events}}^{\text{normal stream}}$	$n_{\text{events}}^{\text{delayed+overlap stream}}$
total events	871 647 227	417 493 026
trigger	12 886 319	33 967 850
GRL	9 918 952	32 461 435
vertex	9 918 894	32 461 223
calorimeter errors	9 863 909	32 349 156
jet η	9 422 143	32 289 087
Hadronic Tile Calorimeter hotspot	9 422 143	32 289 087
ugly jets	8 339 494	28 580 208
bad jets	8 334 537	28 563 192
jet p_{T}	7 610 460	28 516 483
y^*	4 396 317	16 014 287
m_{jj}	4 259 455	16 013 126

Table 6.4: cut flow of the 8 TeV normal and delayed plus overlap datasets. The events from the debug stream (24 in total passing the dijet analysis selection) are not included in this table.

subdetectors and physics objects that are relevant to a specific analysis. The dijet analysis used a general GRL, namely data12_8TeV.periodAllYear_DetStatus-510_v61-pro14-02_DQDefects-00-01-00_PHYS_StandardGRL_All_Good.xml. From the data selected by this GRL, two custom GRLs where then produced to separate the normal stream from the delayed plus overlap.

Calorimeter Errors

Occasionally, information from the calorimeters, Electromagnetic and Hadronic Tile, can be affected by noise or data integrity problems. For this reason flags are implemented and used to veto such events, namely larError and tileError. The dijet analysis, in particular, uses these flags to reject events with data integrity problems. A dedicated flag, coreFlags, is also employed to veto events that have incomplete detector information following a restart of the Timing, Trigger and Control system during data taking. Finally, the TTileTripReader tool [107] is employed to veto all those events where one of the leading jets falls within a Hadronic Tile Calorimeter module whose power supply was tripping at that time.

Jet Cleaning

Jet cleaning cuts are introduced to remove jet not originating from hard scattering events or falling into problematic areas of the calorimeters.

Ugly Jets Jets are defined as *ugly* when they fall in calorimeter regions that do not allow a good reconstruction, such as the transition region between barrel and end-cap or

masked modules. Events are therefore vetoed based on the direction of the jets and on the entity of the BCH_CORR_CELL correction applied (see Section 6.6.1). Since the ugly jet definition is applied on the goodness of the jet reconstruction, the event rejection is based on the leading jets and on all the jets that have a p_{T} that is at least 30% of that of the subleading jet, since a bad reconstruction could cause a leading jet to become the third leading and vice versa.

Bad Jets All the jets originating from beam-induced events, cosmic rays and calorimeter noise fall into the definition of *bad* jets [109]. These jet, also noted as *fake* jets, can be identified by their kinematic properties and the topology of the event. Noise in the calorimeter may lead to false energy releases and hence to fake jets. Despite most of the noise being rejected by the data quality checks implemented on the calorimeter errors, this contribution, can be further reduced by looking at a few additional factors:

- $Q_{\mathrm{cell}}^{\mathrm{LAr}}$: the pulse quadratic difference between an expected signal from simulation and the actual one;
- $\langle Q \rangle$: the jet calorimeter pulse average quality weighted on the cell energy;
- f_{EM}: energy fraction in the LAr calorimeter;
- f_Q^{LAr}: energy fraction in LAr calorimeter cells with poor pulse shape quality;
- f_{HEC}: energy fraction in the HEC calorimeter;
- f_Q^{HEC}: energy fraction in HEC calorimeter cells with poor pulse shape quality;
- E_{neg}: negative energy reading of cells neighbouring a noisy HEC cell.
- f_{ch}: ratio of the scalar sum of the p_{T} of tracks associated to a jet over the jet p_{T};
- f_{max}: maximum jet energy fraction deposit in a single calorimeter layer;
- t_{jet}: cell squared energy-weighted timing of the jet with respect to the trigger timing; the time of flight is subtracted from the computation.

Specifically, f_{HEC}, f_Q^{HEC}, E_{neg} and $\langle Q \rangle$ help to reduce *sporadic noise bursts*, i.e. noise bursts in the HEC calorimeter caused by some noisy cells. On the other hand, f_{EM}, f_Q^{LAr} and $\langle Q \rangle$ help to reduce the so-called *coherent noise* arising in the electromagnetic calorimeter. Non-collision backgrounds, such as cosmic rays and beam-induced backgrounds, can be identified by the topology of the energy deposits through f_{EM} and f_{max}. Fake jets produced in collision events can be discriminated through f_{ch}. Jet timing, t_{jet}, is an excellent discriminant against non-collision background but since the previous factors remove almost all of the background, this is used as an independent variable to quantify the fake jets surviving the selection.

Based on these variables and type of backgrounds, a set of cleaning cuts was defined in 2011 for 7 TeV data that is still valid for 8 TeV [109]. Four set of criteria were defined and

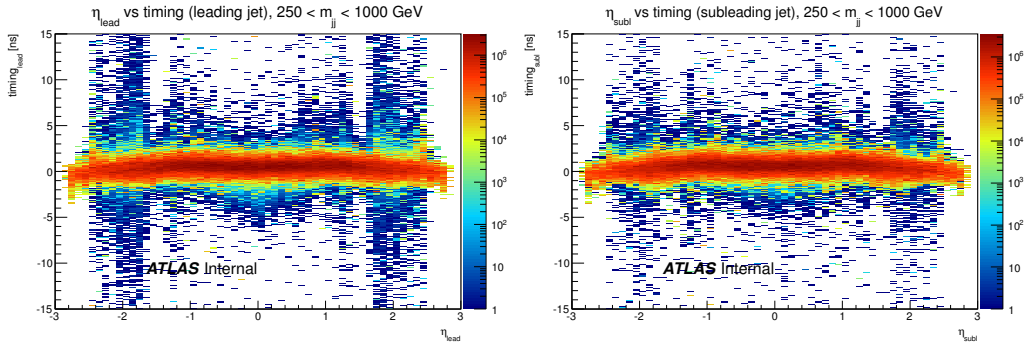

(a) (b)

Figure 6.10: leading (a) and subleading (b) jet timing as a function of jet η for events with m_{jj} between 250 GeV and 1 TeV [85].

classified according to their efficiency in selecting *good* jets, namely: *looser*, *loose*, *medium* and *tight*. The *looser* option has a 99.8% efficiency at selecting good jets with p_{T} above 20 GeV and is the one employed in the dijet analysis selection. Details on these criteria are listed in Table 6.5.

background	cuts
HEC spikes	$(f_{\mathrm{HEC}} > 0.5$ and $\lvert f_Q^{\mathrm{HEC}}\rvert > 0.5$ and $\langle Q\rangle > 0.8)$ or $\lvert E_{\mathrm{neg}}\rvert > 60$ GeV
coherent EM noise	$f_{\mathrm{EM}} > 0.95$ and $f_Q^{\mathrm{LAr}} > 0.8$ and $\langle Q\rangle > 0.8$ and $\lvert\eta\rvert < 2.8$
non-collision background	$(f_{\mathrm{max}} > 0.99$ and $\lvert\eta\rvert < 2.0)$ or $(f_{\mathrm{EM}} < 0.05$ and $f_{\mathrm{ch}} < 0.05$ and $\lvert\eta\rvert < 2.0)$ or $(f_{\mathrm{EM}} < 0.05$ and $\lvert\eta\rvert > 2.0)$

Table 6.5: selection cuts used to identify bad jets using the *looser* definition.

The negligible number of events falling outside of the 5 ns band in Figure 6.10, shows that the bad jet rejection cuts derived on 7 TeV data perform well at 8 TeV too.

Hadronic Tile Calorimeter Masked Modules

An early η-ϕ map of the leading jets passing the basic analysis cuts revealed the presence of two *hot-spots* of similar shape and dimensions, as shown in Figure 6.11.

These hot-spots are characterised by having a rectangular shape enclosing an inner region with significantly less counts than the surrounding bins. A dedicated investigation has shown that these two regions correspond to two modules of the Hadronic Tile Calorimeter: LBA05 ($0.0 < |\eta| < 0.8$, $4\frac{\pi}{32} < \phi < 5\frac{\pi}{32}$) and LBC16 ($-0.8 < |\eta| < 0.0$, $15\frac{\pi}{32} < \phi < 16\frac{\pi}{32}$). These two modules are known for having been off throughout the

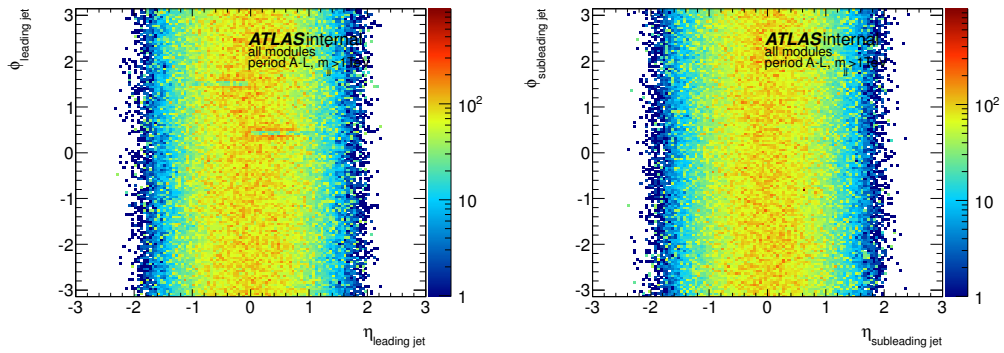

(a) (b)

Figure 6.11: leading (a) and subleading (b) jet η-ϕ maps for jets with p_{T} above 1 TeV [85]. Compare to the leading jets η-ϕ maps after applying the masked Hadronic Tile Calorimeter modules veto in figure 6.15.

8 TeV data taking: LBA05 since the beginning while LBC16 soon after, since June 2012. Other modules have been unresponsive for shorter periods of time in 2012. Figure 6.12 shows a map of modules that have been masked over the course of data taking.

module	η range	ϕ range	masked luminosity [%]
LBA05	$-0.1 < \eta < 1.0$	$2.95 < \phi < 5.89$	100
LBC16	$-1.0 < \eta < 0.1$	$1.37 < \phi < 1.67$	82
LBA18	$-0.1 < \eta < 1.0$	$1.57 < \phi < 1.87$	36
LBA35	$-0.1 < \eta < 1.0$	$-3.04 < \phi < -2.74$	29
EBC01	$0.8 < \eta < 1.7$	$-0.98 < \phi < 0.196$	4
others			< 0.05

Table 6.6: masked Hadronic Tile Calorimeter modules with their coverage and fraction of total luminosity masked.

BCH_CORR_CELL In order to compensate for the missing energy readings from masked (because momentarily unresponsive or completely off) Hadronic Tile Calorimeter cells, a correction is applied at the cell level during the jet reconstruction stage that is named BCH_CORR_CELL: Bad Channel Correction Cell. This correction operates by averaging the energy readings from neighbouring cells to evaluate the missing information of the masked cell. However, this approximation reaches its limits when applied to well-collimated high-p_{T} jets. When a jet releases most of its energy on an unresponsive cell, the average value computed from its neighbours will underestimate the true value, while, on the other hand, when the highest jet energy release falls in a cell next to an unresponsive one, the value estimated by the correction will overshoot the real one. These effects

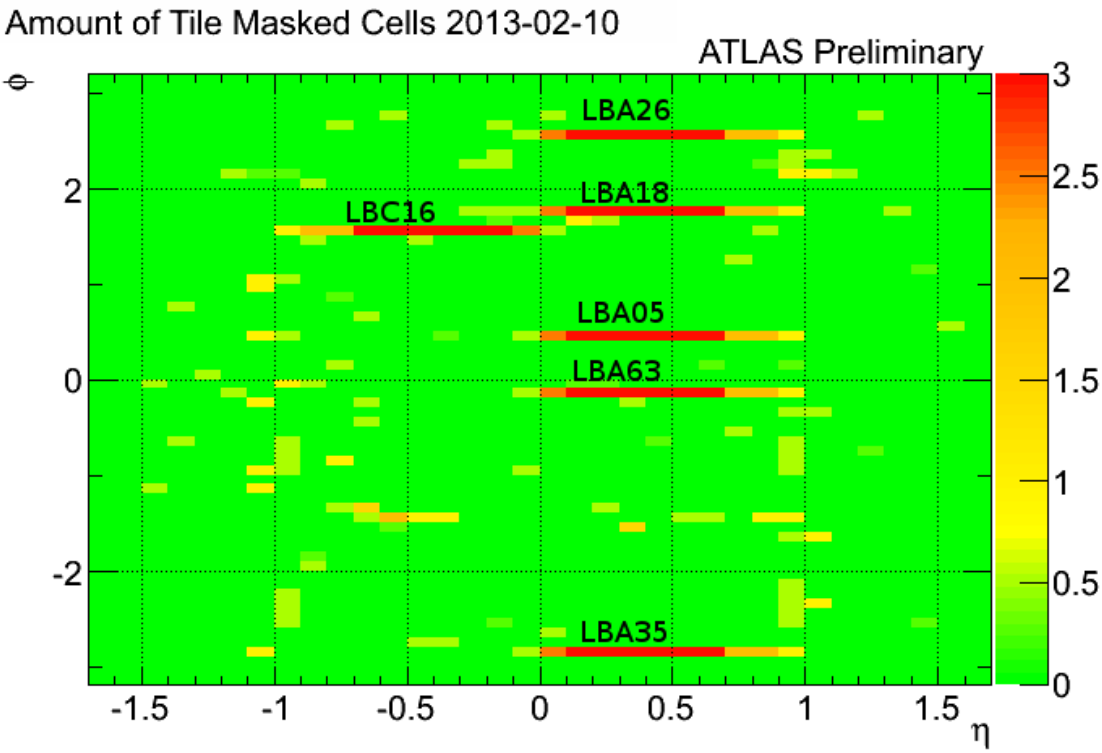

Figure 6.12: η-ϕ map of the Hadronic Tile Calorimeter cells masked on October 2nd 2012 [110].

are increased when a full Hadronic Tile Calorimeter module is non-responsive, not just one of its cells. Therefore the core-edge structure observed in Figure 6.11a is understandable. Moreover, this also explains why the hot-spots are observed only for the leading jet and not for the subleading jet: since a jet falling next to an unresponsive module receives an over-correction, it is likely for it to become the leading jet of the event, on the other hand, a jet that receives an under-correction is likely to become a non-leading jet.

Jet p_{T} Asymmetry The effects of the BCH_CORR_CELL correction on the jets entering the dijet analysis have been evaluated using a *tag and probe* method, where the tag is a good leading jet away from any unresponsive Hadronic Tile Calorimeter cell, while the probe is the other leading jet located either in the edge region or within the core of one of these cells. Given the expected p_{T} balance of dijet events, the asymmetry produced by the correction has been taken as a reference parameter and defined as:

$$A_{p_{\mathrm{T}}} = 2 \cdot \frac{p_{\mathrm{T}}^{probe} - p_{\mathrm{T}}^{tag}}{p_{\mathrm{T}}^{probe} + p_{\mathrm{T}}^{tag}} \tag{6.25}$$

Figure 6.13 shows the jet p_{T} asymmetry as measured for events where the probe jet falls in the edge or the core of the LBC16 Hadronic Tile Calorimeter module. It is remarkable that due to the BCH_CORR_CELL correction, the mean values diverge by 13%, with the core events having a negative asymmetry and the edge events a positive asymmetry. The jet p_{T} asymmetry has been evaluated also as a function of the correction itself, both for edge and core events. Figure 6.14 shows the example of module LBA05 for events with m_{jj} between 1 TeV and 1.5 TeV. Focusing on the bulk of the distributions, it is possible to observe that medium-low correction values give negative $A_{p_{\mathrm{T}}}$ values for the core events, while for edge events the bigger the correction the bigger is the asymmetry. A similar behaviour is observed for jet p_{T} and m_{jj} response measured in MC events, where the masked LBA05 Hadronic Tile Calorimeter module has been included in the simulation.

Events Veto To resolve the problem posed by under-corrected and over-corrected jets by BCH_CORR_CELL, it was decided to discard any event that would have a jet with p_{T} at least as large as 30% of the subleading jet p_{T} in a masked module. This solution was adopted as the most reliable and efficient, since it does not involve the removal of the BCH_CORR_CELL correction, the introduction of an additional correction factor nor of another jet p_{T} uncertainty. For this purpose, a dedicated tool has been developed: the BCHCleaningTool [111], which works in combination with the TileTripReader tool [107] to determine whether a jet falls or not in a masked Hadronic Tile Calorimeter module. An additional edge of width $\eta = 0.1$ is also built around masked Hadronic Tile Calorimeter barrel modules, extended to $\eta = 0.2$ for jet in the Hadronic Tile Calorimeter extended barrel. The leading jets η-ϕ map after applying the masked Hadronic Tile Calorimeter modules veto is shown in Figure 6.15. This veto complicates the handling of MC samples, since these contain only one masked module (LBA05) while the list of masked modules was continuously updating throughout the 8 TeV data taking. The Hadronic Tile Calorimeter masking, and so the event removal, has been thus emulated by randomly selecting run

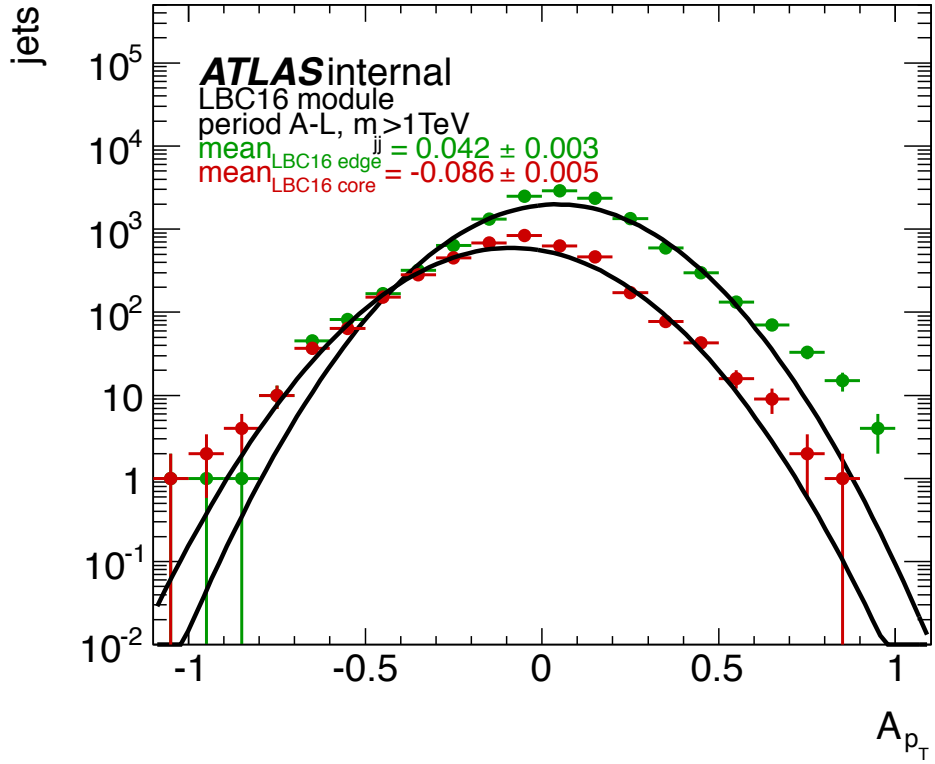

Figure 6.13: jet p_{T} asymmetry for events where one of the two leading jets is in the edge or the core region of the Hadronic Tile Calorimeter module LBC16 [85]. Only events from the blinded dataset with dijet invariant mass values above 1 TeV are considered. The mean jet p_{T} asymmetry values are distant by 13%.

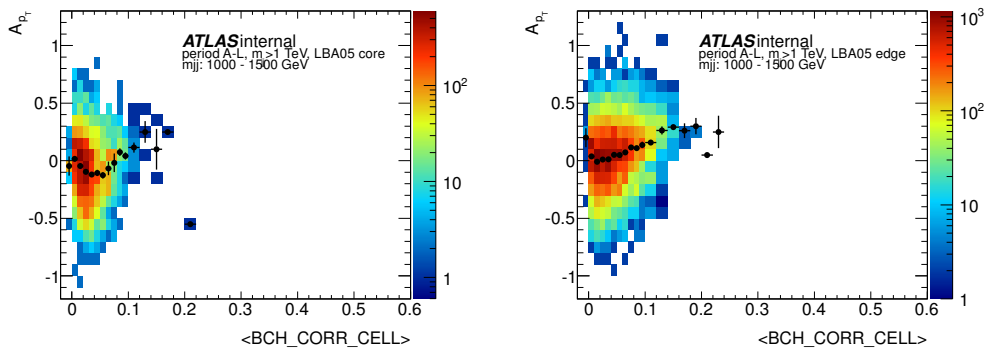

(a) (b)

Figure 6.14: jet p_{T} asymmetry vs. BCH_CORR_CELL correction value for jets in the core (a) and in the edge region (b) of Hadronic Tile Calorimeter module LBA05. Only events from the blinded dataset with m_{jj} between 1 TeV and 1.5 TeV are considered [85].

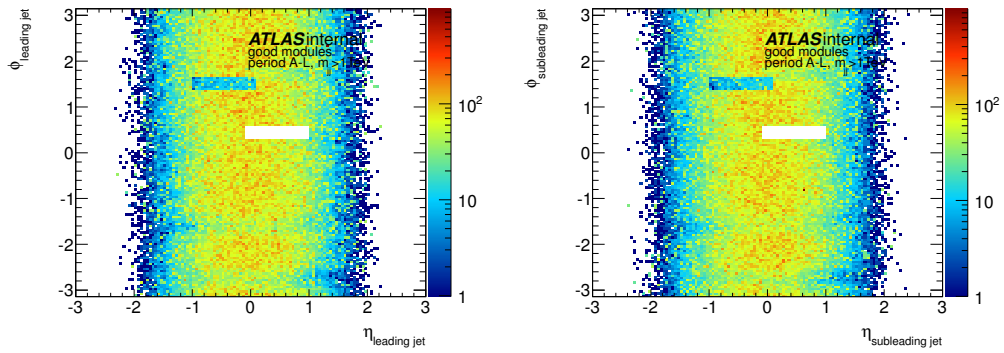

(a) (b)

Figure 6.15: leading (a) and subleading (b) jet η-ϕ map for jets with p_{T} above 1 TeV after applying the masked Hadronic Tile Calorimeter modules veto [85]. The empty region is that corresponding to module LBA05, masked since the beginning of data taking. The second region with significantly less events is that corresponding to module LBC16, masked since June 2012. Compare to the leading jets η-ϕ maps before applying the veto in Figure 6.11.

numbers and luminosity block from the data GRL and by applying the BCHCleaningTool as if it was data. The net effect of this veto on the dijet invariant mass distribution is a loss of 10-15% events at large masses.This however should not be regarded as an issue, since most of the events lost in the m_{jj} tail were effectively produced by the BCH_CORR_CELL over-correction.

6.6.2 13 TeV

The 13 TeV dijet analysis shares most of the events selection cuts of the 8 TeV one. However, since the resonant dijet analysis is carried out in parallel with its complementary dijet angular analysis [12] and a collection of jet performance studies, the event selection is organised in a pre-selection that is common to all the three scenarios and set of cuts that are analysis-specific.

The pre-selection is summarised by the following cuts.

1. **Total events**. The number of events available from the normal and debug streams before any selection.

2. **GRL**. Events must be from a run and luminosity block listed on the Good Run List: data15_13TeV.periodAllYear_DetStatus-v56-pro19-01_DQDefects-00-01-02_PHYS_StandardGRL_All_Good.xml.

3. **LAr error**. Reject events that present LAr EM Calorimeter data integrity problems (xAOD::EventInfo::LAr).

4. **Tile error**. Reject events that present Hadronic Tile Calorimeter data integrity problems (xAOD::EventInfo::Tile).

5. **Core error**. Reject events with missing information (xAOD::EventInfo::Core).

6. **Vertex**. The reconstructed primary vertex must have more than one track: $n_{\mathrm{trk}}^{\mathrm{vtx}} > 1$.

7. **Trigger pre-selection**. The event must pass at least one of the triggers: L1_J75, L1_J100, HLT_j360, HLT_j380, HLT_j400.

8. **Jet recalibration**. Jet are recalibrated according to the most recent recommendations before moving on with the event selection.

9. **Leading jets**. Require the event to have at least two jets with $p_{\mathrm{T}} > 50$ GeV.

10. **Leading jet p_{T} pre-selection**. Require the leading jet to have $p_{\mathrm{T}} > 200$ GeV.

The dijet resonance analysis specific cuts are then applied on top of these cuts.

1. **Trigger**. The event must fullfil the trigger strategy requirements, as detailed in Section 6.4.2.

2. **Jet cleaning**. Require the event to fullfil the jet cleaning cuts. See Section 6.6.2

3. **Leading jet p_{T}**. Require the leading jet p_{T} to be above the HLT_j360 trigger full efficiency threshold: $p_{\mathrm{T}} > 440$ GeV. See Table 6.3.

4. **m_{jj}**. Require the event to have $m_{\mathrm{jj}} > 1100$ GeV to remove the bias from the jet p_{T} cut. See Section 6.5.2.

5. **y^***. Require the leading jets to have $|y^*| < 0.6$ to enrich the event selection with central hard scatter events. See Section 6.1.1.

It should be noted again that for MC samples only the kinematic selection cuts are applied.

Jet Cleaning

The same jet cleaning cuts applied in the 8 TeV analysis (see Section 6.6.1) have proven to be effective in removing fake jets in 13 TeV collisions too. The same *BadLooser* definition (see Table 6.5), now called *BadLoose*, is used and its efficiency in selecting good jets is measured to be greater than 99.5% for jet with p_{T} above 20 GeV [112].

Jet timing, as well as raw calorimeter distributions have been cross checked without finding any suspicious feature in data. The jet calibration has also been thoroughly checked with multijet balance and punch-through dedicated studies.

	selection criteria	n_{events}
pre-selection	total events	35 477 718
	LAr error	35 398 888
	Tile error	35 395 678
	Core error	35 393 381
	vertex	35 391 453
	trigger pre-selection	23 350 594
	leading jets	23 020 926
	leading jet p_{T} pre-selection	12 740 838
dijet resonance selection	trigger	11 995 952
	jet cleaning	11 988 448
	leading jet p_{T}	4 979 860
	m_{jj}	2 480 182
	y^*	677 852

Table 6.7: cut flow of the 13 TeV dataset for the dijet resonance analysis.

Hadronic Tile Calorimeter Calorimeter Masked Modules

The Hadronic Tile Calorimeter masked modules that have caused some problems in the 8 TeV analysis, have not given any issue at 13 TeV, since only two modules have been masked throughout data taking (one of which is included in the MC simulation). Most importantly, the BCH_CORR_CELL correction was not applied anymore, removing the need for a veto.

6.7 Dijet Mass Binning

The search for localised excesses in the dijet invariant mass spectrum is directly related to the binning of the distribution. The optimal choice should have bins that are narrower than the signal width, in order for localised resonances to stand out, and at the same time bins should be larger than the detector mass resolution, in order to reduce the effect of migration from one bin to another. Following these two guidelines, and considering that the intrinsic width of most benchmark signals is much narrower than the detector mass resolution, the binning for the dijet analysis has been defined to closely follow the dijet mass resolution. This same method has been applied to both the 8 TeV and the 13 TeV analyses, with only some minor differences.

As a first step, the dijet mass resolution is measured from a MC QCD background sample. The invariant mass of two truth-jets, $m_{\text{jj}}^{\text{truth}}$, is first divided into coarse bins. Then, for each one of these coarse bins, the $m_{\text{jj}}^{\text{reco}}/m_{\text{jj}}^{\text{truth}}$ distribution is built from matching reconstructed and truth jets. While the 8 TeV analysis used ΔR matching, the 13 TeV analysis used ghost-matching. The distributions are then fitted with a gaussian and its width divided by the mean value is taken as the dijet mass resolution in the range of that specific $m_{\text{jj}}^{\text{truth}}$ bin. The dijet mass resolution for 8 TeV and 13 TeV data is shown in

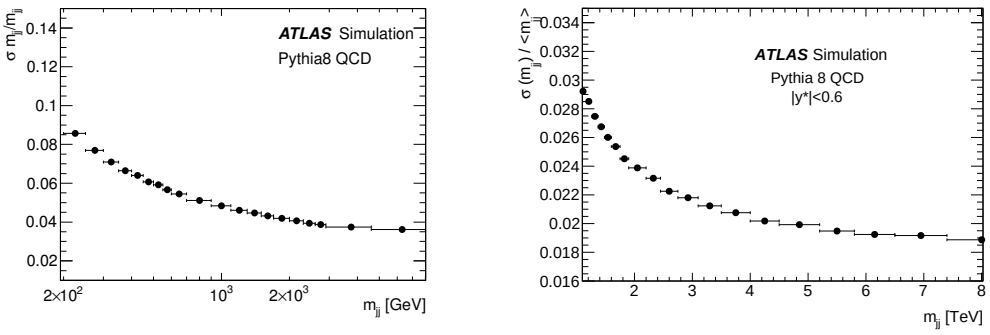

(a) (b)

Figure 6.16: dijet invariant mass resolution as measured in 8 TeV (a) and 13 TeV (b) Pythia Mc samples. The m_{jj} resolution in Run-2 is visibly better than that in Run-1 thanks to the introduction of the Gsc correction (see Section 4.3.5).

Figure 6.16. For a smoother dijet mass binning, the m_{jj} resolution for 13 TeV collisions has been fitted, and then replaced, with a sixth order polynomial. Starting from the chosen lower edge of the dijet mass distribution (253 GeV and 946 GeV for the 8 TeV and 13 TeV dijet analyses respectively), the bin widths are iteratively computed as the lower edge times the m_{jj} resolution measured at that mass value, until the upper limit given by the collision energy is reached. For the 13 TeV binning, the detector resolution is conservatively kept constant above ∼8 TeV.

A comparison of the detector mass resolution with the width of reconstructed benchmark models, such as excited quarks and W', has shown that the binning is always well within the chosen guidelines.

6.8 Background extraction

In order to state if any localised resonance is observed in the dijet mass spectrum, an estimation of the background distribution is required.

As the background events are mostly from Qcd processes, with minor contributions from other Sm processes, an option could be the use of Nlo, or higher order, Mc samples to emulated the expected data distribution. However this solution would add the need to account for theoretical uncertainties, such as non-perturbative effects, experimental uncertainties, such as detector resolution, kinematic selection and jet energy scale, just to list some of the most relevant sources.

A more practical solution would be to employ QCD calculations to estimate the background. This solution has been adopted in previous publication by the Cdf [113] (Lo) and DØ [114] (Nlo) Collaborations. Nevertheless, obtaining a good description of the data distribution is still challenging and the associated uncertainties reduce the sensitivity of the search, especially the Jes uncertainty applied to the background.

The most viable solution for background extraction is a data-driven estimation ob-

tained from a fit of the dijet mass distribution with a smooth function. This expedient has been first adopted by the UA2 [115] and CDF [116] Collaborations and has proven to be a solid method also for the dijet searches performed at the LHC by ATLAS [100, 101, 102, 103, 11, 12] and CMS [117, 118, 119, 105, 106].

The *standard* functional form to describe the dijet background in ATLAS publications is:

$$f(x) = p_0(1-x)^{p_1} x^{p_2+p_3 \ln x} \tag{6.26}$$

where p_i are parameters and $x \equiv \frac{m_{\mathrm{jj}}}{\sqrt{s}}$. There is no real reason why Equation 6.26 should fit so well the dijet invariant mass distributions, yet this ansatz has demonstrated its reliability for very different center of mass energies and over a large range of m_{jj} values. Equation 6.26 was first employed by the CDF Collaboration [120] and then adopted by ATLAS for all its dijet searches. Over the years, this form has undergone a constant evolution in order to adapt to the needs of the experiments [76]. The x^{p_i} term was originally introduced to describe the LO QCD matrix element behaviour while the $(1-x)^{p_i}$ is a parametrisation of the effects of the parton PDFs. Additional factors of the form $x^{p_i(\ln x)^n}$ have been considered, up to $n = 2$, in order to introduce additional degrees of freedom to the fit of the m_{jj} distributions. As a matter of fact, with the increase of the integrated luminosity values and the extension of the spectra, structures from QCD may become more and more evident and functions that were appropriate for previous experiments or datasets may not be suitable anymore without the addition of new degrees of freedom. Beside its predisposition to describe the m_{jj} distribution, the smooth and steeply falling profile of Equation 6.26 does not accommodate local excesses, making it therefore a good choice for background extraction. Non-resonant signals, however, might be absorbed and hidden by the fit function. For these kind of signals, the exotic dijet resonance search is unsuitable and other strategies must be adopted, such as that of the dijet angular analysis [121, 12]. Unlike the other background extraction solutions mentioned above, the use of a fit introduces only two sources of uncertainties: the fit function choice and the fit quality.

6.9 Fit Function Choice

Despite all ATLAS exotic dijet publications [100, 101, 102, 103, 11, 12] having used a functional form directly derived from Equation 6.26 to fit the background distributions, preliminary studies were performed each time to choose the best among the options available. Two different approaches were used for the 8 TeV [11] and 13 TeV [12] ATLAS publications.

6.9.1 8 TeV

Due to the blinding strategy adopted for the 8 TeV analysis, the studies for the choice of the fit function were performed on a partial dataset, corresponding to one fourth of the total integrated luminosity collected, and on MC samples, corresponding to the total integrated luminosity of data. Despite the results these had provided, at the time of

unblinding, when the full data spectrum was fitted, the quality of the fit did not match the expectations, showing clear signs that the chosen fit function was not adequate to the purpose. Further studies were performed post-unblinding to understand the cause of the problem and assign an adequate uncertainty.

Fit Studies on Partial Dataset

The fit function from Equation 6.26 was tested on a partial dataset together with a set of three other functions previously used by UA2 and CDF. One of these functions has three parameters while the other two have four. The results, collected in Table 6.8, show that Equation 6.26 has the best performance in terms of smallest $\frac{\chi^2}{\text{n.d.f.}}$, log-likelihood and largest BUMPHUNTER p-value (see Section 6.10.1 for more details on BUMPHUNTER). It should be noted that all the four functions considered give good fitting results, though those with four parameters perform better than that with three.

function	publication	$\frac{\chi^2}{\text{n.d.f.}}$	log-likelihood	BUMPHUNTER p-value
$\frac{p_0}{m^{p_1}} e^{-(p_2 m + p_3 m^2)}$	UA2 [115]	0.934	316.4	0.014
$\frac{p_0}{m^{p_1}} (1 - \frac{m}{\sqrt{s}})^{p_2}$	CDF [116]	1.52	334.2	0.003
$\frac{p_0}{m^{p_1}} (1 - \frac{m}{\sqrt{s}} + \frac{p_3 m}{s})^{p_2}$	CDF [122]	0.947	316.2	0.007
$p_0 (1-x)^{p_1} x^{p_2 + p_3 \ln x}$, $x \equiv \frac{m}{\sqrt{s}}$	CDF [120]	0.679	307.3	0.168

Table 6.8: comparison of the fit results performed on a partial 8 TeV dataset corresponding to 5.1 fb^{-1} using four different functions. These results show that the last function in the table, corresponding to Equation 6.26, gives the best results in terms of smallest $\frac{\chi^2}{\text{n.d.f.}}$, log-likelihood and largest BUMPHUNTER p-value.

Fit Studies on MC

A comprehensive test of the performance of a fit function demands the use of a background distribution that is comparable in terms of extension, entries and error bars to that of data. The use of MC simulations is thus unavoidable. In order to meet the needs imposed by the statistical compatibility of the simulated distributions, two approaches are available.

Pseudo-data From Theory Distribution A dedicated Pythia LO MC sample has been produced with very large statistics to be used as a PDF to generate pseudo-data. However, the fits to the generated distributions have shown, for different values of integrated luminosity, that the same set of bins would always be systematically above or below the fitted function (see Figure 6.17). This effect was traced back to the insufficient statistics of the generated sample. For this reason the test has been discarded. Nonetheless,

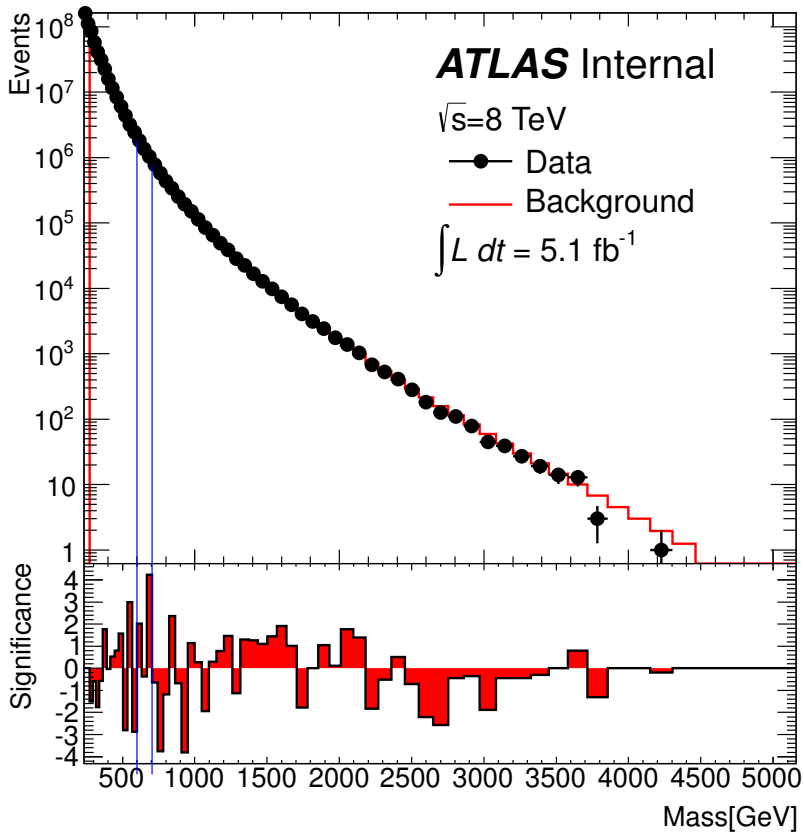

Figure 6.17: fit of the pseudo-data distribution generated from Pythia LO MC sample [85]. Significant fluctuations are observed for low m_{jj} values. The blue vertical lines indicate the region that is most discrepant with respect to the fitted background using the BUMPHUNTER algorithm.

this has shown that the chosen set of functions is able to fit LO dijet mass distributions corresponding to integrated luminosities equal to data.

MC Data-like Distributions Another option is represented by the possibility of building a spectrum that has the same statistical power as data. This can be achieved, bin by bin, by randomly drawing events and assigning them unitary weight, instead of applying a scale factor. Necessary condition for this procedure to be applicable is the number of effective MC entries available in a bin to be greater than that of data. For each bin of the spectrum, we require MC to have at least as many effective entries as data:

$$n^{\text{MC}}_{\text{effective entries}} > n^{\text{data}}_{\text{effective entries}} \tag{6.27}$$

Recalling Equation 6.21, we can write:

$$n^{\text{data}}_{\text{effective entries}} = \frac{n^{\text{data}}_{\text{entries}}}{p_{\text{effective}}} \tag{6.28}$$

where $p_{\text{effective}}$ is the average effective trigger prescale for the bin. Similarly, for MC we can write:

$$n^{\text{MC}}_{\text{effective entries}} = \frac{n^{\text{MC}}_{\text{entries}}}{w^{\text{MC}}_{\text{effective}} L} \tag{6.29}$$

where $w_{\text{effective}}$ is the average effective weight for MC events in the bin and L is the integrated luminosity scale factor to normalize MC to data. Considering that scaled data and MC entries are ultimately the same:

$$n^{\text{data}}_{\text{entries}} = n^{\text{MC}}_{\text{entries}} \tag{6.30}$$

Equation 6.27 may be rewritten as:

$$f = \frac{n^{\text{data}}_{\text{effective entries}}}{n^{\text{MC}}_{\text{effective entries}}} = \frac{n^{\text{data}}_{\text{entries}}}{p_{\text{effective}}} \frac{w^{\text{MC}}_{\text{effective}} L}{n^{\text{MC}}_{\text{entries}}} = \frac{w^{\text{MC}}_{\text{effective}} L}{p_{\text{effective}}} < 1 \tag{6.31}$$

The factor f here sets the condition on whether the data-like method can be applied or not. For $f < 1$, the MC distribution has more effective entries than data, so a data-like content can be generated. This means that for this bin it is possible to generate from MC a content that has the same statistical power and random fluctuations proper of data. On the other hand, for $f > 1$ a weight greater than one needs to be applied to MC in order to have the same content as data.

In case data is not weighted, as it would be if there were no trigger prescales, this all reduces to:

$$n^{\text{MC}}_{\text{effective entries}} > n^{\text{MC}}_{\text{entries}} \tag{6.32}$$

so that:

$$f = \frac{n^{\text{MC}}_{\text{entries}}}{n^{\text{MC}}_{\text{effective entries}}} = w^{\text{MC}}_{\text{effective}} L < 1 \tag{6.33}$$

Whenever $f < 1$ it is therefore possible to take two distinct ways in order to get the expected bin content, hence distribution shape: assign to all the events the weight f or retain only a fraction f of all the available MC events. The first option gives the common MC shape, i.e. reflecting the precision and the statistical power of the sample employed. The second option, instead, returns a spectrum whose entries follow a poissonian distribution centered around the expected MC value of the first option. Also the bin errors are poissonian. This is the MC data-like distribution. Once the f factor for a given bin is computed, a fraction f of the available MC entries can be retained by iterating over the available effective entries and randomly extracting a number, x, from a flat distribution in the $[0, 1]$ interval. Whenever $x < f$, the event is retained.

Sometime it is useful to emulate the progress of data taking, where the events collected are accumulated over time. This is of particular relevance, for example, when testing the

evolution of the performance of a fit function with the increase of the integrated luminosity. Events with very large m_{jj} values can significantly alter the outcome of a fit and therefore they need to be retained in all the following steps of the emulated data taking. In these cases, it is fundamental to coherently set the seed for the generation of the random number x bin by bin, so that the events that are retained for a given integrated luminosity value L_i are retained also for larger integrated luminosity values $L_j > L_i$. This can be achieved, for example, by using the bin lower edge as seed.

Given the benefits provided by data-like spectra and their random nature, it is sometimes advantageous to use a set of these and not just one. This might be the case, for example, if we want to make sure that the perfromance of a fit is not just an accident. For this purpose, different set of seeds for the random extraction can be used. However, for values of f close to unity, $f \sim 1$, the different spectra will be highly correlated, as most of the available MC effective entries are retained in each spectrum.

For the fit function choice studies, data-like distributions have been built from PYTHIA 8 MC samples with NLO k-factors applied. Due to the large weights of some MC slices, it was not possible to generate a pure data-like m_{jj} spectrum along the whole range, resulting in a mix of data-like (at large m_{jj}) and scaled (at low m_{jj}) MC distributions.

As it can be seen in Figure 6.18, the fit to this distribution has shown that the standard fit function from Equation 6.26 can accurately describe the 20 fb^{-1} dijet mass spectrum, including the high mass tail, which is the least known region. These studies indicate that the standard fit function is indeed a good choice even at the integrated luminosity and dijet mass range extension of the 8 TeV analysis. There are no hints that the standard fit function might show any limitations on data, under the assumption that MC reasonably describes the data shape.

Fit Studies on Full Dataset

After the unblinding of the data, the fit of the m_{jj} spectrum with the standard fit function revealed a poor ability of the function at describing the background distribution. Even though the fit function choice was set by the studies on the partial dataset and the MC distributions, additional studies have been performed after the unblinding to better understand the limitations of the fit and assign a proper uncertainty to the fit function choice.

An extended set of six fit functions has been defined with the intent of comparing the performance of functions with a number of parameters ranging from three up to six (see Table 6.9). Functions with five and six parameters (numbers 4-6 in Table 6.9) include additional degrees of freedom to the standard fit function of Equation 6.26 (number 3 in Table 6.9).

A ten-fold cross-validation procedure has been adopted to test the ability of the functions at fitting the unblinded m_{jj} spectrum. The steps can be summarised as:

- split the unblinded dataset in ten sub-datasets of equivalent integrated luminosity;
- iteratively combine nine of the sub-datasets, leaving one out. These are the training sample and the test sample respectively;

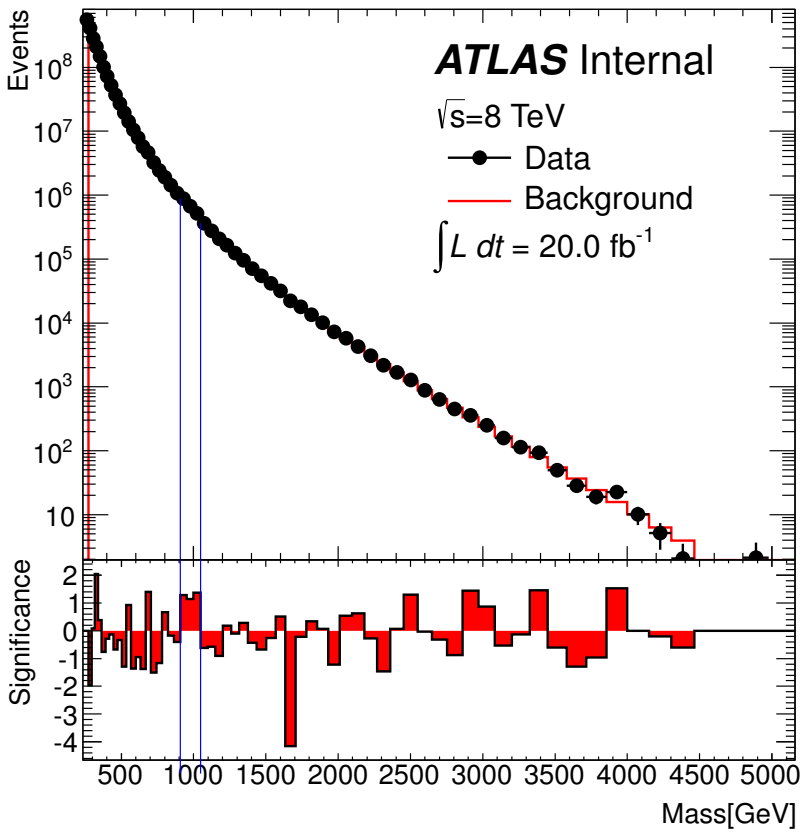

Figure 6.18: fit of the mixed data-like (at large values) and scaled (at low values) MC m_{jj} distribution using the standard four parameters fit function [85]. The integrated luminosity is 20 fb^{-1}. The function is able to describe the spectrum, including the large mass tail. The blue vertical lines indicate the region that is most discrepant with respect to the fitted background using the BumpHunter algorithm.

#	function	publication	$n_{\text{parameters}}$
1	$\frac{p_0}{m^{p_1}}(1-\frac{m}{\sqrt{s}})p_2$	CDF [116]	3
2	$(1-x)^{p_0}x^{p_1+p_{42}\ln x}$, $x \equiv \frac{m}{\sqrt{s}}$	ATLAS [123]	3
3	$p_0(1-x)^{p_1}x^{p_2+p_3\ln x}$, $x \equiv \frac{m}{\sqrt{s}}$	CDF [120]	4
4	$p_0(1-x)^{p_1}x^{p_2+p_3\ln x}$, $x \equiv \frac{m}{p_4}$		5
5	$p_0(1-x)^{p_1}x^{p_2+p_3\ln x+p_4(\ln x)^2}$, $x \equiv \frac{m}{\sqrt{s}}$		5
6	$p_0(1-x)^{p_1}x^{p_2+p_3\ln x+p_4(\ln x)^2}$, $x \equiv \frac{m}{p_5}$		6

Table 6.9: functions used to test the fit of the unblinded 8 TeV m_{jj} spectrum. Function number 3 is the standard fit function of Equation 6.26. Functions 4 to 6 have been obtained from the standard fit function by including additional parameters.

- fit the training sample with one of the functions from the set;
- scale the fit down by a factor of nine;
- use the fit as a description of the test sample and perform the relevant statistical tests: $\frac{\chi^2}{\text{n.d.f.}}$, log-likelihood and BUMPHUNTER (see Section 6.10.1);
- average the results of the iterations and compare the values.

The results, summarised in Table 6.10, show that the two three parameter fit functions are insufficient to describe the full m_{jj} distribution and at the same time the other four functions have comparable performance. While the $\frac{\chi^2}{\text{n.d.f.}}$ values are overall acceptable for the functions considered, the p-values of any of the tests considered are systematically low for the three parameter options, indicating not only that the fit is of poor quality but also that the BUMPHUNTER algorithm finds non-negligible sets of consecutive bins above the fitted background. Using six parameters to describe the spectrum does not improve the results over the four and five parameter options and only adds the problem of possibly fitting away any interesting feature that may arise. Among the four and five parameter fit functions there is no clear best choice in terms of fit quality and ability at predicting the spectrum. For this reason, an uncertainty on the fit function is introduced, whose value is given by the difference between the standard fit function and the five parameter fit function with the additional $x^{p_4(\ln x)^2}$ term (functions number 3 and 5 in Table 6.9).

6.9.2 13 TeV

The difficulties experienced in the 8 TeV analysis to correctly identify the function that would best fit the background distribution, before the data was unblinded, required the implementation of a more robust method at 13 TeV. As the post-unblinding fit tests described in the previous section have shown, even with the full data distribution at hand

#	$\frac{\chi^2}{\text{n.d.f.}}$	χ^2 p-value	log-likelihood p-value	BumpHunter p-value
1	1.370	0.107	0.122	0.086
2	1.528	0.048	0.057	0.047
3	0.993	0.499	0.159	0.406
4	1.086	0.465	0.490	0.444
5	1.012	0.513	0.529	0.513
6	1.031	0.51	0.535	0.515

Table 6.10: results of the ten-fold studies on the fit of the full dataset m_{jj} distribution. The standard fit function is number 3. Function number 4 is used to estimate the fit function systematic.

it may not be evident which of the functional forms considered works best by comparing their χ^2, log-likelihood and BumpHunter values and p-values. A method was therefore sought to quantitatively accept or reject a fit function in favour of another. A solution has been found in the likelihood ratio using the approximation from Wilks' theorem [124]. This states that the likelihood ratio distribution of a null and an alternative hypoteses, $-2\log\Lambda$, is asymptotically distributed like a χ^2 distribution whose number of degrees of freedom is equal to the difference of the number of parameters of the two hypotheses. Wilks' theorem allows therefore to take the ratio of the likelihoods of the background fits performed with two different functions and analytically compute its p-value, often called *Wilks' p-value*. If this value falls below a certain threshold, the null hypothesis should be rejected in favour of the alternative hypothesis. To put it in terms that are relevant to this working case: one fit function can be quantitatively compared to another and, ultimately, can be rejected in favour of this. It is possible, therefore, to define a procedure to select the function that describes most accurately the background distributions by directly using data. There is no need anymore to run tests on partial datasets or MC distributions to select one functional form before the whole dataset is unblinded. Given a list of nested functions ordered by the number of their parameters (see Table 6.11) and starting from the simplest function of the collection, the p-value of the likelihood ratio with respect to the following function in complexity, is constantly computed as data is added to the analysis dataset. As soon as the p-value drops below the threshold of 0.05, the simpler function is discarded in favour of the alternative, since it is not able to describe the background anymore, and the loop restarts. As a guideline, in case more than one function gives a good description of the background distribution, the function with less parameters should always be favoured, since it is less prone to fit away possible resonances from new physics. The advantages of this method are twofold. On one hand the choice of the fit function is completely automated. On the other hand, the analysis does not need to be run blinded, since its strategy can be frozen before the data taking starts.

For the 13 TeV dijet analysis, the fit function described by Equation 6.26 has been considered in its three, four and five parameter configurations, where the fifth parameter

is of the form $x^{p_4(\ln x)^2}$ (see Table 6.11). Other functional forms, that are not directly related to Equation 6.26, have been tested but none of them gave clear advantages over these three functions.

function	$n_{\text{parameters}}$
$p_0(1-x)^{p_1}x^{p_2}$, $x \equiv \frac{m}{\sqrt{s}}$	3
$p_0(1-x)^{p_1}x^{p_2+p_3\ln x}$, $x \equiv \frac{m}{\sqrt{s}}$	4
$p_0(1-x)^{p_1}x^{p_2+p_3\ln x+p_4(\ln x)^2}$, $x \equiv \frac{m}{\sqrt{s}}$	5

Table 6.11: functions considered for the fit of the 13 TeV dijet mass spectrum ordered by their number of parameters. All the functions are based on the standard fit function from Equation 6.26.

Preliminary tests performed on Pythia Mc samples have shown that the three parameter fit function from Table 6.11 is able to adequately fit the m_{jj} distribution up to integrated luminosities of 2-3 fb^{-1}. The four parameter option gives only marginal improvements above 1 fb^{-1}, while the five parameter function is not stable enough at these relatively low integrated luminosities.

As data was collected, the evolution of the p-value from the comparison of the three parameter fit function to the four and five parameter options has been constantly kept under observation and its value has been measured to be well above the 0.05 threshold set to switch function. A comparison of the fits performed with three and four parameter functions using the whole statistics collected in 2015 has returned a p-value of 0.77, confirming that the three parameter fit function is still safely the best choice at 3.6 fb^{-1}.

6.10 Search Phase

Once the background is extracted, it is finally possible to determine the presence of any localised excess in data. Tests such as χ^2 and log-likelihood are helpful statistical tools to quantify the agreement between data and its fitted background distribution. The χ^2 test can tell how well the data entries are normally distributed around the expected values given by the background fit. However, the test shows its limitations in the tails of the m_{jj} distribution, where the statistics is low and hence the gaussian approximation of seeing d events out of b expected is not valid. The log-likelihood test, on the other hand, solves this problem by assuming the observed values to be distributed according to poissonian probability around the mean value given by the background fit. Both tests can provide p-values that tell how extreme the data is with respect to the null hypothesis and for this reason they are fundamental to assess the best fit function, as it was shown in Section 6.9. This is because large $\frac{\chi^2}{\text{n.d.f.}}$ values or small χ^2 and log-likelihood p-values are index of disagreement between the data and the background fit. Nonetheless, these tests make no difference whether the discrepancies are distributed all over the spectrum or are

localised just in one region. A different statistical test is therefore needed to answer this specific need.

6.10.1 The BumpHunter Algorithm

The BumpHunter algorithm is a *statistical hypertest* capable of identifying localised excesses[4], or *bumps*, in the data distribution with respect to the background, or *null hypothesis*, H_0 [77]. The algorithm evaluates the compatibility of the two distributions and returns the region which is most discrepant, together with the p-value that such an excess could arise from a fluctuation of the background, accounting, at the same time, for the trials factor, or *look elsewhere effect*. This p-value can be used to reject the null hypothesis and claim the observation of a localised excess that is not compatible with the background. No inference of any kind is made by the algorithm on signals.

The BumpHunter algorithm works by progressively scanning the data distribution using windows of varying width, ranging from two bins up to half the width of the spectrum[5]. For each iteration, the cumulative data bin content, d, is compared to that of the background, b. A statistical test, t, can be defined so that:

$$t = \begin{cases} 0 & \text{if } d \leq b \\ f(d-b) \geq 0 & \text{if } d > b \end{cases} \tag{6.34}$$

A monotonically increasing function $f(d-b)$, that quantifies the excess observed in data with respect to the background, could be specified so that $t \geq 0$. However, here the interest is in the *false positive* probability of observing as many entries as in data given a null hypothesis. This can be achieved analytically by assuming the poissonian distribution of the events in the region considered, without the need to add any further details to the statistical test of Equation 6.34 or having to throw pseudo-experiments:

$$P(d,b) = \sum_{n=d}^{\infty} \frac{b^n}{n!} e^{-b} \quad \text{if } d > b \tag{6.35}$$

Therefore, for a given set of bins and their data and background entries, the p-value is given by:

$$p\text{-value} = \begin{cases} 1 & \text{if } d \leq b \\ \sum_{n=d}^{\infty} \frac{b^n}{n!} e^{-b} & \text{if } d > b \end{cases} \tag{6.36}$$

Using the Γ function:

$$\Gamma(d) = \int_0^{\infty} t^{d-1} e^{-t} dt \tag{6.37}$$

we may write:

$$\sum_{n=d}^{\infty} \frac{b^n}{n!} e^{-b} = \frac{1}{\Gamma(d)} \int_0^{b} t^{d-1} e^{-t} dt = \Gamma(d,b) \tag{6.38}$$

[4]The BumpHunter algorithm could be extended to identify all kind of discrepancies, whether these are localised excesses or deficits. For the purpose of the exotic dijet analysis, the focus here is exclusively on the identification of localised excesses.

[5]This is the choice made for the exotic dijet analysis. Other options are possible.

The p-value for observing in a set of bins as many events as in data, d, given an expected value of b from the null hypothesis, can be computed as:

$$p\text{-value} = \begin{cases} 1 & \text{if } d \leq b \\ \Gamma(d, b) & \text{if } d > b \end{cases} \tag{6.39}$$

The smallest of the p-values measured by iterating over all the allowed combinations of consecutive bins, however is not the p-value of finding an excess as significant as that one, since the look elsewhere effect is not taken into account. Given the considerable number of tests performed, n, and considering also these to be independent, the probability of obtaining at least one p-value that is below the threshold, α, is:

$$P(\text{at least one } p\text{-value} < \alpha) = 1 - \prod_{i=1}^{n} P(p\text{-value} \geq \alpha) = 1 - (1 - \alpha)^n \geq \alpha \tag{6.40}$$

It is not correct to assume the trials to be independent in Equation 6.40, since they all have some degree of correlation due to the fact that each interval shares bins with others. Nevertheless, the statement:

$$P(\text{at least one } p\text{-value} < \alpha) \geq \alpha \tag{6.41}$$

still stands.

In order to take into account the number of trials, an *hypertest* statistics is defined from the pool of the p-values computed for all the allowed combinations of consecutive bins from the previous test statistics:

$$t = -\log(p\text{-value}_{\text{min}}) \tag{6.42}$$

where p-value$_{\text{min}}$ is the smallest of the p-values measured. This is the BumpHunter hypertest statistic. Since it combines the results of hypothesis tests performed on different regions of different widths all together, including at the same time the trials factor, the BumpHunter is a statistical hypertest, not just a test.

Pseudo-experiments are then built from the H_0 hypothesis and their BumpHunter hypertest statistic is computed, building a distribution that is then used compare the t_0 value measured from data. The p-value obtained from these measurements is the BumpHunter p-value, representing the probability of finding an excess that is extreme as that measured in data.

Removing Bumps From The Background

The presence of localised excesses in the data distribution may affect the background extraction if, like in the case of the exotic dijet analysis, this is extracted by performing a fit. Despite the fit functions being smooth and not able to accommodate bumps, as it will be shown in Section 6.11, the presence of a signal in data may drive the background estimation up or even change the shape of the background description, biasing the identification of significant excesses. In these events, the results of the BumpHunter can help to improve the quality of the background extraction.

When the BumpHunter p-value is measured to be below a certain threshold, the most discrepant region identified is removed from the fitted range and the background estimation is repeated. This avoids the background estimation being biased by the presence of a signal. At this stage, the BumpHunter is re-run. If the new most discrepant region has a p-value that is still below threshold and is next to the region removed, the excluded window is enlarged by one bin on that side and a new iteration is performed. If, on the other hand, the new most discrepant region has p-value that is still below threshold but is located elsewhere, then a bin is added on either side to the already excluded region and a new iteration is performed. This whole procedure is repeated until a region of the spectrum is removed so that the BumpHunter p-value is above the chosen threshold. For the 13 TeV analysis, an additional bin is always added to the left of the final excluded window, since this was found to help removing signal tails at low masses. No regions are removed at the beginning of the spectrum since sidebands are needed to perform a good fit of the background. In case the most discrepant region is located at the beginning of the spectrum, the second most discrepant region is excluded instead.

The threshold value adopted to tell whether a background is biased or not is given by a compromise between two factors. On one side, it should be small enough not to trigger a window removal on statistical fluctuations. On the other side, it should be large enough not to require the removal of a region that is too wide in order to recover an acceptable p-value. It was observed that the choice of 0.01 is a good compromise. It should be stressed that this threshold value is exclusively used to remove possible sources of bias from the fit, not to reject the background-only hypothesis.

6.10.2 Representation Of The Differences Between Data And Expectations

When comparing data, d, to the background, b, distribution, it is useful to provide a measure of the differences between the two. An intuitive representation is provided by the significance of the deviation of the data entries in each bin with respect to the background estimation [125]. Assuming the poissonian distribution of the data around the background expectation, it is possible to compute analytically the associated p-value, similarly to what was shown in Equation 6.35:

$$p\text{-value} = P(d,b) = \begin{cases} \sum_{n=0}^{d} \frac{b^n}{n!} e^{-b} & \text{if } d \leq b \\ \sum_{n=d}^{\infty} \frac{b^n}{n!} e^{-b} & \text{if } d > b \end{cases} \tag{6.43}$$

Note that in this case both excesses and deficits are considered. This p-value can then be converted into the equivalent number of standard deviations that the observation is located on the right side of the mean of a normal distribution. The relation between p-value and z-value is given by:

$$p\text{-value} = \int_{z\text{-value}}^{\infty} \frac{1}{\sqrt{2\pi}} e^{-\frac{x^2}{2}} dx \tag{6.44}$$

It follows that z-value > 0 implies p-value < 0.5. Since significant deviations have small p-values, it is convenient to just neglect p-values above 0.5 and hence z-values below

0. Instead, it is more useful to set the sign of the z-value according to the nature of the discrepancy: whether it is an excess, z-value > 0, or a deficit, z-value < 0. Any data observation that is consistent with the background up to p-value $= 0.5$ is assigned z-value $= 0$. Thanks to this expedient, discrepancies between data and background distributions can be easily compared over the whole spectrum, as shown in Section 6.14.1.

6.11 Fit Stability And Signal Sensitivity

The stability of the background extraction procedure has been tested against various sources of bias to prove its robustness and reliability, pointing also to the evaluation of the analysis sensitivity to its benchmark signals.

6.11.1 8 TeV

As explained in Section 6.10.1, the BumpHunter results can be used to improve the background fit in case of signal. The most discrepant region identified by the algorithm is removed from the fit range in order to return the p-value above the established agreement threshold of 0.01. There are two possible situations that can be envisioned where the background is biased at its most: the presence of a nearly detectable signal that gives a p-value still above the threshold and the presence of a large signal whose tails are not completely removed by the window exclusion.

Nearly Detectable Signals

In situations where a signal is close to the detection threshold, the fit is maximally biased. For this reason the ability of the fit function to compensate and absorb potential small signals can be tested. Also, the effectiveness of the threshold value is put under stress. For these tests, an equivalent amount of 5.1 fb^{-1} of pseudo-data has been generated from a fit of Pythia Mc distribution using the standard, four parameter, fit function. Breit-Wigner shapes of various masses and width-to-mass ratios ranging from 0.07 to 0.20 have been used as signals. For each of the signals generated, the normalisation has been iteratively tuned to give a BumpHunter p-value in the range 0.010 to 0.012, just above the exclusion threshold. For signals located in the tail of the spectrum, the addition or subtraction of one single event can make a large difference in the tuning process. In these cases, the signal normalisation that gave the closest value to 0.01 was used. The generated background only and signal plus background distributions have then been run through the BumpHunter and their fits have been compared, as shown in Figure 6.19. Results show that the BumpHunter is already able to identify the region of the injected signals as the most discrepant, despite the p-value not being small enough to trigger a window exclusion. It should be noted that the significance of the bins corresponding to the excesses is underestimated due to the biased fit. The ratio of the fit functions obtained from the signal plus background and background alone shows that the bias introduced by the presence of a signal affects mostly the tails, no matter the mass of the signal, with differences that reach 15%, although compatible with each other within two sigmas. More

extensive tests have shown that the fit function deviation increases with the width of the signal, although it always remains within acceptable distance from the background only fit. The significance of the bin-by-bin fit deviations have been computed as the fit difference divided by the quadratic sum of the errors. As shown in Figure 6.20, the most significant deviations are observed in the low mass region. Considering that these examples are extreme cases, it is encouraging to observe that the significance values never exceed four sigmas and are often well below one.

Signal Sensitivity

Given the signal tuning operated, the tests performed on nearly detectable signals may also be used to infer the minimum number of signals events that are needed to observe a significant bump. For each mass point, the number of signal events falling within the central 68% of the Breit-Wigner was computed. For that same region of m_{jj}, the number of events was also computed for the background. The ratio of the two numbers provides the minimum value to which the BumpHunter is sensitive. Results are reported in Table 6.12 and show that higher signal to background ratios are needed for large signal mass values, where the statistical errors are dominant.

Large Signals

In presence of a signal that is large enough to trigger the exclusion of the most discrepant region from the fit, the tails might not be completely removed and therefore introduce a bias in the background fit. For this study, a background distribution corresponding to an integrated luminosity of 5.1 fb^{-1} has been generated from a standard fit of the blinded dataset and excited quarks and scalar octet signals (see Section 6.3.3) have been used as benchmarks. Background and signal pseudo-data distributions have been generated applying also the trigger prescale weights. Signal plus background distributions and background only distributions have then been run through the BumpHunter and their fit results have been compared. The results have shown that the biggest bias is introduced by signals with low masses, since they have the largest cross section and they significantly alter the shape of the spectrum. Safely enough, these mass points have already been excluded by previous iteration of the analysis and represent here only an extreme exercise. At large masses, the effectiveness of the window removal is much better and deviations beyond 50% are rarely observed between the signal plus background and background only fits. The fits are observed to be more stable when broad signals are injected instead of sharp ones. This is a confirmation that the chosen threshold of 0.01 for the window removal is indeed a valid choice.

6.11.2 13 TeV

Following what has been done for the 8 TeV dijet analysis, tests on the fit stability have been repeated and further expanded to unveil the circumstances under which the

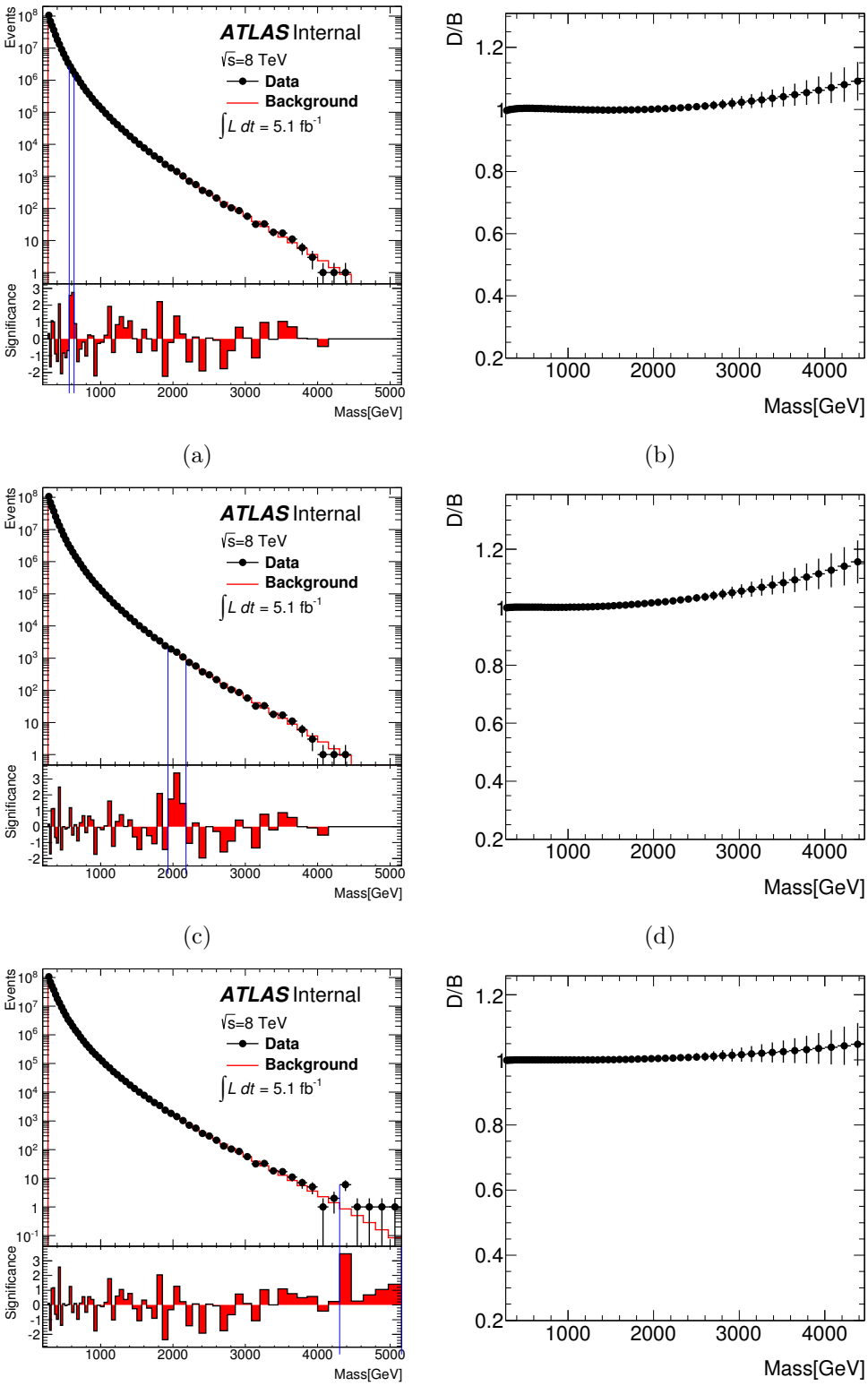

Figure 6.19: BumpHunter results on pseudo-data with injected Breit-Wigner signals corresponding to 600 GeV and width-to-mass ratio of 0.07 (a), 2000 GeV and width-to-mass ratio of 0.10 (c), 4400 GeV and width-to-mass ratio of 0.15 (e) [12]. The signals are normalised to give a p-value just above the exclusion window threshold. The ratio of the fit to the signal plus background distribution over the background only fit is shown for the three signals considered in (b), (d) and (f).

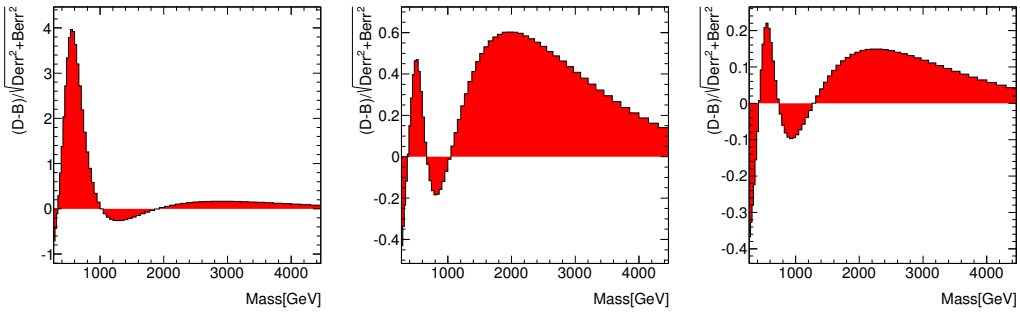

(a) (b) (c)

Figure 6.20: significance of the differences observed between the fits of background plus signal over background only distributions for the examples reported in Figure 6.19.

background extraction procedure may fail[6]. Moreover, the fact that the fit function is not chosen a priori adds an extra degree of freedom that needs dedicated studies.

Nearly Detectable Signals

The stability and robustness of the fitting procedure has been stress-tested by injecting excited quarks, q^*, and gaussian signals of different mean values and widths into the MC background. The normalisation of the signals has been tuned to be right above (0.015 - 0.010) and right below (0.010 - 0.005) the BUMPHUNTER p-value threshold (0.010) set to remove the most discrepant region of the mass spectrum from the fit. The three, four and five parameter fit function alternatives (see Table 6.11) have been tested and in each case the initial background distribution has been generated from a fit of the data-like PYTHIA MC dijet mass spectrum using the selected function. The distributions generated are smooth, without any Poisson fluctuation around the expected value that would make them look like real data, so that the random effects on the following fits are eliminated. An equivalent integrated luminosity of 1 fb^{-1} has been generated in each test. The gaussian signal widths considered, defined as $\frac{\sigma}{\text{mean}}$, are 20% and 30%: two much larger widths than the benchmark signals usually adopted, such as the q^*.

Figure 6.21 shows the injection of the gaussian signals into the background dijet mass distribution (in these examples obtained from a four parameter fit function). The normalisation of the gaussian is such that the signal is just above the BUMPHUNTER threshold. An excited quark signal with the same mass as the gaussian and at the nominal cross section is included for comparison. It is evident how the q^* width is much sharper than a gaussian with 20% width. Figure 6.22 shows the injection of the excited quarks signal into the background dijet mass distribution (also obtained from a four parameter fit function in these examples). As for the gaussians, the strength of the q^* signal is tuned so that it is just above the BUMPHUNTER threshold.

Comparing the results obtained from running the BUMPHUNTER on smooth QCD MC

[6]The studies reported here are based on an excerpt of [126], where they have been originally included.

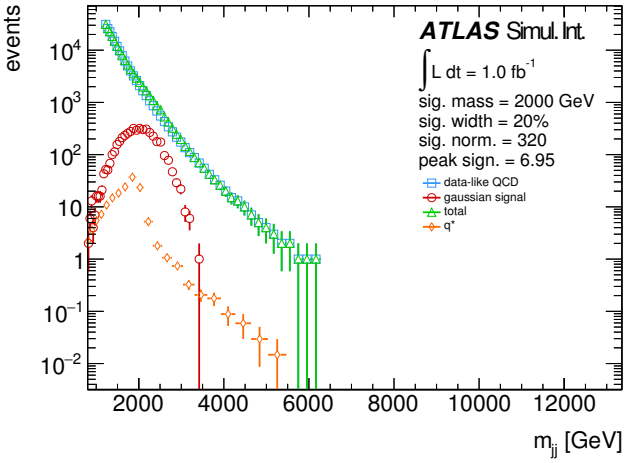

(a) 2 TeV gaussian, 20% width.

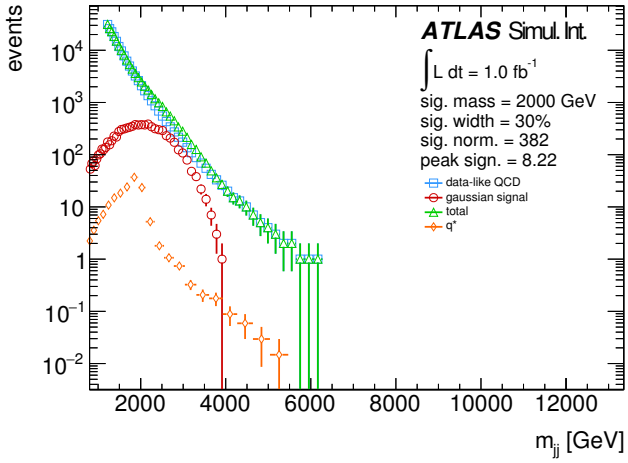

(b) 2 TeV gaussian, 30% width.

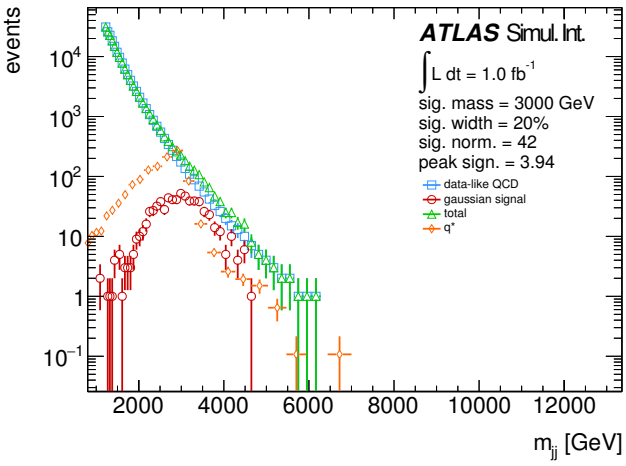

(c) 3 TeV gaussian, 20% width.

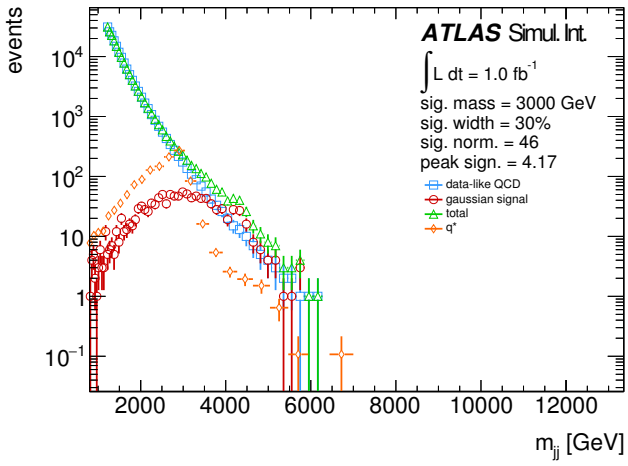

(d) 3 TeV gaussian, 30% width.

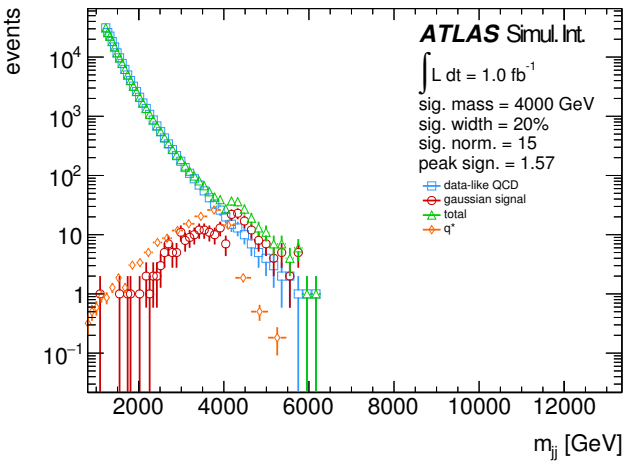

(e) 4 TeV gaussian, 20% width.

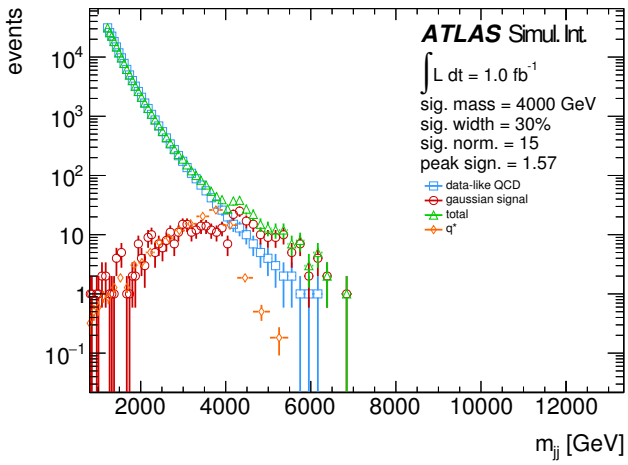

(f) 4 TeV gaussian, 30% width.

Figure 6.21: injection of gaussian signals into a background generated from a four parameter fit of the PYTHIA MC distribution. Gaussian signal masses are 2, 3 and 4 TeV and their widths are 20% and 30%. For each gaussian, the q^* signal of equal mass is also plotted for comparison. The equivalent integrated luminosity is 1 fb^{-1}.

signal mass [GeV]	s	b	s/b
400	615 797	56 345 975	0.0109
600	35 446	12 944 776	0.0028
800	7655	2 272 363	0.0034
1000	3496	577 622	0.0061
1200	1457	253 953	0.0057
1400	984	85 507	0.012
1600	677	37 252	0.018
1800	441	15 952	0.028
2000	276	9004	0.031
2200	265	3717	0.071
2400	189	1929	0.098
2600	116	1563	0.074
2800	77	534	0.14
3000	43	208	0.21
3200	26	226	0.12
3400	18	100	0.18
3600	14	79	0.18
3800	15	38	0.39
4000	13	12	1.08
4200	10	23	0.43
4400	9	12	0.75
4600	6	2	3.00

Table 6.12: minimum signal normalisation of Breit-Wigner signals for the BumpHunter to be sensitive. s is the number of events in the central 68% m_{jj} window of the signal, while b is the number of background events in that same region.

distributions with signals injected, it is possible to observe how the choice of the fit function affects the signal identification and how the signal biases the background fit. The results obtained are shown in Figures 6.23-6.28 for the gaussian signals and in Figures 6.29 and 6.30 for the excited quarks. These plots show a complete picture of the effects that signals have on the background fitting procedure. Each one of the results shown in Figures 6.23-6.30 corresponds to a given combinations of signal model, mass, width and fit function and it is organised in four panels. The bottom three panels show the significance of the background fits residuals for just as many different signal normalisations: the bottom panel is a background-only fit, the second from the bottom has a signal just above the BumpHunter threshold and the third from the bottom has a signal just below the threshold. The vertical lines shown in these three panels delimit the most discrepant region identified by the BumpHunter. These lines are blue if the region has not been removed for the fit, meaning that the p-value is above the 0.01 threshold, while they are green if the p-value is small enough to trigger the window exclusion from the fit. The top panel shows the ratios of the background fit functions from the bottom three panels. The

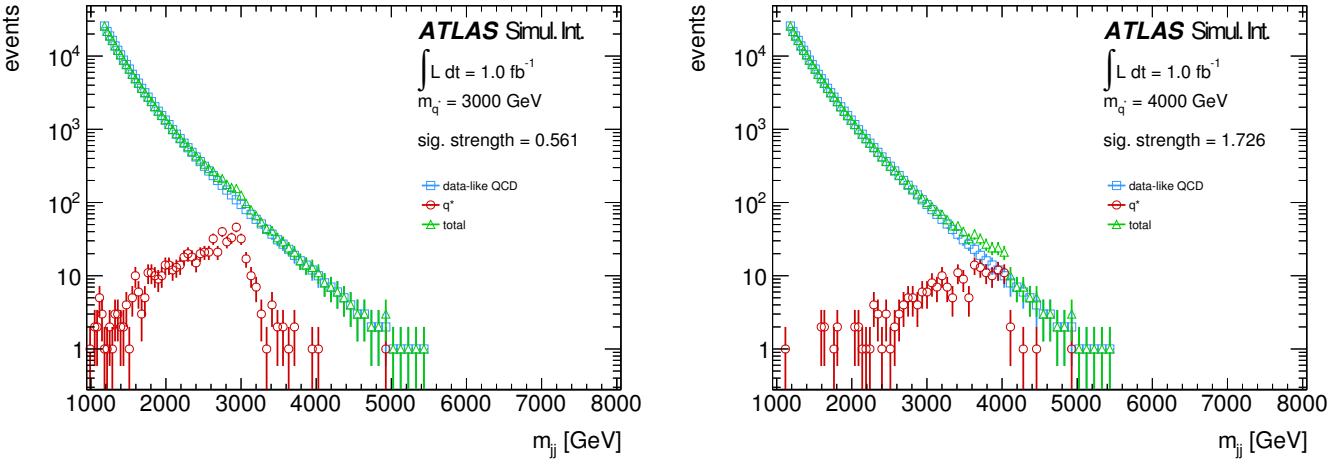

(a) 3 TeV q^*.

(b) 4 TeV q^*.

Figure 6.22: injection of 3 TeV and 4 TeV excited quarks into a background generated from a four parameter fit of the PYTHIA MC distribution. The equivalent integrated luminosity is 1 fb^{-1}.

blue line is the ratio between the background-only fit and the fit where the signal window is still included, giving the fit its maximum bias. This blue line is expected to be the one that is most far from being flat and it is equivalent to the 8 TeV studies presented in Section 6.11.1. The green line is the ratio between the background-only fit and the fit where the signal window is excluded. A flat green line means the signal has been successfully identified and its bias to the fit has been completely removed. The red line is the ratio of the fits performed with and without the signal window being excluded. This line shows how much the fit changes just from excluding the signal window (remember that the tuning of the signal is very close for the two situations). This study was performed before the extension of the signal exclusion window by one bin on the low mass side was adopted (see Section 6.10.1). The resulting message would not change, but the residual plots after a signal is removed would be a bit smoother. It is possible to notice how the three parameter fit function does a good job at fitting the background distribution, identifying the signal at strength values that are lower than the other options. The exclusion of the signal region is also more efficient, as it can be seen from the flatter green lines of the top panel, especially for signals that have relatively small masses. On the other hand, the four and five parameter fit functions tend to accommodate the signals into their shape, as it can be told from the shape of the blue and green lines of the top panels. This is directly reflected in the signal normalisation, since more events are systematically required to reach the BUMPHUNTER p-value threshold than the three parameter fit function. Overall, the behaviour of the four parameter fit function is in between that of the other two options: behaving like the five parameter fit function when small signals are injected in the bulk of the m_{jj} distribution and like the three parameter fit function when large signals are

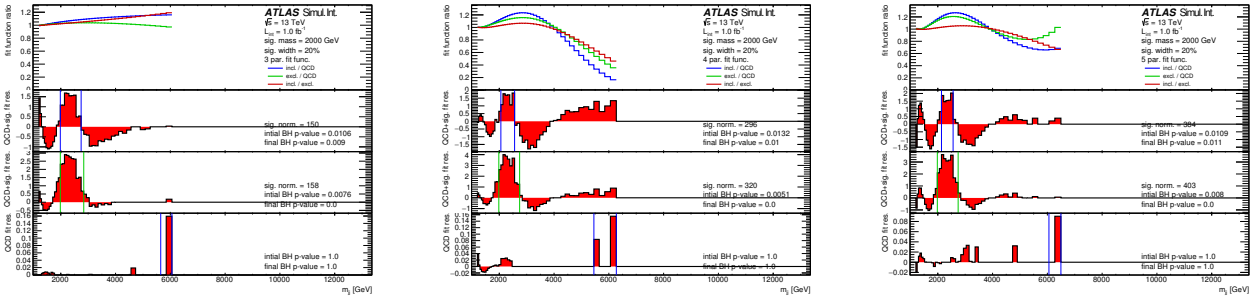

(a) 3 parameter fit function. (b) 4 parameter fit function. (c) 5 parameter fit function.

Figure 6.23: 2 TeV gaussian, 20% width, 1 fb^{-1}.

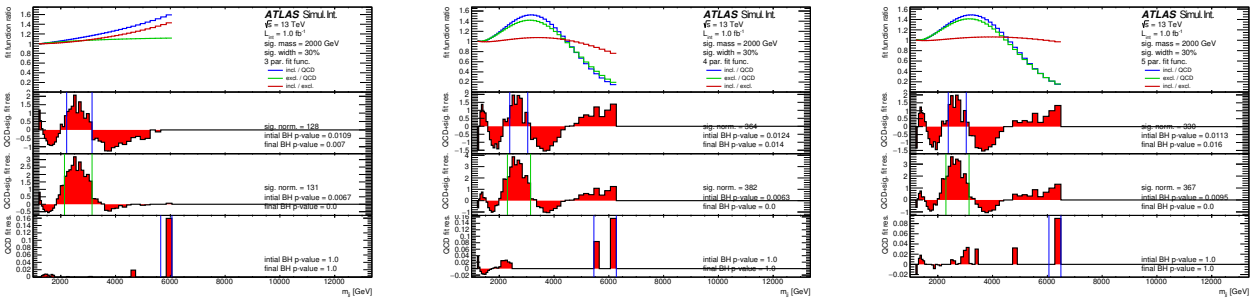

(a) 3 parameter fit function. (b) 4 parameter fit function. (c) 5 parameter fit function.

Figure 6.24: 2 TeV gaussian, 30% width, 1 fb^{-1}.

injected in the tails.

To asess the interplay between the fit function choice and the signal strength necessary to exclude the signal window, dedicated studies have been performed and are presented in Section 6.11.2.

Fit Function Choice In Presence Of A Signal

Since the fit function choice is based on the p-value of the likelihood ratio between a baseline function and an alternative with a higher number of parameters, the presence of a signal may affect this choice and requires a dedicated study.

As it was just observed in Section 6.11.2, fit functions with less parameters require fewer signal events to identify a significantly discrepant region, while fit functions with more parameters tend to accommodate possible discrepancies in their shape, therefore hiding bumps until the integrated luminosity is much larger. Such test can be performed similarly to what has been done in Section 6.11.2, with the addition of performing the fit with the baseline and an alternative fit functions. The tuning of the signal strength, in order to be on the BumpHunter threshold, is based on the performance of the baseline function but the BumpHunter is then run using both functions. The results can therefore

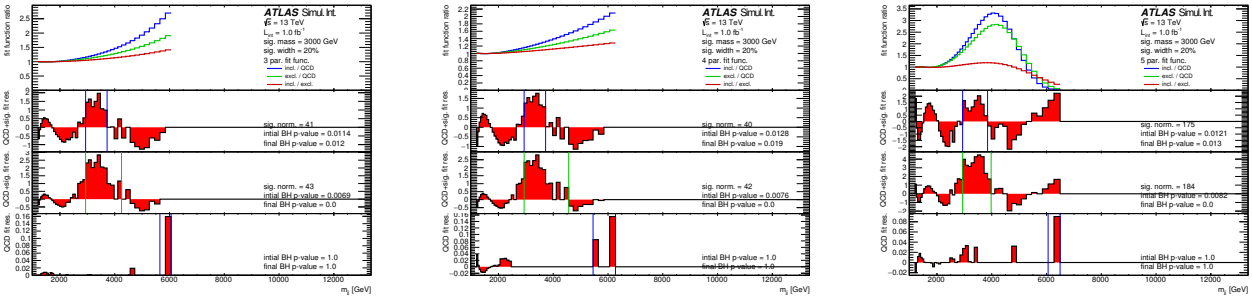

(a) 3 parameter fit function. (b) 4 parameter fit function. (c) 5 parameter fit function.

Figure 6.25: 3 TeV gaussian, 20% width, 1 fb^{-1}.

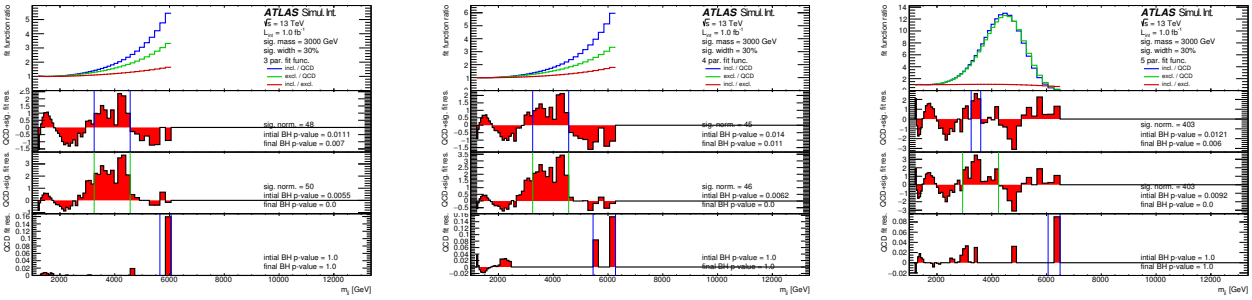

(a) 3 parameter fit function. (b) 4 parameter fit function. (c) 5 parameter fit function.

Figure 6.26: 3 TeV gaussian, 30% width, 1 fb^{-1}.

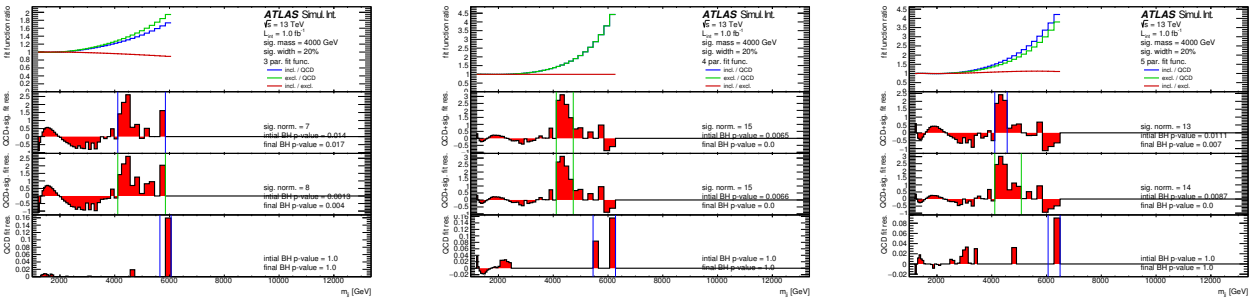

(a) 3 parameter fit function. (b) 4 parameter fit function. (c) 5 parameter fit function.

Figure 6.27: 4 TeV gaussian, 20% width, 1 fb^{-1}.

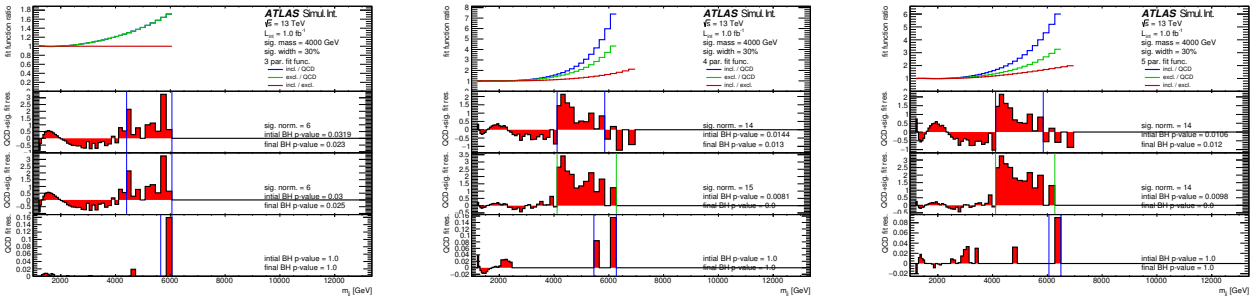

(a) 3 parameter fit function. (b) 4 parameter fit function. (c) 5 parameter fit function.

Figure 6.28: 4 TeV gaussian, 30% width, 1 fb^{-1}.

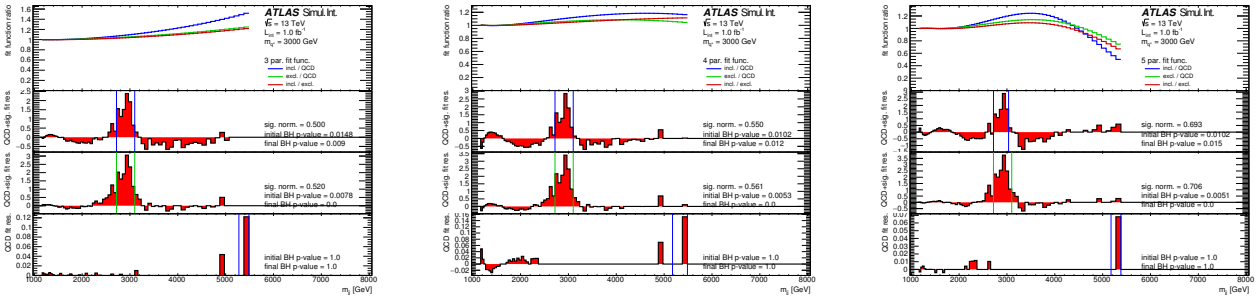

(a) 3 parameter fit function. (b) 4 parameter fit function. (c) 5 parameter fit function.

Figure 6.29: 3 TeV excited quark, 1 fb^{-1}.

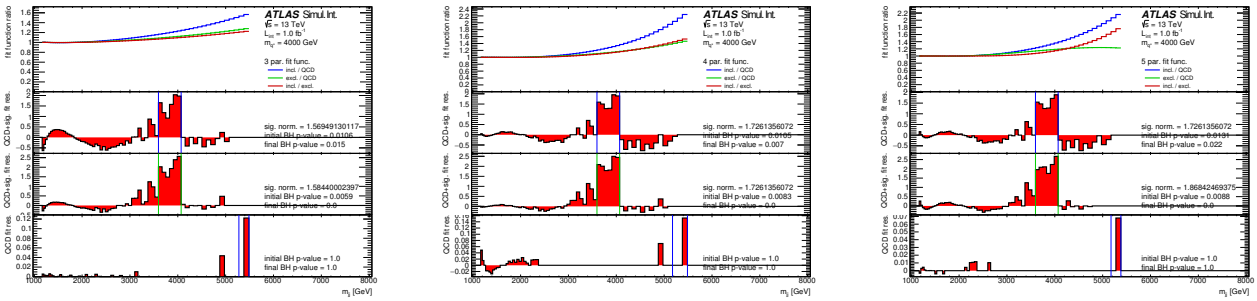

(a) 3 parameter fit function. (b) 4 parameter fit function. (c) 5 parameter fit function.

Figure 6.30: 4 TeV excited quark, 1 fb^{-1}.

be directly compared, showing if a function would exclude the signal window before the other. At the same time, the p-value of their likelihood ratio will tell whether one or the other function should be used to describe the background. The test has been performed using pseudo-data generated from PYTHIA MC distributions, both in the scenario without any Poisson fluctuation applied, to remove possible random effects, and with Poisson-fluctuated distributions. Results have been observed to be compatible and only those obtained from non-fluctuated distributions are reported here. The signals employed are excited quarks with tuned signal strength. Results are shown in Figures 6.31-6.33.

Following the structure of the plots featured in Section 6.11.2, the bottom three panels show the significance of the background fits residuals, each time for the baseline and the alternative fit functions considered. The bottom panel is background-only, the second panel from the bottom has the signal just below the BUMPHUNTER threshold and he third one from the bottom has the signal just above the threshold. In each scenario, the signal strength tuning is performed using the baseline fit function. The significance of the fit residuals for the baseline function is shown in red, while that of the alternative function is shown in orange. The dark blue and dark green vertical lines identify the BUMPHUNTER regions that have p-values right above and right below the threshold, respectively, for the baseline fit function. Similarly, for the alternative function, the vertical lines are shown in light blue and light green. The signal strength and the likelihood ratio p-value obtained using Wilks' theorem are reported in each panel. The top panel shows the ratios of the baseline and alternative fit functions in cyan as taken from the third panel. The red and orange lines are the ratios of the baseline and alternative fit functions from the third panel over over their fit to the QCD background in the fourth panel.

Results from Figure 6.31a, where a 2 TeV excited quark is injected, show a Wilks' p-value of 0.016 when comparing the three parameter fit function with signal window removed and the four parameter function fit with no windows removed. This indicates that it is indeed possible, in some circumstances, for the likelihood ratio p-value to suggest the use of the alternative function, with a higher number of parameters, while at the same time the baseline function is capable of identifying the presence of a significant bump ($p\text{-value}_{\text{BUMPHUNTER}} \simeq 0.0$). Similarly, this happens also in Figure 6.32a ($p\text{-value}_{\text{Wilks}} = 0.040$) and almost in Figure 6.32a ($p\text{-value}_{\text{Wilks}} = 0.052$), where 3 and 4 TeV excited quarks are injected. On the other hand, when the four parameter fit function is set as the baseline, the three parameter fit function often identifies the signal window when its counterpart does not. See Figures 6.32b and 6.33b for reference. In this cases Wilks' p-value (respectively 0.035 and 0.038 in the two examples taken) even suggests to switch back to use the three parameters fit function as baseline.

All in all, the results of these studies show that fit functions with higher number of parameters can accommodate small signals and still give better results than a fit function with less parameters where the signal window has been removed. In extreme circumstances, this can lead to a change of fit function, whereas the baseline function would have led to the identification of a bump with a non-negligible BUMPHUNTER p-value. For this reason, the dijet analysis results will always provide a conservative estimation of the contribution from new physics phenomena to the SM. Until now, the BUMPHUNTER p-values

obtained from data distributions have never gone below the 0.01 threshold and the Wilks' p-value has never suggested that a switch from the three to the four parameter fit function was necessary.

JES Variations

The robustness of the fitting procedure has been tested also against the JES variations given by its nuisance parameters (see Section 4.3.8). The test has been performed by running the search phase, using the three, four and five parameter fit functions, on PYTHIA MC data-like distributions, corresponding to an integrated luminosity of 1 fb^{-1}, where the JES nuisance parameters have been iteratively scaled up and down by one sigma. No significantly discrepant regions have been identified and the BUMPHUNTER p-value has been measured to be always greater than 0.5.

Mixed Quark And Gluon Components

Further studies have addresses the stability of the fit in case of a mismodeling of the quark and gluon jet contributions in the MC m_{jj} spectrum. These studies have been realised by separating the qq, qg, gq and gg dijet final states[7] (as shown in Figure 6.34) and by performing the search on 1 fb^{-1} of data-like distributions where one of the components has been doubled in normalisation. Results show good fit performance in all cases and no significant bump is identified with BUMPHUNTER p-value above 0.25.

6.12 Systematic Uncertainties

The systematic uncertainties affecting the limit setting on benchmark models with dijet the final states are described in this section. Note that no uncertainties are considered on the signal cross section.

6.12.1 Fit Quality

The uncertainty on the quality of the fit of the dijet background distribution is computed by means of fits of pseudo-experiments thrown from the nominal fit to the data. For each bin of the distribution, the 1σ uncertainty is defined as the RMS of the values that the fit takes in all the pseudo-experiments. A nuisance parameter, θ, is associated to the fit uncertainty that lets the background content vary between -3σ and $+3\sigma$. The size of the fit uncertainty is shown in Figure 6.35 alongside with the fit function choice uncertainty.

6.12.2 Fit Function Choice

The fit function choice uncertainty has been introduced since the 8 TeV dijet analysis with the full statistic [11] to account for the fit difference between the chosen function

[7] These are the truth flavours of the leading and subleading partons respectively.

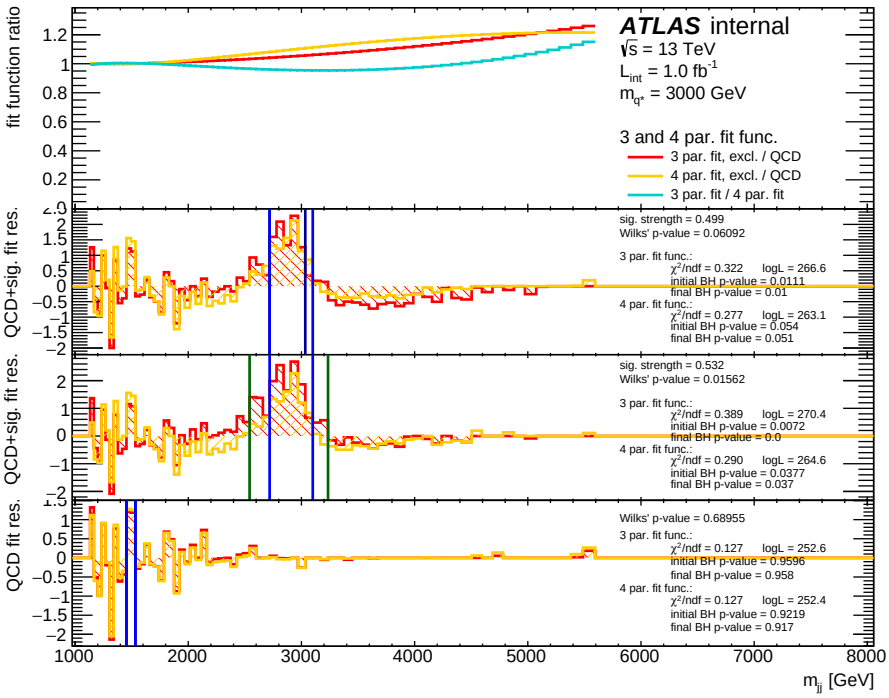

(a) baseline function: 3 parameters; alternative function: 4 parameters.

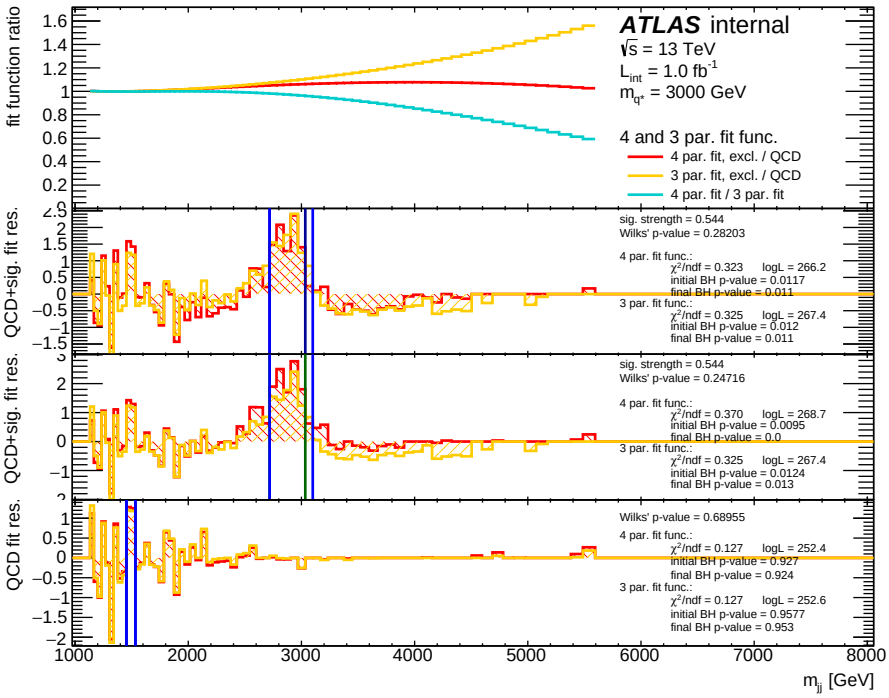

(b) baseline function: 4 parameters; alternative function: 3 parameters.

Figure 6.31: fit function choice studies in presence of an injected signal. The three (a) and the four (b) parameter fit functions are alternatively used as baseline functions. A 3 TeV excited quark is used as benchmark model. The equivalent integrated luminosity is 1 fb^{-1}. See Section 6.11.2 for more details.

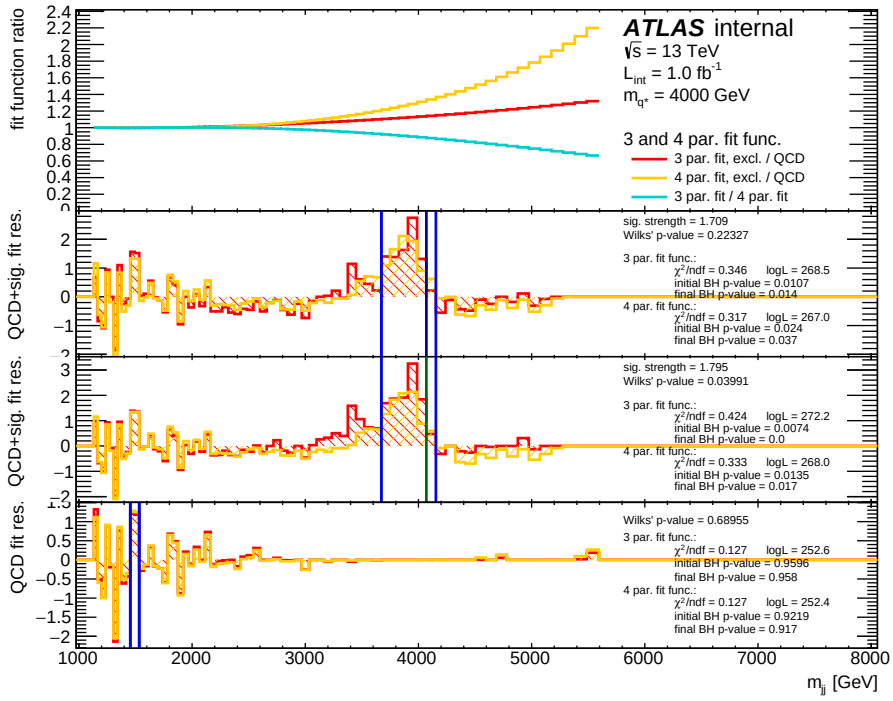

(a) baseline function: 3 parameters; alternative function: 4 parameters.

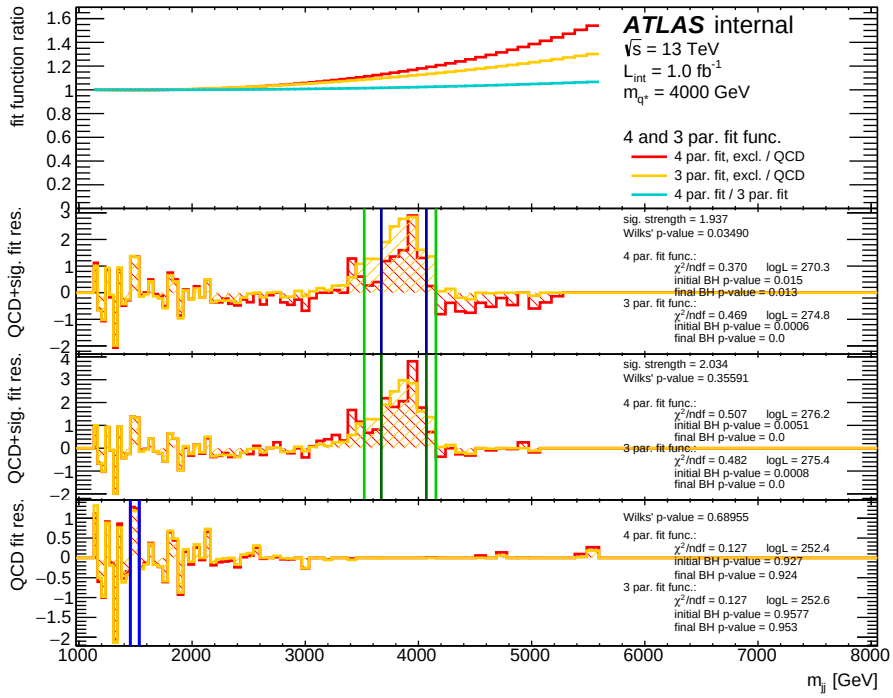

(b) baseline function: 4 parameters; alternative function: 3 parameters.

Figure 6.32: fit function choice studies in presence of an injected signal. The three (a) and the four (b) parameter fit functions are alternatively used as baseline functions. A 4 TeV excited quark is used as benchmark model. The equivalent integrated luminosity is 1 fb^{-1}. See Section 6.11.2 for more details.

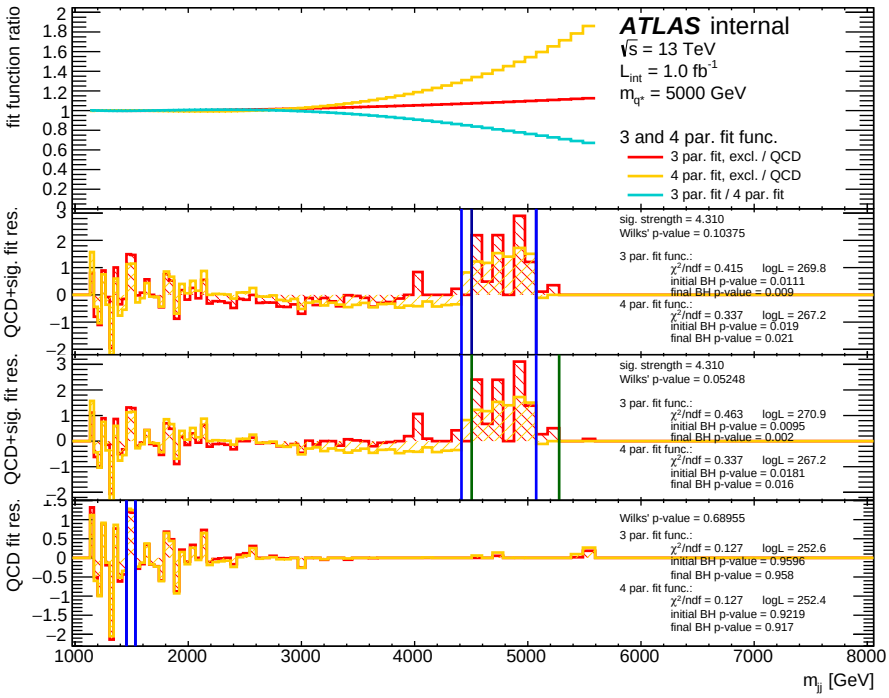

(a) baseline function: 3 parameters; alternative function: 4 parameters.

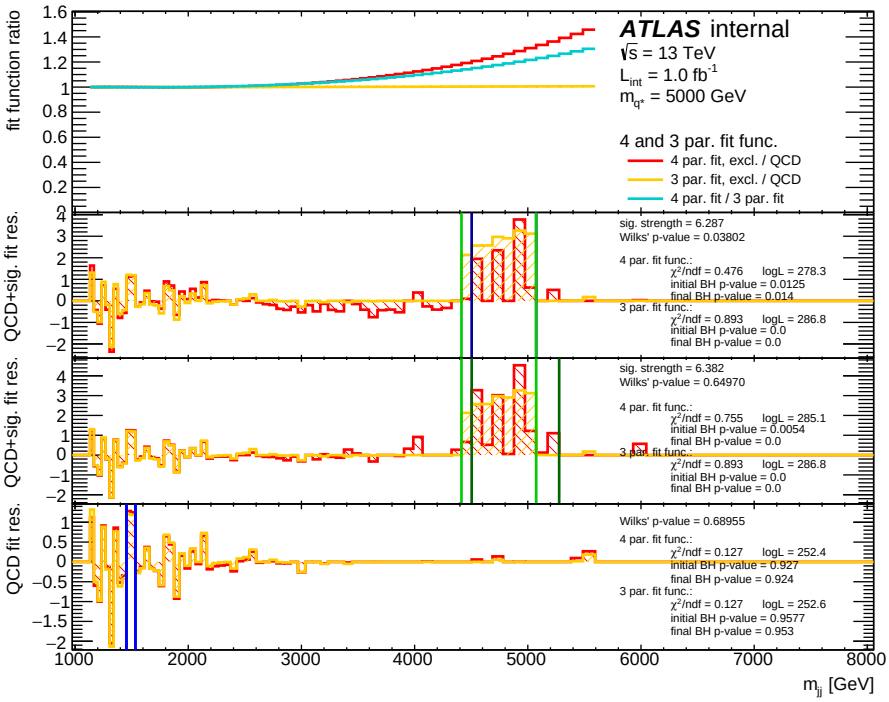

(b) baseline function: 4 parameters; alternative function: 3 parameters.

Figure 6.33: fit function choice studies in presence of an injected signal. The three (a) and the four (b) parameter fit functions are alternatively used as baseline functions. A 5 TeV excited quark is used as benchmark model. The equivalent integrated luminosity is 1 fb^{-1}. See Section 6.11.2 for more details.

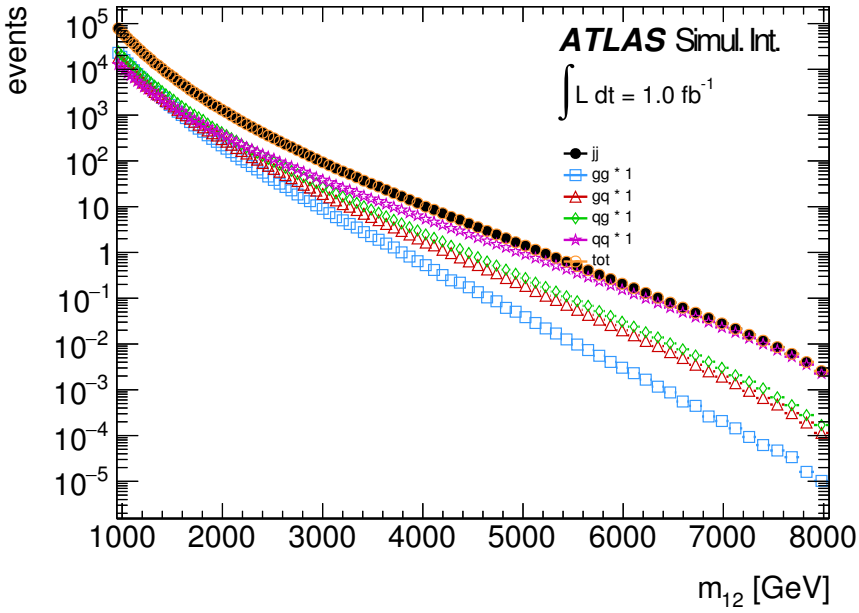

Figure 6.34: breakdown of the MC dijet invariant mass distribution into the qq, qg, gq and gg components. The equivalent integrated luminosity is 1 fb^{-1}.

and a valid, alternative function, as described in Section 6.9.1. The uncertainty is taken, bin by bin, as the difference between the nominal fit and the alternative fit of the data distribution. The prior distribution of the nuisance parameter is a gaussian centered at zero and with unit width. The allowed range is $\theta \in [0, 1]$, where zero corresponds to the nominal fit and one corresponds to the alternative fit. With this choice, the nominal fit is only slightly favoured with respect to the alternative. The size of the fit function choice uncertainty is shown in Figure 6.35.

6.12.3 Luminosity

The uncertainty on the integrated luminosity is 2.8% for the 8 TeV analysis and 9% for the 13 TeV analysis. The associated nuisance parameter follows a gaussian distribution and can vary in the range $\theta \in [-3\sigma, +3\sigma]$.

6.12.4 JES

The uncertainties on the Jet Energy Scale have been introduced in Section 4.3.8. The effects of the JES uncertainties on the dijet analysis have been estimated using a reduced set of nuisance parameters. For each of the 23 reduced nuisances available in Run-1, the effect on the analysis has been derived independently. All the parameters that gave a variation of less than 2% to the signal distributions have been merged in a single contribution while the rest have been treated independently. In Run-2, a reduced set of three nuisance

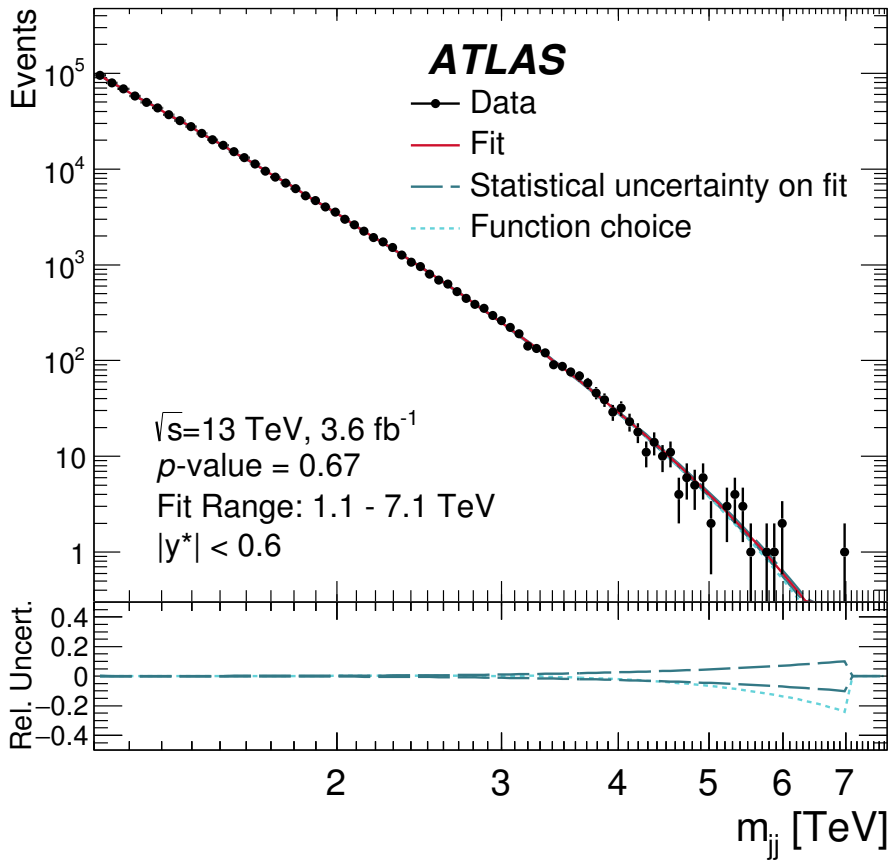

Figure 6.35: fit function uncertainty and fit function choice uncertainty for the 13 TeV analysis [12].

parameters (provided centrally by the jet/$E_{\mathrm{T}}^{\mathrm{miss}}$ group and proven to retain most of the un-correlated uncertainty information [61]) has been used without any further merging. Within the JES uncertainty components, that associated to the single particle response gives the highest contribution for high-p_{T} jets. Priors are given a gaussian distribution and nuisance parameters are varied within the $\theta \in [-3\sigma, +3\sigma]$ range.

Concerning the limit setting on generic signal shapes (see Section 6.13.5), since no actual decay to jets is simulated, the full JES systematic uncertainties do not apply. Instead, a single systematic uncertainty capable of shifting the signal peak by 3% for a 1σ deviation is considered. This effect has been evaluated from the propagation of the JES systematics in fully-simulated MC signal samples.

6.12.5 JER

The uncertainty given by the Jet Energy Resolution, JER, has been evaluated by smearing the jet energy and p_{T} by the resolution. No significant deviation has been identified with respect to the nominal m_{jj} distribution. For this reason, the effects of the JER are considered negligible and no uncertainty is applied.

6.12.6 JAR

The Jet Angular Resolution (see chapter 5) has been used to smear the jets' η and ϕ. No significant difference has been observed between the nominal m_{jj} and the smeared distribution. The JAR uncertainty is therefore considered as negligible and is not applied.

6.12.7 PDF

The effects of the PDF uncertainties have been estimated by reweighting the signal samples to the MSTW2008LO and NNPDF2.1LO PDF sets. The envelope obtained is taken as the 1σ uncertainty around the nominal distribution.

The PDF uncertainty has a twofold effect: it can change the shape of the signal and change its acceptance. Since the shape-changing uncertainty obtained from reweighting a signal from one set of PDFs to another can lead to unphysical results, where the original signal shape is significantly altered, it was decided not to include this as an uncertainty. As a consequence, only the scaling effects on the signal acceptance are considered, which may reach as high as 2%. The associated nuisance parameter is given a gaussian prior in the $\theta \in [-3\sigma, +3\sigma]$ range.

6.12.8 Factorisation And Renormalisation Scales

The factorisation and renormalisation scales adopted for the signals generation have been set at the signal mass value (see Section 3.3). However, the use of different values may lead to rather different cross sections. To test the uncertainty introduced by this choice, samples have been produced with twice as large and twice as small renormalisation scale, while the factorisation scale has been weighted by factors of 0.5 and 2. No effects above

2% have been observed in the signal shape nor acceptance. Therefore, no scale uncertainty is considered.

6.12.9 Beam Energy

The effects of the uncertainty on the beam energy are probed by reweighting the beam energy up and down by 1σ. The envelope given by these two variations is taken as the uncertainty. This uncertainty affects both the signal shape and acceptance and it is also reported around the theoretical cross section curves in the 8 TeV limit plots (see Section 6.2.3). The nuisance parameter prior is chosen to be gaussian within the $\theta \in [-3\sigma, +3\sigma]$ range.

6.13 Limit Setting

In case no significant local excess are identified by the BumpHunter in the search phase, limits are set on benchmark signal models. The procedure works by finding how many signal events can be fitted within the data distribution while still providing a good description of the observation. For this purpose, the Bayesian method is adopted to compute the posterior probability of the signals as a function of their signal strength. For each of the signal mass points considered, the 95% quantile of such distribution is taken as the upper limit on the number of signal events that may be contained in the data distribution. This number, divided by the integrated luminosity of the data, gives the 95% Credibility Level, CL, value on the signal cross section times acceptance, $\sigma \times A$. By comparing this measured $\sigma \times A$ value with the theoretical value, it is possible to tell whether it is below the expectation and can thus be excluded.

The limit setting is common to the 8 TeV and 13 TeV exotic dijet analyses and their results are reported in Section 6.14.

6.13.1 Bayesian Method

The bayesian method has been chosen for the limit setting as it directly addresses the question on what is the probability of a given signal model given the data observed, which is the question we ultimately want to answer. The frequentist method, on the other hand, focuses on the probability of the data observed given the models considered. Both methods can be exploited to set limits but the bayesian method gives a better handling on the systematic uncertainties, since it integrates over the possible different models and nuisance parameters, at the cost of a more computational-expensive procedure [127]. Last but not least, the bayesian method provides probabilities on models, unlike the frequentist method. While the frequentist method proceeds by maximising a likelihood function over the parameter space, the bayesian method integrates over the nuisance parameters to return the probability density distribution, PDF, of the signal strength. From this PDF, the 95% quantile can be taken as the upper limit defining the 95% credible interval. The bayesian method is sometime criticised because of the use of prior probabilities, $\pi(H)$, representing the degree of belief on an hypothesis, H, to express the posterior probability

on that same hypothesis given the observation, $P(H|x)$. This may be regarded as a lack of objectivity, however there are standards in the choice of reasonable priors to limit such possibility. Moreover, it is observed that the choice of priors can be irrelevant if data strongly supports the parameters values in a different way.

Bayes' theorem can be used to compute the posterior probability of a given hypothesis given the data observed, $P(H|x)$:

$$P(H|x) = \frac{P(x|H)P(H)}{P(x)} \tag{6.45}$$

where $P(x|H)$ is the probability of data x given the hypothesis H. Similarly to the frequentist approach, this probability can be described by the likelihood of the hypothesis H given x: $L(H|x)$. $P(H)$ is the prior knowledge on the hypothesis before the analysis is performed: $\pi(H)$. $P(x)$ is a normalisation factor, which can be expressed as the intergal of the numerator over all the hypothesis considered. Therefore, Equation 6.45 becomes:

$$P(H|x) = \frac{L(H|x)\pi(H)}{\int L(H|x)\pi(H)dH} \tag{6.46}$$

In general, the hypothesis under test can be expressed in terms of a parameter of interest, μ, whose PDF we want to measure, and a set of nuisance parameters, $\boldsymbol{\theta}$, whose values affect the results but are not of interest. In the specific case of the dijet resonance analysis, μ represents the strength of the benchmark signal while $\boldsymbol{\theta}$ are the parameters describing the systematic uncertainties. Dropping the normalisation factor at denominator for the time being, Equation 6.46 can be written as:

$$P(\mu, \boldsymbol{\theta}|x) \propto L(\mu, \boldsymbol{\theta}|x)\pi(\mu, \boldsymbol{\theta}) \tag{6.47}$$

Since the interest is on the posterior probability distribution function of the signal strength, the dependence of Equation 6.47 on the nuisance parmaters can be integrated out, or *marginalised*. Also, the prior on the signal strength and the nuisance parameters can be factorised, since they are independent in most of the scenarios. Therefore:

$$P(\mu|x) \propto \int L(\mu, \boldsymbol{\theta}|x)\pi(\mu)\pi(\boldsymbol{\theta})d\boldsymbol{\theta} \tag{6.48}$$

The calculation of the posterior probability of the signal strength given the data requires the integration of the likelihood and priors over the phase space of the nuisance parameters. This is achieved by means of Markov Chain Monte Carlo, MCMC, which performs a numerical integration by using μ values extracted from an approximate distribution that is updated at every iteration, allowing a fast iteration and a good sampling of the most relevant regions of the nuisance parameters phase space. The MCMC employed is implemented within the Bayesian Analysis Toolkit, BAT, package [128]. This implementation takes in input the prior distributions of the signal strength and nuisance parameters and returns the posterior for each of the parameters marginalised with respect to all the other parameters. One of the challenging aspects ot the limit setting is the inclusion of the systematics in the marginalisation process.

6.13.2 Priors

Bayesian priors can be differentiated into *informative* and *non-informative*. As the name suggests, informative priors provide some degree of information on the parameter, such as that coming from previous studies. On the other hand, non-informative priors are free from any constraint and can be regarded as being as objective as possible. In this case, no bias is introduced in the posterior probability calculation, since it is entirely driven by the data.

For the dijet resonance analysis, a flat, non-informative prior, has been chosen for the signal strength, allowing a more direct interpretation of the results. The range of the prior on the signal strength has been chosen so that the likelihood for the maximum signal strength considered, μ_{Max}, is 10^5 times smaller than that of the maximum likelihood:

$$\pi(\mu) = \begin{cases} \frac{1}{\mu_{\text{Max}}} & x \in [0, \mu_{\text{Max}}] \\ 0 & \text{otherwise} \end{cases} \tag{6.49}$$

where:

$$L(\mu_{\text{Max}}|x) = 10^{-5} L(\hat{\mu}|x) \tag{6.50}$$

Gaussian priors have been chosen instead for all the nuisance parameters.

6.13.3 Inclusion Of Systematic Uncertainties

Systematics uncertainties affect the nominal shapes of the benchmark signals and of the background distributions. During the marginalisation process of the nuisance parameters that govern the systematic uncertainties, the phase space of such parameters is explored and the likelihood of the comparison between the data on one side and the background and signal on the other is computed. It is therefore necessary to reproduce all the signal and background MC distributions for each set of nuisance parameters. Performing the whole analysis procedure for each iteration of the marginalisation is the most accurate way to go, however, it is time consuming and impractical. Instead, systematic uncertainties have been grouped by the effects they produce, sampled over discrete steps of their nuisance parameters, linearly interpolated and applied to the signal and background distributions separately. The order in which the systematics are applied is dictated by their effects, so that their implementation returns a sensible final result.

Template Systematics

Systematics that have bin-wise effects are applied for first. Template distributions are sampled in steps of 0.5σ around the nominal value of the nuisance parameter. The correction applied to a bin with content b for a given nuisance parameter value, θ, is given by a linear combination of the two closest templates sampled, $b_{\theta_\pm}$:

$$b_{\text{corr}}(\theta) = b_{\theta^-} + \frac{b_{\theta_+} - b_{\theta_-}}{\theta_+ - \theta_-}(\theta - \theta_-) \quad \text{for } \theta_+ < \theta < \theta_- \tag{6.51}$$

where θ_+ and θ_- are the closest sampled values to θ. The total correction from all the template systematics applied to the nominal bin content is computed as the sum of all the corresponding template corrections from Equation 6.51:

$$b_f = b + \sum_i b^i_{\text{corr}} \tag{6.52}$$

To this group of systematics belong the fit quality, the fit function choice and the beam energy.

Migration Systematics

Second in line are the systematics whose effects cause the migration of entries from one bin to another. Similarly for what is done for the template systematics, transfer matrices, M, are sampled in steps of of 0.5σ around the nominal value of the nuisance parameter. The correction applied to the nominal distribution for a given nuisance parameter value, θ, is given by a linear combination of the two closest transfer matrices sampled, $M_{\theta_\pm}$:

$$M(\theta) = M_{\theta^-} + \frac{M_{\theta_+} - M_{\theta_-}}{\theta_+ - \theta_-}(\theta - \theta_-) \quad \text{for } \theta_+ < \theta < \theta_- \tag{6.53}$$

where θ_+ and θ_- are the closest sampled values to θ. The total correction from all the migration systematics applied to the nominal distribution is computed as the product of all the corresponding transfer matrices from Equation 6.53:

$$\boldsymbol{b}_f = \prod_i M_i \boldsymbol{b} \tag{6.54}$$

For this method to work, it is necessary for the matrices to commute or the correction would not be invariant under permutation of the transfer matrices. This group of systematics gathers all JES systematics.

Scale Systematics

The last set of systematics to be applied is yet the simplest. The scale systematics, in fact, simply scale the whole distribution by a factor, f, with no dependencies on the m_{jj} bin. The implementation of the correction is quite straightforward:

$$\boldsymbol{b}_f = \prod_i f_i \boldsymbol{b} \tag{6.55}$$

Luminosity and PDF scale uncertainties belong to this family of systematics.

By taking as an example the distribution of a benchmark signal, it is now clear that the template and the migration systematics do not commute. In fact, the first systematics applies a correction bin by bin, effectively changing the shape of the signal. The second systematic, on the other hand, moves entries from one bin to the other, therefore moving the signal along the distribution. Once all three families of systematics are applied, the distributions are employed for the likelihood computation entering Equation 6.48.

6.13.4 Expected Limits

Expected limits are computed from pseudo-experiments generated from the background only hypothesis. A total of one hundred pseudo-experiments is thrown for every signal mass point considered and the limits setting procedure is iterated on each one of these. The 95% quantile distribution for the signal strength is measured. Its mean and sigma values are then extrapolated to produce the expected limit curve together with its one and two sigma bands. As for the observed limits, the expected limit curve is generated by interpolating its points with an exponential curve. The use of an expected limit curve gives a visual and better grasp on the observed limits, as it highlights any discrepancy between the two that may be due to effects of new physics that have not yet produced BumpHunter p-values particularly extreme[8].

6.13.5 Model-Independent Limits

Beside the benchmark models presented in Section 6.3.3, limits are also provided using generic signal shapes, providing a direct way to reinterpret the results obtained using additional theories. The limit setting procedure is maintained the same as that for the Mc benchmark signals. The only difference is that, being these limits model-independent, the results are expressed in terms of $\sigma \times A \times \text{Br}$, therefore the Branching Ratio, Br, needs to be taken into account when interpreting the results for a new physics model. The uncertainties taken into account are reduced to the fit uncertainty, the fit function choice, a simplified Jes and the luminosity.

Limits on new signal models can be set starting from model-independent limit curves using the following steps[11].

1. Given a signal with mass m, compute the branching ratio into jets in the final state. Then apply analysis kinematic cuts, such as: η, p_{T} and y^*.
2. Smear the signal according to the detector mass resolution in that region of the spectrum.
3. Remove the signal tails by selecting the mass region $0.8m < m < 1.2m$.
4. The fraction of events surviving the previous steps, defines the signal acceptance, A.
5. Select from the model-independent limit curve the mass point that is closest to that of the signal in consideration and is most conservative
6. Select from the model-independent limit curve the closest $\frac{\sigma_G}{m_G}$ value to that of the signal and is most conservative.
7. Compare the signal $\sigma \times A \times \text{Br}$ to the selected point in the model-independent limit curve.

Two families of generic signals have been considered: gaussians and Breit-Wigner.

[8]Remember that limits are set at the 95% quantile ($\sim 2\sigma$), while a discovery is claimed for p-values corresponding to 5σ or more.

Gaussian Limits

The simplest of the signals considered is given by gaussian distributions. This assumes a generic signal to have gaussian-like shape after the event selection and kinematic cuts have been applied. A series of gaussian signals have been distributed in the range between 200 GeV and 4 TeV, with width-to-mass ratios, $\frac{\sigma_G}{m_G}$, of 7%, 10% and 15%. $\frac{\sigma_G}{m_G}$ values equal to the detector dijet mass resolution have also been used to estimate the best limits available. This values are the same used for the definition of the dijet mass binning described in Section 6.7. The signal tails are trimmed so to retain only the 95% core and no statistical fluctuations are applied. Limits are set for gaussian signals that are at least 2σ away from either edge of the m_{jj} distribution, not to bias the background fit in this sensitive regions.

Breit-Wigner Limits

Sometime, the gaussian limits can be too simplistic to set limits on new models, especially when PDF effects play a significant role in the shaping of the signal. For this reason, model-independent limits are set using also Breit-Wigner signals convoluted with PDF effects, which enhance the lower mass tail of the signal and suppress those at larger values. The intrinsic widths of the Breit-Wigner signals employed range from 0.5% to 3%, as some of the signals considered for the model-dependent limits. As shown in Equation 6.9, the momentum fractions carried by the colliding partons determine the rapidity boost of their products, affecting the acceptance of the signal. This is considered in the implementation of the generic signals through an acceptance weight curve defined as a function of the mass of the resonance. Finally, the signal is convoluted with the detector dijet mass resolution curve. Examples of Breit-Wigner samples convoluted with PDF, acceptance and detector resolution are shown in Figure 6.36 for 8 TeV *pp* collisions. The signal obtained are then used similarly to their gaussian counterparts to set generic $\sigma \times A \times \mathrm{Br}$ limits.

6.14 Results

The results obtained in the 8 TeV Run-1 and the 13 TeV Run-2 exotic dijet analyses are presented below.

6.14.1 Search Phase

The results of the search phase, as described in Section 6.2.2, are shown in Figure 6.37 for the 8 TeV dijet analysis performed on 20.3 fb^{-1} of data and for the 13 TeV dijet analysis performed on 3.6 fb^{-1}. No evidence of significant localised excesses have been identified in either of the 8 TeV and 13 TeV dijet invariant mass distributions.

As mentioned in Section 6.9.1, the quality of the fit of the 8 TeV spectrum is poor and it can be observed in the bottom panel of Figure 6.37a. Here the significance of the discrepancy between the data and the fit is shown and an oscillating behaviour can be identified, indicating that the number of parameters of the fit function, four in this case,

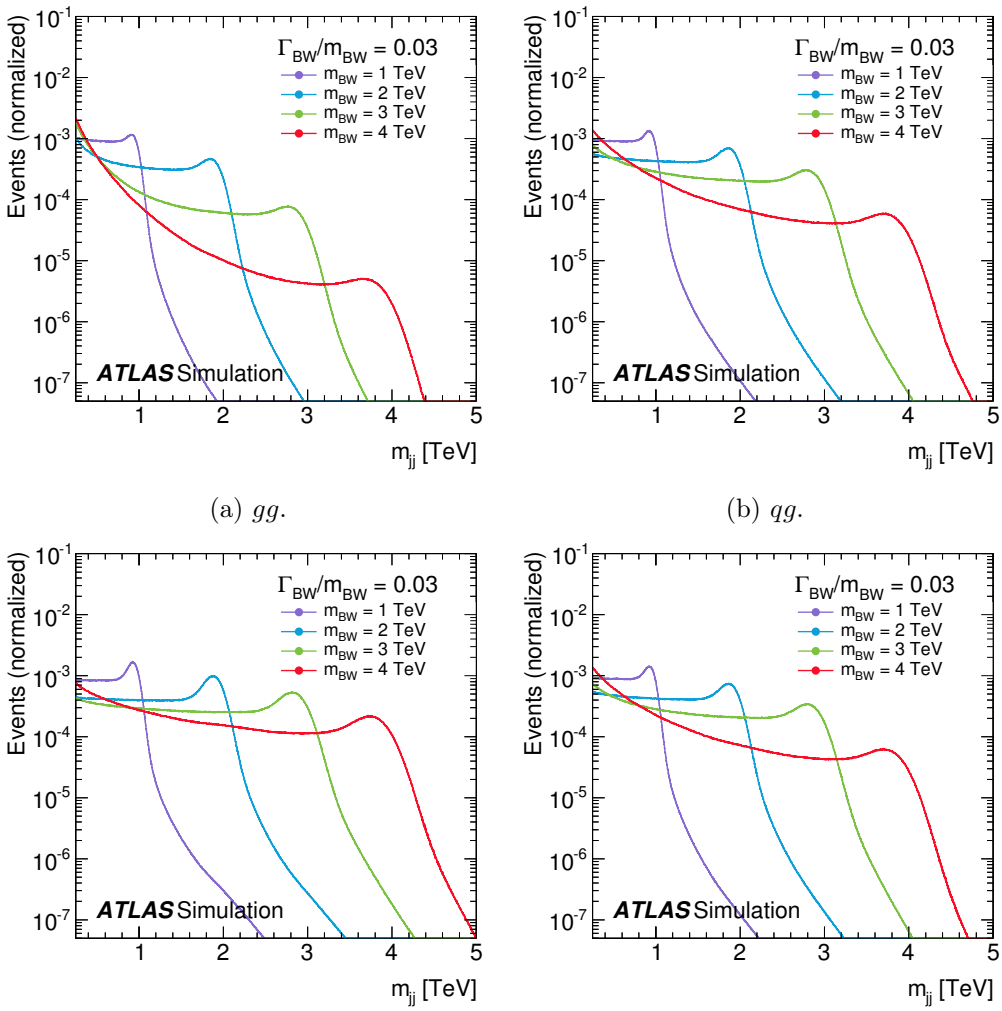

(a) gg. (b) qg.

(c) qq. (d) $q\bar{q}$.

Figure 6.36: Breit-Wigner generic signals convoluted with PDF effects, acceptance and detector resolution for 8 TeV pp collisions [85]. Signal curves are centered at 1, 2, 3 and 4 TeV and are organised into gg (a), qg (b), qq (c) and $q\bar{q}$ (d) production.

are not enough to describe the shape of the measured m_{jj} spectrum. A χ^2 value of 79 for 56 degrees of freedom has been measured, with a corresponding p-value of 0.027. No significant discrepancies between data and the fit have been identified by the BumpHunter algorithm. The biggest excess is found in the 390-599 GeV range with a corresponding p-value of 0.075, or z-value of 1.44σ. Overlaid on the data distribution are the excesses that excited quarks of mass 0.6, 2.0 and 3.5 TeV would have given. This are reported also in the second panel, where the data-fit difference normalised to the fit is shown.

The quality of the 13 TeV dijet mass spectrum is better than the 8 TeV, as it can be seen in Figure 6.37, thanks also to its smaller range and number of events. In this case, the single bin discrepancy significance is well behaved and does show a random distribution of up and down fluctuations of the data with respect to the fit. The data is compared to a Pythia Mc distribution with Nlo and Ew corrections in the bottom panel of the figure, showing a good agreement between the two within the Jes uncertainty. The quality of the fit is measured with a likelihood test statistic giving a p-value of 0.87. The BumpHunter identifies as the most significant excess the interval 1.53-1.61 TeV, highlighted by the blue vertical lines in the plot. The associated p-value is measured to be 0.67, corresponding to a z-value of 0.44σ, which is well compatible with a statistical fluctuation. An excited quark signal with mass of 4 TeV and cross section scaled by a factor 3.0 and a Quantum Black Hole generated with BlackMax of mass 6.5 TeV are overlaid on top of the data distribution for comparison.

The intervals tested by the BumpHunter algorithms and the p-value of each excess to originate from a fluctuations considering poissonian statistic is shown in Figure 6.38. The horizontal red lines indicate the m_{jj} window while the coordinate on the y-axis is the associate p-value. The interval with the lowest p-value is used to compute the BumpHunter hypertest statistic value.

The BumpHunter hypertest statistic distributions obtained from pseudo-experiments are shown in Figure 6.39 for the 8 TeV and 13 TeV analyses. The red arrows indicate the values obtained from the data distribution. The p-values, respectively 0.076 and 0.67, are obtained as the fractions of events standing on the right of the red arrows.

6.14.2 Limits

The results of the limit setting are shown in Figures 6.37-6.49 and summarised in Table 6.13.

As an example, the results of the marginalisation procedure described in Section 6.13.1 are presented in Figure 6.40 for an excited quark of mass 3 TeV in the 13 TeV mass spectrum. The prior and posterior probability distributions are presented for the seven sources of systematic uncertainties considered (see Section 6.12) together with the number of signal events posterior (Figure 6.40h). The agreement between priors and posteriors is remarkable for all distributions except for the fit quality (Figure 6.40a). In this case the posterior is narrower than the prior, indicating that the uncertainty considered is quite conservative. It is interesting to observe also that the posterior of the fit function choice (Figure 6.40b), unlike what happened for the 8 TeV analysis, is clearly in favour of the nominal fit function, corresponding to a nuisance parameter of zero. The posterior on the

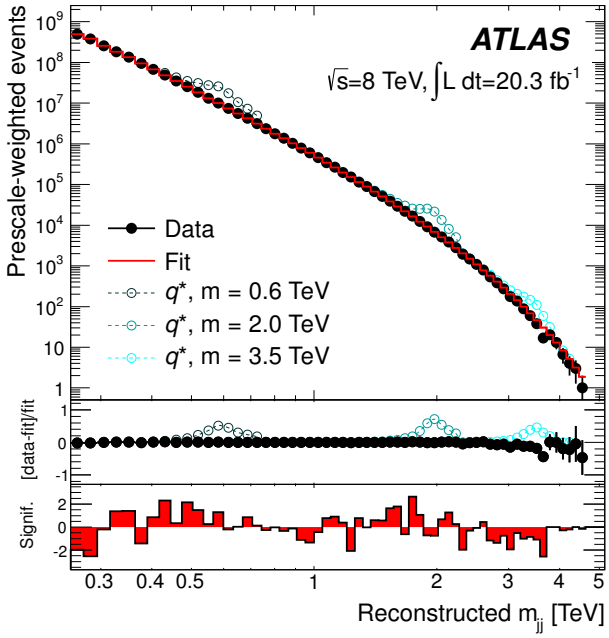

(a) 8 TeV.

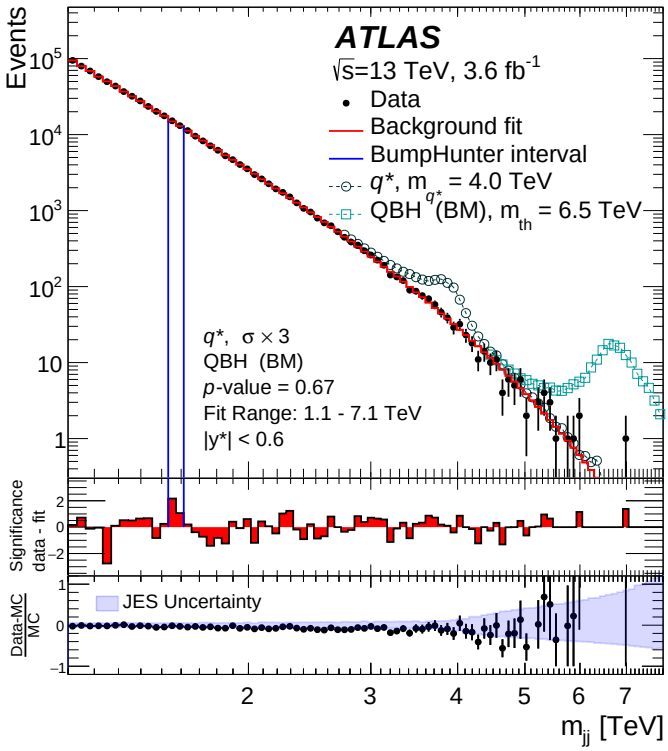

(b) 13 TeV.

Figure 6.37: search phase results from 8 TeV (a) and 13 TeV (b) analyses [11, 12].

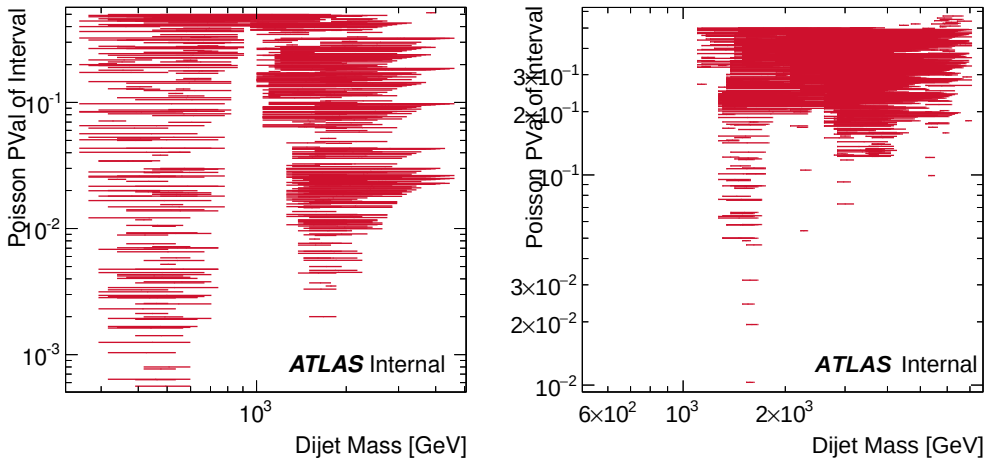

(a) 8 TeV. (b) 13 TeV.

Figure 6.38: p-values of all the regions tested by the BumpHunter algorithm in the 8 TeV (a) and 13 TeV (b) dijet invariant mass spectra [85, 126]. The BumpHunter hypertest statistic values indicated in Figure 6.39 are computed from the lowest p-value reported here through Equation 6.42.

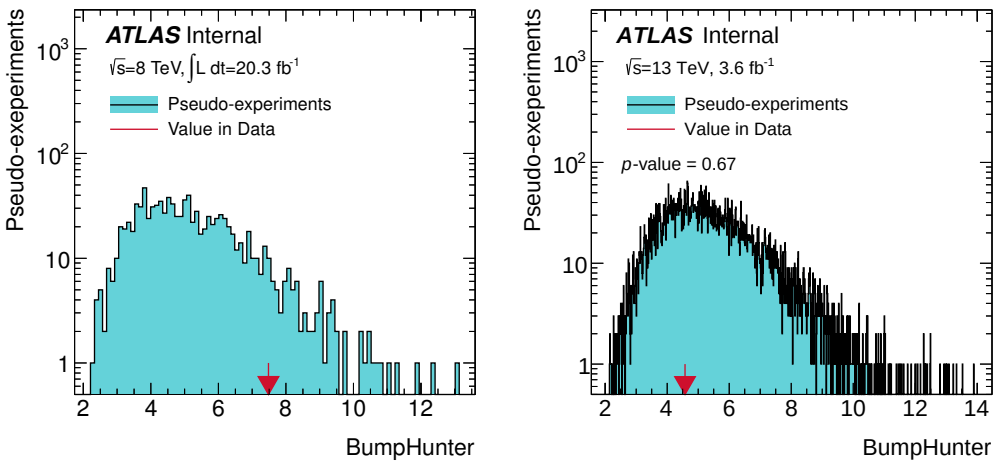

(a) 8 TeV. (b) 13 TeV.

Figure 6.39: BumpHunter test statistic distribution for 8 TeV (a) and 13 TeV (b) analyses [85, 126]. The p-values are 0.076 and 0.67 respectively.

number of signal events (Figure 6.40h) is peaked slightly above zero. The 95% quantile of the distribution corresponds to roughly 400 events, indicating that we can exclude at 95% credibility level an excited quark with cross section above σ_{Max}:

$$\sigma_{\text{limit}} = \frac{n_{\text{events 95\% quantile}}}{L} \simeq \frac{400}{3.6\ \text{fb}^{-1}} \simeq 0.11\ \text{pb} \tag{6.56}$$

By repeating this procedure for all the benchmark models considered, the limit curves shown in Figures 6.41-6.49 are obtained. Limits on excited quarks, Quantum Black Holes, W' and generic gaussian signals are reported for 8 TeV and 13 TeV alongside. For model-dependent limits, the 95% CL exclusion is taken at the value where the dashed line representing the theoretical signal cross section crosses the observed cross section curve represented by the connected black points. The expected limits, obtained by using the background distribution, are represented by the black dotted curve and one and two standard deviations bands are represented in green and yellow respectively. The signal cross section theoretical curves drawn for the 8 TeV limits have a band representing the beam energy uncertainty. It should be noted that while the Run-1 limits have been reported in terms of $\sigma \times A$, the Run-2 limits have not been corrected for the signals' Branching Ratios into dijet final states and are therefore reported in terms of $\sigma \times A \times \text{BR}$. This choice does not change the final limit values but it should be taken into account when directly comparing the limit curves from the two LHC runs. Limits on QBH are set apart as in this case BR is not well defined, hence the limits set for $\sigma \times A$.

model	Run-1 (20.3 fb^{-1}) expected [TeV]	Run-1 (20.3 fb^{-1}) observed [TeV]	Run-2 (3.6 fb^{-1}) expected [TeV]	Run-2 (3.6 fb^{-1}) observed [TeV]
q^*	3.98	4.06	4.9	5.2
QBH (ADD, QBH gen.)	5.66	5.66	8.3	8.3
QBH (ADD, BLACKMAX gen.)	5.62	5.62	8.1	8.1
QBH (RS, QBH gen.)			5.3	5.1
W'	2.51	2.45	2.6	2.6
W^* leptophobic	1.95	1.75		
W^* leptophilic	1.66	1.65		
color-octet scalar	2.70	2.80		

Table 6.13: 95% credibility level limits obtained in Run-1 and Run-2.

The limits on excited quarks are reported in Figure 6.41, showing the improvement of the Run-2 5.2 TeV limit over the Run-1 4.06 TeV limit using 3.6 fb^{-1} of data collected at 13 TeV instead of 20.3 fb^{-1} at 8 TeV.

Figure 6.42 shows a comparison of the limits on simulated QBH according to the ADD model and using the QBH generator. From Run-1 to Run-2 the limits improves from 5.7 TeV to 8.3 TeV. As a term of comparison, the limits on the same ADD QBH model but using the BLACKMAX generator are reported in Figure 6.43, showing slightly lower values: 5.62 TeV and 8.1 TeV respectively. The theoretical cross section curves for ADD and RS

quantum black holes simulated using the QBH generator are overlaid. It is important to notice how, at large dijet mass values, the observed and expected limits tend to coincide and the one and two standard deviations bands tend to reduce in size. This is due to the lack of events in data at such large values and to the very large cross section of ADD quantum black holes.

The limit on the W' model (Figure 6.44) receives only a mild improvement in Run-2, going from 2.45 TeV to 2.6 TeV, due to the limited enhancement given by the boost in the collision center of mass energy.

Excited W vector boson and color-octet scalar limits have been set only in the Run-1 analysis and are shown in Figures 6.45 and 6.46.

The Run-2 limits on Z' have been set for different mass values and couplings to quarks. A summary of the results is shown in Figure 6.47. Bins with $\frac{\sigma_{\text{limit}}}{\sigma_{\text{theory}}}$ values below unity are excluded.

Finally, model independent limits are shown for gaussian-shaped signals (Figure 6.48) and Breit-Wigner signals convoluted with PDF effects (Figure 6.49). The limits are presented in terms of $\sigma \times A \times$ BR since there is no BR to correct for.

The gaussian limits are computed for four values of signal width ranging from 0.15 down to the detector resolution, therefore showing the best limits the analysis can set. It is possible to observe that as the signal width becomes smaller, the limit curves become more sensible to statistical fluctuations in the m_{jj} distribution. Signals that are less than two standard deviations from either end of the spectrum are not used to set limits, hence the shorter range of the limit curves for wider signals.

The Breit-Wigner limits have been computed in the 8 TeV analysis only. Results in Figure 6.49 are organised for initial partons: gg, qg, qq and $q\bar{q}$. While in the low mass range the limit curves are comparable in the four scenarios, at large m_{jj} values the PDF suppression of gluons and anti-quarks delivers worse limits than the qq initial state.

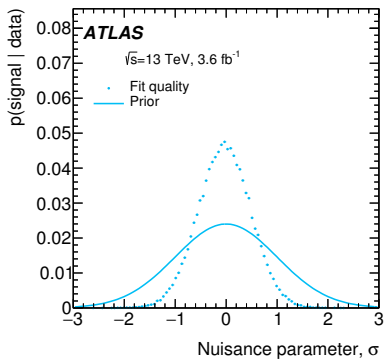

(a) fit quality.

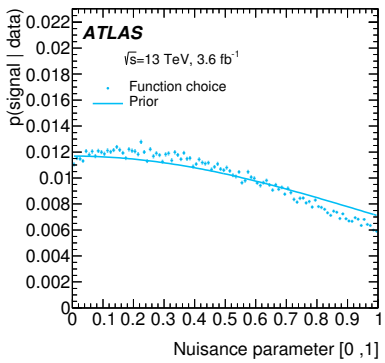

(b) fit function choice.

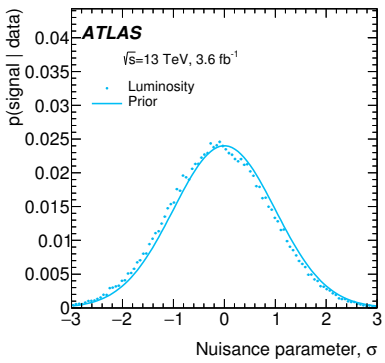

(c) luminosity.

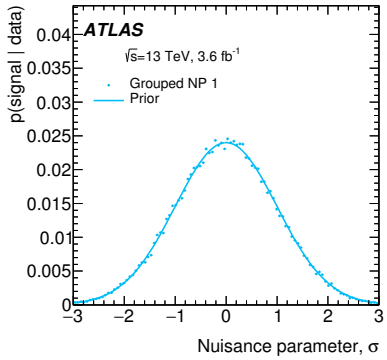

(d) JES nuisance parameter 1.

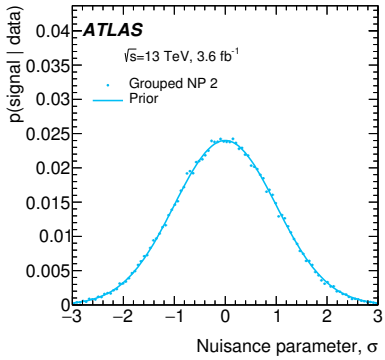

(e) JES nuisance parameter 2.

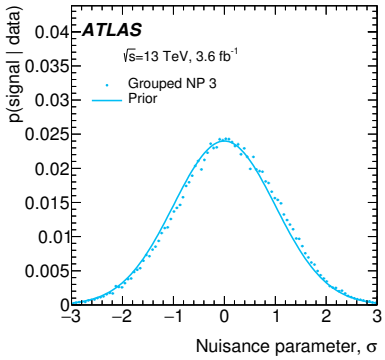

(f) JES nuisance parameter 3.

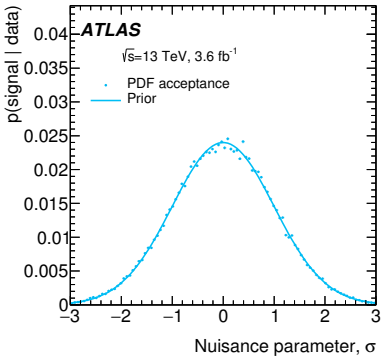

(g) PDF.

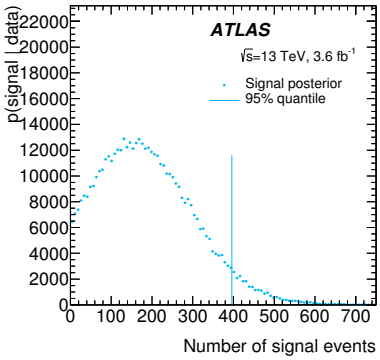

(h) signal events.

Figure 6.40: posterior distributions obtained after the marginalisation procedure ran using a 3 TeV excited quark as benchmark model [126]. The signal posterior (h) is reported together with the 95% quantile used to set the 95% CL limit.

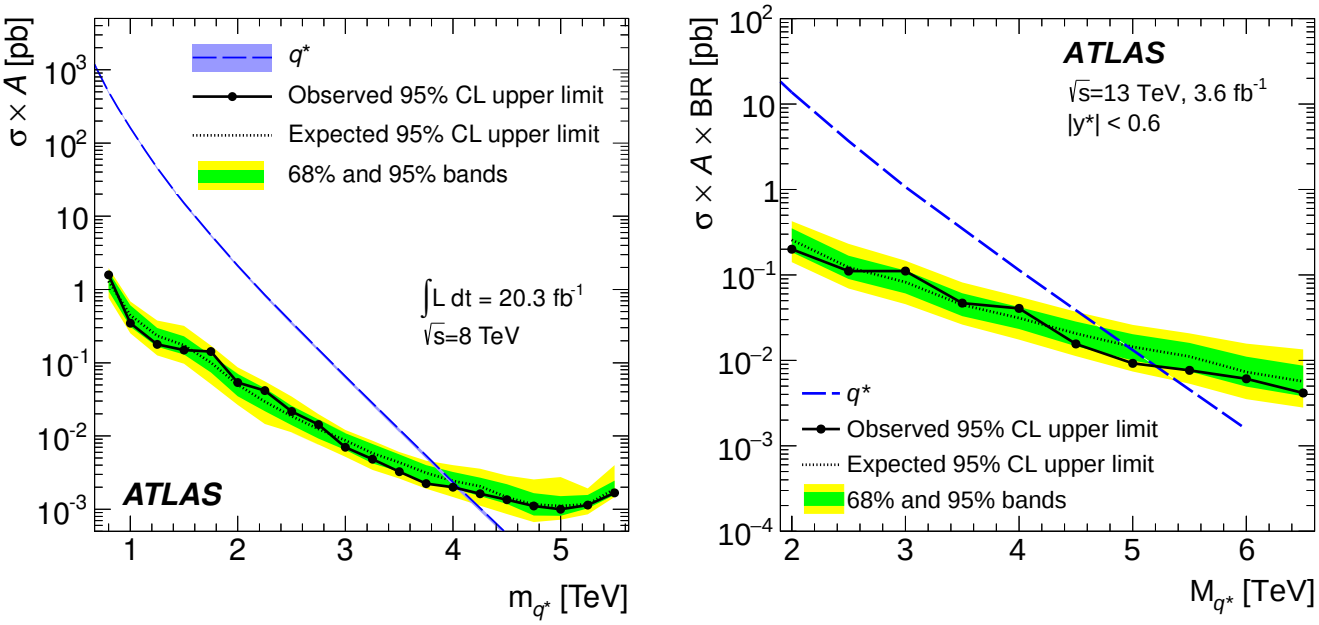

(a) 8 TeV. (b) 13 TeV.

Figure 6.41: excited quarks limits [11, 12].

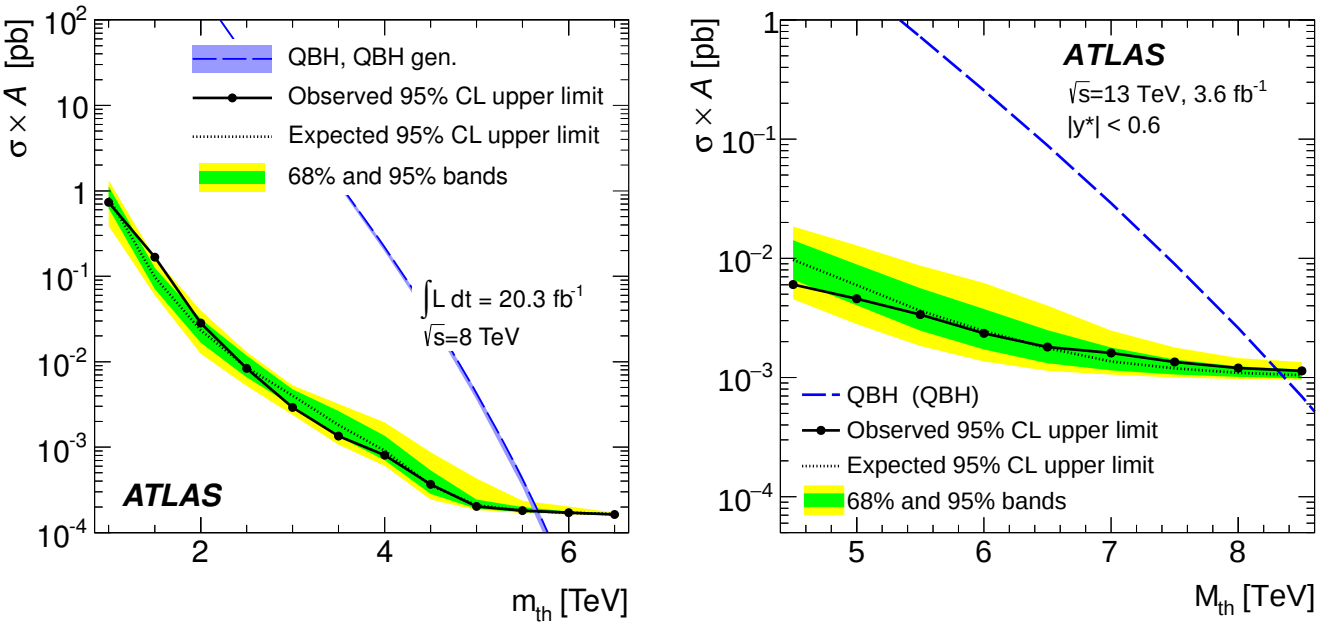

(a) 8 TeV. (b) 13 TeV.

Figure 6.42: Quantum Black Holes (QBH generator) limits [11, 12].

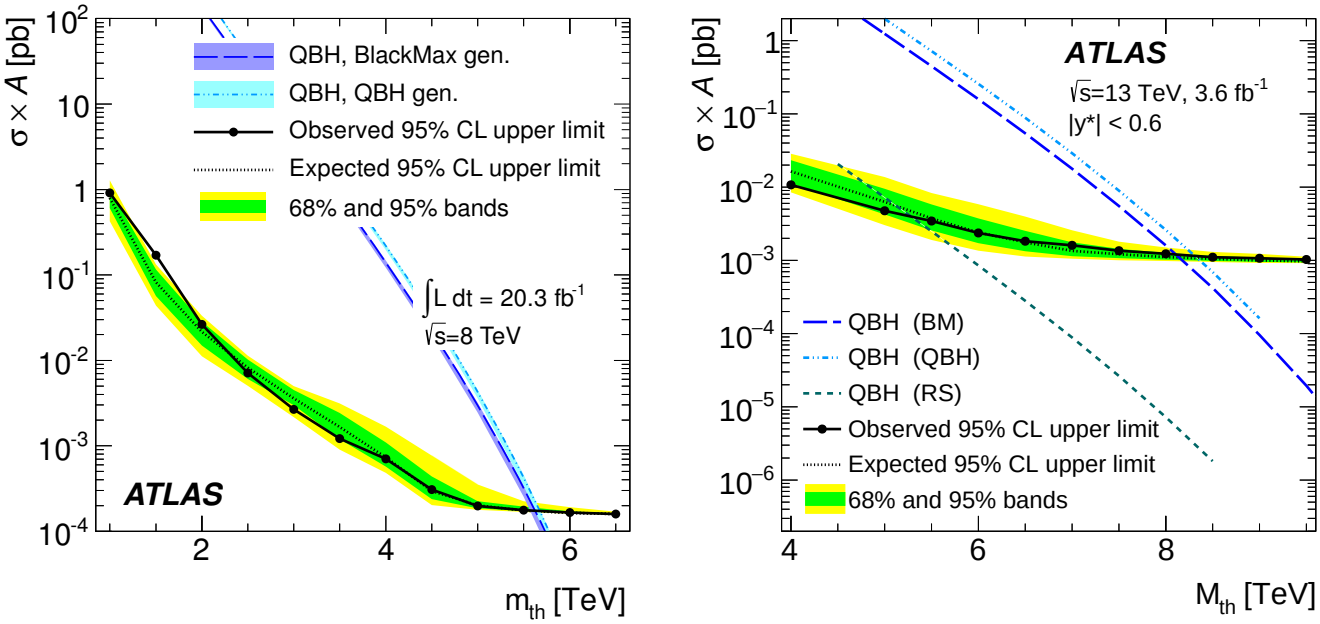

(a) 8 TeV. (b) 13 TeV.

Figure 6.43: Quantum Black Holes (BlackMax generator) limits [11, 12].

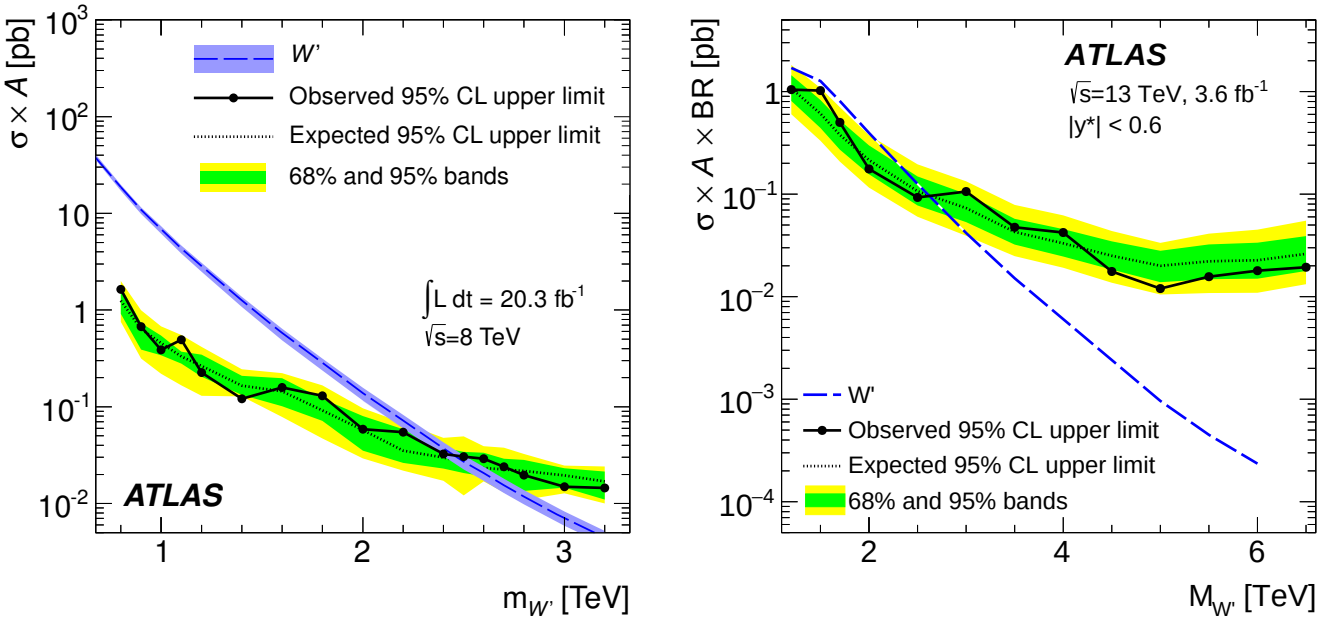

(a) 8 TeV. (b) 13 TeV.

Figure 6.44: W' limits [11, 12].

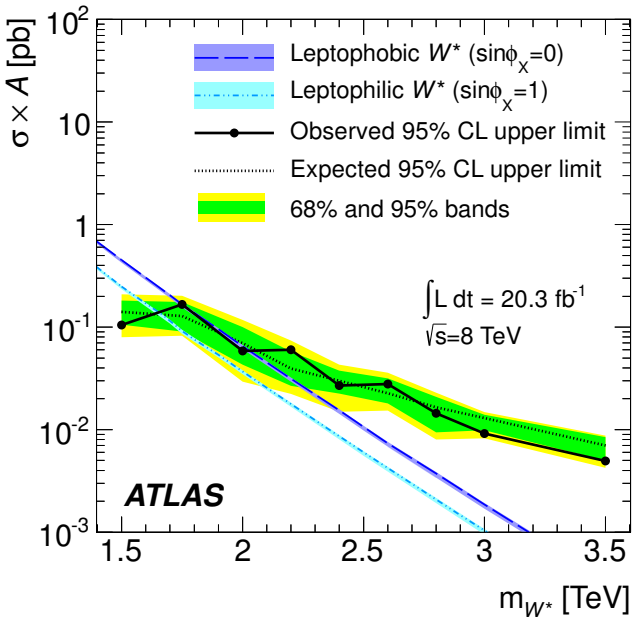

Figure 6.45: W^* limit set using 8 TeV data [11].

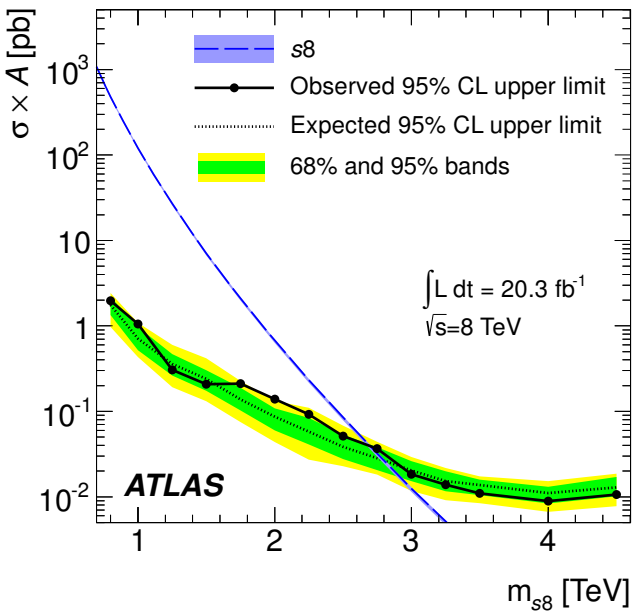

Figure 6.46: scalar octet limit set using 8 TeV data [11].

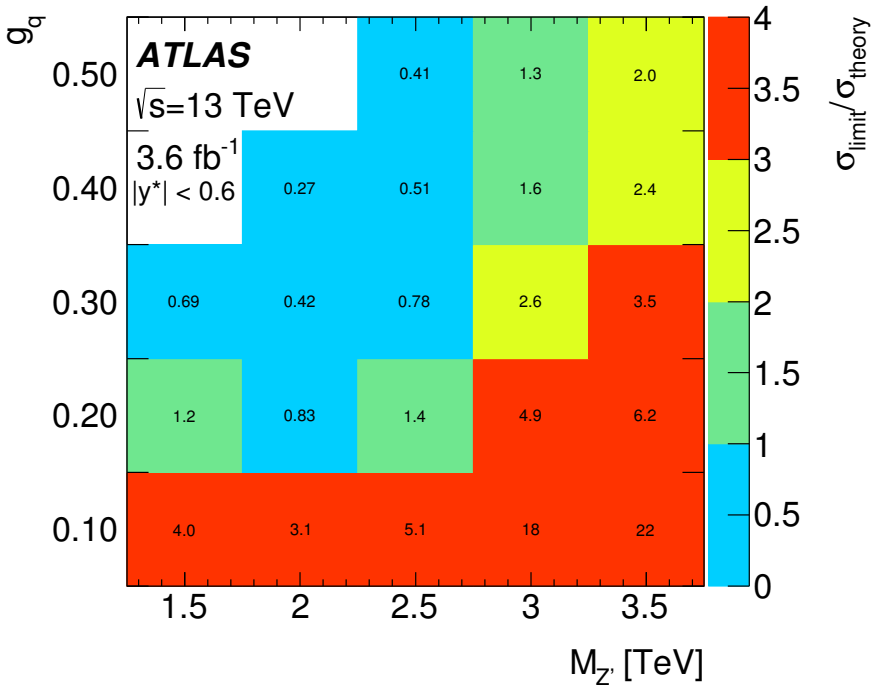

Figure 6.47: Z' limits on signal strength shown for different mass values and quark couplings [12]. Results are based on 13 TeV data.

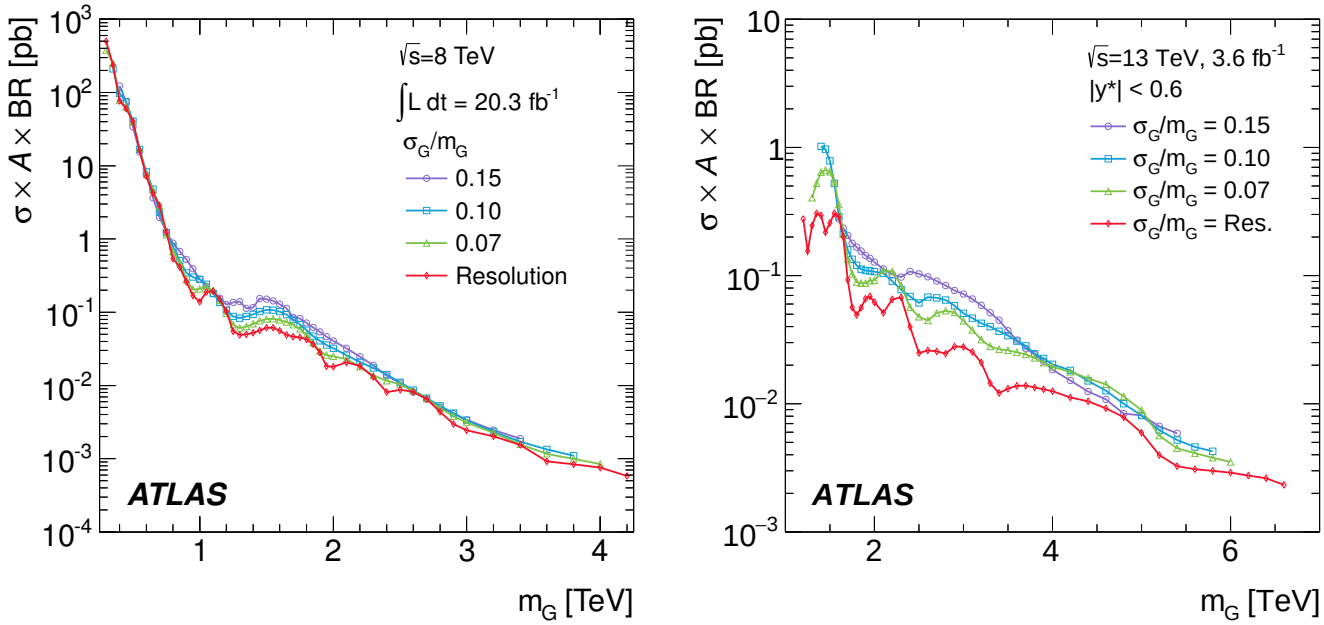

(a) 8 TeV.

(b) 13 TeV.

Figure 6.48: limits on generic gaussian-shaped signals [11, 12].

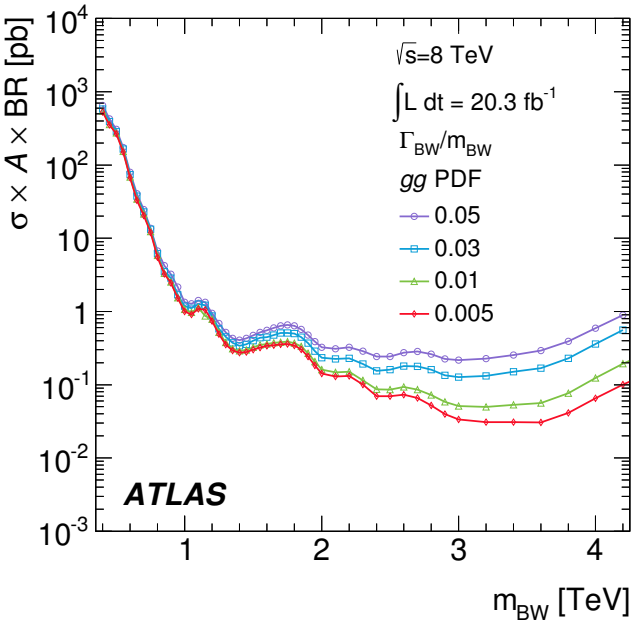

(a) gg.

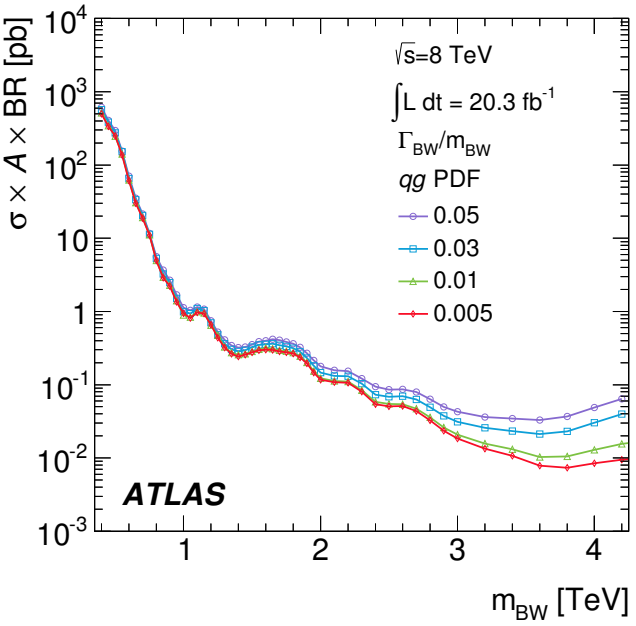

(b) qg.

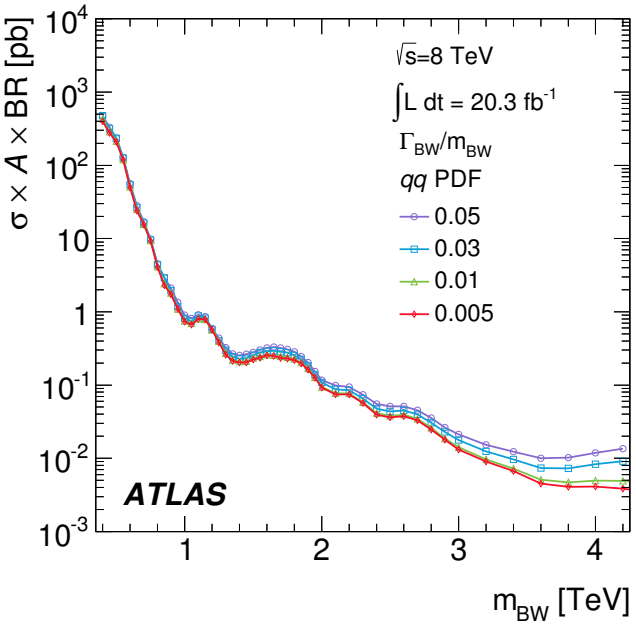

(c) qq.

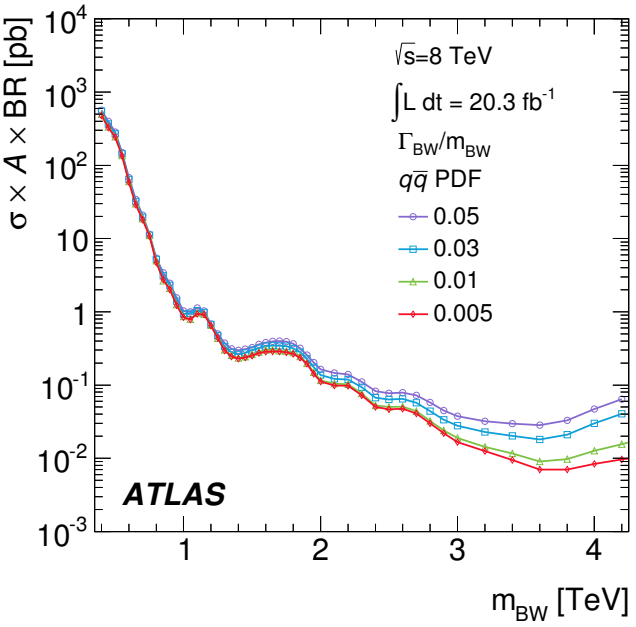

(d) $q\bar{q}$.

Figure 6.49: limits on generic Breit-Wigner signals convoluted with PDF effects [11]. Results are based on 8 TeV data.

Chapter 7

Quo Vadis Exotic Dijet?

In the context of the search for evidence of physics phenomena beyond the SM, it is of primarily interest to investigate the reach of analyses such as the exotic dijet in the long run. This chapter presents the expected sensitivity improvement of future dijet resonance searches using 14 TeV pp collision data recorded over the different LHC phases and performed with the ATLAS detector[1]. However, since neither ATLAS performance nor exact LHC running conditions have been fully determined yet, these studies should only be considered as an indication of the discovery and sensitivity prospects of the analysis.

The analysis presented here applies the same selection and techniques as in the 8 TeV ATLAS dijet publication [11] to generated MC events. Smearing factors, as evaluated for the ECFA upgrade studies [130], are used to reproduce the effects of detector and pile-up conditions on the measurements.

7.1 Simulation

Background QCD events have been produced at a center of mass energy of 14 TeV using PYTHIA 8.183 event generator [42], tuned to the AU2 settings [70] for the ATLAS underlying event data parameters, and in combination with CT10 PDFs [71]

Similarly to the 8 TeV and 13 TeV data analyses, excited quarks and Quantum Black Holes have been used as benchmark models (see Section 6.3.3). Excited u and d quarks have been simulated through the PYTHIA 8.162 generator [42], using the CT10 PDFs [71] and the AU2 tune [70]. Excited quarks are assumed to decay to a quark and a gauge boson via gauge couplings set to unity, leading to a qg final state approximately 83% of the times (the remaining generated decays involve W/Z or γ emission), all decays are considered in the search. A total of 12 signal mass points have been generated for the q^*, ranging from 2 to 13 TeV. QBHs decaying to all allowed two-body final states have been simulated using the BLACKMAX [45] generator. This produces a simple two-jet final-state scenario of quantum gravitational effects at the fundamental Planck scale, M_{D}, with 6 extra spatial dimensions in the context of the ADD model [88]. The Planck scale is set

[1] This chapter is based on the results documented in [129]. All the studies and measurements reported there, with the only exception of the limit setting, have been performed by the author of this thesis.

equal to the threshold mass for the QBH production, m_{th}. The PDF used for the signal generation and parton shower is CT10 [71] and non-perturbative effects are simulated with PYTHIA 8.170 [42] using the AU2 tune [70]. In total, 9 signal mass points have been generated, ranging from 4 to 12 TeV.

Jets employed for this study are reconstructed by means of the anti-k_{t} jet algorithm [54, 55, 56] with distance parameter $R = 0.4$ and using as inputs particles with a lifetime longer than 10 ps, excluding muons and neutrinos. Jets are subsequently smeared according to the projected energy resolution due to detector effects and pile-up [130]. The parameterisation of the JER does not depend significantly on the pile-up conditions at the energies of the jets considered in this analysis. For this reason, a single value of the average interactions per bunch crossing, $\langle\mu\rangle$, equal to 80 is used.

Mass spectra corresponding to integrated luminosities ranging from 0.1 fb^{-1} to 3000 fb^{-1} are randomly drawn from the m_{jj} distribution obtained from the smeared MC events (see Section 7.3).

7.2 Event Selection

The analysis strategy adopted in these studies follows that of the exotic dijet analysis in Run-1 [11].

Trigger effects are considered to be negligible in these studies since the analysis is restricted to the high m_{jj} region, where the lowest un-prescaled single-jet triggers are expected to be fully efficient. Trigger thresholds of 1.5 TeV and 2 TeV in m_{jj} are applied depending on the simulated integrated luminosity.

The leading jets must be found within $|y| < 2.8$ and the next-to-leading jet is required to have a p_{T} greater than 50 GeV. In the 8 TeV analysis this selection ensured that more than 98% of the two leading jets were associated with the hard scatter collision vertex. Leading jets must have a rapidity in the center of mass frame, $|y^*| = \frac{1}{2}|y_1 - y_2|$, smaller than 0.6.

No jet identification criteria are implemented for this study, as neither beam backgrounds nor detector effects are simulated. In the 8 TeV analysis, the kinematic selection above efficiently filtered out fake jets. Specific cleaning cuts [109] remove an additional 2% of events before the full kinematic selection, introducing a negligible inefficiency on real jets.

7.3 Dijet Mass Spectrum

In order to have a spectrum with the statistical accuracy equal to that of observed data at a given integrated luminosity, the MC m_{jj} distribution is extracted using the *data-like* method, as described in Section 6.9.1. The data-like method is based on the effective entries available in MC, which is the number of entries that would have the same statistical power if all entries had weight 1. For each bin, the number of effective entries is computed

as:

$$n_{\text{effective entries}} = \frac{(\sum w_i)^2}{\sum w_i^2} \tag{7.1}$$

where w_i is the weight of the ith MC event. This would be identically equal to the number of entries if all w_i were equal to 1. When the number of effective entries is greater than the number of weighted MC entries, it is possible to apply the data-like method, i.e. to randomly draw events and assign them a unitary weight instead of using all the entries available with their weight applied. A random number from a flat distribution in the range between 0 and 1 is compared to the ratio, f, of the total number of weighted MC entries to the effective entries for each MC event:

$$f = \frac{n^{\text{MC}}_{\text{entries}}}{n^{\text{MC}}_{\text{effective entries}}} < 1 \tag{7.2}$$

The event in question is accepted if the random number is smaller than f. It is thus clear that the use of the method is limited by the number of entries of the MC sample. In this analysis sufficient MC statistics to produce the entire m_{jj} spectrum are only available for integrated luminosities up to 25 fb^{-1}. At larger integrated luminosities, whenever the f ratio of a bin is above unity, the bin content is obtained using pseudo-data from a fit to the 25 fb^{-1} spectrum that is scaled to the needed luminosity. The bin content provided by the scaled fit is then fluctuated according to a Poisson distribution to reproduce a *pseudo-data-like* spectrum (see Figure 7.1). In performing luminosity scans the MC is integrated so as to simulate real data taking. As the luminosity increases, f approaches unity and a constant bin-dependent seed for the random number generator ensures that once a MC event is selected, it is always selected for larger luminosities.

7.3.1 Signal Injection

The signals injected in the MC QCD background are also extracted using the data-like method in the first place. Figure 7.2 shows the injection of a 6 TeV q^* in a 200 fb^{-1} background spectrum and the injection of a 10 TeV QBH in a 500 fb^{-1} background. It is possible to observe that the signal entries and effective entries distributions perfectly overlap since, recalling equation 7.1, the MC signal event weights are all unitary.

7.4 Background Extraction

The background distribution shape is extracted directly by performing a fit of the dijet mass distribution using a smooth function, as illustrated in Section 6.8. This allows the search to be independent of theoretical uncertainties on the background MC generation and detector smearing. The uncertainties taken into account are those on the functional form chosen and those on the parameters of the fit [11].

The standard four parameter fit function (see Section 6.8 and equation 6.26) is used to estimate the background distribution:

$$f(x) = p_0(1-x)^{p_1} x^{p_2 + p_3 \ln x} \quad x \equiv \frac{m_{jj}}{\sqrt{s}} \tag{7.3}$$

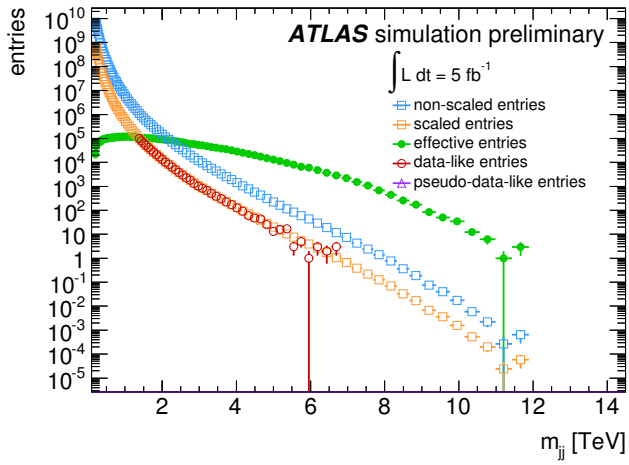

(a) 5 fb^{-1}.

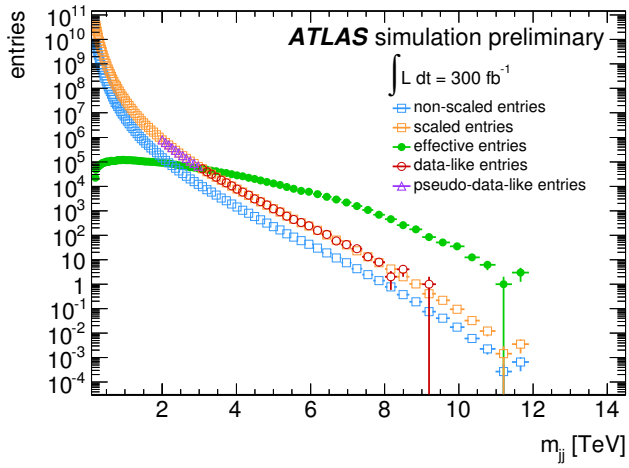

(b) 300 fb^{-1}.

Figure 7.1: data-like dijet mass spectra for 5 fb^{-1} (a) and 300 fb^{-1} (b). The distribution of effective entries available from the MC sample used is represented by the green points. Since at 300 fb^{-1} the crossing of the scaled distribution (orange squares) and the effective entries distribution happens at m_{jj} values above 2 TeV (the lower threshold chosen for the studies), a pseudo-data-like distribution (violet triangles) is used to cover the gap in the lower mass region.

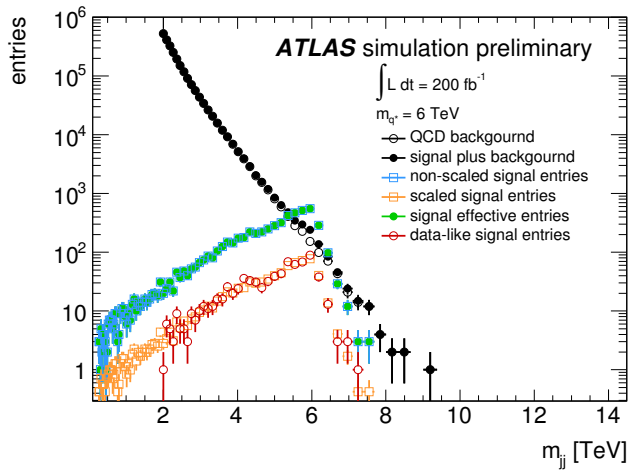

(a) 6 TeV q^*, 200 fb^{-1}.

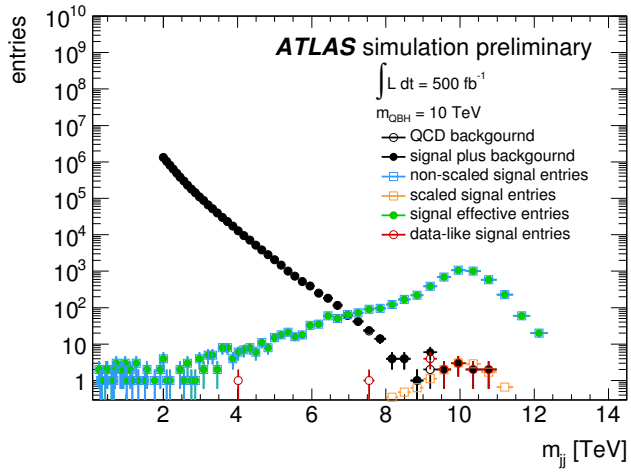

(b) 10 TeV QBH, 500 fb^{-1}.

Figure 7.2: signals injected into the QCD background spectrum. The black open points are the MC QCD background from the previous step (see Figure 7.1), the light blue points represent the non-scaled signal, the orange points the signal scaled to the given luminosity, the green points are the effective signal entries, the red points the data-like signal entries and the black filled points are the final distribution containing background and signal.

where p_i are the parameters. A cross-check of the analysis has been performed using the five parameter fit function:

$$f_5(x) = p_1(1-x)^{p_2} x^{p_3 + p_4 \ln x + p_5 (\ln x)^2} \quad x \equiv \frac{m_{jj}}{\sqrt{s}} \tag{7.4}$$

which adds the term $x^{p_5(\ln x)^2}$ to equation 7.3. Results are found to be compatible with those obtained using the four parameter fit function.

7.5 Search Phase

Once the background shape is extracted, the BumpHunter algorithm [77] is then used to identify the bins in the m_{jj} spectrum that are most discrepant from the fit, as described in Section 6.10.1.

Figure 7.3 shows two examples of search performed on a QCD background with a 6 TeV q^* signal injected with 200 fb^{-1} and a QCD background with a 10 TeV QBH signal injected and corresponding to 500 fb^{-1}. The blue vertical lines delimit the bins with the most significant excess.

7.6 Sensitivity to New Physics Benchmarks

The sensitivity to resonant dijet signals is assessed by injecting the benchmark signals into the QCD background spectrum at different steps of integrated luminosities, ranging from 0.1 fb^{-1} to 3000 fb^{-1}, and performing the full search phase. A potential discovery for a given signal mass point at a given luminosity is defined as a 5σ deviation in the BumpHunter hypertest statistics p-value.

Figure 7.4 shows two examples of luminosity scans: one for a q^* of 6 TeV and one for a QBH of 10 TeV mass. The evolution of the local excess identified by the BumpHunter (represented by the red points) and its corresponding p-value (represented by black points) are shown together as a function of the integrated luminosity until either a 5σ excess level or the highest luminosity value is reached. With a small integrated luminosity the BumpHunter is unable to identify the excesses given by the signals injected but, for sufficiently high integrated luminosity values, the algorithm starts to converge on the signal (see for example Figure 7.4a for luminosities above 25 fb^{-1}) and in a few luminosity steps the associated p-value drops enough to claim a 5σ discovery.

Once the luminosity scan is performed for each of the benchmark signal points, it is finally possible to collect the discovery luminosity values and plot them as a function of the signal mass, as shown in Figure 7.5. The integrated luminosity values corresponding to 1, 25, 300 and 3000 fb^{-1} are highlighted by red lines, since at the time the analysis [129] was performed these were the estimated amounts of data to be collected by the end of the first month, the end of the first year, the end of Phase-1 and by the end of Phase-2/ respectively. Signals whose discovery luminosity is outside the range tested are not shown.

It is important to notice that for each additional order of magnitude of data collected, the sensitivity to the benchmark models is extended by $\sim$1 TeV. In the perspective of

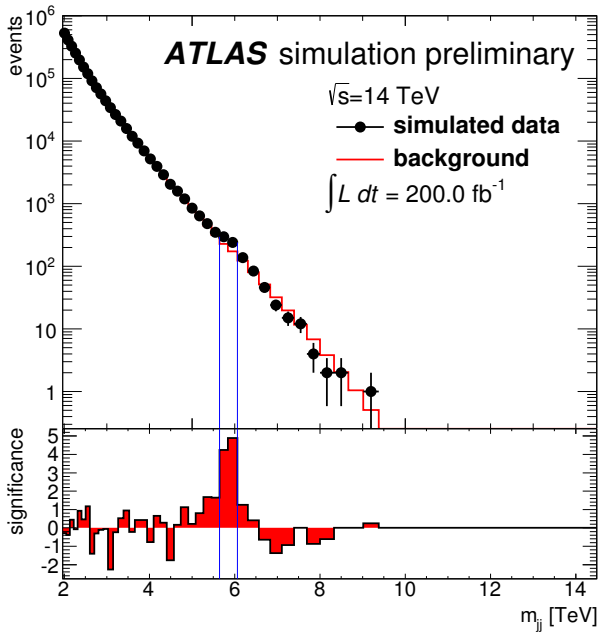

(a) 6 TeV q^*.

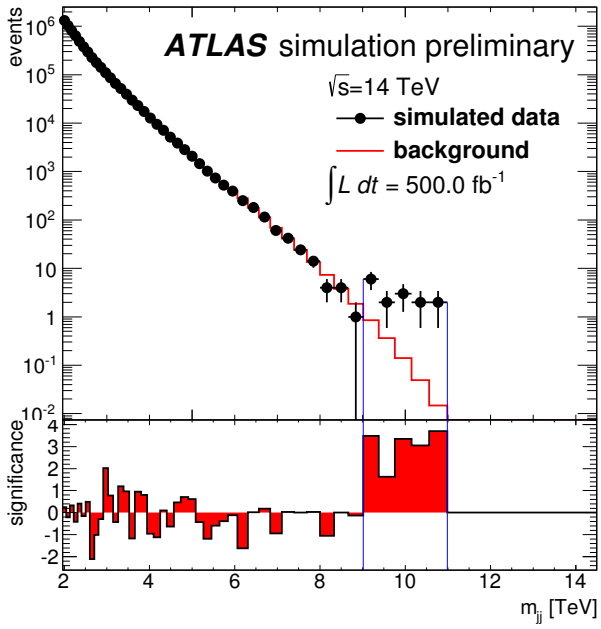

(b) 10 TeV QBH.

Figure 7.3: results of the search phase performed on the dijet mass spectrum containing a 6 TeV q^* with integrated luminosity of 200 fb^{-1} (a) and a 10 TeV QBH with 500 fb^{-1} (b). The local excesses identified by the BUMPHUNTER in these two examples correspond to deviations beyond 5σ.

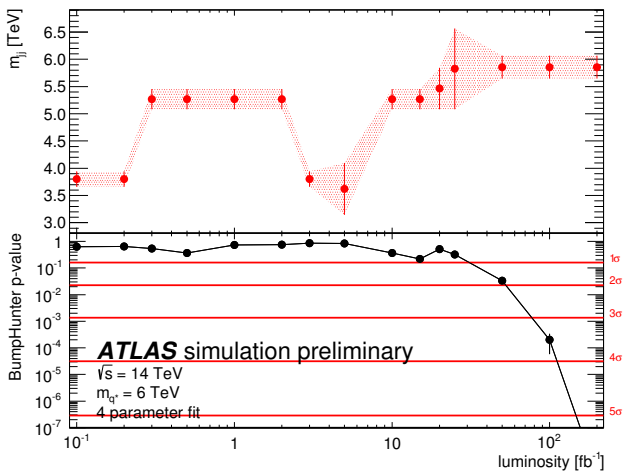

(a) 6 TeV q^*.

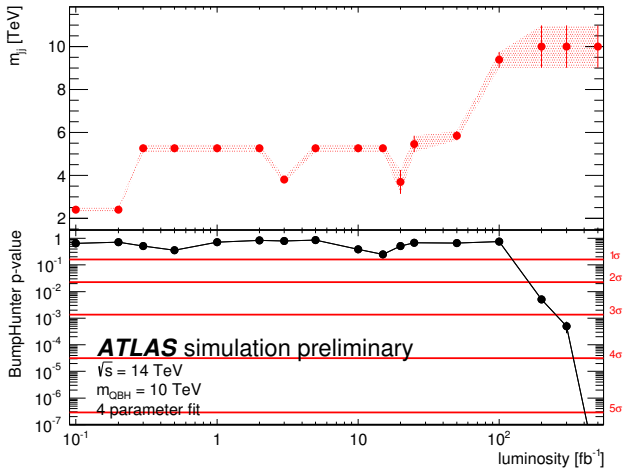

(b) 10 TeV QBH.

Figure 7.4: luminosity scan on 6 TeV q^* (a) and 10 TeV QBH (b) signals. The evolution of the local excess identified by the BUMPHUNTER (associated p-value) as a function of the integrated luminosity is shown by the red (black) points. For each signal mass point, the scan is terminated when either the associated p-value reaches a deviation corresponding to 5σ or the maximum luminosity of 3000 fb^{-1} is reached.

150 fb^{-1} of data collected by ATLAS by the end of Run-2 [23], this means that our current 5σ sensitivity to new physics will be considerably extended by 2 TeV.

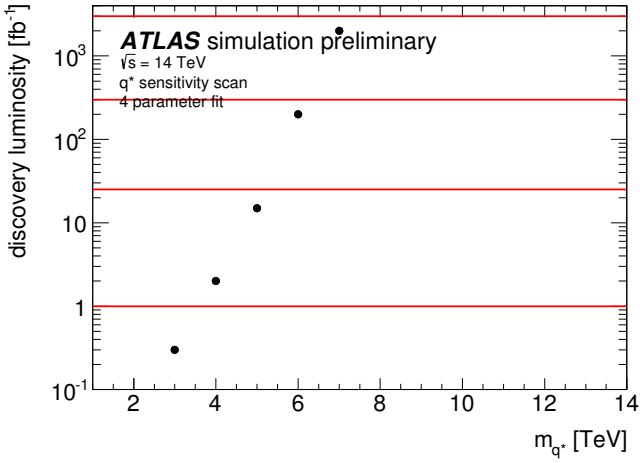

(a) q^*.

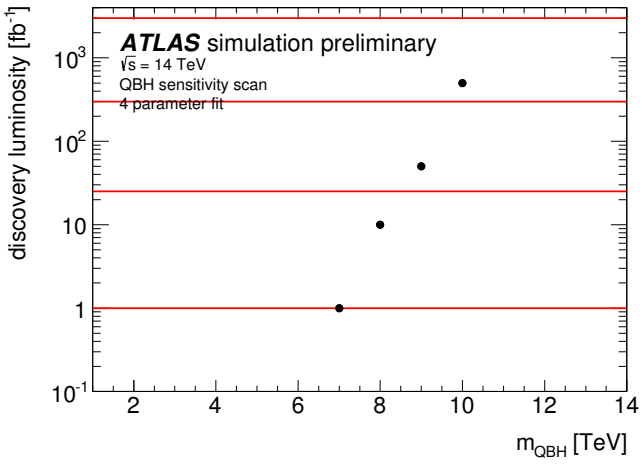

(b) QBH.

Figure 7.5: sensitivity scan results for the q^* (a) and the QBH (b). Red lines indicate 1, 25, 300 and 3000 fb^{-1} integrated luminosity values.

7.7 Expected Limits

Finally, expected limits have been set on the simulated benchmark models. As described in Section 6.13, the bayesian method has been used to set 95% Credibility Level exclusion limits on the cross section times acceptance of the q^* and QBH signals. A flat prior distribution has been used for the signal normalisation while Gaussian priors have been assigned to the nuisance parameters of the systematic uncertainties taken into account (see Section 6.12), namely:

- **fit**: uncertainties on the fit quality and on the choice of fit function (see Sections 6.12.1 and 6.12.2);

- **Jes**: the 8 TeV Jes uncertainty has been used as baseline; the uncertainty corresponding to jets of a given p_{T} at 8 TeV is applied to jets with 1.75 $\cdot p_{\mathrm{T}}$ at 14 TeV[2], to emulate the higher kinematic reach of the jets; The effects of the nuisance parameters of the Jes uncertainty are propagated separately. This is the dominant source of uncertainty;

- **luminosity**: a flat 2.8% uncertainty has been used, as measured in 2012 data [131].

No uncertainties are associated with the theoretical models. The expected limits on q^* and Qbh are shown in Figure 7.6 and summarised in table 7.1. The limit curve has been fully derived for an equivalent integrated luminosity of 25 fb^{-1}, while the limit curves for the other luminosity values, L, have been obtained from this one scaling its values by the factor:

$$\frac{\sigma \times A|_L}{\sigma \times A|_{25/\mathrm{fb}}} = \sqrt{\frac{25\ \mathrm{fb}^{-1}}{L}} \tag{7.5}$$

By comparing these results with the limits illustrated in Section 6.14.2, it possible to observe that as little as 0.1 fb^{-1} of 14 TeV data would have been sufficient to match the 8 TeV results on the q^* and significantly improve those on Qbh, thanks to the enormous increase of the signal cross section at higher $\sqrt{s}$ values. On the other hand, the agreement between these limits and those obtained on 3.2 fb^{-1} of 13 TeV data are in fairly good agreement, despite these being smeared truth simulations at a slightly higher collision energy, which give an optimistic estimation with respect to the data collected.

integrated luminosity [fb^{-1}]	m_{q^*} [TeV]	m_{QBH} [TeV]
0.1	4.0	8.2
1	5.0	8.9
5	5.9	9.2
25	6.6	9.7
300	7.4	10.0
3000	8.0	10.1

Table 7.1: expected limits on q^* and Qbh for luminosities ranging from 0.1 fb^{-1} up to 3000 fb^{-1}. Values taken from Figure 7.6.

[2] 14 TeV/8 TeV = 1.75.

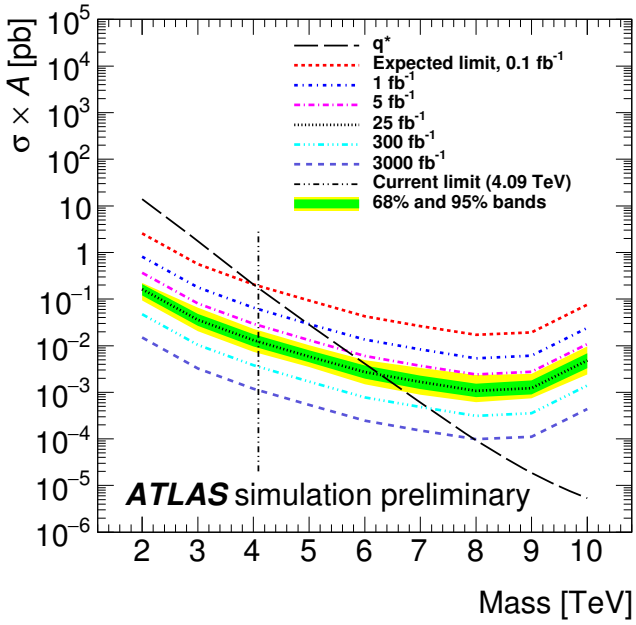

(a) q^*.

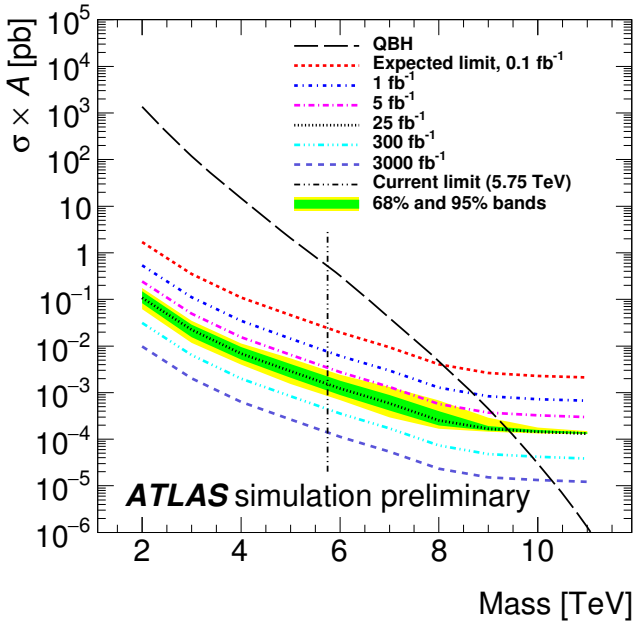

(b) QBH.

Figure 7.6: expected limits on q^* (a) and QBH (b) models. The dashed vertical lines represent the limits set using 20.3 fb^{-1} of 8 TeV data: 4.09 TeV for the q^* and 5.75 TeV for the QBH(see Section 6.14.2).

Conclusions

Physics phenomena outside of the Standard Model of particle physics may produce narrow resonances in the invariant mass distributions of jet pairs from proton-proton collisions at the LHC. This thesis presented several iterations by the ATLAS Collaboration of one of the searches for such new phenomena: the dijet analysis, looking for narrow resonances in events containing high-p_{T} jets.

The description of the jet angular measurement, a source of uncertainty to all jet-related analyses, has been presented. This measurement has been performed by looking at the $\Delta\eta$ and $\Delta\phi$ separation between matching truth-jets from MC, calorimeter-jets and track-jets. Results have shown that jet reconstructed from energy deposits in the calorimeter often have a better angular resolution than jets reconstructed from tracks. Data and MC measurements agree well to within one sigma and this is also confirmed by the negligible smearing factors needed to adjust the MC resolution to that of data. Moreover, the improvement to the angular resolution produced by the jet origin correction has lead to its reintroduction in the set of calibrations applied for 2012 analyses.

The dijet analysis has been described in detail and a comparison of the techniques and results from the analyses performed on the 2012 and 2015 datasets has been given, highlighting the improvements introduced over time and the solutions adopted to overcome the problems encountered. No evidence of localised excesses have been identified using the BUMPHUNTER algorithm. A set of resonant benchmark models has been employed to set limits using the bayesian method at 95% Credibility Level. Using 20.3 fb^{-1} of data collected at $\sqrt{s} = 8$ TeV in 2012, excited quarks with masses below 4.06 TeV and Quantum Black Holes[3] with masses below 5.2 TeV have been excluded. The 2015 dataset, corresponding to 3.6 fb^{-1} of pp collisions at $\sqrt{s} = 13$ TeV, allowed the limits to be pushed up to 5.66 TeV and 8.3 TeV for excited quarks and QBHs respectively. Compatible results have been found by the CMS Collaboration at 8 TeV [105] and 13 TeV [106]. Complementary searches have been performed with the ATLAS detector to identify new physics phenomena in case of non-resonant signals [121, 12] or signals producing heavy flavour jets such as b-jets [64]. None of these searches has observed evidence of physics beyond the Standard Model either.

The reach of the dijet analysis at large integrated luminosities for $\sqrt{s} = 14$ TeV proton-proton collisions has also been presented. Results have shown that the sensitivity to excited quarks and QBHs for a 5σ discovery grows of around 1 TeV for each additional

[3] ADD model, QBH generator.

order of magnitude of integrated luminosity. Considering that the LHC will deliver ATLAS with an integrated luminosity reaching the order of 100 fb^{-1} before the end of Run-2 in 2018, the dijet analysis will be able to discover excited quarks and QBHs with a 5σ significance if these have masses below 6 TeV and 9-10 TeV respectively. Moreover, the 95% CL limits on benchmark models set using the 14 TeV simulated samples have returned values compatible to those of the 13 TeV dataset for an equal integrated luminosity.

The remarkable integrated luminosity to be delivered by LHC to the ATLAS experiment by the end of Run-2 will allow the ongoing analyses to quickly supersede their current best results and will make exotic searches particular appealing for the years to come. As the dijet analysis probes even higher mass values, a renewed interest in the lower mass region of the dijet spectrum has recently sparked. This attention has been driven by the possibility of investigating benchmark models with even lower cross sections, thanks to the integrated luminosity values never reached before. A set of spin-off analyses inspired by the dijet analysis looks for evidence of physics phenomena beyond the Standard Model at low invariant mass values using b-tagged jets selected by lower-threshold b-jet triggers, jets reconstructed at trigger level or jet pairs recoiling against another jet or a photon.

For the reasons and the results outlined in this thesis, the exotic dijet analysis represents the perfect way to rapidly identifying striking evidence of physics beyond the Standard Model.

Bibliography

[1] J. J. Aubert et al., *Experimental Observation of a Heavy Particle J*, Phys. Rev. Lett. 33 (1974) 1404–1406. DOI:10.1103/PhysRevLett.33.1404.

[2] J. E. Augustin et al., *Discovery of a Narrow Resonance in e^+e^- Annihilation*, Phys. Rev. Lett. 33 (1974) 1406–1408. DOI:10.1103/PhysRevLett.33.1406.

[3] M. L. Perl et al., *Evidence for Anomalous Lepton Production in $e^+ - e^-$ Annihilation*, Phys. Rev. Lett. 35 (1975) 1489–1492. DOI:10.1103/PhysRevLett.35.1489.

[4] S. W. Herb et al., *Observation of a Dimuon Resonance at 9.5 GeV in 400 GeV Proton-Nucleus Collisions*, Phys. Rev. Lett. 39 (1977) 252–255. DOI:10.1103/PhysRevLett.39.252.

[5] G. Arnison et al., *Experimental observation of lepton pairs of invariant mass around 95 GeV/c^2 at the CERN SPS collider*, Physics Letters B 126 no. 5, (1983) 398 – 410. DOI:10.1016/0370-2693(83)90188-0.

[6] G. Arnison et al., *Experimental observation of isolated large transverse energy electrons with associated missing energy at s=540 GeV*, Physics Letters B 122 no. 1, (1983) 103 – 116. DOI:10.1016/0370-2693(83)91177-2.

[7] CDF Collaboration, F. Abe et al., *Observation of top quark production in $\bar{p}p$ collisions*, Phys. Rev. Lett. 74 (1995) 2626–2631. DOI:10.1103/PhysRevLett.74.2626, arXiv:hep-ex/9503002 [hep-ex].

[8] D0 Collaboration, S. Abachi et al., *Observation of the top quark*, Phys. Rev. Lett. 74 (1995) 2632–2637. DOI:10.1103/PhysRevLett.74.2632, arXiv:hep-ex/9503003 [hep-ex].

[9] ATLAS Collaboration, G. Aad et al., *Observation of a new particle in the search for the Standard Model Higgs boson with the ATLAS detector at the LHC*, Phys. Lett. B716 (2012) 1–29. DOI:10.1016/j.physletb.2012.08.020, arXiv:1207.7214 [hep-ex].

[10] CMS Collaboration, S. Chatrchyan et al., *Observation of a new boson at a mass of 125 GeV with the CMS experiment at the LHC*, Phys. Lett. B716 (2012) 30–61. DOI:10.1016/j.physletb.2012.08.021, arXiv:1207.7235 [hep-ex].

[11] ATLAS Collaboration, G. Aad et al., *Search for new phenomena in the dijet mass distribution using pp collision data at $\sqrt{s} = 8$ TeV with the ATLAS detector*, Phys. Rev. D91 no. 5, (2015) 052007. DOI:10.1103/PhysRevD.91.052007, arXiv:1407.1376 [hep-ex].

[12] ATLAS Collaboration, G. Aad et al., *Search for new phenomena in dijet mass and angular distributions from pp collisions at $\sqrt{s} = 13$ TeV with the ATLAS detector*, Phys. Lett. B754 (2016) 302–322. DOI:10.1016/j.physletb.2016.01.032, arXiv:1512.01530 [hep-ex].

[13] L. E. (ed.) and P. B. (ed.), *LHC machine*, JINST 3 (2008) S08001. DOI:10.1088/1748-0221/3/08/S08001.

[14] O. Bruning and P. Collier, *Building a behemoth*, Nature 448 no. 7151, (2007) 285–289. DOI:10.1038/nature06077.

[15] ALICE Collaboration, K. Aamodt et al., *The ALICE experiment at the CERN LHC*, Journal of Instrumentation 3 no. 08, (2008) S08002. DOI:10.1088/1748-0221/3/08/S08002.

[16] CMS Collaboration, S. Chatrchyan et al., *The CMS experiment at the CERN LHC*, Journal of Instrumentation 3 no. 08, (2008) S08004. DOI:10.1088/1748-0221/3/08/S08004.

[17] LHCb Collaboration, A. A. Alves Jr. et al., *The LHCb Detector at the LHC*, Journal of Instrumentation 3 no. 08, (2008) S08005. DOI:10.1088/1748-0221/3/08/S08005.

[18] C. Lefevre, *LHC: the guide*, `https://cds.cern.ch/record/1092437`, Jan, 2008.

[19] ATLAS Collaboration, *Luminosity Public Results*, `https://twiki.cern.ch/twiki/bin/view/AtlasPublic/LuminosityPublicResults`.

[20] ATLAS Collaboration, *Luminosity Public Results Run-2*, `https://twiki.cern.ch/twiki/bin/view/AtlasPublic/LuminosityPublicResultsRun2`.

[21] ATLAS Collaboration, *ATLAS Data Summary*, `https://atlas.web.cern.ch/Atlas/GROUPS/DATAPREPARATION/DataSummary/`.

[22] *LHC Commissioning*, `http://lhc-commissioning.web.cern.ch/lhc-commissioning/`.

[23] ATLAS Collaboration, *ATLAS Phase-II Upgrade Scoping Document*, Tech. Rep. CERN-LHCC-2015-020. LHCC-G-166, CERN, Geneva, Sep, 2015. `https://cds.cern.ch/record/2055248`.

[24] *High Luminosity Large Hadron Collider*, `http://hilumilhc.web.cern.ch/about/hl-lhc-project`.

[25] ATLAS Collaboration, *The ATLAS experiment at the CERN Large Hadron Collider*, JINST 3 (2008) S08003. DOI:10.1088/1748-0221/3/08/S08003.

[26] M. Capeans, G. Darbo, K. Einsweiller, M. Elsing, T. Flick, M. Garcia-Sciveres, C. Gemme, H. Pernegger, O. Rohne, and R. Vuillermet, *ATLAS Insertable B-Layer Technical Design Report*, Tech. Rep. CERN-LHCC-2010-013. ATLAS-TDR-19, CERN, Geneva, Sep, 2010. `http://cds.cern.ch/record/1291633`.

[27] *IBL Module Loading onto Stave and Quality Check*, Tech. Rep. ATL-INDET-PUB-2015-003, CERN, Geneva, Dec, 2015. `https://cds.cern.ch/record/2110639`.

[28] R. Wigmans, *Advances in hadron calorimetry*, Ann. Rev. Nucl. Part. Sci. 41 (1991) 133–185. DOI:10.1146/annurev.ns.41.120191.001025.

[29] *2015 start-up trigger menu and initial performance assessment of the ATLAS trigger using Run-2 data*, Tech. Rep. ATL-DAQ-PUB-2016-001, CERN, Geneva, Mar, 2016. `https://cds.cern.ch/record/2136007`.

[30] F. Halzen and A. D. Martin, *Quarks and leptons: an introductory course in modern particle physics.* John Wiley & sons, New York, NY, 1984.

[31] W. E. Burcham and M. Jobes, *Nuclear and particle physics.* Longman, Essex, UK, 1995.

[32] M. Maggiore, *A modern introduction to quantum field theory.* Oxford Master Series in Statistical, Computational and Theoretical Physics. Oxford University, Oxford, UK, 2005.

[33] F. Guescini, *Measurement of $Z/\gamma^* \to \mu\mu$ differential cross section with the ATLAS experiment at LHC*, Master's thesis, University of Rome Tor Vergata, Rome, 2011. CERN-THESIS-2011-154. Presented 30 Sept. 2011. `https://cds.cern.ch/record/1398200`.

[34] S. L. Glashow, *Partial-symmetries of weak interactions*, Nuclear Physics 22 no. 4, (1961) 579 – 588. DOI:10.1016/0029-5582(61)90469-2.

[35] S. Weinberg, *A Model of Leptons*, Phys. Rev. Lett. 19 no. 21, (1967) 1264–1266. DOI:10.1103/PhysRevLett.19.1264.

[36] A. Salam, *Weak and Electromagnetic Interactions*, Elementary Particle Theory, Proceedings of the 8th Nobel Symposium (1968) 367–377.

[37] F. Englert and R. Brout, *Broken Symmetry and the Mass of Gauge Vector Mesons*, Phys. Rev. Lett. 13 no. 9, (1964) 321–323. DOI:10.1103/PhysRevLett.13.321.

[38] P. W. Higgs, *Broken Symmetries and the Masses of Gauge Bosons*, Phys. Rev. Lett. 13 no. 16, (1964) 508–509. DOI:10.1103/PhysRevLett.13.508.

[39] G. S. Guralnik, C. R. Hagen, and T. W. B. Kibble, *Global Conservation Laws and Massless Particles*, Phys. Rev. Lett. 13 no. 20, (1964) 585–587. DOI:10.1103/PhysRevLett.13.585.

[40] T. Plehn, *LHC Phenomenology for Physics Hunters*, pp. , 125–180. 2010. DOI:10.1142/9789812838360_0003, arXiv:0810.2281 [hep-ph].

[41] S. Agostinelli et al., *Geant4 - a simulation toolkit*, Nuclear Instruments and Methods in Physics Research Section A: Accelerators, Spectrometers, Detectors and Associated Equipment 506 no. 3, (2003) 250 – 303. DOI:10.1016/S0168-9002(03)01368-8.

[42] T. Sjostrand, S. Mrenna, and P. Z. Skands, *A Brief Introduction to PYTHIA 8.1*, Comput. Phys. Commun. 178 (2008) 852–867. DOI:10.1016/j.cpc.2008.01.036, arXiv:0710.3820 [hep-ph].

[43] S. Frixione, P. Nason, and C. Oleari, *Matching NLO QCD computations with Parton Shower simulations: the POWHEG method*, JHEP 11 (2007) 070. DOI:10.1088/1126-6708/2007/11/070, arXiv:0709.2092 [hep-ph].

[44] M. Bahr et al., *Herwig++ Physics and Manual*, Eur. Phys. J. C58 (2008) 639–707. DOI:10.1140/epjc/s10052-008-0798-9, arXiv:0803.0883 [hep-ph].

[45] D. Dai. et al., *BlackMax: A black-hole event generator with rotation, recoil, split branes and brane tension*, Phys. Rev. D 77 (2008) 076007. DOI:10.1103/PhysRevD.77.076007, arXiv:0711.3012 [hep-ph].

[46] D. M. Gingrich, *Monte Carlo event generator for black hole production and decay in proton-proton collisions*, Comput. Phys. Commun. 181 (2010) 1917–1924. DOI:10.1016/j.cpc.2010.07.027, arXiv:0911.5370 [hep-ph].

[47] T. Gleisberg, S. Hoeche, F. Krauss, A. Schalicke, S. Schumann, and J.-C. Winter, *SHERPA 1. alpha: A Proof of concept version*, JHEP 02 (2004) 056. DOI:10.1088/1126-6708/2004/02/056, arXiv:hep-ph/0311263 [hep-ph].

[48] A. Belyaev, N. D. Christensen, and A. Pukhov, *CalcHEP 3.4 for collider physics within and beyond the Standard Model*, Comput. Phys. Commun. 184 (2013) 1729–1769. DOI:10.1016/j.cpc.2013.01.014, arXiv:1207.6082 [hep-ph].

[49] J. Alwall, M. Herquet, F. Maltoni, O. Mattelaer, and T. Stelzer, *MadGraph 5 : Going Beyond*, JHEP 06 (2011) 128. DOI:10.1007/JHEP06(2011)128, arXiv:1106.0522 [hep-ph].

[50] J. E. Huth, N. Wainer, K. Meier, N. J. Hadley, F. Aversa, M. Greco, P. Chiappetta, J. P. Guillet, S. Ellis, Z. Kunszt, and D. E. Soper, *Toward a standardization of jet definitions*, Tech. Rep. FERMILAB-CONF-90-249-E, Dec, 1990. `https://cds.cern.ch/record/217490`.

[51] G. P. Salam, *Towards Jetography*, Eur. Phys. J. C67 (2010) 637–686. DOI:10.1140/epjc/s10052-010-1314-6, arXiv:0906.1833 [hep-ph].

[52] C. Buttar et al., *Standard Model Handles and Candles Working Group: Tools and Jets Summary Report*, pp. , 121–214. 2008. arXiv:0803.0678 [hep-ph].

[53] G. P. Salam and G. Soyez, *A Practical Seedless Infrared-Safe Cone jet algorithm*, JHEP 05 (2007) 086. DOI:10.1088/1126-6708/2007/05/086, arXiv:0704.0292 [hep-ph].

[54] M. Cacciari, G. P. Salam, and G. Soyez, *The Anti-k(t) jet clustering algorithm*, JHEP 04 (2008) 063. DOI:10.1088/1126-6708/2008/04/063, arXiv:0802.1189 [hep-ph].

[55] M. Cacciari, G. P. Salam, and G. Soyez, *FastJet User Manual*, Eur. Phys. J. C72 (2012) 1896. DOI:10.1140/epjc/s10052-012-1896-2, arXiv:1111.6097 [hep-ph].

[56] M. Cacciari and G. P. Salam, *Dispelling the N^3 myth for the k_t jet-finder*, Phys. Lett. B641 (2006) 57–61. DOI:10.1016/j.physletb.2006.08.037, arXiv:hep-ph/0512210 [hep-ph].

[57] ATLAS Collaboration, *Event Displays from Collision Data*, `https://twiki.cern.ch/twiki/bin/view/AtlasPublic/EventDisplayRun2Collisions`.

[58] ATLAS Collaboration, G. Aad et al., *Jet energy measurement and its systematic uncertainty in proton-proton collisions at $\sqrt{s} = 7$ TeV with the ATLAS detector*, Eur. Phys. J. C75 (2015) 17. DOI:10.1140/epjc/s10052-014-3190-y, arXiv:1406.0076 [hep-ex].

[59] *Monte Carlo Calibration and Combination of In-situ Measurements of Jet Energy Scale, Jet Energy Resolution and Jet Mass in ATLAS*, Tech. Rep. ATLAS-CONF-2015-037, CERN, Geneva, Aug, 2015. `https://cds.cern.ch/record/2044941`.

[60] W. Lampl, S. Laplace, D. Lelas, P. Loch, H. Ma, S. Menke, S. Rajagopalan, D. Rousseau, S. Snyder, and G. Unal, *Calorimeter Clustering Algorithms: Description and Performance*, Tech. Rep. ATL-LARG-PUB-2008-002, ATL-COM-LARG-2008-003, CERN, Geneva, Apr, 2008. `https://cds.cern.ch/record/1099735`.

[61] *Jet Calibration and Systematic Uncertainties for Jets Reconstructed in the ATLAS Detector at $\sqrt{s} = 13$ TeV*, Tech. Rep. ATL-PHYS-PUB-2015-015, CERN, Geneva, Jul, 2015. `https://cds.cern.ch/record/2037613`.

[62] ATLAS Collaboration, G. Aad et al., *Performance of pile-up mitigation techniques for jets in pp collisions at $\sqrt{s} = 8$ TeV using the ATLAS detector*, arXiv:1510.03823 [hep-ex].

[63] M. Cacciari, G. P. Salam, and G. Soyez, *The Catchment Area of Jets*, JHEP 04 (2008) 005. DOI:10.1088/1126-6708/2008/04/005, arXiv:0802.1188 [hep-ph].

[64] ATLAS Collaboration, M. Aaboud et al., *Search for resonances in the mass distribution of jet pairs with one or two jets identified as b-jets in proton–proton collisions at $\sqrt{s} = 13$ TeV with the ATLAS detector*, Phys. Lett. B759 (2016) 229–246. DOI:10.1016/j.physletb.2016.05.064, arXiv:1603.08791 [hep-ex].

[65] ATLAS Collaboration, *Commissioning of the ATLAS high-performance b-tagging algorithms in the 7 TeV collision data*, Tech. Rep. ATLAS-CONF-2011-102, CERN, Geneva, Jul, 2011. `http://cds.cern.ch/record/1369219`.

[66] *Calibration of the performance of b-tagging for c and light-flavour jets in the 2012 ATLAS data*, Tech. Rep. ATLAS-CONF-2014-046, CERN, Geneva, Jul, 2014. `https://cds.cern.ch/record/1741020`.

[67] *Expected performance of the ATLAS b-tagging algorithms in Run-2*, Tech. Rep. ATL-PHYS-PUB-2015-022, CERN, Geneva, Jul, 2015. `http://cds.cern.ch/record/2037697`.

[68] *The Optimization of ATLAS Track Reconstruction in Dense Environments*, Tech. Rep. ATL-PHYS-PUB-2015-006, CERN, Geneva, Mar, 2015. `https://cds.cern.ch/record/2002609`.

[69] F. Guescini and B. P. Nachman, *Measurement of Jet Angular Resolution*, Tech. Rep. ATL-COM-PHYS-2013-1467, CERN, Geneva, Oct, 2013. `https://cds.cern.ch/record/1617313`.

[70] *Summary of ATLAS Pythia 8 tunes*, Tech. Rep. ATL-PHYS-PUB-2012-003, CERN, Geneva, Aug, 2012. `https://cds.cern.ch/record/1474107`.

[71] H.-L. Lai, M. Guzzi, J. Huston, Z. Li, P. M. Nadolsky, et al., *New parton distributions for collider physics*, Phys.Rev. D82 (2010) 074024. DOI:10.1103/PhysRevD.82.074024, arXiv:1007.2241 [hep-ph].

[72] S. Gieseke, C. Rohr, and A. Siodmok, *Colour reconnections in Herwig++*, Eur. Phys. J. C72 (2012) 2225. DOI:10.1140/epjc/s10052-012-2225-5, arXiv:1206.0041 [hep-ph].

[73] J. Pumplin, D. R. Stump, J. Huston, H. L. Lai, P. M. Nadolsky, and W. K. Tung, *New generation of parton distributions with uncertainties from global QCD analysis*, JHEP 07 (2002) 012. DOI:10.1088/1126-6708/2002/07/012, arXiv:hep-ph/0201195 [hep-ph].

[74] ATLAS Analysis Software group, *PileUpReweightingTool*, `https://twiki.cern.ch/twiki/bin/viewauth/AtlasProtected/ExtendedPileupReweighting`.

[75] G. Aad, P. Behera, W. H. Bell, U. Bitenc, G. Brandt, T. Eifert, H. M. Gray, J. Katzy, A. Kastanas, M. Kayl, O. Kepka, T. Kuhl, R. Kwee, M. Leyton, M. Limper, A. Lister, R. Meera-Lebbai, S. Nektarijevi, E. Nurse, K. Rosbach, A. Salzburger, M. Warsinsky, and R. Zaidan, *Track Reconstruction Efficiency in* $\sqrt{s} = 7$ TeV *Data for Tracks with* $p_{\mathrm{T}} > 100$ MeV, Tech. Rep. ATL-PHYS-INT-2011-001, CERN, Geneva, Jan, 2011. `https://cds.cern.ch/record/1319318`.

[76] R. M. Harris and K. Kousouris, *Searches for Dijet Resonances at Hadron Colliders*, Int. J. Mod. Phys. A26 (2011) 5005–5055. DOI:10.1142/S0217751X11054905, arXiv:1110.5302 [hep-ex].

[77] G. Choudalakis, *On hypothesis testing, trials factor, hypertests and the BumpHunter*, in *Proceedings, PHYSTAT 2011 Workshop on Statistical Issues Related to Discovery Claims in Search Experiments and Unfolding*. January, 2011. arXiv:1101.0390 [physics.data-an].

[78] ATLAS Collaboration, *Search for New Phenomena in the Dijet Mass Distribution updated using 13.0* fb^{-1} *of pp Collisions at sqrts* $= 8$ *TeV collected by the ATLAS Detector*, Tech. Rep. ATLAS-CONF-2012-148, CERN, Geneva, Nov, 2012. `https://cds.cern.ch/record/1493487`.

[79] *ATLAS Run 1 Pythia8 tunes*, Tech. Rep. ATL-PHYS-PUB-2014-021, CERN, Geneva, Nov, 2014. `http://cds.cern.ch/record/1966419`.

[80] S. Carrazza, S. Forte, and J. Rojo, *Parton Distributions and Event Generators*, pp. , 89–96. 2013. arXiv:1311.5887 [hep-ph].

[81] S. Dittmaier, A. Huss, and C. Speckner, *Weak radiative corrections to dijet production at hadron colliders*, JHEP 11 (2012) 095. DOI:10.1007/JHEP11(2012)095, arXiv:1210.0438 [hep-ph].

[82] Z. Nagy, *Three jet cross-sections in hadron hadron collisions at next-to-leading order*, Phys. Rev. Lett. 88 (2002) 122003. DOI:10.1103/PhysRevLett.88.122003, arXiv:hep-ph/0110315 [hep-ph].

[83] Z. Nagy, *Next-to-leading order calculation of three jet observables in hadron hadron collision*, Phys. Rev. D68 (2003) 094002. DOI:10.1103/PhysRevD.68.094002, arXiv:hep-ph/0307268 [hep-ph].

[84] S. Catani and M. H. Seymour, *A General algorithm for calculating jet cross-sections in NLO QCD*, Nucl. Phys. B485 (1997) 291–419. DOI:10.1016/S0550-3213(96)00589-5, arXiv:hep-ph/9605323 [hep-ph], [Erratum: Nucl. Phys.B510,503(1998)].

[85] A. Ashkenazi et al., *ATLAS search in 2012 data for new phenomena in dijet mass distributions using pp collisions at* $\sqrt{s} = 8$ *TeV*, Tech. Rep.

ATL-COM-PHYS-2013-1518, CERN, Geneva, Nov, 2013. `https://cds.cern.ch/record/1626591`.

[86] U. Baur, I. Hinchliffe, and D. Zeppenfeld, *Excited Quark Production at Hadron Colliders*, Int. J. Mod. Phys. A2 (1987) 1285. DOI:10.1142/S0217751X87000661.

[87] U. Baur, M. Spira, and P. M. Zerwas, *Excited-quark and -lepton production at hadron colliders*, Phys. Rev. D 42 (1990) 815–824. DOI:10.1103/PhysRevD.42.815.

[88] N. Arkani-Hamed, S. Dimopoulos, and G. Dvali, *Phenomenology, astrophysics and cosmology of theories with submillimeter dimensions and TeV scale quantum gravity*, Phys.Rev. D59 (1999) 086004. DOI:10.1103/PhysRevD.59.086004, arXiv:hep-ph/9807344 [hep-ph].

[89] L. Randall and R. Sundrum, *A Large mass hierarchy from a small extra dimension*, Phys. Rev. Lett. 83 (1999) 3370–3373. DOI:10.1103/PhysRevLett.83.3370, arXiv:hep-ph/9905221 [hep-ph].

[90] G. Altarelli, B. Mele, and M. Ruiz-Altaba, *Searching for New Heavy Vector Bosons in $p\bar{p}$ Colliders*, Z. Phys. C45 (1989) 109. DOI:10.1007/BF01552335, 10.1007/BF01556677, [Erratum: Z. Phys.C47,676(1990)].

[91] M. V. Chizhov, V. A. Bednyakov, and J. A. Budagov, *A unique signal of excited bosons in dijet data from pp collisions*, Physics of Atomic Nuclei 75 no. 1, (2012) 90–96. DOI:10.1134/S1063778812010061.

[92] M. V. Chizhov and G. Dvali, *Origin and Phenomenology of Weak-Doublet Spin-1 Bosons*, Phys. Lett. B703 (2011) 593–598. DOI:10.1016/j.physletb.2011.08.056, arXiv:0908.0924 [hep-ph].

[93] M. V. Chizhov, *A Reference Model for Anomalously Interacting Bosons*, Phys. Part. Nucl. Lett. 8 (2011) 512–516. DOI:10.1134/S1547477111060045, arXiv:1005.4287 [hep-ph].

[94] T. Han, I. Lewis, and Z. Liu, *Colored Resonant Signals at the LHC: Largest Rate and Simplest Topology*, JHEP 12 (2010) 085. DOI:10.1007/JHEP12(2010)085, arXiv:1010.4309 [hep-ph].

[95] D. Abercrombie et al., *Dark Matter Benchmark Models for Early LHC Run-2 Searches: Report of the ATLAS/CMS Dark Matter Forum*, arXiv:1507.00966 [hep-ex].

[96] M. Chala, F. Kahlhoefer, M. McCullough, G. Nardini, and K. Schmidt-Hoberg, *Constraining Dark Sectors with Monojets and Dijets*, JHEP 07 (2015) 089. DOI:10.1007/JHEP07(2015)089, arXiv:1503.05916 [hep-ph].

[97] J. Alwall, R. Frederix, S. Frixione, V. Hirschi, F. Maltoni, O. Mattelaer, H. S. Shao, T. Stelzer, P. Torrielli, and M. Zaro, *The automated computation of tree-level*

and next-to-leading order differential cross sections, and their matching to parton shower simulations, JHEP 07 (2014) 079. DOI:10.1007/JHEP07(2014)079, arXiv:1405.0301 [hep-ph].

[98] *ATLAS Luminosity Calculator*, `https://atlas-lumicalc.cern.ch/`.

[99] V. Lendermann, J. Haller, M. Herbst, K. Kruger, H.-C. Schultz-Coulon, and R. Stamen, *Combining Triggers in HEP Data Analysis*, Nucl. Instrum. Meth. A604 (2009) 707–718. DOI:10.1016/j.nima.2009.03.173, arXiv:0901.4118 [hep-ex].

[100] ATLAS Collaboration, *Search for New Particles in Two-Jet Final States in 7 TeV Proton-Proton Collisions with the ATLAS Detector at the LHC*, Phys. Rev. Lett. 105 (2010) 161801. DOI:10.1103/PhysRevLett.105.161801, arXiv:1008.2461 [hep-ex].

[101] ATLAS Collaboration, *Search for New Physics in Dijet Mass and Angular Distributions in pp Collisions at $\sqrt{s} = 7$ TeV Measured with the ATLAS Detector*, New J. Phys. 13 (2011) 053044. DOI:10.1088/1367-2630/13/5/053044, arXiv:1103.3864 [hep-ex].

[102] ATLAS Collaboration, G. Aad et al., *Search for New Physics in the Dijet Mass Distribution using 1 fb^{-1} of pp Collision Data at $\sqrt{s}$ =7 TeV collected by the ATLAS Detector*, Phys. Lett. B708 (2012) 37–54. DOI:10.1016/j.physletb.2012.01.035, arXiv:1108.6311 [hep-ex].

[103] ATLAS Collaboration, *ATLAS search for new phenomena in dijet mass and angular distributions using pp collisions at $\sqrt{s} = 7$ TeV*, JHEP 01 (2013) 029. DOI:10.1007/JHEP01(2013)029, arXiv:1210.1718 [hep-ex].

[104] N. Morange, J. T. Childers, S. Hillier, and B. Mansoulié, *Study and validation of the BCID of the L1Calo at very high transverse energies*, Tech. Rep. ATL-DAQ-INT-2011-001, CERN, Geneva, May, 2011. `https://cds.cern.ch/record/1352150`.

[105] CMS Collaboration, V. Khachatryan et al., *Search for resonances and quantum black holes using dijet mass spectra in proton-proton collisions at $\sqrt{s} = 8$ TeV*, Phys. Rev. D91 no. 5, (2015) 052009. DOI:10.1103/PhysRevD.91.052009, arXiv:1501.04198 [hep-ex].

[106] CMS Collaboration, V. Khachatryan et al., *Search for narrow resonances decaying to dijets in proton-proton collisions at $\sqrt{s} = 13$ TeV*, arXiv:1512.01224 [hep-ex].

[107] ATLAS TileCal working group, *TileTripReader*, `https://twiki.cern.ch/twiki/bin/view/Atlas/TileTripReader`.

[108] M. Baak, C. Guyot, M. Hauschild, R. Hawkings, B. Heinemann, A. Höcker, M. Martínez-Pérez, D. Malon, P. Onyisi, and E. Torrence, *Data Quality Status Flags and Good Run Lists for Physics Analysis in ATLAS*, Tech. Rep.

ATL-COM-GEN-2009-015, CERN, Geneva, Mar, 2009. https://cds.cern.ch/record/1168026.

[109] ATLAS Collaboration, *Selection of jets produced in proton-proton collisions with the ATLAS detector using 2011 data*, Tech. Rep. ATLAS-CONF-2012-020, CERN, Geneva, Mar, 2012. https://cds.cern.ch/record/1430034.

[110] S. G. Cole, *Private communication*,.

[111] ATLAS JetETMiss working group, *BCHCleaningTool*, https://twiki.cern.ch/twiki/bin/view/AtlasProtected/BCHCleaningTool.

[112] *Selection of jets produced in 13 TeV proton-proton collisions with the ATLAS detector*, Tech. Rep. ATLAS-CONF-2015-029, CERN, Geneva, Jul, 2015. https://cds.cern.ch/record/2037702.

[113] CDF Collaboration, F. Abe et al., *Search for quark compositeness, axigluons, and heavy particles using the dijet invariant mass spectrum observed in $p\bar{p}$ collisions*, Phys. Rev. Lett. 71 (1993) 2542–2546. DOI:10.1103/PhysRevLett.71.2542.

[114] DØ Collaboration, V. Abazov et al., *Search for new particles in the two-jet decay channel with the DØ detector*, Phys. Rev. D 69 (2004) 111101. DOI:10.1103/PhysRevD.69.111101.

[115] UA2 Collaboration, J. Alitti et al., *A measurement of two-jet decays of the W and Z bosons at the CERN $\overline{p}p$ collider*, Z. Phys. C 49 no. CERN-PPE-90-105, (1990) 17–28. 35 p, https://cds.cern.ch/record/210698.

[116] CDF Collaboration, F. Abe et al., *Search for new particles decaying to dijets in $p\bar{p}$ collisions at $\sqrt{s} = 1.8$ TeV*, Phys. Rev. Lett. 74 (1995) 3538–3543. DOI:10.1103/PhysRevLett.74.3538, arXiv:hep-ex/9501001 [hep-ex].

[117] CMS Collaboration, V. Khachatryan et al., *Search for Dijet Resonances in 7 TeV pp Collisions at CMS*, Phys. Rev. Lett. 105 (2010) 211801. DOI:10.1103/PhysRevLett.105.211801, 10.1103/PhysRevLett.106.029902, arXiv:1010.0203 [hep-ex].

[118] CMS Collaboration, S. Chatrchyan et al., *Search for Resonances in the Dijet Mass Spectrum from 7 TeV pp Collisions at CMS*, Phys. Lett. B704 (2011) 123–142. DOI:10.1016/j.physletb.2011.09.015, arXiv:1107.4771 [hep-ex].

[119] CMS Collaboration, V. Khachatryan et al., *Search for narrow resonances using the dijet mass spectrum in pp collisions at $\sqrt{s}$=8 TeV*, Phys. Rev. D87 no. 11, (2013) 114015. DOI:10.1103/PhysRevD.87.114015, arXiv:1302.4794 [hep-ex].

[120] CDF Collaboration, T. Aaltonen et al., *Search for new particles decaying into dijets in proton-antiproton collisions at $\sqrt{s}$ = 1.96 TeV*, Phys. Rev. D79 (2009) 112002. DOI:10.1103/PhysRevD.79.112002, arXiv:0812.4036 [hep-ex].

[121] ATLAS Collaboration, G. Aad et al., *Search for New Phenomena in Dijet Angular Distributions in Proton-Proton Collisions at $\sqrt{s} = 8$ TeV Measured with the ATLAS Detector*, Phys. Rev. Lett. 114 no. 22, (2015) 221802. DOI:10.1103/PhysRevLett.114.221802, arXiv:1504.00357 [hep-ex].

[122] CDF Collaboration, F. Abe et al., *Search for new particles decaying to dijets at CDF*, Phys. Rev. D55 (1997) 5263–5268. DOI:10.1103/PhysRevD.55.R5263, arXiv:hep-ex/9702004 [hep-ex].

[123] ATLAS Collaboration, G. Aad et al., *Search for microscopic black holes and string balls in final states with leptons and jets with the ATLAS detector at sqrt(s) = 8 TeV*, JHEP 08 (2014) 103. DOI:10.1007/JHEP08(2014)103, arXiv:1405.4254 [hep-ex].

[124] S. S. Wilks, *The Large-Sample Distribution of the Likelihood Ratio for Testing Composite Hypotheses*, Ann. Math. Statist. 9 no. 1, (1938) 60–62. DOI:10.1214/aoms/1177732360.

[125] G. Choudalakis and D. Casadei, *Plotting the Differences Between Data and Expectation*, tech. rep., Nov, 2011. DOI:10.1140/epjp/i2012-12025-y, arXiv:1111.2062 [physics].

[126] T. P. A. Åkesson et al., *Search for New Phenomena in Dijet Events with the ATLAS Detector at $\sqrt{s}$ = 13 TeV with the full 2015 dataset*, Tech. Rep. ATL-COM-PHYS-2015-1205, CERN, Geneva, Sep, 2015. `https://cds.cern.ch/record/2055242`.

[127] C. Rover, C. Messenger, and R. Prix, *Bayesian versus frequentist upper limits*, pp. , 158–163. January, 2011. arXiv:1103.2987 [physics.data-an].

[128] A. Caldwell, D. Kollár, and K. Kröninger, *BAT - The Bayesian analysis toolkit*, Computer Physics Communications 180 no. 11, (2009) 2197 – 2209. DOI:10.1016/j.cpc.2009.06.026.

[129] *Dijet resonance searches with the ATLAS detector at 14 TeV LHC*, Tech. Rep. ATL-PHYS-PUB-2015-004, CERN, Geneva, Mar, 2015. `https://cds.cern.ch/record/2002136`.

[130] *Performance assumptions for an upgraded ATLAS detector at a High-Luminosity LHC*, Tech. Rep. ATL-PHYS-PUB-2013-004, CERN, Geneva, Mar, 2013. `https://cds.cern.ch/record/1527529`.

[131] ATLAS Collaboration, *Improved luminosity determination in pp collisions at $\sqrt{s}$ = 7 TeV using the ATLAS detector at the LHC*, Eur.Phys.J. C73 (2013) 2518. DOI:10.1140/epjc/s10052-013-2518-3, arXiv:1302.4393 [hep-ex].